Integrated Manipulation, Detection and Counting of Cells in Biofluids

A thesis for the degree of

MASTER OF SCIENCE

Mary O'Sullivan BSc.

School of Physical Sciences

Dublin City University

Research Supervisor

Prof. Jens Ducrée

September 2014

Declaration

I hereby certify that this material, which I now submit for assessment on the programme of study leading to the award of Master of Science is entirely my own work, that I have exercised reasonable care to ensure that the work is original, and does not to the best of my knowledge breach any law of copyright, and has not been taken from the work of others save and to the extent that such work has been cited and acknowledged within the text of my work.

Signed: _____

ID No.:_____

Date: _____

Acknowledgements

First, I would like to thank Prof. Jens Ducrée for all his help during the last number of years, as well as affording me the opportunity to work in his accomplished research group in DCU. Thank you for all of the advice, guidance and understanding throughout my time in the microfluidics group.

I would also like to thank all of my colleagues in the microfluidics research group in DCU – particularly those who have offered valuable advice and guidance with my research work and answered my questions. Special thanks go to Robert, Damien, Macdara, Dan and Jen for being there to bounce ideas off of and help me find solutions to research challenges I faced.

I would also like to thank all those who have guided and supported me over the years from my undergraduate degree in DCU, during my research in the NCSR and beyond – thank you to Dr. Rob Copperwhite, Dr. Mohamed Oubaha, Dr. Cathy Boothman and Prof. Colette McDonagh – the research experience I gained in the NCSR was a thoroughly enjoyable and invaluable one. Similarly, thanks go to the lecturing staff in the physics department who were always on hand to answer queries and support learning and foster a scientific curiosity that becomes part of every graduate in the department.

Another thank you goes to Pat and Lorcan who were always on hand for technical queries, as well as Celine and Lisa who were incredibly helpful and knowledgeable regarding any administrative issues or queries that I may have had.

I would also like to thank my friends who have listened to my worries and supported and helped me through challenges I faced, academic or otherwise, over the past few years. Thank you to Damien, Jen, Marian, Gráinne, Adam, Cathal, Mike, Sinéad, Maura, Ciarán and Nina.

Special thanks go to my family, without whom I would not have been able to attend third level education or embark on a career in physics. Their support and encouragement during my undergraduate and postgraduate studies has been unwavering and I cannot thank them enough for that.

Finally I would like to thank Sam who has been my greatest cheerleader to date, despite dealing with all of the worries and challenges that my studies have generated. Her advice, support and empathy have made the whole process possible, and her patience, care and understanding throughout are greatly appreciated.

Publications

2014

King, D., **O'Sullivan, M.**, & Ducrée, J. (2014). Optical detection strategies for centrifugal microfluidic platforms. Journal of Modern Optics, 61(2), 85-101.

2012

Burger, R., Kirby, D., Glynn, M., Nwankire, C., **O'Sullivan, M**., Siegrist, J., Kinahan, D., Aguirre, G., Kijanka, G., Gorkin, R., & Ducrée, J. (2012). Centrifugal microfluidics for cell analysis. Current opinion in chemical biology, 16(3), 409-414.

2011

Copperwhite, R., **O'Sullivan, M**., Boothman, C., Gorin, A., McDonagh, C., & Oubaha, M. (2011). Development and characterisation of integrated microfluidics on waveguide-based photonic platforms fabricated from hybrid materials. *Microfluidics and nanofluidics*, *11*(3), 283-296.

Gorin, A., Copperwhite, R., Boothman, C., **O'Sullivan, M.**, McDonagh, C., & Oubaha, M. (2011). Low loss optical channel waveguides for the infrared range using niobium based hybrid sol–gel material. *Optics Communications*, *284*(8), 2164-2167.

Oubaha, M., Copperwhite, R., Gorin, A., Purlys, V., Boothman, C., **O'Sullivan, M.**, R, Gadonas., McDonagh, C., & MacCraith, B. D. (2011). Novel tantalum based photocurable hybrid sol–gel material employed in the fabrication of channel optical waveguides and three-dimensional structures. *Applied Surface Science*, *257*(7), 2995-2999.

Contents Page No:

Contents **Page No:**

Integrated Manipulation, Detection and Counting of Cells in Biofluids

by

Mary O'Sullivan

Abstract

The manipulation, trapping, detection and counting of cells in biological fluids is of critical importance to the areas of disease diagnosis, drug delivery and genomic applications in biomedical research. In recent times, this research has focussed on utilising the superior metering, separation, routing, mixing and incubation capabilities of centrifugal microfluidic "Lab on a Disk" (LOAD) technologies to tackle the challenge of handling numerous types of cells, proteins, genes and their reagents simultaneously. Furthermore, integrated optical detection systems are being developed in parallel to the aforementioned microfluidic technologies, to facilitate the accurate and inexpensive detection, imaging and counting of cells. This thesis describes a number of novel centrifugal microfluidic approaches towards the separation, capture and detection of white blood cells from whole blood. Firstly, a thorough review of the state-of-the art research in the areas of centrifugo-microfluidic cell handling and detection is outlined. Secondly, a series of physical size filtration and microcontact printing approaches for the capture and detection of biomimetic particles are described. Finally, the author assesses the suitability of sol-gel materials for waveguiding applications on disposable LOAD platforms and outlines areas of future work that would build upon the research undertaken in this thesis.

List of Figures Page No:

List of Figures Page No:

List of Figures Page No:

List of Figures Page No:

List of Tables: Page No:

List of Abbreviations

BSA	Bovine Serum Albumin
CCD	Charge-Coupled Device
CD	Compact Disk
CEC	Circulating Endothelial Cells
CTC	Circulating Tumour Cell
DC	Direct Current
DLD	Deterministic Lateral Displacement
DVD	Digital Versatile Disk
FITC	Fluoresceine Isothiocyanate
FOV	Field-of-View
HIV	Human Immunodeficiency Virus
IgG	Immunoglobulin G
LOAD	Lab-on-a-Disk
LOC	Lab-on-a-Chip
LOD	Limit of Detection
LUO	Laboratory Unit Operations
NA	Numerical Aperture
ODD	Optical Disk Drive
OTS	Octadecyltrichlorosilane
PBS	Phosphate Buffered Silane
PCR	Polymerise-Chain Reaction
PDMS	Polydimethylsiloxane
RBC	Red Blood Cell
RPM	Revolutions Per Minute
WBC	White Blood Cell

Chapter 1: Background and Motivation

1.1 Introduction

The capture, manipulation and analysis of cells has proven to be central to biomedical diagnostics in recent years, from disease diagnosis[1-8] and treatment[9-12] to drug discovery applications [13,14]. In particular, the drive to develop diagnostic devices for low resource environments such as third world countries has grown at a rapid rate, with devices becoming smaller, cheaper and more integrated with each passing year. Microfluidics, and more specifically, centrifugal microfluidics, offers a unique set of biofluid and cell handling capabilities that makes it ideal for carrying out a range of diagnostic tests, typically carried out on bulky, expensive and complex equipment in a laboratory environment.

This work focuses on combining the fluid and cell handling capabilities of centrifugal microfluidics and novel optical detection methods to develop an easy to use, inexpensive and integrated platform, capable of performing a 3-fold differential white blood cell count. Physical size filtration methods were investigated on a polymeric centrifugal microfluidic platform to differentiate and capture biometric beads of various sizes (section 2.1). As an alternative and/or complementary cell capture and detection approach, microcontact printing on functionalised glass slides was tested (section 3.2), towards the integration of this technology onto a centrifugal platform. Finally, optical detection components in the form of photocurable sol-gel waveguides were investigated in parallel to the above work (section 3.3), to create a complete sample-to-answer diagnostic platform. The methodologies, results and challenges of this research work will be discussed in the chapters that follow, concluding with future perspectives on how to build upon the work undertaken, along with areas of likely future development in this field. Before the work carried out over the course of this thesis is outlined and discussed, sections 1.2-1.5 will outline the theory and advantages associated with centrifugal microfluidic platforms and provide a brief review of the current literature on state-of-the-art developments in such platforms for cell-based applications. In addition, a review of the literature on optical detection technologies for centrifugal microfluidic platforms will be undertaken in section 1.6, with particular focus on optofluidics; a new field of integrated optical detection for microfluidic platforms.

1.2 Centrifugal Microfluidics

1.2.1 Background

The field of microfluidics - as we know it today - followed on from the explosion of micro electro mechanical systems, MEMS, into the scientific community in the 1980s [15,16]. Early research into developing microfluidic systems began by trying to adopt many of the fabrication and machining techniques that had been so well utilized by the MEMs industry. Microfluidic systems, in their modern form, have their foundations in the work of Manz *et al.* [17], with the development of Miniaturised Total Analysis Systems (uTAS) in the early 1990s. Since then microfluidics has been utilised to tackle a diverse field of technical and medical challenges such as point-of-care diagnostics, laboratory testing, military defence research, drug discovery and environmental testing [18,19]. Microfluidic devices manipulate small quantities of fluids, ranging from μL to ml volumes, in micron and submicron channels. As the field of microfluidics is founded upon much of the expertise of MEMs technologies, silicon and glass were initially used as core materials for microfluidic platforms [15]. Today, however, the vast majority of microfluidic devices are manufactured in polymers such as Polymethylmethacrylate (PMMA) and polydimethylsiloxane (PDMS) due to their biocompability, low cost and the ease and speed of fabrication associated with them [20-22].

From the inception of this field of research, there has been much interest in using microfluidics for point-of-care diagnostic applications [23-25]. Microfluidics shows great potential in catering for a multitude of global healthcare diagnostic challenges, with a growing need to deliver rapid diagnosis of diseases such as diabetes and heart disease in the first world. Point-of-care diagnostics could result in the aforementioned tests being carried out in a GP's office, facilitating significantly reduced waiting times for consultations and rapid disease diagnosis. More importantly, these diagnostic devices could be a key driver in delivering inexpensive and disposable diagnostics for diseases in resource poor settings such as the third world. While microfluidic technologies have made some progress towards tackling these issues, with a number of commercial successes [26], these so called “lab-on-a-chip” technologies have been hampered by the frequent need to provide external pumping mechanisms to drive the fluid flow within these devices. Centrifugal microfluidics provides a solution to this problem, by utilising the centrifugal force to drive and manipulate liquids in micron and submicron channels. Another significant advantage of centrifugally driven

systems is the elimination of off-chip fluid handling steps. A multitude of different fluids and bioparticles, e.g. cells, can be manipulated regardless of their characteristic thermal properties, pH viscosity and surface tension, due to the strength and degree of control associated with this artificial gravity force [27, 28]. Section 1.2.2, which follows, outlines the theory behind centrifugal microfluidic platforms, highlighting the unique advantages associated with this technology, particularly for cell-based applications.

1.2.2 Centrifugal Hydrodynamics

The theory associated with fluid flow and actuation of centrifugally driven microfluidic platforms has been discussed in detail previously [27-29] but will be outlined briefly below for completeness. As noted in the introduction to this section, microfluidics concerns the handling and manipulation of small quantities of fluids, ranging from μL to ml volumes, in micron and submicron channels of varying shapes. Centrifugal microfluidics advances this concept through the generation of an artificial gravity force, i.e. the centrifugal force, that drives liquids within the platform, as well as two other rotationally generated (pseudo) forces, all acting in the plane of rotation of the disk, as outlined in Figure 1.1 below.

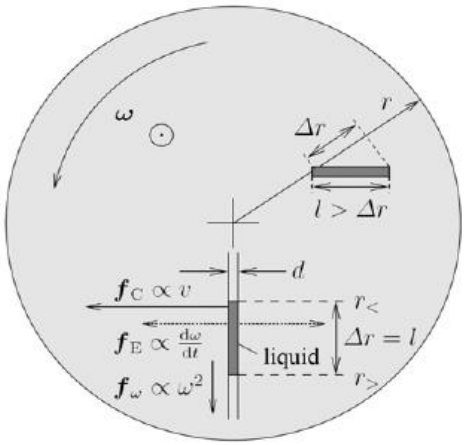

Figure 1.1: Schematic of centrifugal lab-on-a-chip platform rotating at an angular velocity ω, with the velocity vector pointing out of the page towards the reader. The cross at the centre of the diagram indicates the centre of rotation of the disk, while f_ω, f_c and f_E denote the centrifugal force density, the Coriolis force density and the Euler force density, respectively, acting on a liquid plug of length, l, and width, w. The direction of the Euler force, f_E, is dependent on whether the disk is rotating in the clockwise or anticlockwise direction. The liquid plug travels at velocity, v, in a microfluidic channel on the disk, with its absolute width, l, extending between $r_<$ and $r_>$ for a completely radially orientated plug. [Modified from [27]]

The centrifugal force, f_ω, acts directly away from the centre of rotation of the disk,

scaling with the square of the angular rotational frequency, ω.

$$f_\omega = \rho r \omega^2 \tag{1.1}$$

Particles of fluids at a distance r from the centre of a rotating platform, with a volume density, ρ, experience the radially directed centrifugal force density, while secondary forces i.e. the Euler force and the Coriolis force are induced by the spinning reference frame of the disk. The Euler force density acts as an opposing force to any changes in flow velocity, resulting in swirling currents driven by the rotation of the disk. It is denoted as follows:

$$f_E = \rho r \frac{d\omega}{dt} \tag{1.2}$$

Finally, the Coriolis force density acts in a direction perpendicular to the motion of particles/fluid and is proportional to the velocity, ν, of the liquid plug, as illustrated in Figure 1.1.

$$f_c = 2\rho\omega\nu \tag{1.3}$$

These three (pseudo) forces can be controlled to carry out advanced fluid and, consequently, bioparticle actuation and unit operations such as metering, siphoning, valving, flow splitting and mixing without external driving mechanisms [27]. As the experiments performed in this work are carried out under "stopped flow" conditions, sedimentation plays an important role in the actuation and handling of particles and cells under centrifugal actuation. The sedimentation of particles in their surrounding fluid medium is represented by the buoyancy force, F_g:

$$F_g = \Delta m r \omega^2 \tag{1.4}$$

The buoyancy force, F_g, is determined by the mass difference, Δm, between the particle and the liquid volume it displaces in its carrier medium. Acting in the opposing direction of the buoyancy force, F_g, is the viscous Stokes drag, F_d;

$$F_d = 6\pi\eta R\nu \tag{1.5}$$

where R and η represent the radius of a (spherical) particle and the fluid viscosity, respectively. Equilibrium between the buoyancy force and Stokes drag, i.e. a constant speed of sedimentation, can be achieved, for a given rotational frequency, ω, due to the direct proportionality of the Stokes drag, F_d, to the radial speed of the particle within the suspending fluid.

A final point of interest for particle handling in a centrifugal microfluidic platform is the delineation of the phase boundary, or so-called "shock interface", between the particle-free supernatant and the concentrated suspension, as illustrated in Figure 1.2 below.

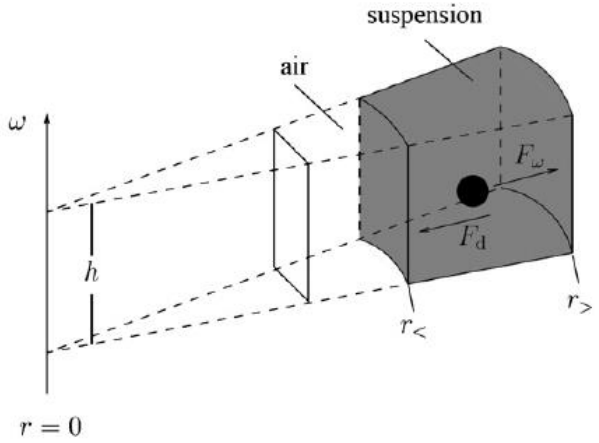

Figure 1.2: Schematic of the sedimentation of a particle suspended in a liquid medium, under the actuation of the centrifugal force, f_ω.[27] The liquid plug is contained within a volume of height h and outer and inner radial boundaries of $r_>$ and $r_<$. The motion of the particle is denoted by the buoyancy corrected force f_ω, which is determined by the mass difference, Δm, between the mass of the particle and the fluid it displaces.

The radial speed of this shock interface is given by the following formula by Haeberle *et al.* [30], modified below to keep notation consistent with the formulae in 1.1-1.5;

$$v_r = \frac{m}{\overline{f}}.\omega^2 r\left(1-\frac{\rho_{liquid}}{\rho_{particle}}\right) \tag{1.6}$$

where

$$\overline{f} \cong 6\pi\eta R v \tag{1.7}$$

denotes the so-called friction coefficient [30], resulting from the Stokes drag force acting in the opposing direction to the centrifugal force. R represents the particle radius and ρ_{liquid} and $\rho_{particle}$ represent the liquid and particle densities respectively. Readers

should note that the above equation for the radial speed of the shock interface, otherwise known as the drift velocity of the particle is only valid for spherical particles under laminar flow conditions, and neglects mutual interactions between particles [27, 31]. To compare the sedimentation rates between particles of various sizes and densities, the sedimentation coefficient, s_p, can be used;

$$s_p = \frac{m_p}{6\pi\eta R}\left(1 - \frac{\rho_{liquid}}{\rho_{particle}}\right) \tag{1.8}$$

where m_p is the mass of the particle. Differences in the sedimentation rates between particles of different sizes is utilised in the work on physical size filtration in section 3.1, in order to optimise the performance of the proposed bead separation and trapping platform. The use of sedimentation as well as a number of other recent state-of-the-art approaches for cell handling and capture on centrifugal platforms will be reviewed in sections 1.3 -1.5, which follow.

1.3 Metering, Purification and Separation of Cell Suspensions on Centrifugal Microfluidic Platforms

Centrifugal microfluidics offers a multitude of unit operations that enable the metering and purification of whole blood samples, as well as the separation, handling and capture techniques necessary to perform a variety of biological assays. Cell handling and detection operations typically begin with cell purification/separation to obtain one or more of the following:

1. Cell free liquid fraction e.g. plasma extraction from whole blood
2. The removal of cells in their entirety from their suspending liquid e.g. removal of RBCs from whole blood or, more commonly,
3. The retrieval of a particular cell population from a background population e.g. white blood cells from whole blood.

A number of comprehensive reviews, with particular relevance to this thesis, discussing recent state-of-the-art biomedical and cell based applications of centrifugal microfluidics have been undertaken by Burger *et al.*[32-33] and Gorkin *et al.* [34]. This thesis will briefly review some of the common methods of metering and purifying cell suspensions using centrifugal microfluidic techniques, before taking a more in depth

look at recent advances in cell and bioparticle handling and capture in section 1.5.

1.3.1 Sample Metering, Valving and Bioparticle Sedimentation

For a completely sample-to-answer centrifugal microfluidic assay, sample metering is undertaken to derive a precise volume of sample for analysis. In addition, for cell-based assays, plasma is usually extracted from whole blood, with centrifugally driven sedimentation, as discussed in the section that follows, being one of the most common approaches.

Metering on a centrifugal microfluidic assay is typically carried out through the use of an overflow channel, as demonstrated by Haeberle *et al.* [30] in his centrifugal platform for plasma extraction. Under centrifugation, a long narrow throttling channel is used to extract the predetermined blood volume into a decanting structure, with the shock interface moving radially outwards at the drift velocity, as defined in section 1.2.2. The plasma, measured to contain just 0.11% cell volume, is collected in the collection chamber, to the right of Figure 1.3 (a). An alternative to this was illustrated by Steigert *et al.* (Figure 1.3 (b)), again on a plasma-extraction platform [35]. An overflow channel is used to meter the sample, while the plasma is separated from the cellular component of the blood through a number of sequential centrifugation steps. The extraction channel primes following the complete sedimentation of the cellular pellet from the plasma and the centrifugal force subsequently pumps the plasma into the collection chamber, provided that the net radial length Δr of the downstream meniscus and the liquid level in the separation chamber is negative.

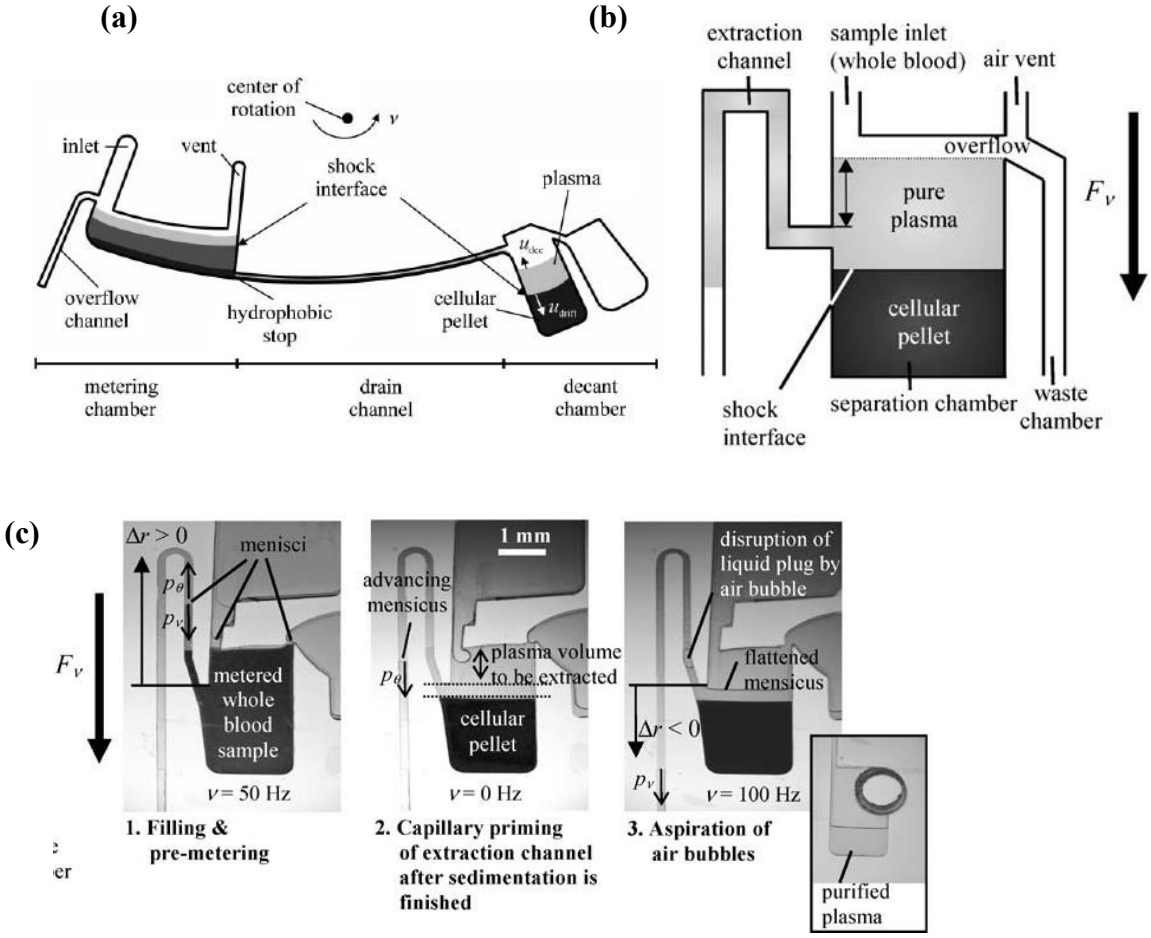

Figure 1.3 (a)-(c): Overflow and siphon based metering structures on centrifugo-microfluidic platforms. (a) Blood in excess of the volume between the overflow channel and hydrophobic stop flows into the overflow channel and the waste chamber, leaving a controlled volume of blood in the metering chamber. This pre-metered liquid is throttled as it passes through the drain channel under centrifugation, ensuring that only purified plasma sits on top of the cellular pellet in the decant chamber. [30] (b) Steigert *et al.* again used an overflow channel to control sample volume, with a siphon structure, separating the plasma from the cellular pellet following sedimentation by the sequential centrifugation steps illustrated in (c).[35]

Sedimentation has gained widespread use as a method to separate red blood cells (RBCs) from purified plasma as illustrated by the aforementioned examples and research by Li *et al.* [36], Zhan *et al.* [37] and Godino *et al.* [38], amongst others. Large sample volumes of up to 2ml of blood have been processed by Amasia *et al.*, with purified plasma achieved within 2.5 minutes [39]. In addition, induced sedimentation by centrifugation on microfluidic platforms has been applied to a range of other biomedical platforms. Lee *et al.* created an "in-situ optofluidic microsensor for high throughput screening or light filters in integrated adaptive optical devices" through the high speed sedimentation of silica and monodisperse polystyrene latex beads by centrifugation [40]. Garcia-Cordero *et al.* developed a cytometry device to monitor bovine mastitis through the use of centrifugally-driven sedimentation [41], while Gong *et al.* utilised the

centrifugal force to create packed silica microbeads to produce micro/nanofluidic devices for applications in electro osmotic pumping and liquid and electro chromatography [42].

Valving presents another alternative to overflow channels or siphoning for controlling liquid volumes and carrying out general liquid handling tasks. The careful positioning of sacrificial valves to control reagent/sample volumes has been demonstrated by Cho *et al.* [43], who utilised paraffin wax valves to create a metered plasma volume on a DNA extraction platform. Park *et al.* [44] improved upon the above approach by embedding iron oxide nanoparticles to reduce the complexity and cost of the heating components needed to open the sacrificial valve. Steigert *et al.* [45] utilised hydrophobic capillary burst valves to meter a sample of whole blood for real-time absorption measurement of alcohol concentration in blood. By modifying the height of the liquid column and the channel cross section, as illustrated in Figure 1.4 (1), capillary burst valves which break at differing centrifugal spin speeds were created to meter the sample and transport it into a detection chamber. The sample was then mixed by frequently changing the direction and speed of rotation i.e. “shake mode” to promote enzymic reaction, followed by a final spin speed of 30Hz for 90 seconds to induce sedimentation of the red blood cells to the bottom of the assay, eliminating their interference with the optical beam path.

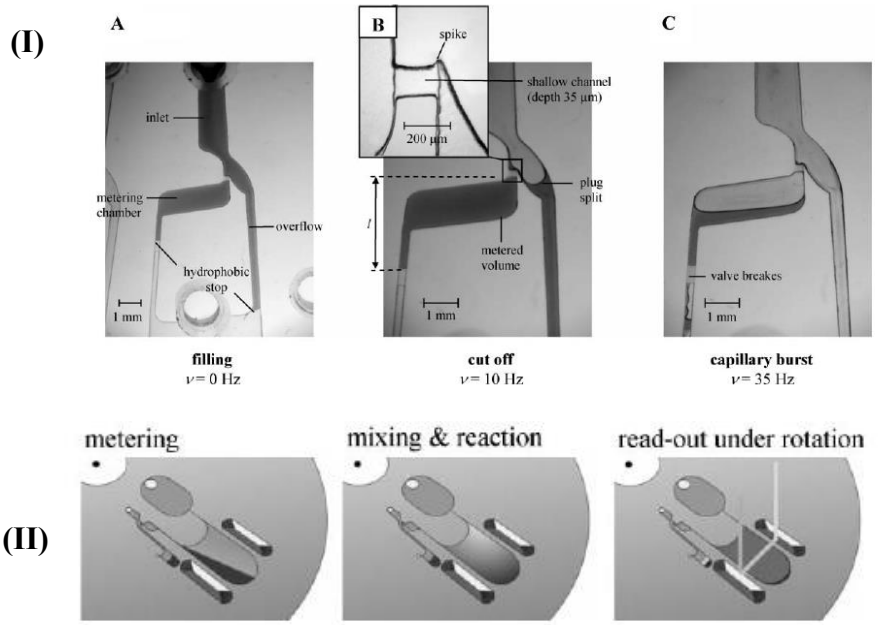

Figure 1.4 (1)-(2) Centrifugally driven valve metering, mixing and sedimentation unit operations on a real-time colorimetric alcohol concentration assay. [45] (I) Following insertion of the patient blood sample, the capillary primes to the hydrophobic stop. At a spin speed of 10Hz the first capillary valve breaks and excess sample is metered off. At a higher frequency of 35Hz the metered sample is driven into the detection chamber, as the second capillary burst valve breaks. (II) This process is followed by mixing and sedimentation steps for the eventual colorimetric read-out of alcohol concentration by optical detection.

As valving is a key unit operation on centrifugal microfluidic platforms for metering, reagent storage, and reagent and sample handling, a number of novel valving schemes have been developed. The reader is directed to the literature for further examples and discussion of these schemes[46-53], including, but not limited to, pneumatic valving [46-48], serial siphon valving[49], capillary and hydrophobic burst valving [50-52] and the aforementioned paraffin wax valving [43,44,53].

1.3.2 Cell Lysis

Cell lysis is another blood preparation technique used for the purification of blood based samples, as well as DNA, RNA, protein and metabolome analysis. Nan *et al.* have recently reviewed emerging lysis techniques on microfluidic and centrifugal microfluidic platforms including mechanical, chemical, electroporation, thermal and laser lysis, as well with other novel approaches [54]. Lysis methods are chosen based on the degree to which the cell membrane of the target cell of interest needs to be disrupted before lysis will occur. For example, many cells, as in the case of RBCs can be lysed through the addition of a lysing agent and batch mode mixing as demonstrated by Lutz

et al. [55]. In this example Lutz *et al.* utilised "shake mode" centrifugation to reduce RBC lysis time almost 5-fold; from 90s to 20s. However, other biomolecules such as E.Coli and S. Cerevisiae bacteria require harsher treatment to lyse the cells such as thermal treatment [56], electrical lysis [57] or thorough mixing with microparticles [58,59]. As the designs by Lutz *et al.* and others demonstrate, centrifugal microfluidics is particularly well tailored for cell lysis due to the unique fluid handling and batch mode mixing capabilities it offers. DNA and RNA analysis have also been carried out effectively on a number of microfluidic and centrifugo-microfluidics platforms as outlined in a recent review by Sun *et al.* [60]. The unique mixing capabilities coupled with the ability to carry out multiple assays in a single disc significantly reduces assay time and improves the homogeneity of the samples as demonstrated by Dimov *et al.* [61] and Amasia *et al.* [62] in their RNA analysis and PCR amplification platforms respectively. In addition, Siegrist *et al.* recently validated a centrifugal microfluidic chip for nucleic acid extraction using clinical samples. [63] Micron-sized magnetic beads have also been coupled with external magnets to increase the effectiveness of the mechanical lysis, as illustrated in the example by Grumann *et al.* [64]. Figure 1.5 below illustrates a number of recent state-of-the-art inertial and centrifugally driven lysis schemes, with a brief discussion of their functionality.

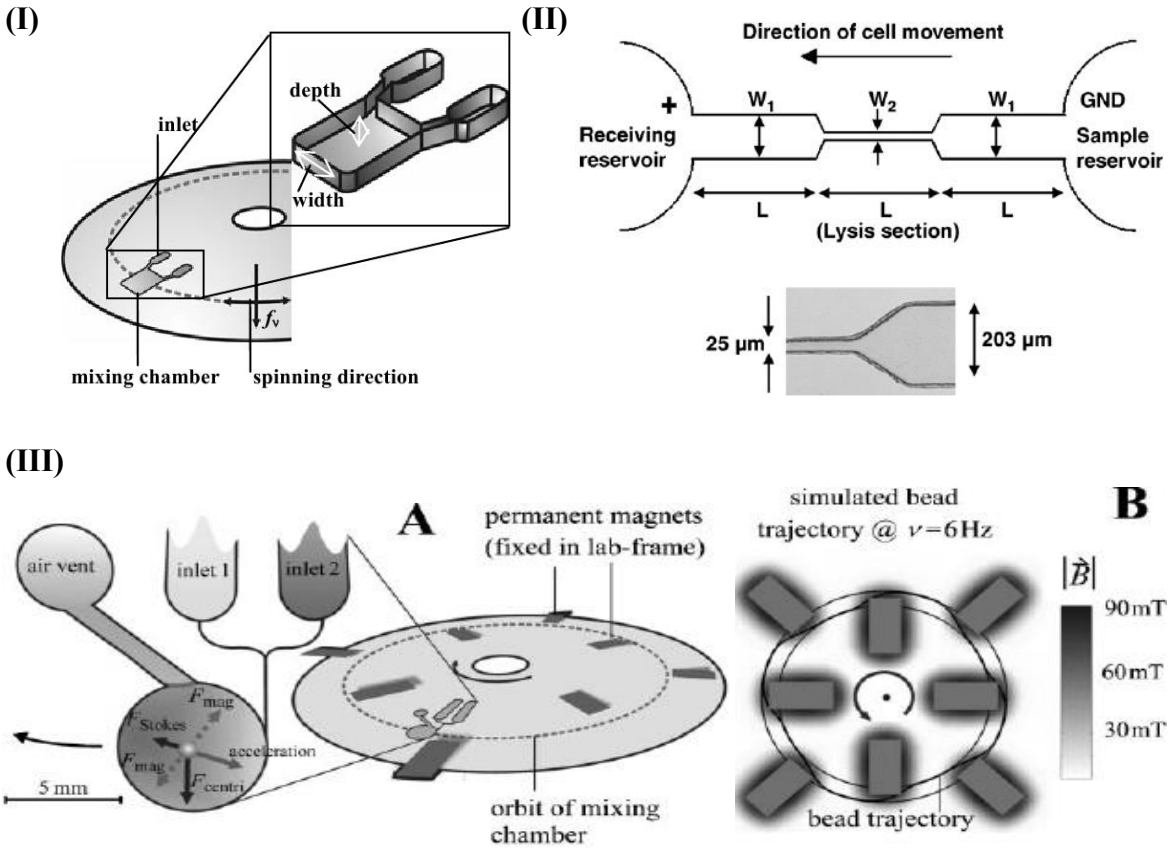

Figure 1.5: (I)-(III) Various cell lysis schemes on inertial and centrifugal microfluidic platforms. (I) Lutz *et al.* utilised batch-mode mixing on a COC disc, lysing nearly 100% of blood cells in 20 seconds through the combination of "shake mode" mixing and a lysis buffer [55]. (II) Wang *et al.* used a DC current of 1000V/cm - 1500V/cm to lyse GFP expressing E Coli cells [57]. Cells were inserted into the sample reservoir and transported to the detection reservoir, which is exposed to a DC electric field. Cell lysis occurs in the targeted narrow section of the microfluidic device. (III) Illustration of the centrifugal microfluidic platform with embedded magnets developed by Grumann *et al.* [64]. (A) The embedded magnets are orientated within and outside the mean chamber radius (indicated by the dotted line), such that the magnetic beads on the chip experience movement in the trajectory outlined in (B) at ~6.5Hz. This is due to the orientation of the on chip magnets, which deflect the beads, coupled with the centrifugal force acting radially outwards.

1.3.3 Cell Volume Fraction Measurement

A final blood sample preparation step of interest is the measurement of the cell volume fraction for a range of biomedical assays. Rigger *et al.* [65] produced a known sample volume through capillary priming and overflow channels, under centrifugation. Subsequent centrifugations lead to the sedimentation of RBCs into a cellular pellet, with the haematocrit level being measured from the top of the pellet in the sedimentation chamber. A further extension to the above approach is density gradient sedimentation; where a density gradient material such as ficoll or percoll is added to the blood sample to separate bands of cells according to their differing densities. This was demonstrated by Schaff *et al.*, who separated three bands of microparticles (1µm, 5µm and 6µm in

size) by layering the mixture on top of 30% and 50% Percoll media in a centrifugally driven chamber [66]. Under centrifugation at 4000rpm for 30 seconds, the three bands of microparticles are separated. This demonstrated proof of concept, with an additional experiment demonstrating the separation of a mixed solution of K562 and Jurkat cells from culture, through the layering of the cells on 35% Percoll media in a buffered salt solution. Again, the disc was spun at 4000rpm for 30 seconds and fluorescence microscopy was used to image and quantify the cells separated above and below the density media. This density gradient technique has been applied to separate cells in whole blood samples as well as stem cells from whole blood, as illustrated in the work by Shiono *et al.* [67, 68]. In other work Shiono *et al.* demonstrate the separation of human cells from fibroblasts in suspension [69]. In addition, Park *et al.* have utilised this method towards the retrieval of circulating tumour cells from whole blood, with separation rates of 99% and 86%, depending on device design, for MCF-7 and DMS-79 cells used to model CTCs off chip [70]. The cancer cells were amplified using EpCAM/TROP1 antibody conjugated microbeads, resulting in a density difference between the cancer cells and leukocytes in whole blood. The integration of this approach onto a centrifugal platform, as illustrated by Schaff *et al.*[66] could offer another alternative to existing CTC retrieval schemes.

1.4 Cell Separation, Handling and Trapping on Centrifugo-Microfluidic Platforms

Following on from the more general blood purification and cell quantification approaches outlined in section 1.3, this section will demonstrate the more specific handling and capture of cell populations and individual cells. In a typical laboratory scenario these functions would be carried out by a conventional flow cytometer, which utilises fluorescence detection, impedance measurement and light scattering to determine cell counts of individual cell lines and provide information on the morphology and composition of the cells. Hydrodynamic focusing using two sheath fluids is used to separate and direct cells within the device toward an optical detector. While flow cytometry has gained widespread use in clinical and research environments due to its accurate and high-throughput cell quantification capabilities, it remains a bulky and expensive technology, which requires regular maintenance and supply of sheath liquids. In addition, it is challenging to operate and, as a result of this and the

aforementioned points, is not suitable for low resource settings. Therefore microfluidic, and more recently, centrifugal microfluidic technologies, offer a cost effective, compact and easy to use alternative to the conventional methods associated with cell detection and imaging. The following section will outline some of the recent key examples of miniaturised flow cytometry platforms, as well as a discussion of a number of other approaches to cell handling and investigation such as pinched flow fractionation, counter-flow elutriation, centrifugo-dielectrophoresis and centrifugo-magnetophoresis. As these approaches have already been comprehensively reviewed in the literature, for both inertial [71,72] and centrifugal platforms[32-34], this discussion will be brief. However, a more focused discussion of gravity based and centrifugally driven bead and cell capture using geometric traps will be undertaken in section 1.5, due to its relevance to the work in this thesis.

1.4.1 Miniaturised Flow Cytometry

The transition of flow cytometry from bench top platforms to microfluidic devices has gathered increased momentum in recent years, as documented in various reviews in the literature [73-75]. A range of cell sorting schemes have been adopted such as impedance-based [76], magnetophoresis[77], fluorescence[78-81] and dielectrophoresis[82-83] based cytometry. In addition, Bhagat *et al.* utilised spiral microchannels to combine Dean forces with inertial lift forces for cell handling, removing the necessity of a sheath fluid typically used in flow cytometry schemes [84]. The challenge of high-throughput screening has also been tackled, as demonstrated by the work of Hur *et al.* in their sheathless cell positioning system, which yields interrogation rates of up to 1 million cells s^{-1} with the appropriate imaging components [85]. As the reader will see in section 1.6 on optical detection schemes for microfluidic and centrifugo-microfluidic platforms, a number of research groups are marrying microfluidics and miniaturised optical detection components such as LEDs, CCDs and photodiodes with cell phones to create accurate and inexpensive miniaturised flow cytometry devices. This work is at the forefront of bringing vital point-of-care diagnostics to low-resource environments, with commercialised point-of-care microfluidic platforms being discussed further in Chapter 4.

1.4.2 Flow-Based Cell Sorting and Handling Schemes on Centrifugal Platforms

In addition to flow cytometry approaches to cell differentiation and handling, two other flow-based methods have been adapted to centrifugal platforms; namely pinched flow fractionation and counter-flow elutriation. Pinched flow fractionation has been utilised on inertial microfluidic platforms by a number of research groups, [86-88] using external pumping mechanisms to drive the flow containing the cells toward a microfluidic wall to achieve a "pinching" effect. Cells line up against the wall to varying degrees; depending on the size and the density of the target cells, with fluidic resistances in the outlet channels determining which outlet each cell stream takes. Yamada *et al.* separated 15μm and 30μm polystyrene beads under laminar flow conditions and captured the separate bead types in different chambers [87]. Cupelli *et al.* tested two different pinched flow fractionation designs, coupling inertial microfluidics with syringe pumping to separate leukocytes and erythrocytes with separation efficiency of 100% and 85% respectively [89]. A centrifugal implementation of the pinched-flow technique has been implemented by Morijiri *et al.*, with separation of 3μm and 5μm polystyrene beads and 5μm silica beads in suspension[90], demonstrating a more efficient separation scheme over the externally pumped inertial alternative.

Another novel flow-based cell and bioparticle separation scheme is centrifugal counter-flow elutriation or CCE. This technique has a long history, with Wahl *et al.* demonstrating the technique as far back as 1984 to separate T- and B- lymphocytes and monocytes [91]. More recently, Banfalvi *et al.* developed a nature protocol on the same vein, separating phase-enriched subpopulations from Chinese hamster ovary cells [92].

However, as with conventional flow cytometers, the equipment used is bulky, complex and expensive to acquire. Centrifugal microfluidics offers a compact, inexpensive and simplified alternative, due to the easy fabrication of an elutriation chamber combined with the compact rotor scheme developed for many centrifugal platforms. During elutriation, a cone shaped chamber, as outlined in Figure 1.6 utilises the balance of the centrifugal force, pumping liquid radially outwards, with the counterflow drag forces exerted on particles. These forces are manipulated by changing the rotation speed and, consequently, the flow rate of the counter flow. This leads to the separation of cells and bioparticles based on density and size, with larger particles residing in the narrower part of the elutriation chamber with a relatively high flow rate, with smaller/less dense particles residing in the outer part of the chamber. Recent

examples of centrifugal counter-flow elutriation include the work of Morijiri *et al.*, who separated polymeric particles with diameters of 1-5um as well as RBCs from WBCs on a PDMS platform [93].

Figures 1.6 and 1.7 describe the functionality and some centrifugal examples of pinched-flow fractionation and elutriation. The reader is directed to a review by Pamme et al for further discussion of continuous flow based cell handling and separation techniques [94].

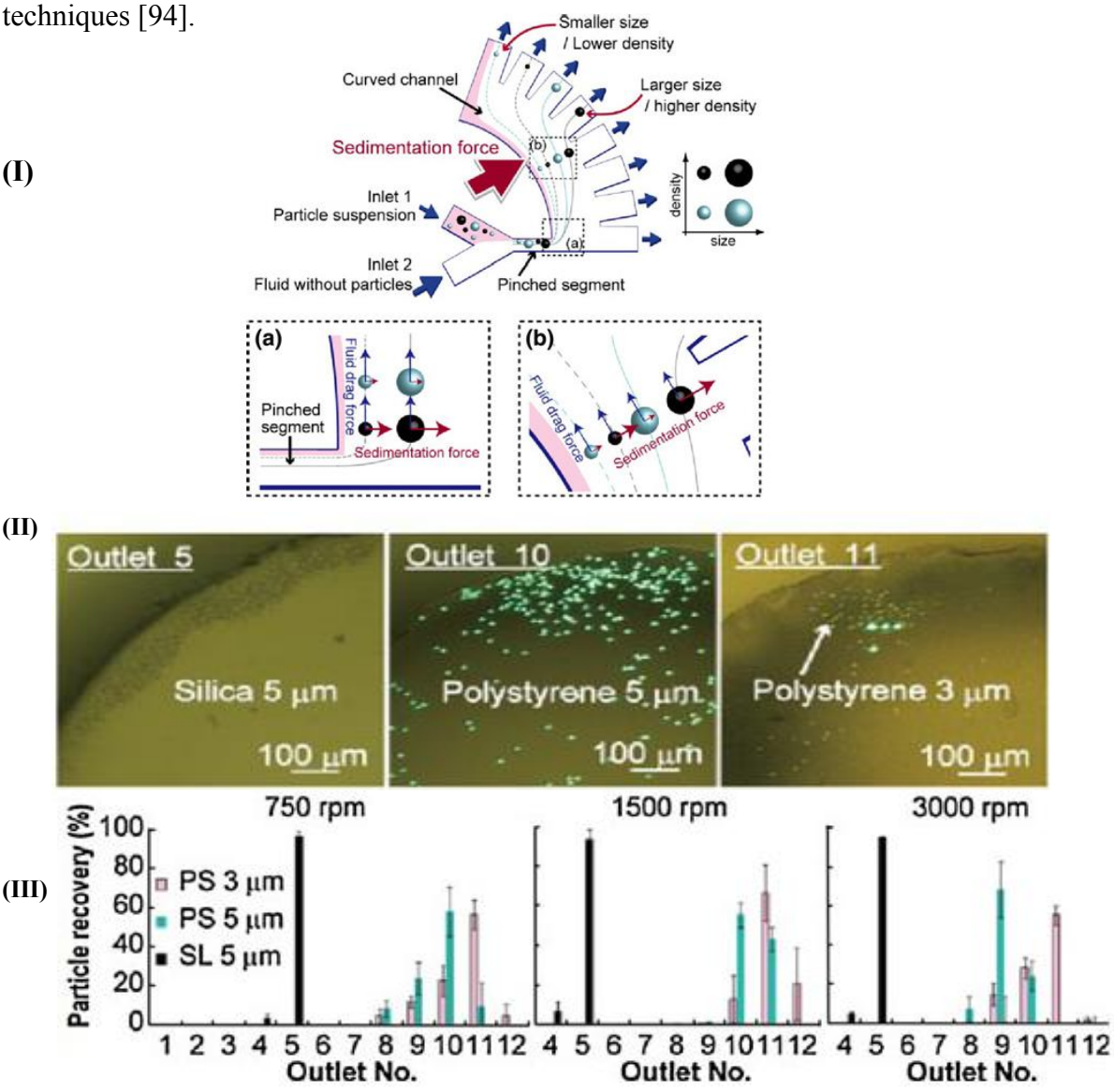

Figure 1.6 (I)-(III) Schematic of the operating principle of pinched-flow particle/cell separation, with an example of a centrifugal platform by Morijiri *et al.* [90]. (I) Zoomed in images (a) and (b) are of sections labelled (a) and (b) in upper image. Particles remain pushed against the walls of the chip in the pinched segment. When the sedimentation force is applied in the radially outwards direction (by the centrifugal force due to the disc rotation) on particles flowing in the curved microchannel, the larger particles (black) move beyond the streamline, causing separation of particles according to density. (II) Fluorescence micrographs of outlets for 3.0μm and 5.0μm polystyrene and 5.0μm silica particles following rotation at 750rpm for 300s of the rotationally driven pinched-flow device by Morijiri *et al.* (III) Results of the separation of polystyrene (PS) and silica (SL) particles for n=3, with each data bar representing the mean, including error bars indicating the standard deviation.

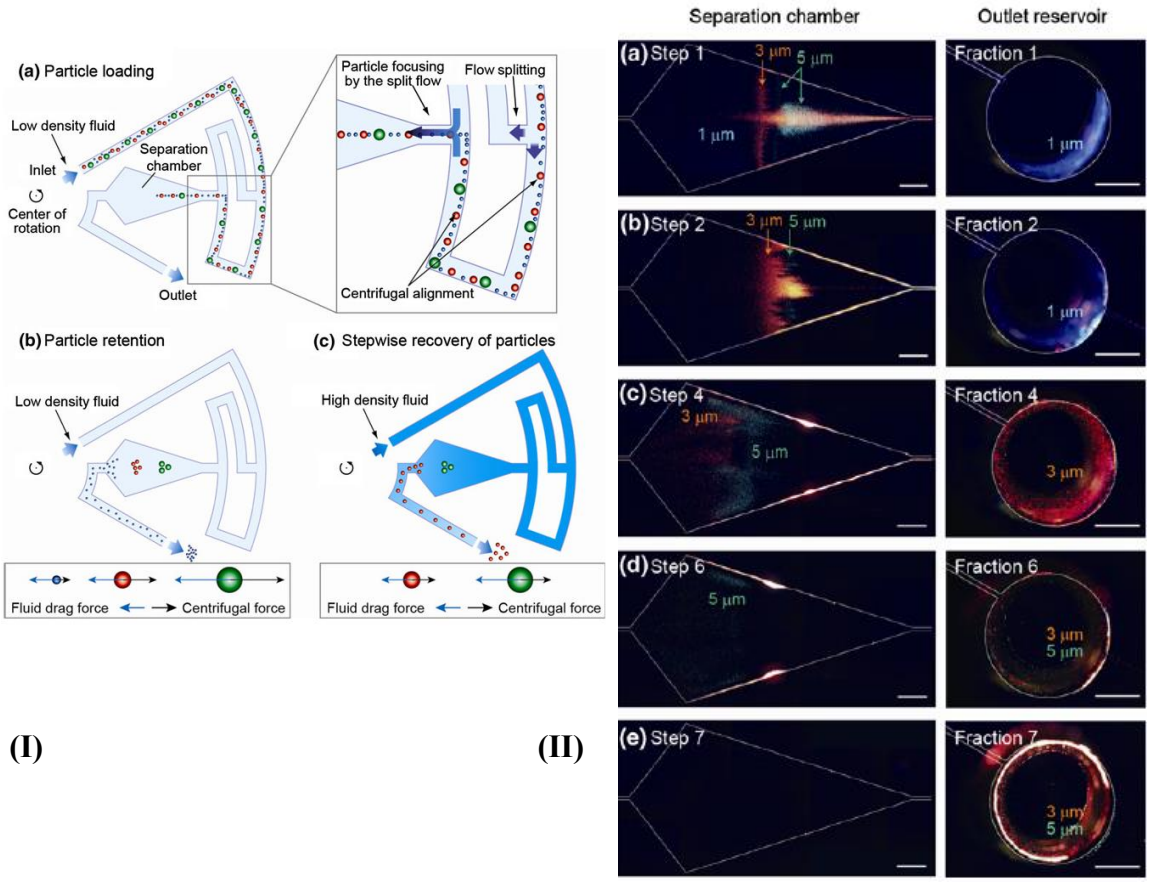

Figure 1.7: (I)-(II) Schematics of the operating principle of counter-flow elutriation and an example of a centrifugal implementation of this technique by Morijiri *et al.* [93]. (I)(a) Particles of mixed size and density in a low density liquid are loaded into the elutriation chamber using the centrifugal force. (b) Particles are separated by size when the centrifugal force and the drag based counter flow are in equilibrium, with the smallest particles exiting the chamber through the outlet. (c) A high density liquid is flowed into the device to elute the remainder of the particles consecutively. (II) (a)-(e) Fluorescence micrographs of separation and outlet chambers for the counter-flow elutriation device developed by Morijiri *et al.* (a)-(b) Input of particle mixture of 1.0μm, 3.0μm and 5.0μm polystyrene particles in a low density i.e. $\rho = 1.0$ g cm^{-3} liquid. (c) Selective elutriation of 3.0μm particles using a higher density liquid $\rho = 1.02$ g cm^{-3} (d)-(e) Selective elutriation of 5.0μm particles using a high density liquid, $\rho = 1.04$ g cm^{-3}, Scale bar = 1mm, with chambers and outlets outlined by dotted lines.

1.4.3 Dielectrophoretic Cell Separation

The flow-based cell separation techniques outlined in previous sections rely on the differences between the size and density of bioparticles and cells to carry out handling and separation operations. Dielectrophoresis, on the other hand, utilises the differences between the inherent characteristics of cells, such as differences in dielectric properties; which is affected by cell size and morphology, to differentiate between different cell types. Çetin *et al.* recently reviewed the application of dielectrophoresis to microfluidic platforms.[95] Other biological organisms such as bacteria, viruses, spores etc. are also separated using this technique,[96] using a concentric cell model, as described by Çetin *et al.* [95] Of more relevance to this thesis however, is the application of this technique

on centrifugal platforms, which has been successfully carried out by a number of research groups [97-99]. For example, the centrifugal system developed by Martinez-Duarte *et al.* demonstrated the separation of viable yeast cells from non-viable yeast cells. [97]. In addition, Martinez-Duarte *et al.* successfully manipulated latex particles through the use of an array of novel 3D carbon electrodes on a silicon/silicon dioxide chip, inserted into a CD-like platform for centrifugation [97]. In addition, Boettcher *et al.* used a centrifugal dielectrophoretic scheme to differentiate between 6.5μm, 9μm and 15μm polystyrene beads as well as U937 cells from whole blood illustrated in Figure 1.8 (I)-(II) [99].

1.4.4 Magnetophoretic Cell Separation

Centrifugally driven magnetophoresis is another alternative cell manipulation and separation method for lab-on-a-chip applications. It differs from the previous example in that it is not label free, with cells/bioparticles of interest being coated in antibody conjugated magnetic beads to enable a high degree of control. This technique has been employed by a large number of groups on inertial [100-105] and centrifugally driven platforms [106-109], for positive and negative selection of cells and particles. As a full discussion of all of the aforementioned examples is outside the scope of this work, only a few notable examples of magnetic sorting on centrifugally driven microfluidic systems will be discussed and outlined in Figures 1.8 and 1.9 that follow.

Plouffe *et al.* devised a pump driven magnetophoretic cell separation scheme, with embedded copper wires on either side of the PDMS microfluidic channel to create a magnetic field (Figure 1.8 (IV)-(V)) [103]. MCF-7 cells, endothelial progenitor cells and hematopoietic stem cells were coated in antibody-conjugated magnetic microparticles to enable separation from non-magnetic cells. Cell separation efficiencies of 85% and >96% were recorded respectively. A novel label free magnetophoretic separation approach was developed by Shen *et al.* [104], based on the inherent magnetic characteristics of the cells themselves and a repulsion force provided by the marriage of an external magnet, nickel microstructure and a paramagnetic salt medium. The nickel microstructure enables the concentration of magnetic flux lines from the external magnet, greatly strengthening the magnetic field effect on the cells in the paramagnetic medium. Figure 1.8 (V) illustrates the operating principle of the inertial microfluidic device, with 8μm and 10μm polystyrene beads successfully differentiated, as well as U-937 cells from RBCs with >90% purity.

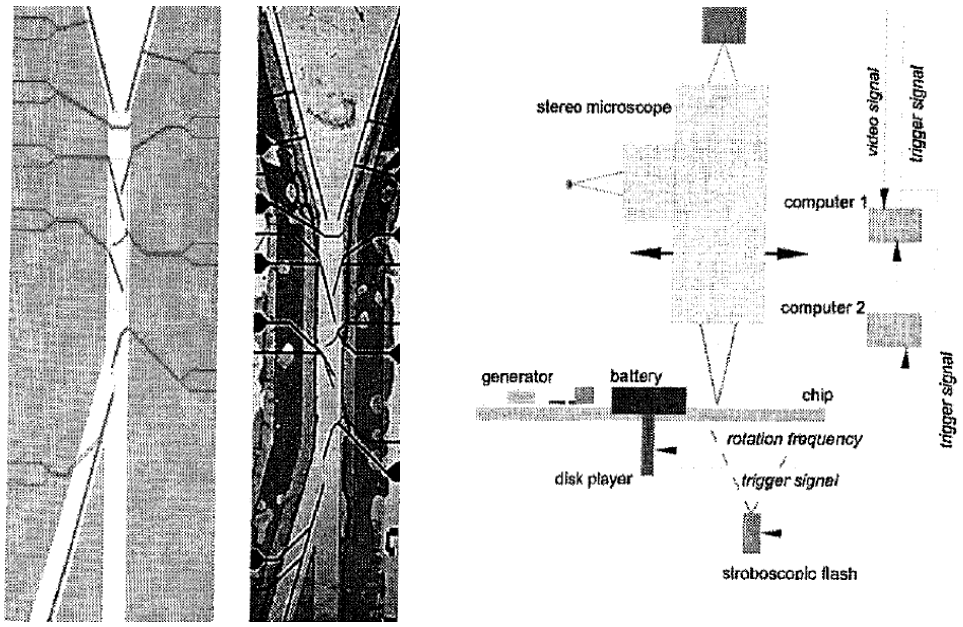

(I) (II)

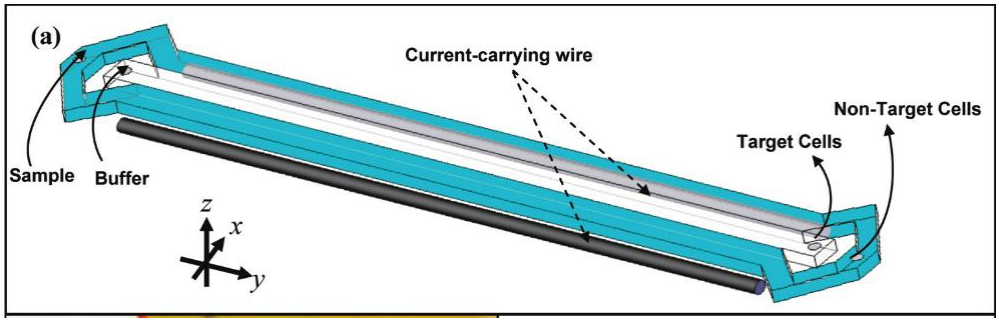

(III)

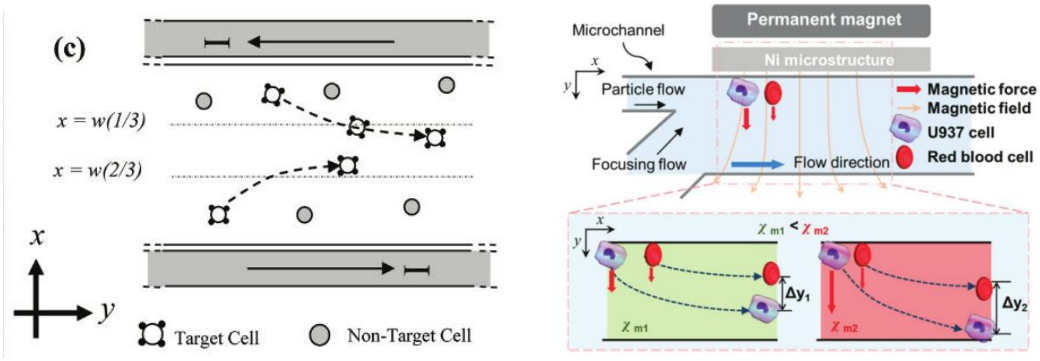

(IV) (V)

Figure 1.8 (I)-(V) Examples and operating principles of (I)-(II) dielectrophoretic and (III)-(VI) magnetophoretic cell separation schemes. (I) Schematic and photograph of the dielectrophoretic microfluidic channel and (II) centrifugal microfluidic set-up by Boettcher *et al.* for the separation of U-937 cells from whole blood [99]. (I) The axis of rotation is above the images, with microelectrodes for DC dielectrophoresis located on both the channel top and bottom. (IV) Pump driven magnetophoretic separation platform developed by Plouffe *et al.* [103]. (IV) Magnetic bead coated target cells are deflected into the centre of the flow stream, due to the y-direction laminar flow stream and x-direction magnetic field. Non-magnetic particles remain in the laminar flow stream, while magnetically tagged particles move to a centre collection stream. (V) Differentiation of RBCs from U937 cells due to an external magnet, Ni microstructure and paramagnetic suspension medium. As illustrated in the bottom images of (V), the change of medium to a paramagnetic salt suspension greatly increases the magnetic susceptibility of the cells, resulting in greater separation of the U-937 cells from RBCs [105].

Centrifugal systems have also utilised magnetophoresis to carry out biomimetic bead separation operations, with Kirby *et al.* developing a device towards the removal of rare cells from whole blood [106]. 1μm and 20μm magnetic beads, as well as 20μm non-magnetic beads were separated with 100% efficiency (Figure 1.9 (I) – (II)), with this approach already being applied to other centrifugal cell separation platforms for CD4+ cell removal from whole blood [108]. A similar cell separation scheme was developed by Siegrist *et al.* [107] for the separation of MCF-7 cells from HeLa cells (Figure 1.9 (III) – (IV)). By tagging the MCF-7 target cells with immuno-functionalised magnetic beads, over 90% separation efficiency between the MCF-7 and HeLa cells was achieved.

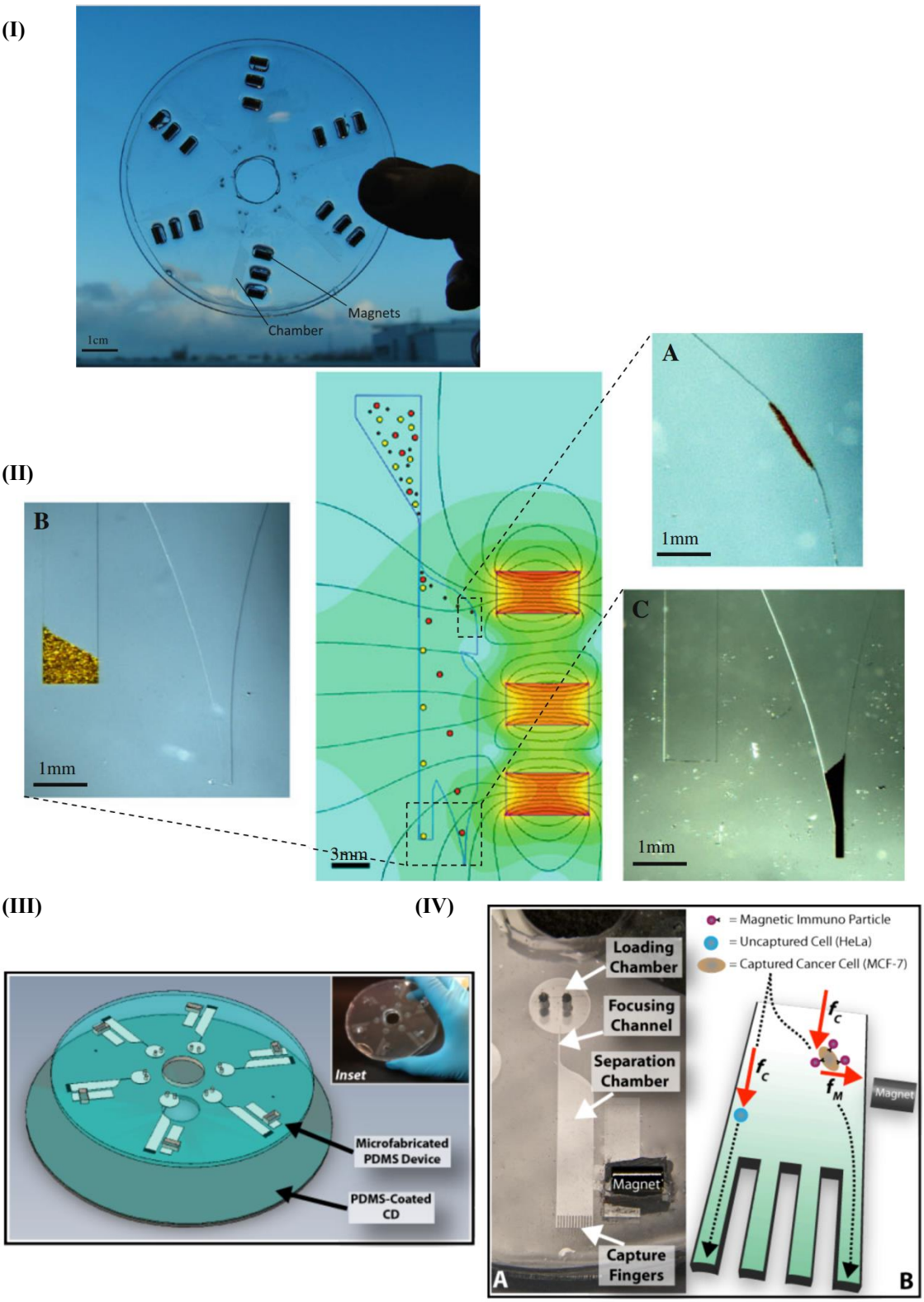

Figure 1.9: (I) Photograph of magnetophoretic, centrifugally-driven LOC device developed by Kirby *et al.* [106], with embedded magnets. **(II)** The embedded magnets serve to deflect magnetic particles to varying degrees, depending on their size, with 1µm and 20µm magnetic particles and 20µm non-magnetic particles separated to 100% efficiency under centrifugally driven stopped flow conditions. **(A)** 1µm magnetic particles are deflected most strongly, due to their small size, and therefore slow sedimentation speed**. (B)** 20µm magnetic particles are deflected into chamber **(B)**, while non-magnetic particles sediment and are captured in chamber **(C). (III)** Another centrifugally driven magnetophoretic cell separation device on a polymeric platform. Stiegert *et al.* [107] developed a disposable platform for the separation of magnetic bead coated MCF-7 cells from HeLa cells to over 90% efficiency.

Furlani *et al.* [109] and Gijs *et al.* [110] conducted recent reviews of the application of magnetophoresis to lab-on-a-chip platforms for diagnostic applications and the reader is directed to this work and the literature referenced above for further examples and applications of magnetophoretic schemes.

1.4.5 Alternative Cell Separation Techniques

In addition to the aforementioned cell separation techniques a number of other approaches such as acoustophoresis[111-114], cell encapsulation[115,116] and optical force manipulation[117-120] have been investigated for cell and bioparticle separation and handling. A review by Tsutsui *et al.* [121] details recent developments in the use of non-inertial forces for cell separation and handling applications, including all techniques discussed from section 1.4.1 to this one. Readers should also note that multicellular organisms have been separated on microfluidic platforms [122-124], including C Elegans[122,123] and Drosophila embryos[124].

1.5 Individual Bioparticle and Cell Capture on Microfluidic Platforms

While the quantification and separation of various cell lines is of great importance to a number of biomedical applications, the capture and analysis of single cells and multicellular organisms enables a greater level of diagnostic information to be derived from a clinical sample. For example, the analysis of cell morphology can be used for disease diagnosis (discussed further in section 3.2), while the real-time reaction of cells to various stimuli such as drugs or other reagents can be monitored when the cells are captured individually. For such analysis to occur, cells or bioparticles are often captured in individual mechanical traps.

1.5.1 Gravity based Traps for Cell and Bioparticle Analysis and Capture

The simplicity of gravity based capture of cells and bioparticles has been exploited by a number of groups to great effect in microfluidic cell separation and capture applications [125-128]. A gravity based separation technique has recently been developed by Devendra *et al.*, utilising gravity driven Deterministic Lateral Displacement (g-DLD) to separate 10um silica particles from 4.32um silica particles and to differentiate a mixture

of 15μm, 20μm, 4.32μm and 10μm silica particles [125]. Deterministic Lateral Displacement functions on the principle that particles flowing in a laminar stream will remain within the stream if they have a smaller diameter than the stream, and will be pushed laterally by the posts in the platform if they are larger in size than the stream. A variety of forcing (tilting) angles were tested for the glass/SU-8 micro-device to encourage particle separation, as illustrated in Figure 1.10 (I). As outlined in section 1.6.2 on optical detection approaches for centrifugal platforms, Lee *et al.* have developed a centrifugal platform which traps cells singly using slanted pits in a spiral microfluidic channel [126]. This assay was used to monitor cytotoxicity due to treatment with paraformaldehyde and to fluorescently differentiate dead HEK293 cells from live HEK293 cells as a result of UV illumination. A capture efficiency of ~80% was obtained for a sample size of 600 cells. In a similar scheme, Kubo *et al.* isolated multiple and single jurkat cells within non-branching and branching microchannel designs [127]. Following rotation at 4500 rpm for 30s, 93% of fluorescently stained cells were found to be alive using a fluorescense microscope. The branching and non-branching microchannel designs and resulting fluorescence images can be seen in Figure 1.10.

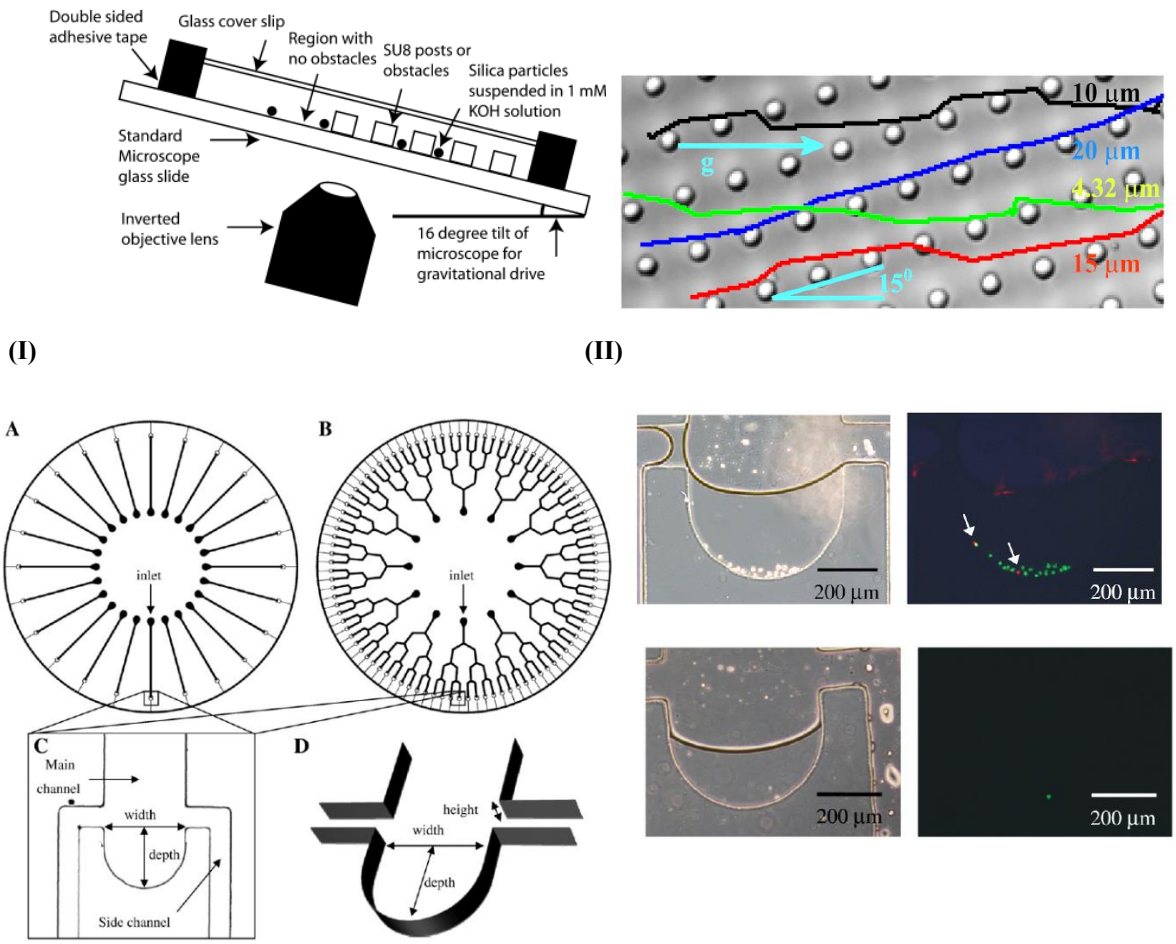

Figure 1.10: (I) Schematic of the g-DLD microfluidic device, with particles moving along different displacement paths due to the gravity induced DLD [125]. **(II)** Illustration of the paths taken by 4.32µm, 10µm, 15µm and 20µm beads, showing differentiation between all of the particles at a given forcing angle of 15°, with gravity in the horizontal direction as illustrated by the arrow (inset). **(III)** Schematic of non-branched and branched network of microchannels and microchambers on the centrifugal microfluidic platform developed by Kubo *et al.* [127]. For the non-branched network, which consisted of 24 microchannels and microchambers, 93% of cells were observed to be alive and 7% were found to be dead after centrifugation at 4500rpm for 30seconds, in good agreement with the original cell solution. The branched network consisted of 12 microchannels, with three bifurcations per microchannel. **(IV)** Top image: Fluorescence microscopy images of a non-branched microchamber, with living cells indicated in green and dead cells indicated in red. **(IV)** Bottom image: Fluorescence microscopy images of a branched microchamber, with a single living jurkat cell indicated in green, captured following centrifugation at 4500 rpm for 30 s.

1.5.2 Arrays of Geometric Traps for Cell and Bioparticle Analysis and Capture

The use of geometric traps for cell and bioparticle capture and assaying is particularly well-tailored for centrifugal microfluidic platforms in stopped flow conditions. In addition, as the reader will see in section 1.6.2, array based trapping of single cells lends itself toward optical detection and imaging in a variety of useful forms for POC diagnostics. The V-Cup geometric trap technology utilised by Burger *et al.*[129-132] for

multiplexed bead-based and cell-based immunoassays was originally a modification of the U-shaped trapping structure developed by Di Carlo *et al.*[133] on an externally pumped microfluidic platform (see Figure 1.11). Di Carlo *et al.* utilised geometric traps on a pumped, flow-based microfluidic platform resulting in a high capture efficiency of HeLa, 293T and Jurkat cells. Burger *et al.* improved upon the above approach by optimising and integrating this technology on a stopped-flow centrifugal platform, altering shape of the cups and the arrangement of the arrays to optimise bioparticle and cell capture. Figure 1.11 illustrates the original platform developed by Di Carlo *et al.* [133] and the centrifugally driven alternative by Burger *et al.* [129-132]. Further discussion of the relevance of this platform to the work in this thesis will be carried out in section 3.1 of Chapter 3.

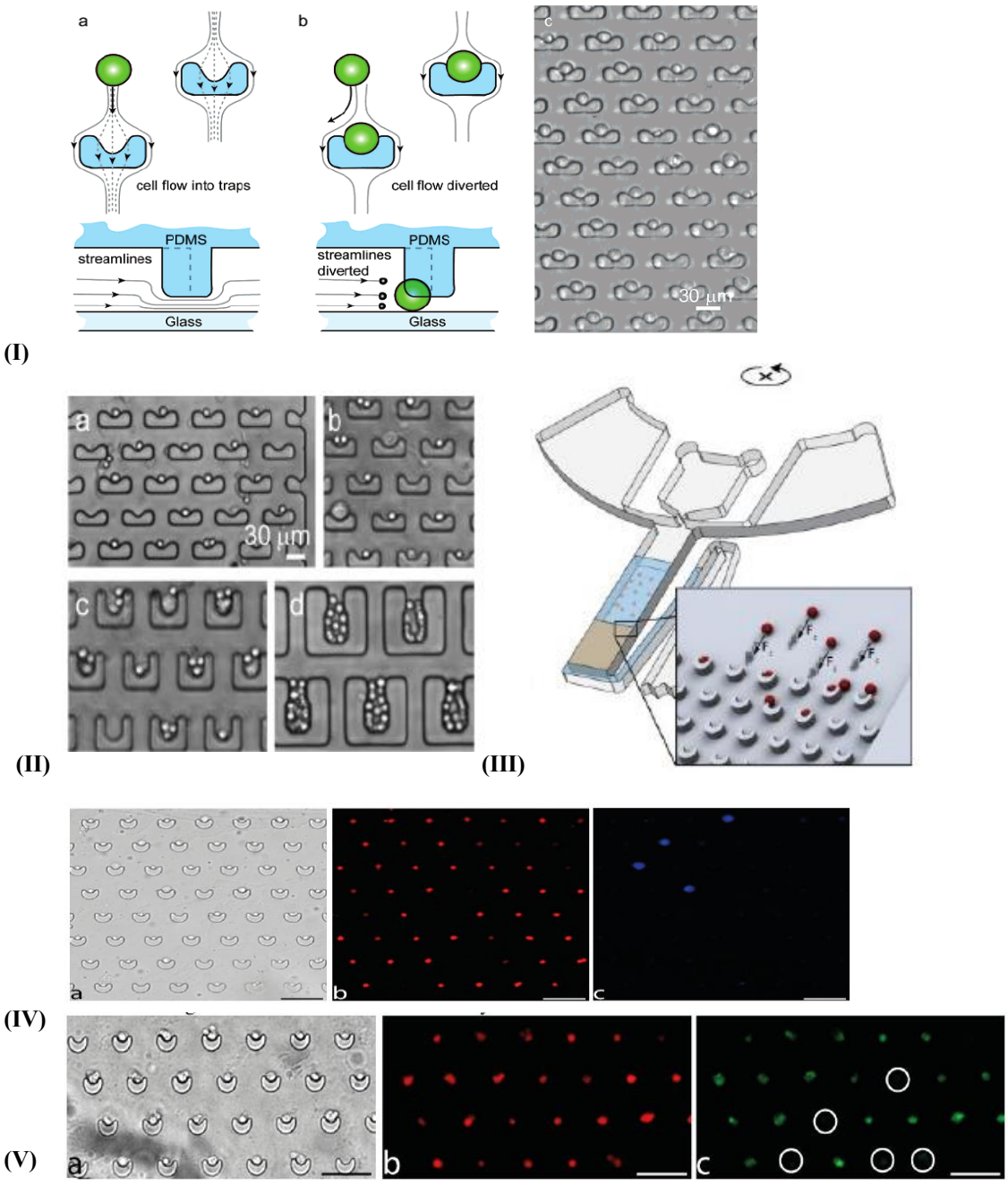

Figure 1.11: (I) Illustration of single cell isolation on U-shaped geometric platform developed by Di Carlo *et al.* [133] The 40um high PDMS structures include a 2um gap between the PDMS and glass substrate – enabling a quantity of the fluid streamlines to enter the traps during pressure driven flow. Once a cell is captured in the U-shaped trap, it acts as a seal, leading to a decrease in the streamlines proceeding through the 2um gap. **(II)** Phase contrast image of an array of captured single cells. **(III)** Phase contrast micrograph images of cells trapping in traps of 10um, 15um, 30um and 60um in height. As expected, the number of cells trapped in each geometric trap increases with size, with single-cell capture more likely with decreased trap size. This scaling effect was also observed by Burger *et al.* [129-132], in their alternative stopped-flow and centrifugally driven platform, Figure **(III)** [131]. **(IV)-(V)** Beads are captured in the shifted V-Cup arrays by sedimentation due to the centrifugal force in stopped flow conditions, with almost 100% capture efficiency observed.[modified from [129]] This platform demonstrated bead-based and cell-based multiplexed immunoassays, with fluorescence images of the single cell capture of **(IV)** RPMI plasma cells (red) in solution, spiked with MCF-7 cells (red, and blue for multiplexed discrimination) and **(V)** HeLa cells (red) and MCF-7 (red, and green for multiplexed discrimination).

1.5.3 Microcontact Printing for Cell Capture and Detection

A final cell capture and counting technique sometimes utilised in microfluidic platforms is microcontact printing [134-137]. The typical process for microcontact printing is outlined in Figure 1.12. A functionalised substrate (usually glass or silicon) is printed with a protein e.g. an antibody by a photolithographically fabricated PDMS stamp. The stamp is "inked" with the binding protein and the stamp is brought in contact with the functionalised surface. This enables cells and other biomaterials to adhere to a surface and be detected using typical optical detection methods e.g. fluorescence microscopy. Microcontact printing will be further discussed in sections 2.2 and 3.2.

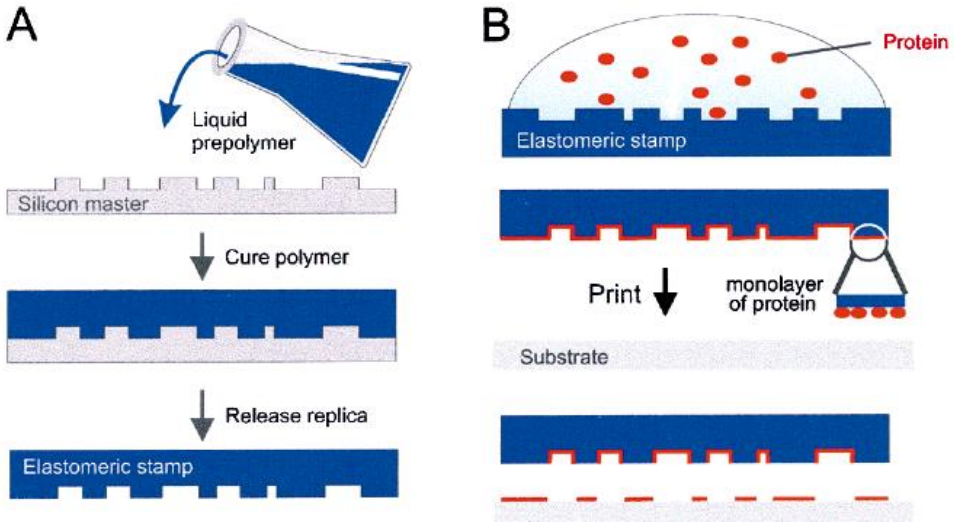

Figure 1.12: Schematic of the PDMS stamp fabrication and micro-contact printing processes [134]. Once the liquid PDMS polymer has cured on the mould, a replica can be used as a hydrophobic stamp. The protein of interest is deposited onto the PDMS substrate, forming a monolayer of protein on its surface. The "stamp" can then be used to create micron and even nanometer sized spots on functionalised substrates for biomolecule and cell capture.

1.6 Optical Detection in Inertial and Centrifugally-Driven Microfluidic Platforms

1.6.1 Introduction to Optical Detection

To complement the rapid expansion of diagnostic capabilities on microfluidic and centrifugal microfluidic devices in recent times, new detection and imaging technologies have been developed in parallel to produce inexpensive, usable and accurate diagnostic platforms. Optical detection is the most widely used form of detection on these platforms due to its superior sensitivity, specificity and the wide array of sensing techniques available. While alternative detection methods including

electrochemical, impedance or colorimetric based systems may be more compact and cost-effective when compared to conventional optical systems, modern microfluidic devices have moved towards smaller and more easily integrated optical components, which can avoid these issues. A range of optical detection schemes including interferometric, absorbance and fluorescence measurements and Raman spectroscopy have been used for a variety of different microfluidic and cell-based assays[138-140], as illustrated in Figure 1.1.

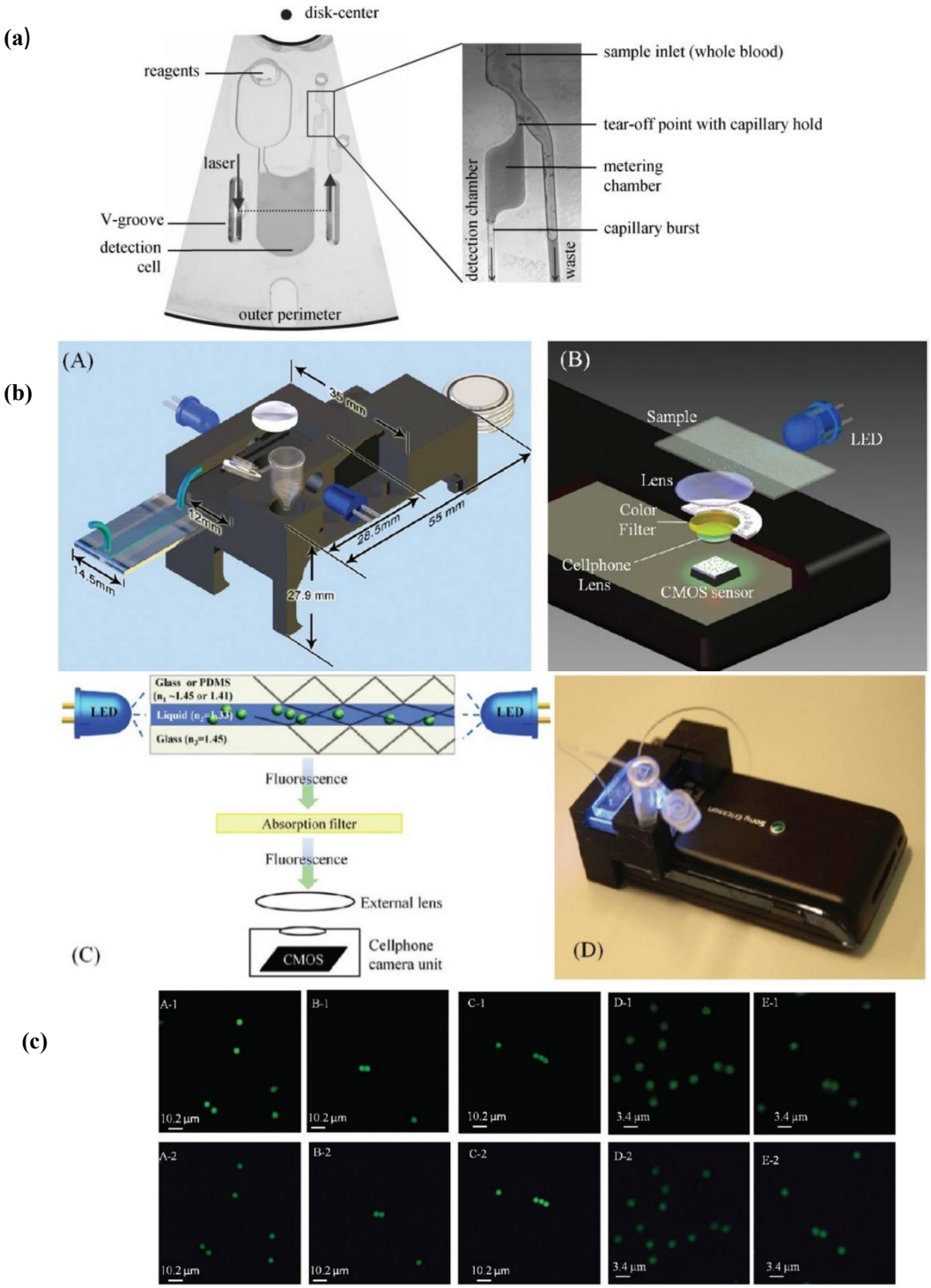

Figure 1.13 (a)-(c) Various optical detection regimes for biomedical diagnostics on microfluidic platforms [141-144]. **(a)** Steigert *et al.* developed a centrifugally-driven platform for the measurement of alcohol concentration in whole blood [141]. The assay sensitivity compared favourably with common breath analysers and greatly improves upon the typical assay time of 6-8 minutes, producing accurate results in just 100 seconds. **(b)** Zhu *et al.* successfully performed flow cytometry on a miniaturised microfludic platform, through the addition of some small optical and electronic components on a standard cell phone [142]. Figure **(c)** illustrates the resolution of green fluorescent beads with diameters of 4μm and 2 μm. The raw cell-phone images of these fluorescent beads is illustrated in the top row, while the bottom row shows a comparative series of images of the same particles obtained using a 40 x microscope objective lens (NA = 0.65) on a standard fluorescent microscope. In addition, Zhu *et al.* performed white blood cell flow cytometry on concentrations of WBCs of 4000 – 8000 cells/μL, demonstrating a good agreement between this miniaturised technology and the commercially available haematology analyzer (Sysmex KX-21N)

(d) **(e)**

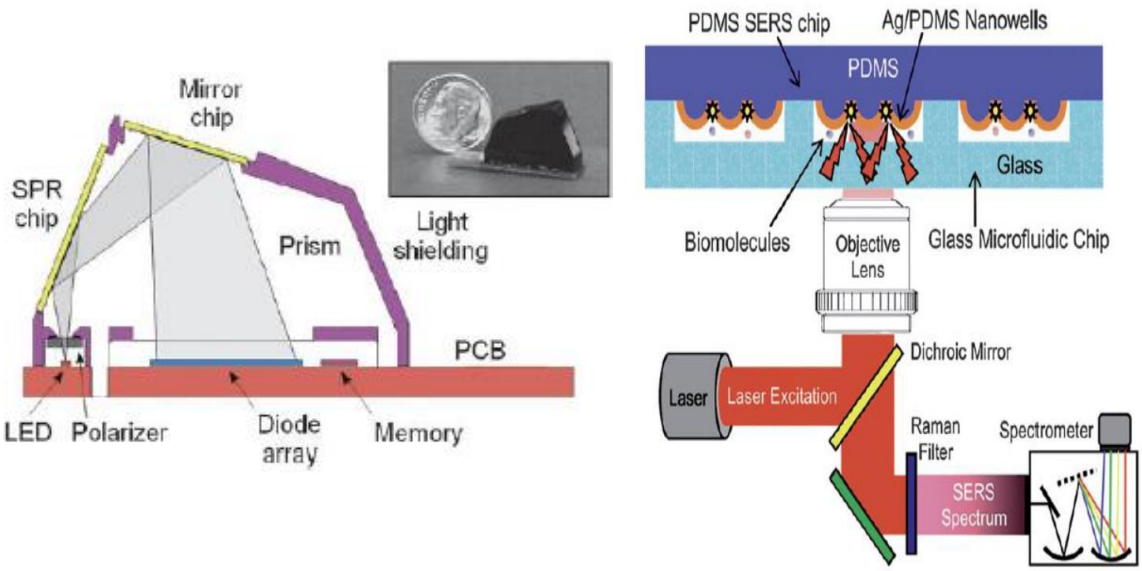

Figure 1.13: (d)-(e) (d) Surface plasmon resonance detection regimes for biomedical diagnostics on microfluidic platforms The Spreeta 2000 system developed by Chinowsky *et al.* [143]. utilises Surface Plasmon Resonance techniques to carry out an automated assay for mouse IgG. This device produced a limit of detection of 80pM for mouse IgG, which is comparable to standard ELISA assays, on a compact, high speed and low noise platform. **(e)** Liu and Lee demonstrated the potential that SERS technology offers to improved sensitivity on microfluidic sensing platforms [144]. Improvements in signal by a factor of 10^7 were recorded when the Ag/PDMS nanowell design in Figure **(e)** above was compared to a smooth Ag layer on PDMS for the detection of Rhodamine 6G and adenosine samples.

These platforms have demonstrated detection, counting and imaging capabilities to rival their much more costly and bulky laboratory based counterparts and have been the subject of a number of excellent reviews [138-140]. Of particular interest to the research community is the application of lensfree holography and contact imaging techniques to inertial and centrifugal microfluidic platforms [145,146]. The simplicity and cost-effectiveness of employing these techniques for optical detection serves to make them very attractive for lab-on-a-chip point-of-care applications. The basic operating principle of holographic and contact-imaging is outlined in Figure 1.14.The importance of these techniques for cell detection and imaging applications is clearly evident in the ground-breaking research being carried out by groups such as Ozcan and Zhu *et al.*[142], as referred to previously. Further examples of the optical capabilities of lensfree techniques for cell imaging can been seen in Figure 1.15.

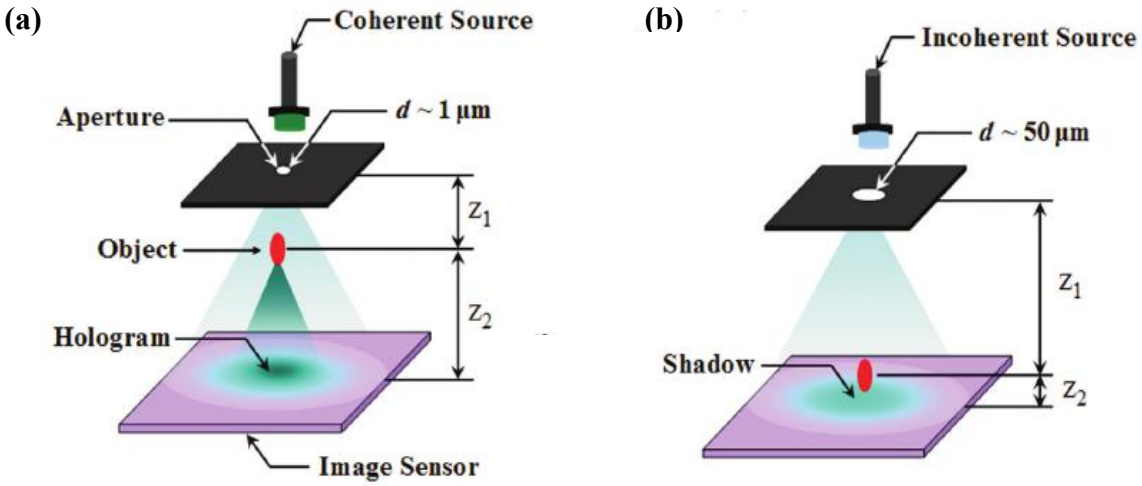

Figure 1.14: **(a)** Schematic of typical digital in line holography (DIH) configuration, with coherent light source. [Modified from [146]] Z_1 is the distance from the pinhole to the object, with Z_2 representing the distance from the image plane to the object**. (b)** Schematic of typical contact imaging configuration, with incoherent light source.[Modified from [146]] Z_1 is the distance from the pinhole to the object, with Z_2 representing the distance from the image plane to the object. In contrast to coherent DIH, the object is placed much closer to the sensor plane (~1-5mm), with a distance from the object to the pinhole of ~40-100mm.

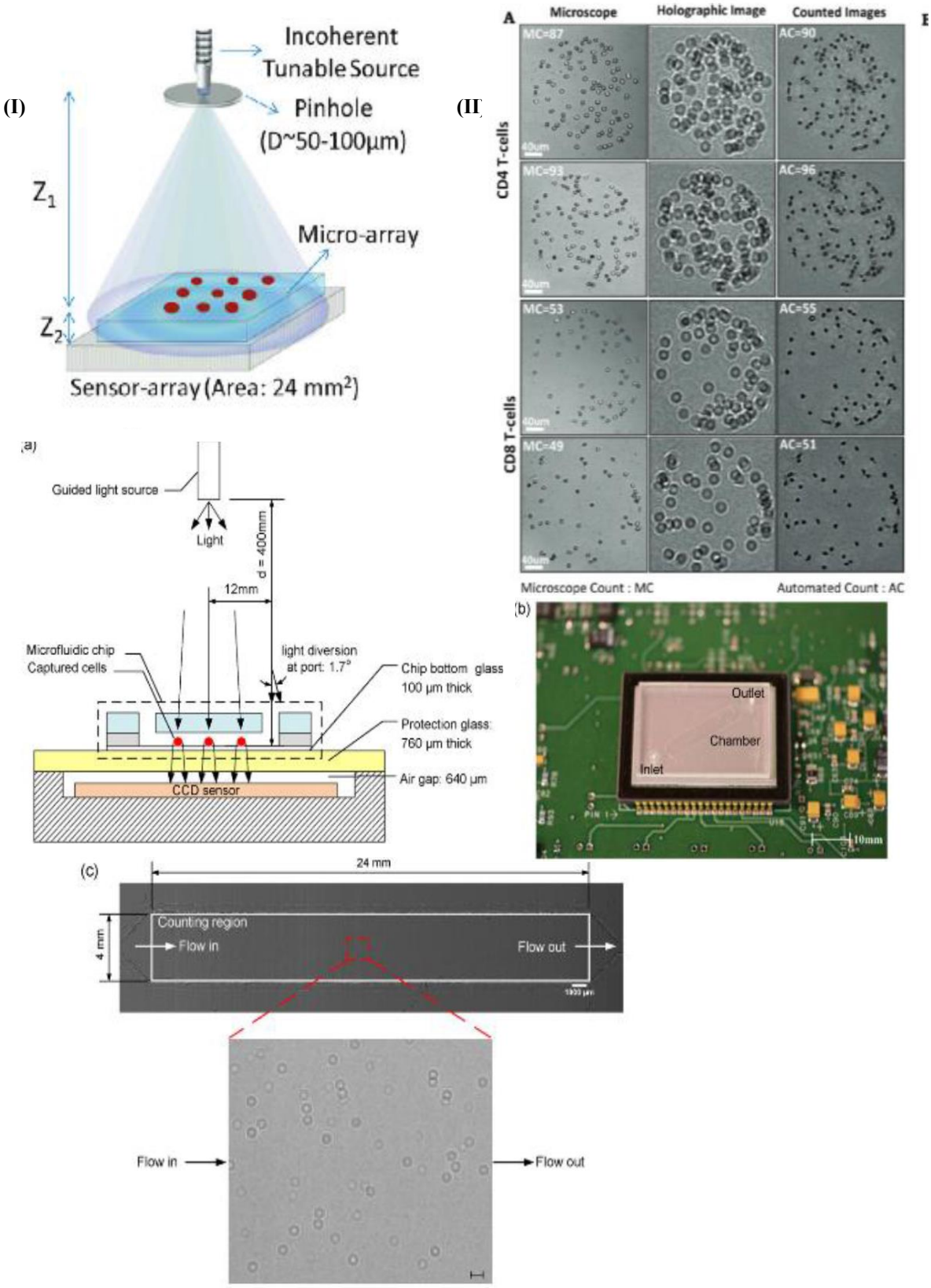

Figure 1.15: (I)-(II) Illustration of lensfree holographic imaging using inexpensive and compact optical and electronic components by Stybayeva *et al.* [147]. The left image **(I)** shows the experimental configuration for this device, while the right image **(II)** compares the resolution of CD4 and CD8 cells on 200µm antibody spots obtained using a 10x objective microscope lens, the raw images from holographic set up developed by Stybayeva *et al.* and the reconstructed holographic images. Bottom image: **(a) - (c)** Lensless CD4+ cell counting on a microfluidic platform by Moon *et al.* [148]. When light falls on the cells from the guided white light source, the cells diffract and transmit light onto the CDD, creating a shadow image in just 1 second. This device demonstrated CD4+ counts for HIV monitoring within 10 minutes from a whole blood sample.

These groups have taken advantage of the continued development of smaller and more cost effective electronics coupled with the widespread availability of inexpensive mobile phones to produce integrated, compact and cost effective imaging devices for microfluidic technologies. With the price of cell phones likely to drop further and the continued expansion of wireless networks globally, this area of optical detection is likely to have an even greater impact on the field of point-of-care diagnostics in years to come. This will be discussed further in Chapter 4.

As stated above, recent developments in the field of optical detection for biomedical platforms illustrate how scientists and clinicians alike are moving away from the typically bulky free-space optics and detection platforms towards smaller, more integrated systems. The miniaturisation of light sources and optical detectors, i.e. LEDs, laser diodes, CCDs and CMOS chips, allows for the elimination of a number of time-consuming and cumbersome alignment steps with "off-chip" light sources and detectors. This is of key importance not only for low resource environments but also for the integration of light sources and detectors onto centrifugally driven microfluidic platforms.

While all of the aforementioned methods have been used to great effect when coupled with inertial microfluidic platforms as illustrated above, the integration of these technologies onto centrifugal platforms remains in the early stages. As the aim of this thesis is to develop components towards an integrated sample-to-answer lab-on-a-chip device for 3-fold WBC differentiation, the following sections will give a brief overview of the approaches to optical detection on centrifugal platforms, noting recent examples of state of the art centrifugo-optical techniques. The focus of the review will then shift to optofluidic platforms; i.e. integrated systems combining microphotonic and microfluidic technologies. Finally, the author will outline how this optofluidic approach could be integrated onto a centrifugal platform, such as the one described in this thesis, for cell detection, counting and imaging.

1.6.2 Optical Detection and Imaging for Centrifugal Microfluidic Platforms

As elucidated clearly in section 1.2.1, centrifugo-microfluidic platforms offer many advantages over their inertial counterparts for liquid handling and, therefore, diagnostic applications. These advantages can also be utilised when developing suitable optical detection technologies. For example, the rotational actuation scheme that is a standard on all centrifugal microfluidic platforms enables periodic and jitter free motion due to

the static nature of the spinning motor. In addition, the intrinsic 1D scanning capability of the platform lends itself to automated scanning and detection of biomolecules. The 1D scanning capability of the platform can be further enhanced through the addition of a simple linear motor, creating a scheme analogous to that of an optical disc drive. This approach has been used to great effect in the detection of microparticles and biomolecules by ODDs and modified ODDs, as we will see in the discussion that follows. It should be noted, however, that there are numerous challenges associated with carrying out optical detection at a comparable level to inertial systems. The predominant issues are associated with disc wobble during rotation, the stopping of the motor, and therefore the disc, at a predefined location and the alignment of off-chip optical detection systems and the rotating disc.

King *et al.* have recently completed a comprehensive review of optical detection methods on centrifugal platforms [149], which can broadly be divided into two categories:

- Lab-on-a-chip systems with integrated laboratory unit operations (LUOs) and on rotor/on disc based optical detection systems.
- "Bio-CD" platforms, which use a functionalised reflective surface (similar to a conventional) CD to carry out interferometric detection.

The first category can be further divided into label-free and label-based optical detection schemes. Label free detection techniques usually take the form of absorbance; scattering or total internal reflection (TIR), based regimes. A recent example of absorbance based optical detection on centrifugally-driven microfluidic platforms by Steigert *et al.* can be seen in Figure 1.16 [141].

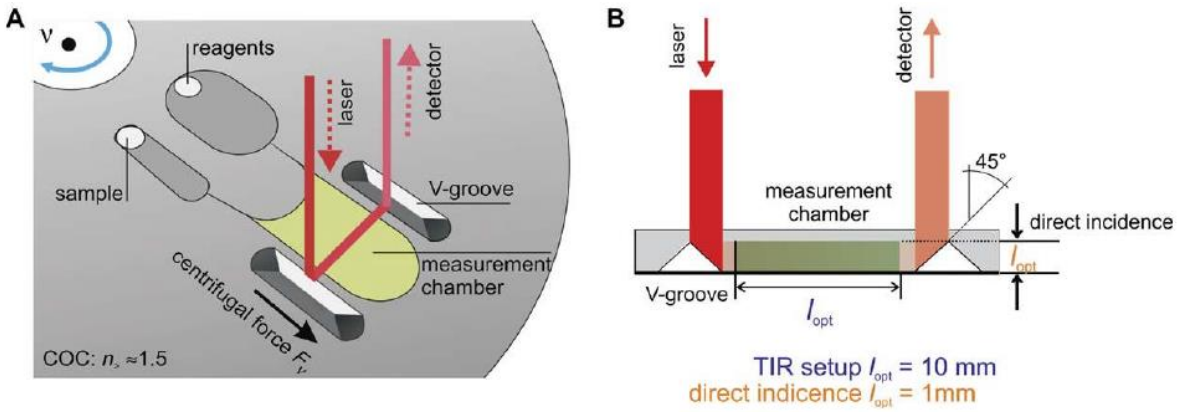

Figure 1.16 Illustration of the working concept of absorbance based centrifugal microfluidic platform using total internal reflection techniques. **(A)** As the disc is spun, the samples of interest are driven into the measurement chamber, where **(B)** V-shaped grooves deflect the input beam from the laser diode through the sample and out to the detector. This assay successfully measured the concentration of glucose [150], haemoglobin[151], and alcohol[141] in human whole blood, with a LOD of 200μM achieved for glucose sensing applications.

In this example by Steigert *et al.* the optical path length (I_{opt}) is lengthened by a factor of 10 through the use of total internal reflection, increasing the signal level and therefore the sensitivity of absorbance based systems. The technique employed by Grumann *et al.* was expanded to precisely measure liquid volumes, flow rates and viscosities by Hoffman *et al.* [152]. In Hoffman's design, a line laser and linear image sensor array were mounted on a stationary plastic platform and enabled the detection of the gas-liquid interface on the centrifugal microfluidic platform up to frequencies of 30Hz. In the case of scattering based optical detection, both elastic scattering in the form of Mie and Rayleigh scattering [153] and inelastic techniques such as surface plasmon [154] and surface-enhanced plasmon resonance[155-158] have been utilised. These methods have been used successfully by Kim *et al.* to detect and image microparticles [155], while Choi *et al.* [156], Cho *et al.* [157] and Han *et al.* [158] have demonstrated surface-enhanced Raman detection of biomolecules.

In contrast to the techniques discussed above, label-based optical detection is typically used in the form of a fluorescent secondary antibody as part of an enzyme linked immunoassay (ELIZA), for the detection of analytes and biomolecules of interest. This approach increases the sensitivity of the assay compared to the commonly used absorbance based ELIZA platform and has been integrated onto a number of assays by Burger *et al.*[129-132] and Lee *et al.*[126], as illustrated in Figure 1.17.

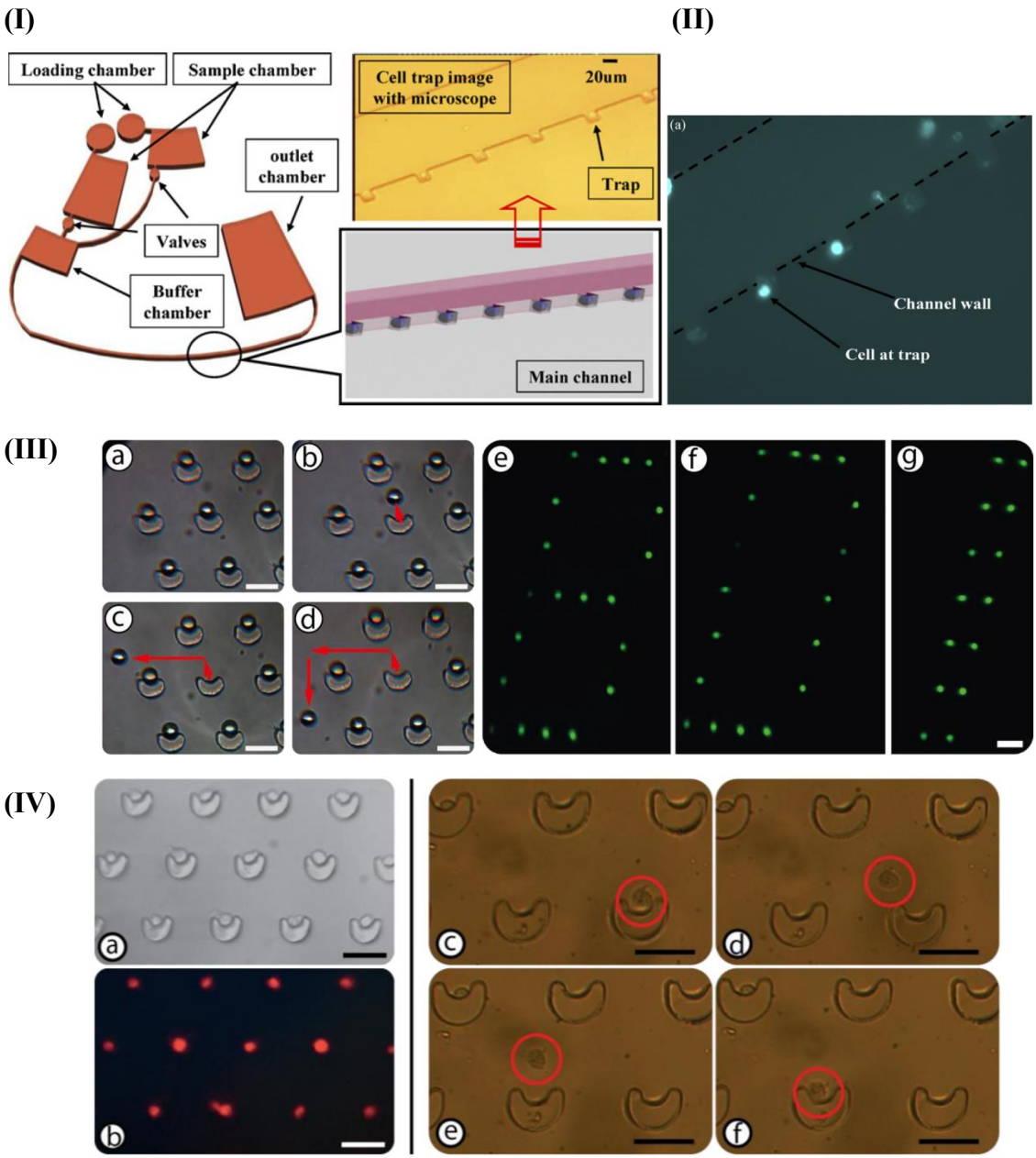

Figure 1.17: (a) & (b) Fluorescence-based detection of beads and cells on centrifugally actuated microfluidic platforms. As discussed in section 1.5.1 on gravity driven cell capture platforms, Lee *et al.* have developed a centrifugal platform which traps cells singly using slanted pits in a spiral microfluidic channel [126]. UV illumination was utilised with fluorescent tagging and a CCD (charge coupled device) camera to differentiate dead HEK293 cells from live HEK293 cells, as illustrated in Figure **(b). (c)** The V-Cup capture structure discussed in section 1.5.2 developed by Burger *et al.* [132] utilised fluorescent tagging to image polystyrene beads of 12.5µm in diameter (scale bar 50µm), as well as cells such as the HL-60 cells captured singly in Figure **(d)** above. The optical set up mounted on a centrifugal test stand platform includes an infrared laser for cell and bead manipulation, a 488nm excitation wavelength laser, which is also equipped with 6 optical filters for multi-colour fluorescence detection and a secondary camera (TXG 14f, Baumer) to image cell and bead manipulation using the optical tweezers.

Further to the aforementioned work, Nwankire *et al.* [159] have exploited optical techniques such as supercritical angle fluorescence (SAF) (Figure 1.18 that follows) to

reduce cost and complexity of the detection system, while maintaining the superior sensitivity associated with label-based systems. Using small and relatively inexpensive optical components such as a focussing lens, a 635-nm, 5-nW laser diode (Hitachi, Ireland), a spherical ring lens structure and a photomultiplier tube (PMT), an optical detection system capable of carrying out human IgG immunoassays was developed. [159]

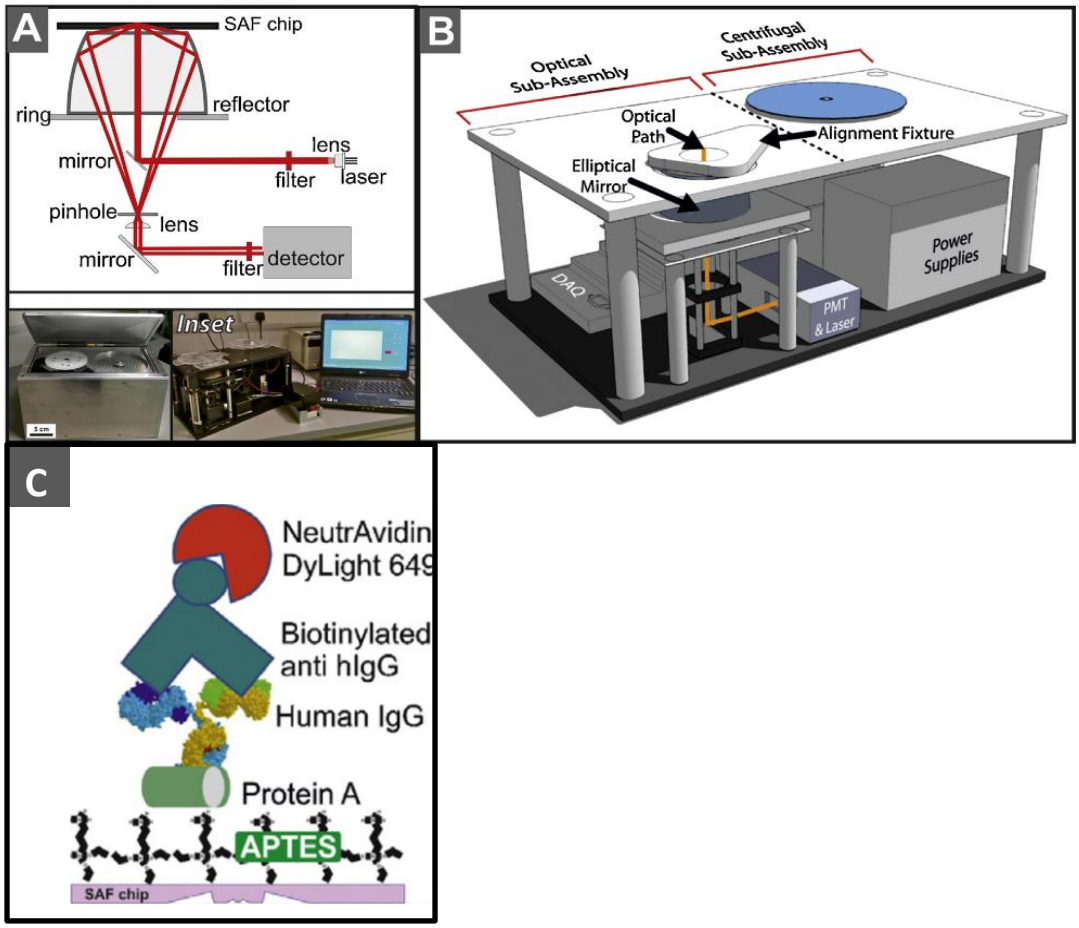

Figure 1.18: (A) Schematic of the optical path direction of Supercritical Angle Fluorescence detection principle by Nwankire *et al.* [159], showing the collection of supercritical angle emission using the novel SAF chip. Inset: Photograph of the prototype system (with and without the protective casing), centrifugal microfluidic set up and laptop for control of the centrifugal system, photo-multiplier tube (PMT) (Hamamatsu, Japan) for fluorescence detection and a 635-nm, 5-nW laser diode (Hitachi, Ireland) for fluorescence excitation. **(B)** Schematic of SAF optical detection set up. **(C)** Schematic of the immunoassay binding procedure; with the fluorescently tagged biotinylated antibody attached to the human IgG, resulting in its capture on the APTES functionalised surface by streptavidin adhesion.[Modified from [159]]

This centrifugal "test-stand" approach to cell capture, detection and imaging has been developed, from its early inception by Grumann *et al.* [160], to detect and image a variety of cells such as circulating endothelial cells (CECs) from peripheral blood mononuclear cells, Jurkat and HL60 cells. These examples are discussed further in the review by King *et al.* [149].

Another approach to optical detection on centrifugal platforms centres on spinning disc interferometry on standard and modified optical disc drives (ODD) (i.e. 1D and 2D) [161,162]. These readout schemes have been used to great effect in the detection and imaging of immobilised biomaterials on centrifugo-microfluidic platforms. The suitability of applying spinning disc interferometry to centrifugal-microfluidic platforms is clearly evidenced by Nolte et al in his review article in 2009 [29]. In one example by Nolte *et al.*, a sensitivity of 100pg/ml for the target antigen was obtained using spinning-disc interferometry, which facilitated a 64-fold multiplexed assay, with a total of 32,000 assays per Bio-CD, illustrating the high-sensitivity and high-throughput of such platforms. However, while this technique has been successfully employed in other centrifugo-microfluidic assays [163-165], it relies on bulky and expensive optical instruments, particularly when compared to alternatives such as ODD detection. Due to the widespread availability and ever decreasing cost of ODDs, coupled with their associated high data resolution, ODDs are an attractive alternative to other spinning disc technologies. In addition, the 2D linear scanning functionality of standard ODDs can be expanded to carry out 2D imaging, in an analogous manner to a laser scanning microscope[166]. Figure 1.19 that follows illustrates some examples of standard ODD and modified ODD detection and imaging systems on centrifugo-microfluidic platforms. Through the addition of simple photonics such as a photodiode, Ramachandraiah et al. created a 2D laser scanning microscope (Figure 1.19), which successfully imaged microparticles and blood-borne CD4+ cells [166].

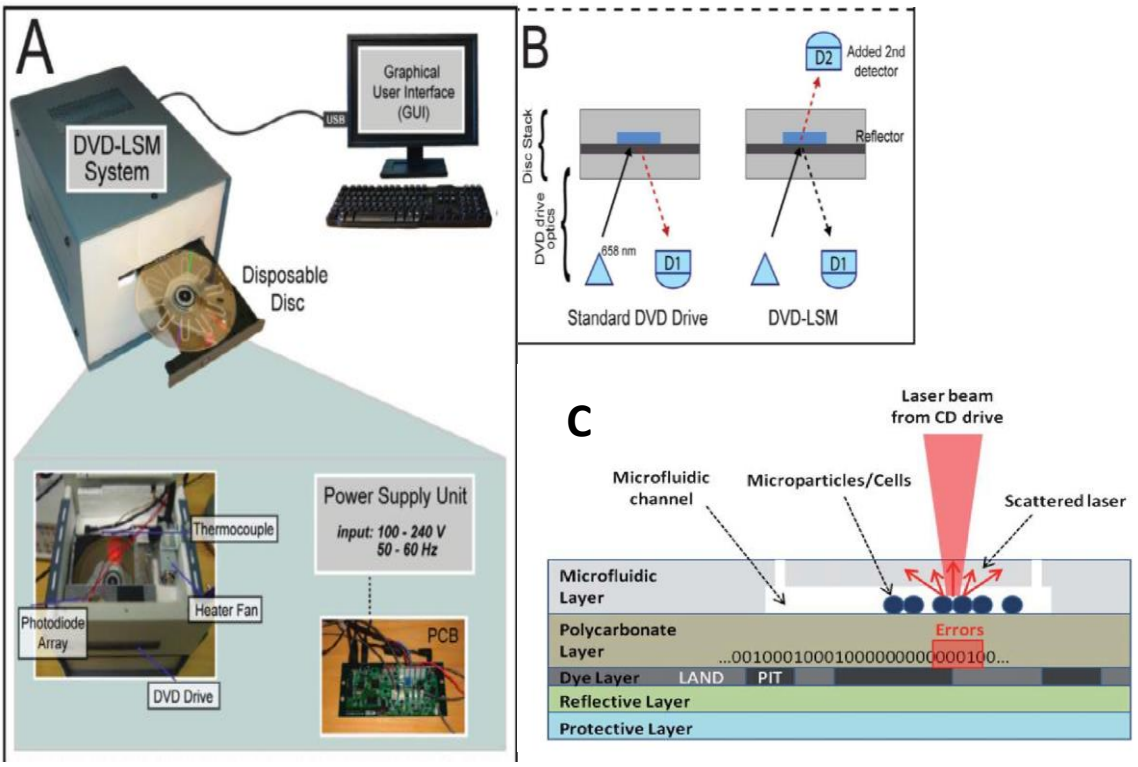

Figure 1.19 **(A)** Schematic of the modified 2D scanning DVD drive detection platform developed by Ramachandraiah et al. [166]. **(B)** Illustration the operating principle of the platform, which includes an additional photodiode to detect the ODD laser light transmitted through the polymeric platform. 2D images of beads of various sizes (1µm, 2.8µm and 5µm) as well as blood-borne CD4+ cells have been recorded. **(C)** Schematic of the microparticle/cell detection platform developed by Imaad *et al.* [167] using a standard ODD. A standard polycarbonate rewritable CD is written with a repeating binary pattern of "100 100 100..". The CD is then milled down into the polycarbonate layer to accommodate a PDMS microfluidic layer, while maintaining the maximum CD thickness of 1.2mm. When the microparticles/cells of interest are inserted into the platform, they produce errors due to the scattering of the laser light incident on the CD. These errors can be used to create a calibration curve and therefore detect the number of particles in the assay.

As illustrated in Figure 1.19 and in the literature [166,167], standard ODDs have been used for the detection and counting of microparticles and CHO cells, while DNA hybridization reactions; protein-protein interaction and biotin-streptavidin binding were monitored on a functionalised Bio-CD surface [168-170]. With similar small modifications to those carried out by Ramachandraiah *et al.*, such as additional photodiodes or laser based detectors, researchers have managed to study genomic information, measure DNA microarrays and perform immunoassays on these Bio-CD platforms.

For the further development and future success of centrifugal microfluidic platforms for diagnostic applications, suitable optical detection platforms must be developed towards full integration and commercialisation. A number of the optical detection platforms referenced in the previous section, such as the Discipher platform

developed by Ling Vitae and outlined in Figure 1.19 previously, are either in the process of or have already been made commercially available, and a review of these devices has been compiled by Chin *et al.* [26]. For further discussion on state-of-the-art developments in the field of centrifugo-optical detection, including a comprehensive list of the functionality and applications of recently developed "on disc" and "BioCD" platforms, the reader is directed to the aforementioned review by King *et al.* [149]. The remainder of this section will focus on optofluidics and the advantages of using optofluidic techniques for detection on microfluidic platforms.

1.6.3 Optofluidics

As outlined in the introduction, optofluidics is the marriage of miniaturised photonics and microfluidics on a single platform. This approach enables greater miniaturisation and enhanced sensing capabilities for typical lab-on-a-chip biomedical diagnostic and analytical devices. Fully integrated optofluidic devices are more compact, sensitive and, unlike off-chip optical detection systems, can circumvent the same cumbersome alignment steps by using embedded, miniaturised light sources and detectors. The general structure of an optofluidic chip is outlined in Figure 1.20.

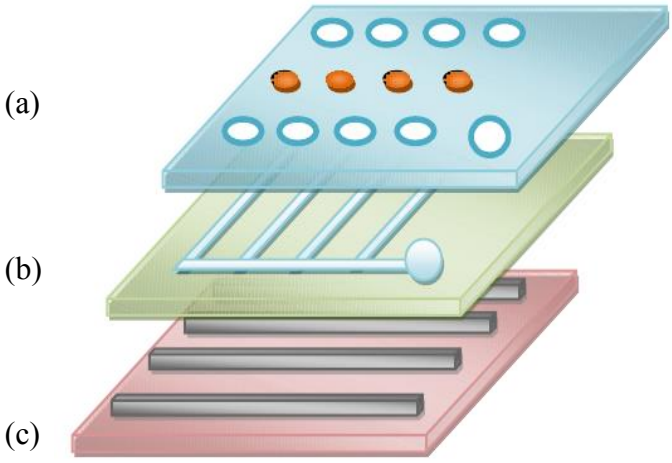

Figure 1.20 A simplified schematic of a typical optofluidic device**. (a)** The top layer consists of the inlet and outlet holes and microfluidic controls such as valves and pumps. **(b)** The second layer consists of microfluidic reservoirs and channels. **(c)** The third and final layer usually consists of the optical detection components such as light sources, waveguides and a variety of light detection elements.

The development of highly sensitive and miniaturised optical components such as optofluidic waveguides, lenses, switches and filters has begun to revolutionise the field of miniaturised optical sensors. The three typical optofluidic configurations, as well as a

discussion of some of the most notable technologies in the field today will be outlined in the section that follows.

1.6.4 Optofluidic Systems – Structure and Materials

Optofluidic devices can generally be divided into three main categories; (1) fluids in solids, (2) fluids in fluids and (3) solids in fluids. These three categories will be briefly explained below.

(1) Fluids in solids

These devices utilise the control of liquids of different refractive indices through microfluidic channels, usually of dimensions larger than the wavelength of light, to transfer and deflect light as needed through an optofluidic device. A good example of this is the ARROW [171,172] – or anti-resonant reflecting optical waveguides. ARROWs operate on the reverse principle of most solid core waveguides; with a higher refractive index solid, coated in an anti-resonant layer, encasing a lower refractive index air or liquid core. Figure 1.21 provides a schematic of the typical ARROW structure, as well as an SEM image of the same.

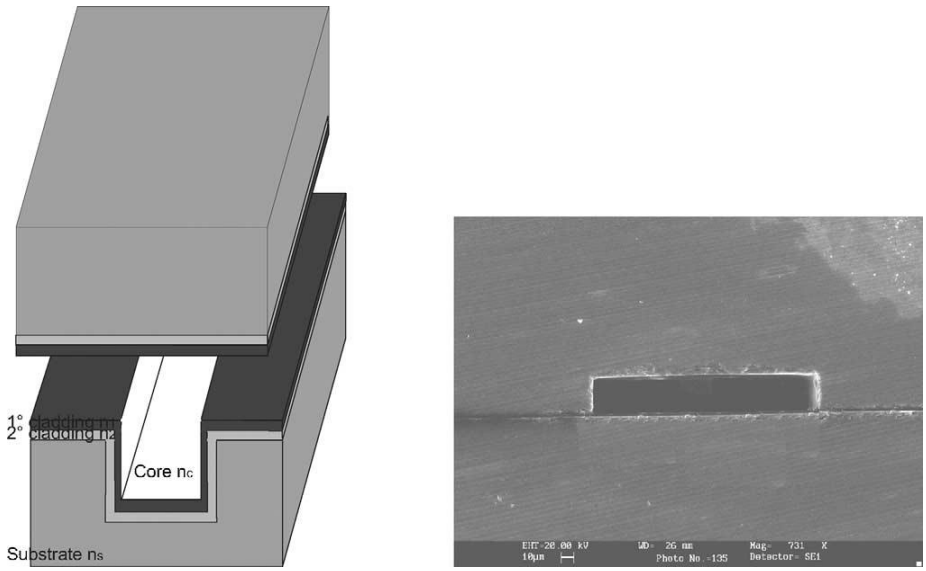

Figure 1.21 ARROW optofluidic configuration. [171] On the left the hollow core, silicon cladding and dielectric anti-resonant layers of the ARROW are illustrated. The image on the right is a transverse SEM image of the ARROW.

(2) Solids in fluids

Solids can be incorporated into the liquid phase of an optofluidic device to form colloidal suspensions. These solids can then be used to change the optical properties of the liquid or to control the transmitted light in a variety of ways. Suspended solids much lower in size than the wavelength of the light passing through the device can be used to change the optical properties of the fluid e.g. its refractive index [153]. Suspended solids much larger in size than the wavelength of the light passing through the device can be used to focus the incident light like spherical lenses[153], as illustrated in Figures 1.22 and 1.23 that follow. These larger solids can be controlled using optical tweezers[173,174], or, in the case of ferromagnetic solids, by magnets embedded in the device or suspended above it [175]. The reader is directed to a thorough review completed by Lee *et al.*[176] for a more detailed discussion on the use of colloidal suspensions in optofluidic technology.

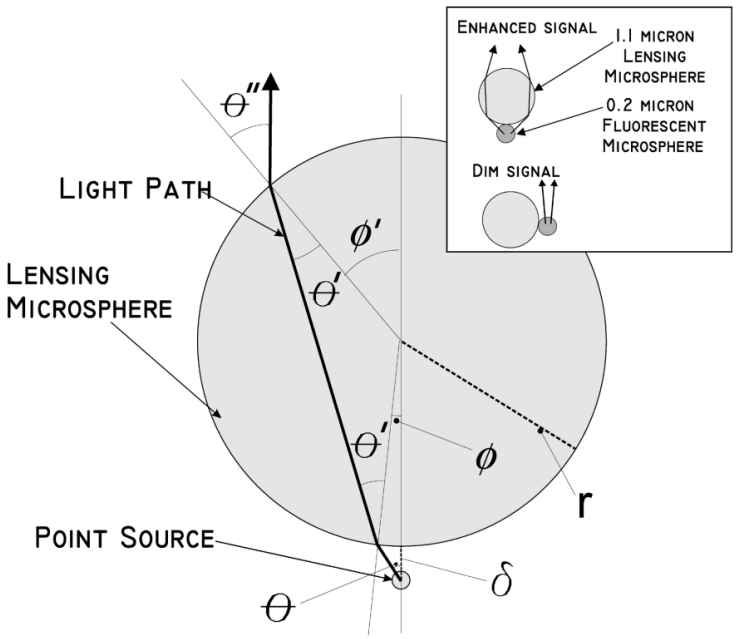

Figure 1.22 Ray schematic of the focusing of light through a "lensing microsphere" i.e. a solid much larger than the wavelength of light transmitting through the colloidal suspension [177].

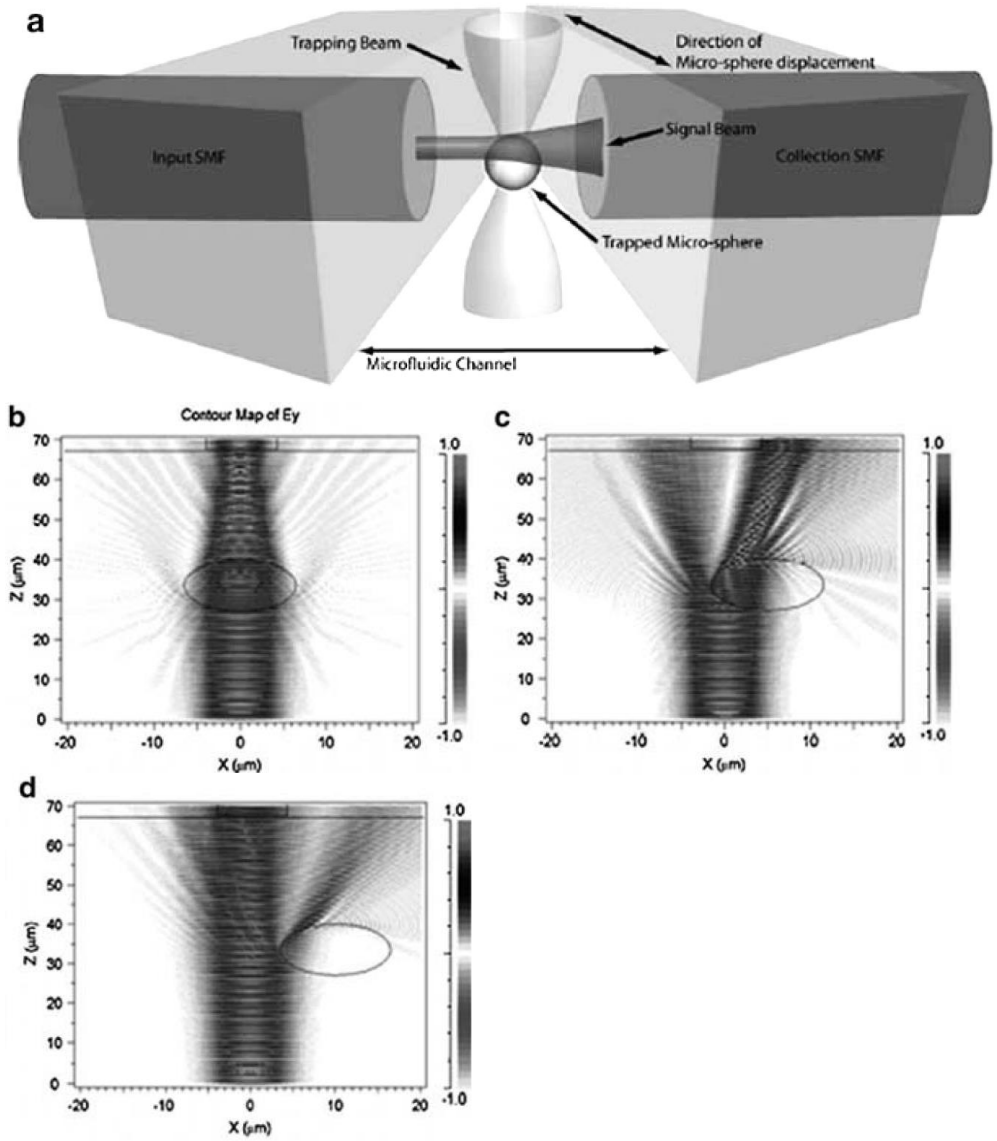

Figure 1.23 (a) Illustration of how an optical tweezers can be used to produce switching in a "solid-fluid" optofluidic device [Modified from [176]]. The optical tweezers can hold the microsphere in the path of the incident and output waveguides until switching is necessary. Finite difference time domain (FDTD) simulation of the electromagnetic field of the microsphere **(b)** In the beam centre; **(c)** off centre and **(d)** leaving the beam [176].

(3) Fluids in fluids

These devices exhibit even greater flexibility and tunability than fluid in solid regimes, particularly in waveguide-like configurations, as illustrated by Wolfe *et al.* [178] in the L2 waveguides. A high refractive index liquid is surrounded by a lower refractive index liquid cladding, enabling light to move within the core using total internal reflection (TIR). While external pumping and actuation mechanisms are still frequently used for optofluidic systems, some recent research has centred on addressing these issues. L2 waveguides have been utilised by Vezenov *et al.* to develop an integrated fluorescent

light source for optofluidic applications by adding a fluorescent dye to the liquid core, as seen in Figure 1.24 [179]. Both liquids can be replaced or rerouted at will using microfluidic channels.

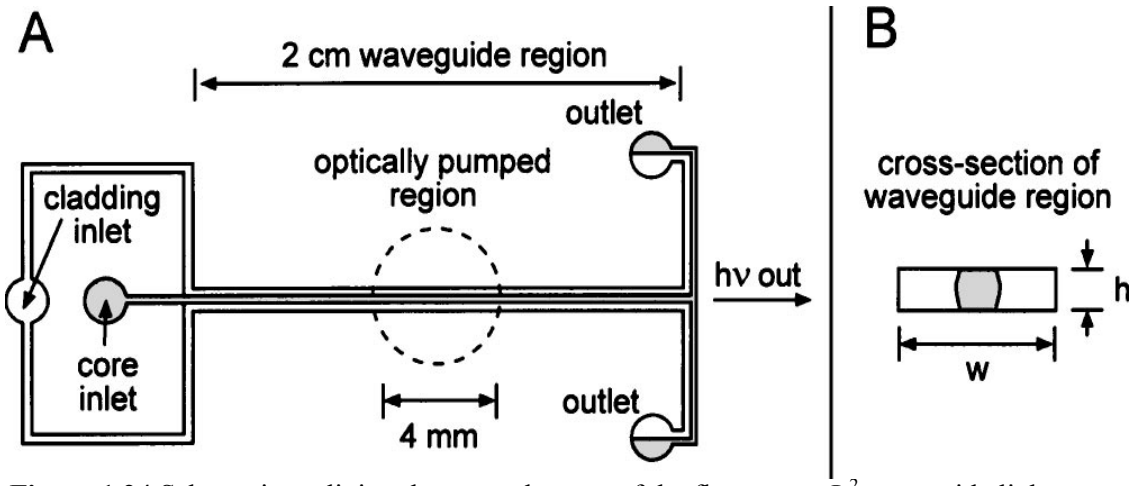

Figure 1.24 Schematic outlining the general set up of the fluorescent L^2 waveguide light source, developed by Vezenov *et al.*[179]. **(a)** The microfluidic channels are fabricated in PDMS, with a core liquid of Rhodamine 6G dye in ethelyne glycol and a cladding liquid of water. The central region was optically pumped using a collimated beam from a 150 W quartz halogen lamp, perpendicular to the channel. **(b)** Transverse cross section of the output region, illustrating the area which was imaged using both a Si photodiode and a CCD camera.

By varying the composition of the liquid core, the emission wavelength of the laser can be controlled [178]. Additionally, manipulation of the fluid flow rates can facilitate control over the output beam size of the laser and its intensity [179]. It is clear from the evidence above, therefore, that the L2 laser source offers a great deal of promise in providing a highly tunable, efficient and integrated light source for a number of optofluidic applications. Other applications demonstrated by Wolfe *et al.* [178] include optical switches (Figure 1.25) and evanescent couplers (Figure 1.26), which have been created by changing the respective flow rate of the liquids to facilitate further control over the guided light. More recently, Testa *et al.* have demonstrated an integrated tunable 3D optical fiber by utilising a novel hydrodynamic focusing scheme [180].

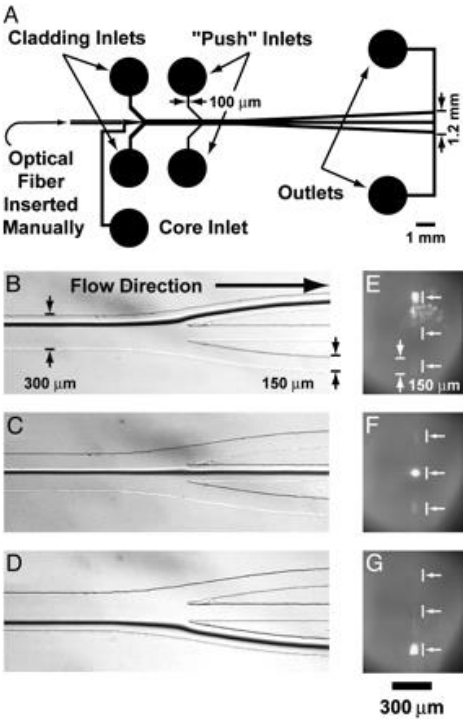

Figure 1.25: General outline of optical switch developed by Wolfe *et al.* [178]. **(A)** Microfluidic optofluidic device, fabricated in PDMS. Deionised water was used as a cladding layer, while a 5M aqueous solution of $CaCl_2$ was used as a high refractive index core material**.(B)** Optical micrographs illustrating that the user can switch the direction of the light transmission by controlling the fluid flow in the core and cladding layers of the liquid-liquid waveguide. The core fluid is dyed for ease of imaging.

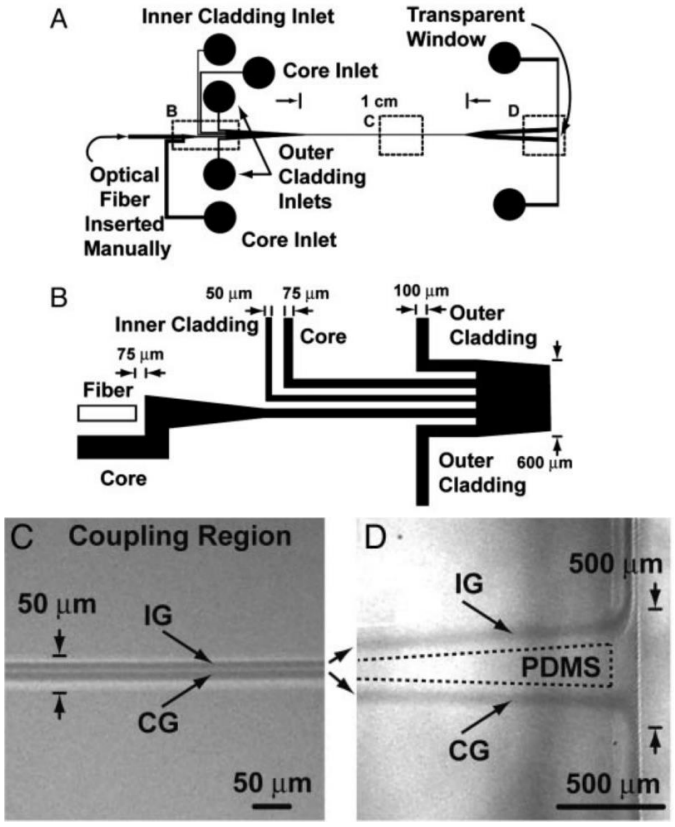

Figure 1.26: General outline of an evanescent coupler developed by Wolfe *et al.* [178]. **(A)** Microfluidic design of the optofluidic device, fabricated in PDMS. **(B)** Schematic of the input area of the microfluidic channels. **(C) & (D)** Optical micrographs of the coupling and output regions liquid-liquid waveguide.

As a result of the aforementioned work there is huge scope for developing new fabrication methods for the integration of optofluidic components into centrifugally driven microfluidic systems. One recent approach towards the development of fully integrated optofluidic devices is the formation of embedded waveguides within polymers such as PMMA [181-182]. Attempts have been made to micromachine a number of other polymeric substrates such as COP and polystyrene with femtosecond lasers, but these polymers did not retain their optical transparency [183]. As a result of this, PMMA is generally favoured for this approach, due to its low cost, thermal stability, optical transparency and widespread use in lab on a chip devices. A recent example of this fabrication process can be found in an article by Sowa *et al.* [181], where embedded symmetric waveguides were created in PMMA by a 1kHz Ti:Sapphire femtosecond laser with laser pulse widths of 85fs, and a wavelength of 800nm. The refractive index of the core of the PMMA is increased by 4.6×10^{-4}, which results in a single mode waveguide for transmission at 632.8 nm and a directional coupler which splits the incident light into a ratio of 1:1. Additionally, femtosecond laser pulses can be used to form diffraction gratings within the PMMA surface [184,185] as well as ablating microfluidic channels into PMMA substrates [186,187].

While fully integrated optofluidic platforms, to the author's knowledge, have yet to be realised on PMMA, a 2007 publication by Osellame *et al.* [188] stated that they had successfully manufactured both microfluidic channels and optical waveguides on the same glass substrate, enabling fluorescence measurements to be carried out on-chip. It is clear, therefore, that the possibilities for extending this work further in the area of centrifugo-optofluidics research are vast. Although this fabrication technique is not as straightforward or low cost due to the complexity and cost of operating a femtosecond laser, it illustrates another field of research that is pushing towards full microfluidic and optical integration on lab-on-a-chip platforms. Another promising method under investigation is the use of organic photocurable materials such as sol-gels or selectively irradiated polymers, such as PMMA, as optofluidic materials. These materials would be used as an alternative to PDMS, which, while offering many favourable properties for rapid and inexpensive fabrication for microfluidic platforms, does not have the same level of optical tunability as the aforementioned sol-gel and PMMA materials. In the case of sol-gels and irradiated polymers, the same base material can be used to form both the microfluidic and optical components of the chip, usually with just a few fabrication steps. Copperwhite *et al.* [189] have taken the first steps in forming a fully integrated evanescent wave based biosensor, utilising photocurable sol-gels to make

high quality, low loss waveguides and microfluidic channels on the same platform. Figure 1.27 illustrates the fabrication process of the integrated microfluidic network on planar waveguides on a silicon substrate.

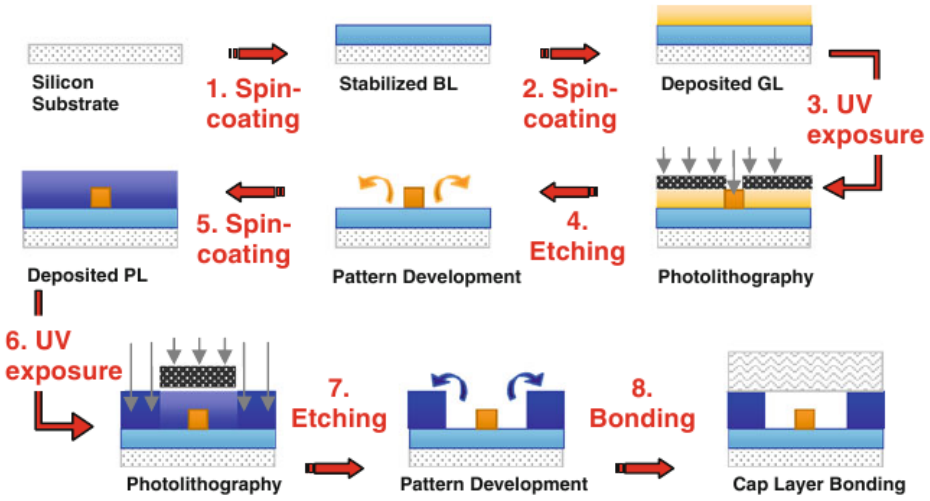

Figure 1.27: Schematic of the fabrication steps involved in creating an integrated sol gel optofluidic platform [189]. Initially the sol-gel waveguide is formed using spin-coating and photolithography techniques, followed by a similar step-wise process for the surrounding microfluidic channels.

A variety of microfluidic channels were fabricated in the sol-gel material, including straight channels, serpentine channels and micropillar arrays to assist capillary action. The platform outlined in Figure 1.27 was successfully fabricated, as can be seen in Figure 1.28 that follows. The microfluidic channels were treated with an O_2 plasma to make them hydrophillic and thus enable capillary flow.

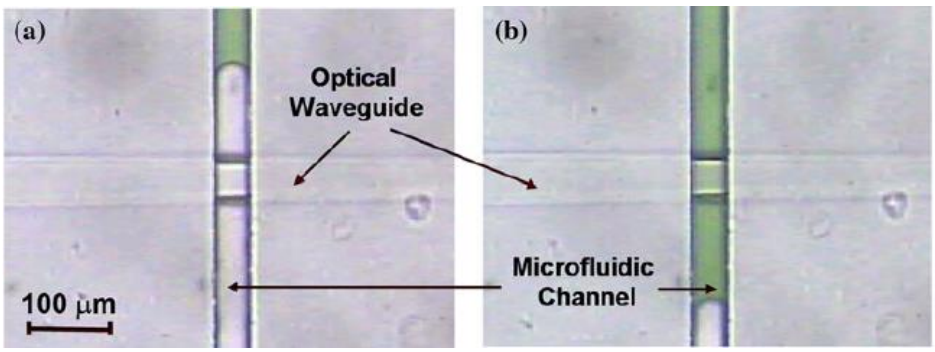

Figure 1.28: Intersecting microfluidic channels and planar waveguides. Fluid flow (a) before and (b) after crossing over the waveguide. [189]

This resulted in flow rates of between 0.012 µL/mm and 0.018 µL/mm of green food dye in H_2O. While the article by Copperwhite *et al.* [189] shows huge promise for fully

integrated systems, further work needs to be done to test the performance and limit of detection of this scheme when implemented as a working biosensor. More importantly, there is huge scope for adapting this platform to a centrifugally driven system rather than one that depends on capillary flow or pump driven flow. While the O_2 plasma treatment is used to enhance the capillary flow in the above article, its effect is temporary and significant hydrophobic recovery ensues in less than 24hrs. This makes the medium to long term storage of this sensing device non-viable as flow rates will significantly reduce over time. A centrifugal platform employing sol-gel technology could produce a reliable, efficient and sensitive biosensor. However, in order to produce a low cost, easily fabricated and centrifugally compatible platform, the silicon substrate used above would need to be replaced with a polymer such as PMMA. This work will be discussed further in sections 2.3 and 3.3, with a view towards the integration of sol-gel waveguiding materials onto centrifugo-optofluidic platforms. Balslev *et al.* have successfully demonstrated a fully integrated monolithic lab-on-a-chip device including an "on-chip optically pumped liquid dye laser, waveguides and fluidic channels with passive diffusive mixers, all defined in one layer of SU-8 polymer, as well as embedded photodiodes in the silicon substrate" [190]. A schematic of the general layout of the chip and an image of the main features of the chip can be seen in Figure 1.29.

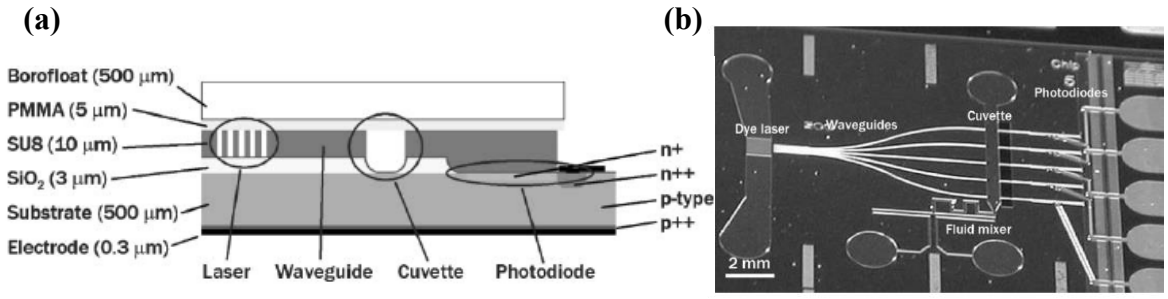

Figure 1.29: (a) Schematic of the materials used to fabricate the integrated optofluidic lab on a chip device. (b) Photograph of the optofluidic chip [190].

A distributed feedback dye-laser was constructed using SU-8 gratings, while the microfluidic channels, which were also fabricated in SU-8, deliver fluorescent dye to the laser and provide mixing capabilities for the analytes. SU-8 slab waveguides carry the transmitted light to an integrated, on chip photodiode. In this way absorbance measurements can be carried out on a single optofluidic chip. Therefore, taking our own results and the work of Balslev *et al.* [190] into account, a fully integrated sol-gel/PMMA centrifugo-optofluidic device could be fabricated using photolithographic steps similar to those in section 1.30. A visualisation of the proposed fully integrated

sol-gel/PMMA centrifugo-optofluidic can be seen in Figure 1.30.

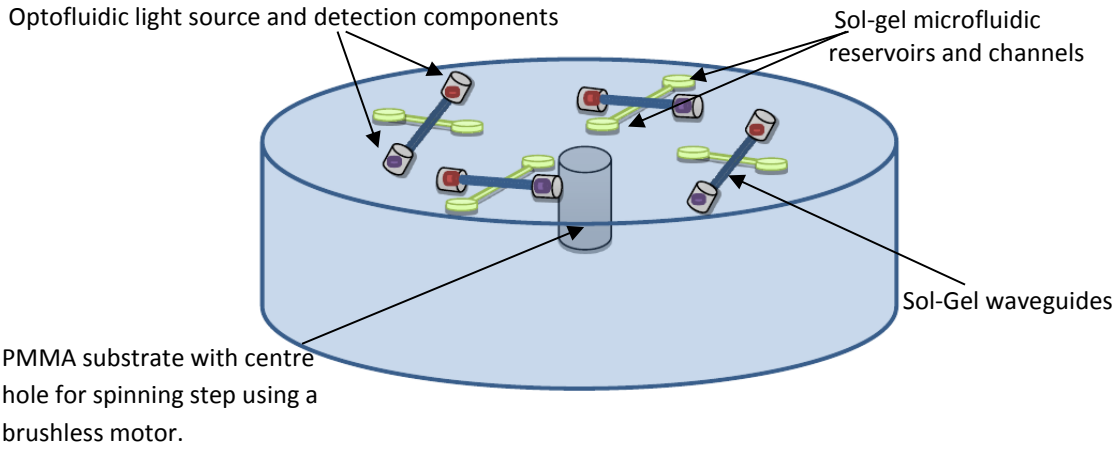

Figure 1.30 The proposed integrated centrifugo-optofluidic sol-gel platform, with four sensing areas. Integrated sol-gel waveguides and micofluidic channels are constructed using hybrid photocurable sol-gel materials, on a PMMA substrate, as outlined in section 2.3. Suitable optofluidic light sources and detectors could be integrated on chip to provide a fully integrated optofluidic platform. The centrifugo-optofluidic disc can then be spun using an external motor to perform analyte delivery, metering and mixing steps.

There are many advantages to this proposed system; low cost of materials and fabrication, rapid fabrication times, high sensitivity, and the full integration of microfluidics and optics on a compact and disposable platform. The development of such a low cost, easy to use disposable optical detection scheme for centrifugo-microfluidic platforms would be a huge step forward for the biomedical diagnostic research community and the widespread commercialisation of lab-on-a-chip devices. sections 2.3 and 3.3 will describe the processes, challenges and results associated with developing such a platform, with chapter 4 outlining further work to develop this research, as well as areas of likely commercialisation in the near future.

Chapter 2 - Materials & Fabrication Methods

2.1 Physical Size Filtration Capture and Assaying

2.1.1 Mask Design and Soft Lithography

Photolithographic techniques were employed to construct miniaturised features on disposable PDMS-PMMA platforms. Initially, the photolithographic masks were designed on AutoCAD design software and then converted into GERBER format. These designs were then sent off to JDphoto-tools for processing, with quartz masks used for features of 10μm or less and acetate masks used for all other designs.

2.1.2 Photolithograpic Mould Fabrication

An OAI 206 CE mask aligner, seen in Figure 2.1, was used for all photolithographic fabrication, with the exception of section 3.1., where the Karl Suss mask aligner was used.

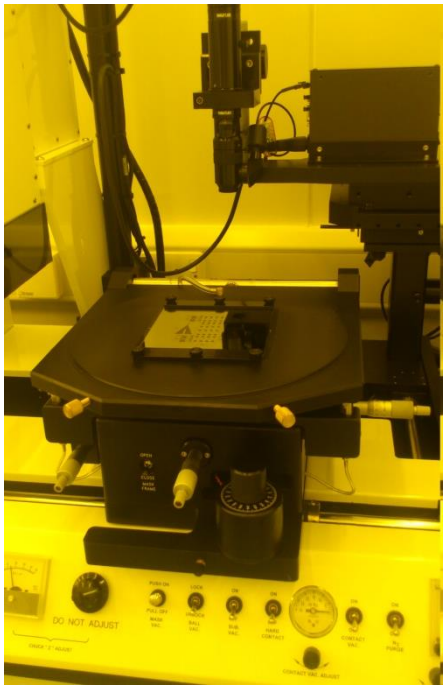

Figure 2.1: Photograph of OAI 206 CE mask aligner, featuring a glass mask secured above the substrate and a Navitar optical set-up to carry out mask alignment. A combination of SU-8 photoresist (Microchem USA), a negative photoresist, and dry film resist (WPR 2100, Dupont, USA) were deposited onto 4" silicon wafers for the fabrication of moulds for the PMDS microfluidic chips. SU-8 is a highly UV sensitive and stable photoresist, which makes it a popular material for the manufacture of high resolution moulds for soft-lithography [191].

Different spin coater spin speeds and viscosities of SU-8 were used depending on the

layer thickness needed for mould fabrication. The typical steps for mould fabrication were as follows:

- The silicon wafer was cleaned with isopropanol (IPA) and air-dried using a nitrogen gun.
- ~5ml of 3025 SU-8 photoresist was deposited onto the silicon wafer.
- A program for a certain thickness was run on a Laurel WS-4032 spin coater, similar to the model illustrated in Figure 2.2 below. (In most cases there is an initial acceleration to a slow spin speed such as 500rpm for 10 seconds, followed by acceleration up to the top spin speed e.g. 3000rpm for 30 seconds, resulting in a ~25 μm layer of 3025 SU-8.)

Figure 2.2: Laurel 400-6NPP spin coater [192].

- The wafer was then "soft-baked" on a hot plate at 95^{o}C for 14 minutes. This step was carried out to prevent sticking of the SU-8 to the glass mask.
- The wafer was exposed on an OAI mask aligner (Figure 2.1) with a glass mask. The exposure time and power varied depending on the size of the features being exposed. For smaller features e.g. filter structures or cups of ~10μm in size, an exposure time of ~10 seconds or less, at a power of 360mW/cm^2 was optimal. For larger features on the order of 50um-100um, a 15 second exposure time, at a higher power of 440mW/cm^2 was necessary. It should be noted that the Karl Suss mask aligner was used to create structures for the microfluidic design outlined in section

3.1. The exposure times for this mask aligner were greater due to the older UV lamp used. The OAI mask aligner outlined above was used for all other photolithographic fabrication.

- The SU-8 layer underwent a post-exposure bake for 3 minutes at 95^{o}C on a hot plate.
- Once the wafer had cooled, it was placed into a dish of Microposit EC Solvent developer, which was rocked for 15 minutes.
- Following the development step, the wafer was rinsed with isopropanol and dried with a nitrogen gun.
- A 1 minute hard bake step at 150^{o}C was necessary before the next layers could be deposited.
- For the 200µm layer, 2 layers of 100µm Dupont dry film resist was laminated (Figure 2.3) onto the SU-8/silicon wafer at a rolling temperature of 95^{o}C.

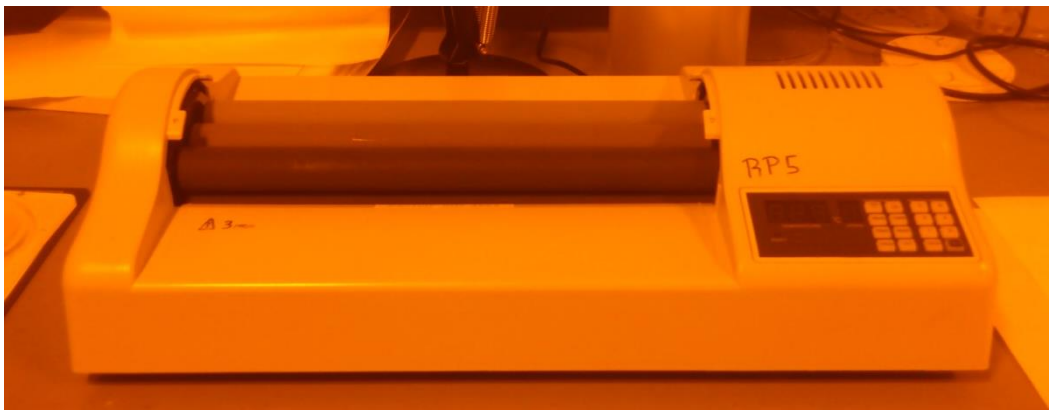

Figure 2.3: Hot roll laminator for the bonding of dry film resist onto SU-8 coated silicon wafers.

- The wafer was then exposed on the OAI mask aligner for 15 seconds at a power of 440mW/cm^{2}.
- After exposure the wafer was baked for 1 minute at 150^{o}C and allowed to cool.
- The exposed wafer was developed in a solution of 1.6% K_2CO_3 for 15 minutes on a rocker.
- Following a wash step with methanol and drying with nitrogen, a hydrophobic coating was deposited onto the SU-8/dry resist mould. The mould was submerged in a solution of 10mM Octadecyltrichlorosilane (OTS) (Sigma Aldrich, IRELAND) in Hexane (Sigma Aldrich, IRELAND) for 2 hours to create a hydrophobic coating, which prevented the PDMS polymer from sticking to the SU-8 and dry film resist.
- The wafer is then rinsed once again with methanol and baked for 1hr at 100^{o}C on a

hot plate.

- The functionalised SU-8 wafer is now ready to use as a mould for soft lithography applications.

2.1.3 Fabrication of PDMS/PMMA Microfluidic Discs.

To create the physical size filtration features from the SU-8 mould described above, a ratio of 10:1 w/w PDMS polymer to curing agent was used.

- A mixture of 10:1 PDMS polymer to curing agent was measured on a balance, mixed with a plastic rod and then poured onto the SU-8 mould.
- The PDMS was degassed under vacuum for 30 minutes or until all of the bubbles were removed from the polymer.
- The PDMS was then partially cured in the oven at 70^{o}C for 1.5 hrs. The PDMS was not fully cured to enable a good seal between it and the PDMS/PMMA backing layer.
- Access holes were punched into the PDMS slab using a 2µm harris punch.
- A mixture of 20:1 PDMS was spun onto a 4" PMMA disc at 1000rpm for 90 seconds. This PDMS layer was then partially cured for 1hr in an oven at 70^{o}C.
- Finally the PDMS layer and the PDMS/PMMA backing were bonded together and placed into an oven at 70^{o}C to cure overnight. Figure 2.4 (a) shows the 10:1 PDMS slab, with access holes punched out, with (b) illustrating a side view of the completed PDMS/PMMA microfluidic disc.

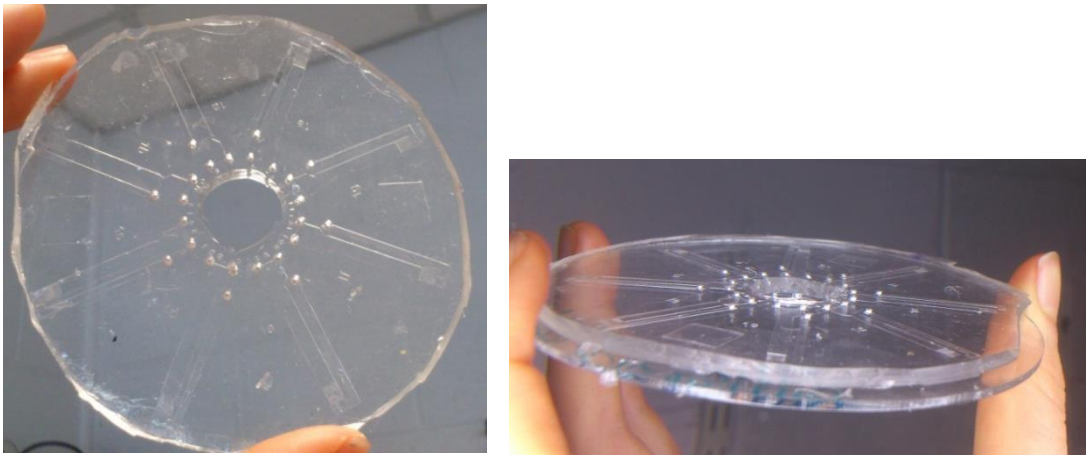

(a) **(b)**

Figure 2.4: (a) Image of PDMS slab fabricated using soft-lithography, with inlet and outlet holes removed. **(b)** Side view of completed PDMS/PMMA disc.

2.1.4 Geometric Trap/Filter Characterisation – Gold Sputter Coating

Transparent samples, such as those fabricated in PMMA or PDMS, were sputter-coated in nanometer gold layers to obtain a reflective surface for 3D imaging.

Figure 2.5: Photograph of gold sputter-coater apparatus.

The following settings were used in all cases:

- Power setting of 100mA
- Sputter time of 2 minutes.
- Pump hold time of 10minutes.
- This process was repeated twice to ensure a sufficiently even layer of gold across the chip surface.

An example of a gold sputter coated SU-8 surface can be seen in Figure 2.6 that follows.

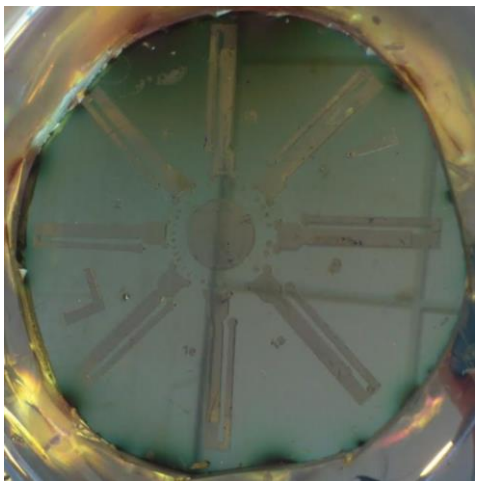

Figure 2.6: Gold sputter coated SU-8 mould, surrounded by PDMS.

2.1.5 Geometric Trap/Filter Characterisation - Optical Profilometry

Following the sputter-coating process of non-reflective samples, a Wyko Optical profilometer was used to analyse the topography of the samples. In the cases of the SU-8 moulds this was done to obtain the optimal photolithographic exposure time for smaller SU-8 features. The shape of the SU-8 features indicated over- and under-exposure of samples, which facilitated the optimisation of exposure time. These patterns will be discussed further in the following sections.

The process for obtaining optical profilometry images for reflective samples was carried out as follows:

- The VSI mode setting was selected on the Veeco software, with settings of a 2mm step and 3nm resolution. A scan length of 15um was selected.
- The interference fringes of the profilometer were then focused on the bottom of the structures and the sample.
- The sample was tilted and rotated until 2-3 high contrast, horizontal interference fringes were observed in the field of view on the profilometer screen.
- The scan function on the profilometer software was then run, resulting in the profiilometry images in the sections that follow.

2.1.6 Microfluidic Materials

While a number of photocurable polymers have been used as the basis for microfluidic devices such as hydrogels[193], perfluoropolyethers(PFPE)[194], thermoset plastics[195], elastomers[196] and photocurable hybrid sol-gels[197,198], PDMS is generally chosen over its counterparts due to its high optical transparency and quality. The prototyping of PDMS microfluidic devices is rapid and inexpensive, with submicron resolution possible using high quality maskless lithographic systems[199]. In addition, PDMS has been successfully used in a number of optofluidic applications such as dye lasers[200], waveguides[201] and lenses[202]. However, while PDMS offers many advantages over other polymeric materials for optofluidic device fabrication, some disadvantages still remain. PDMS swells when put in contact with a variety of non- polar organic solvents[203]. PDMS is also porous, which can introduce bubbles into microfluidic systems and prove challenging to the long term storage of commercial devices due to the risk of evaporation or exposure to air. Despite the aforementioned issues however, PDMS remains a hugely useful material for the rapid prototyping and testing of new microfluidic and optofluidic devices, with the ability to integrate microelectronic and microphotonic components, both reversibly and irreversibly, proving a significant advantage over a number of its counterparts. By combining PDMS and the more robust and commercially viable PMMA material, a number of prototype designs were developed in this work, towards the separation of biomimetic beads and cells.

2.1.7 Bead Solution Preparation

For all of the size filtration and bead capture tests outlined in section 3.1, the biomimetic bead solutions were prepared as follows:

- 0.01g of bovine serum albumin salt was weighed on a balance.
- 10ml of PBS solution was poured into a cell tube.
- The BSA salts were added to the PBS solution and actuated rigorously for 5 minutes or until all of the salts had dissolved.
- 20μL of bead solution was then mixed with 120μL of the 0.01% w/v BSA in PBS solution to generate a bead concentration of ~10^3 beads per μL.

- The beads were then cleaned by spinning them down in a Technico Mini centrifuge (Fisher Scientific), removing the PBS/BSA liquid, adding 120µL of fresh solution and re-suspending using a Vortex Genie 2 (Scientific Industries Inc). This process was repeated twice more to ensure the bead solution is sufficiently clean.

2.1.8 Cell Preparation

MCF-7 and HeLa cell samples tested in section 3.1.7 were prepared as follows:

- Cells were removed from their culture flasks and re-suspended using Trypsin (Sigma Aldrich) and cell media solution.
- Cells were washed in 3mM EDTA media solution by centrifuging them for 3 seconds on a mini centrifuge, then re-suspending using a Vortex Genie 2. This step was carried out twice to clean the cells sufficiently.

2.2 Microcontact Printing

As outlined in section 1.2.2, microcontact printing is utilised in the research community for the inexpensive and rapid deposition of multiplexed proteins onto substrates for use in a variety of biological applications [134,204-206]. PDMS is the favoured material for the fabrication of stamps for microcontact printing due to its biocompatibility, permeability to gases and liquids, ease of fabrication, low cost and flexibility. The following sections will outline the materials and methodologies used to fabricate PDMS stamps, and prepare these stamps and glass substrates for microcontact printing. In addition, the microcontact printing process itself will be described, as it was employed to capture single mammalian cells on a functionalised glass substrate.

2.2.1 PDMS Stamp Fabrication & Functionalisation

PDMS stamps of 10µm, 20µm, 30µm and 40µm in diameter were fabricated using the design, photolithographic and soft lithography steps outlined in sections 2.1.1 – 2.1.3. A spin speed of 4000 rpm was used for the 3025-SU8 mould, which resulted in ~10um high stamp features in the PDMS substrate, as illustrated in the optical profilometry

image in Figure 2.7 that follows. The PDMS stamp was then cast using soft lithography methods. The PDMS stamp was functionalised by exposing it to an O_2 plasma at 1000mT for 5 minutes. This ensured a hydrophilic stamp surface for the antibody solution, resulting in a far more uniform coverage of the antibody solution across the stamp.

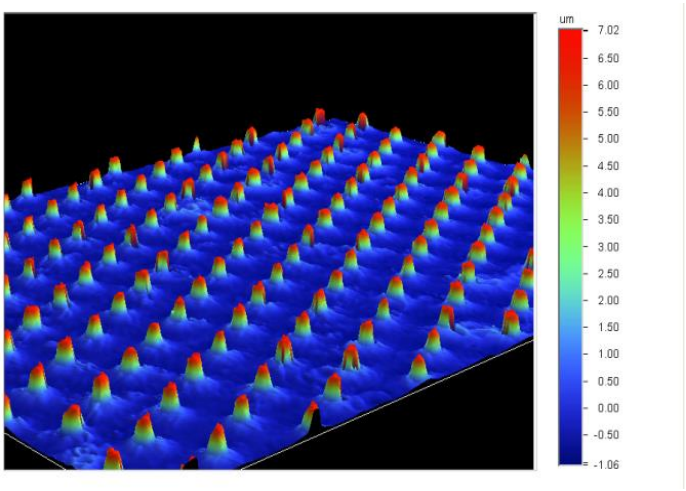

Figure 2.7: Optical profilometer image of 10um pillars on the PDMS stamp for microcontact printing.

2.2.2 APTES Functionalisation of Glass Substrates

A number of variations on the APTES functionalisation of glass and PDMS substrates based on the Nature protocol by Dixit *et al.* were undertaken over the course of this work [207]. Successful functionalisation was indicated by water contact angle of ~ 50-60^o in the case of post functionalised samples, as a result of increased amine groups on the sample surface [208]. Following trials of a number of APTES concentrations and functionalization times (contact angle values outlined in Table 3.2 in section 3.2.2); an optimised protocol was established for the glass substrates:

- The glass substrate was first cleaned with methanol and dried with N2.
- The substrate was exposed to a 1000mTorr O_2 plasma for five minutes, resulting in the formation of hydroxyl-OH groups on its surface. This surface treatment facilitates binding of APTES onto the glass substrate [208].
- A 27ml solution of 90% vol/vol EtOH in deionised H_2O was prepared.
- 3ml of APTES liquid (Sigma Aldrich) was added under a fume hood to the EtOH H_2O solution to produce a 90% vol/vol EtOH:APTES solution.
- The plasma activated glass substrates were submerged in the APTES

solution for 45 minutes.

- The substrates were then rinsed with 90% EtOH solution, followed by DI water and were finally baked in an oven at 120^{o}C for two hours to evaporate the solvent.

This approach and the concentration of 90% vol/vol EtOH:APTES above were used due to the favourable contact angle measurements of ~57^{o} (section 3.2.2) obtained on the APTES functionalised glass substrate.

2.2.3 Microcontact Printing Procedure

- Following O_2 plasma treatment of the PDMS stamp, ~10 μL of the fluorescently tagged antibody of interest (3μg/ml anti-epcam in PBS in the case of MCF-7 cells) was deposited carefully onto the hydrophilic surface area of the stamp using a pipette.
- The PDMS stamps were then stored in a plastic petri dish containing droplets of water to prevent the evaporation of the antibody solution during inking. The dish was covered with a lid and foil to shield the light-sensitive fluorophores in the antibody from bleaching.
- Following 15 minutes of "inking", the antibody was removed from the stamps using a pipette and the stamps were air-dried using a nitrogen gun. (This step was reduced to 5 minutes for each subsequent use of the stamp, due to the initial absorption of the antibody into the porous PDMS)
- Using a tweezers, the PDMS stamps were carefully placed onto the APTES functionalised glass substrates and gently pressed into contact with the substrate.
- The PDMS stamp was left in contact with the substrate for 5 minutes before being carefully removed with a tweezers.
- The substrate was then ready for imaging on a fluorescent microscope and was covered with foil to prevent further photo-bleaching.

2.2.4 Cell staining and Preparation

In order to image cells on the glass substrate and to differentiate them from fluorescent antibody spots, a Hoechst 33342 dye (Sigma Aldrich) was added to MCF-7 cells before

the assay was tested.

- Cells were removed from culture cell media and replaced with fresh media solution.
- 1-2 drops of dye was added per ml of cells, which were covered in foil and incubated in a fridge for 15 minutes.

All samples were observed using a fluorescent microscope fitted with the appropriate filters for the Hoechst dye and FITC fluorophore.

2.3 Optical Detection in Inertial and Centrifugally-Driven Microfluidic Platforms

2.3.1 Sol-Gel Materials and Synthesis

The hybrid organic-inorganic sol-gel material used in this work to create rectangular waveguides is composed of a ratio of 3-methacryloxypropyltrimethoxysilane (MAPTMS) hybrid precursor, zirconium(IV) n-propoxide ($Zr(OPr)_4$ and methacrylic acid (MAA, $C_4H_6O_2$); a chelating agent which stabilises the zirconium precursor in the presence of strong nucleophilic groups [209]. The ratio of the above materials can be varied to finely tune the refractive index of the waveguiding structures, through the formation of a low-refractive index buffer layer (BL), which enables waveguiding in the higher refractive index guiding layer (GL). An increase in the zirconium propoxide (ZPO) concentration leads to a linear increase in the refractive index of the material, while the wettabilty of the sol-gel material is also directly related to the level of ZPO by the level of condensation in the material as outlined by Copperwhite *et al.* [189]. A certain minimum refractive index difference is required between the core of the waveguide and the "cladding" for single mode or multimode waveguiding to occur, with a difference of 4×10^{-4} needed between the BL and the GL for single-mode waveguiding, at an input wavelength of 635 nm. The waveguides were synthesised using the three-step process outlined in the work of Copperwhite *et al.* [189], with a more detailed description of this synthesis in the 2003 article by Oubaha *et al.* [210]. Following sol-gel synthesis, Irgacure 184; a photoinitator obtained from Ciba Speciality Chemicals, was added to the sol-gel liquid to enable photo-polymerisation to occur in the material under UV irradiation. This particular complex was added in a 5% mol

concentration with respect to the methacrylate groups of MAPTMS, and was used "due to its high stabilility in zirconium based sol–gel materials" [211]. It is a negative photoresist and thus, like the SU-8 material used to create moulds for PDMS structures, regions of sol-gel exposed to UV light remain, while unexposed material is etched away. Therefore, the parts of a sol-gel coated wafer not exposed to UV light by the photomask (created using OlympIOS software) are removed by the IPA etchant, while those exposed remain as waveguiding structures. By altering the composition of these materials, the waveguides and cladding layers produced can be easily tuned to the desired refractive index.

To establish working parameters for the fabrication of sol-gel waveguides onto a new surface such as PMMA, waveguides were first created on a silicon substrate, as in image 2.8 that follows.

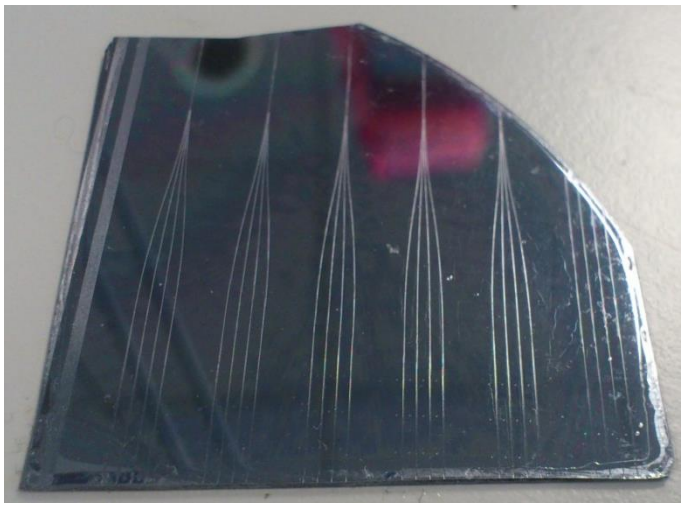

Figure 2.8: Series of diverging 10:2.5:0.25 hybrid sol-gel waveguides on a buffer layer of 10:2.1:0.25 sol-gel material.

Silicon is typically chosen as a base layer due to the ease at which the wafer can be cleaved along its crystallographic planes. This provides a suitably smooth wafer edge to enable good coupling of light into and out of the waveguide, a critical feature in the waveguiding process, as we will see in the results that follow.

The fabrication of waveguides using sol-gel materials is very similar to that of the creation of structures in SU-8, with some small modifications. Due to the size of the waveguiding structures; typically on the order of 10um of less in width and height for rectangular waveguides, the photomasks manufactured by Jdphototools are usually created on glass to facilitate the high resolution necessary to produce such small features. In addition, as these materials are highly photosensitive, the UV exposure

parameters must be carefully modified and tested to ensure that the correct refractive index is produced. Note that optical profilometry images of waveguides fabricated on silicon using this technique can be found in the appendix in section 5.1.

The sol-gel deposition process for both approaches was carried out as follows:

- Nitrogen was bubbled through IPA liquid for 180 seconds to create an IPA saturated environment in the Laurell WS 400 BZ spin coater, before the sol-gel was added to the silicon wafer.
- 0.8ml of 10:2.1:0.25 sol-gel was deposited onto a quarter of a silicon wafer after ~170 seconds had elapsed i.e. just before the spin coater began to accelerate.
- The spin coater was accelerated to 200rpm for 7 seconds and then up to 1000rpm for 35 seconds, to create a 6um buffer layer.
- As the spin speed was reduced down to 200rpm for 2 minutes, the N_2 gas was turned off.
- For the final minute in the spin coater, air was introduced into the spin coater gradually, by opening a 2cm diameter hole in the lid.

The following section will outline the next steps in the sol-gel waveguide fabrication process.

2.3.2 Sol-gel Waveguide Fabrication Process

In this work two configurations of waveguide were fabricated on silicon and PMMA; embedded waveguides and raised waveguides, with the fabrication steps outlined in Figure 2.9. Raised waveguides were tested as a proof of concept to investigate the suitability of producing sol-gel waveguides on PMMA. Embedded waveguides, composed of an initial buffer layer on the silicon substrate and a UV exposed guiding layer embedded within, were also fabricated, with a view towards bonding inexpensive, widely used materials such as PDMS and PMMA directly to the sol-gel surface to create an integrated optofluidic device.

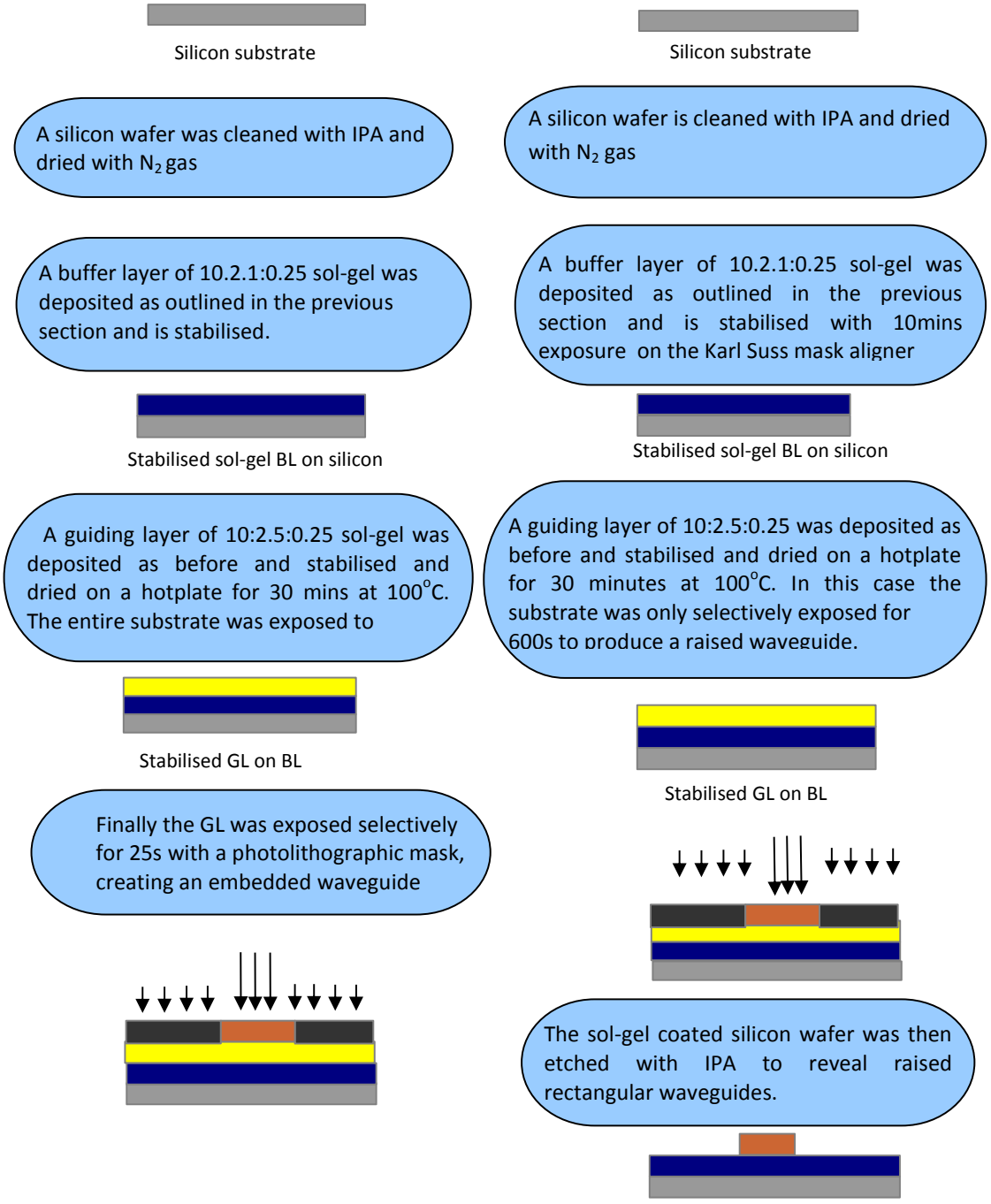

(a) Refractive index change induced in exposed section of GL (orange), leading to an embedded optical waveguide

(b) Raised sol-gel waveguide on BL and silicon wafer.

Figure 2.9 Schematics of the stepwise fabrication process for **(a)** embedded waveguides and **(b)** raised waveguides. Initial spin-coating steps are the same for both approaches, with the selective photolithographic exposure in Figure **(b)** leading to raised waveguides on the 10:2.1:0.25 buffer layer. In contrast, the entire guiding layer of the embedded waveguides receives a flood exposure for 600 seconds, and selective exposure with a photolithographic mask for 25 seconds.

Chapter 3 – Results & Discussion

3.1 Physical Size Filtration Experiments

As outlined in chapter 1, a wide range of approaches have been utilised by the research community such as cell lysis[54], miniaturised flow cytometry[76-83], dielectrophoresis[95], magnetophoresis[100-109] as well as acoustophoresis[111-114] and cell encapsulation[115-116] for the separation, selection and capture of cells and bioparticles from whole blood and from solution. Another method discussed was the use of gravity based and centrifugally-driven physical size separation of cells, as demonstrated by the work of Lee *et al.* [125], Burger *et al.* [129-132] and Di Carlo *et al.*[133] Due to the numerous advantages of the physical size filtration approach over the alternatives noted above i.e. ease of fabrication and, therefore, prototyping of platforms, high sample throughput and the elimination of complex cell labelling steps, this method was favoured in this work for the development of a suitable sample-to-answer platform. In addition, the utilisation of the fluid handling toolkit afforded by the centrifugal platform makes physical size separation approaches such as the V-Cup platform developed by Burger et al.[129-133] a viable and logical choice for the development of a 3-fold differential WBC platform for single cell analysis.

The sections that follow document the results of physical size filtration experiments carried out on novel centrifugal microfluidic platforms for cell differentiation and single cell capture. Some initial tests were carried out to gauge the general size and configuration of the microfluidic channel that would optimise the cell separating capabilities of the microfluidic chip (section 3.1.1). Once this design was established, a number of different physical size filtration structures were tested over the course of the research work, with the functionality of the original structures and the results of the modified structures employed in this work outlined in sections 3.1.2-3.1.6.

3.1.1 Initial tests on assay dimensions

In order to optimise the likelihood of bead/cell separation for the microfluidic device being developed, an assessment of some of the fundamental dimensions and parameters for a new size filtration design were necessary. Some initial tests using 10um and 20um beads and the following design (Figure 3.1) resulted in a rough quantification of the chip length needed to induce size separation for the beads in stop-flow conditions. The

design was made on AutoCAD software and then cut into 1.5mm PMMA using the Epilog Zing Laser Cutter (30W power).

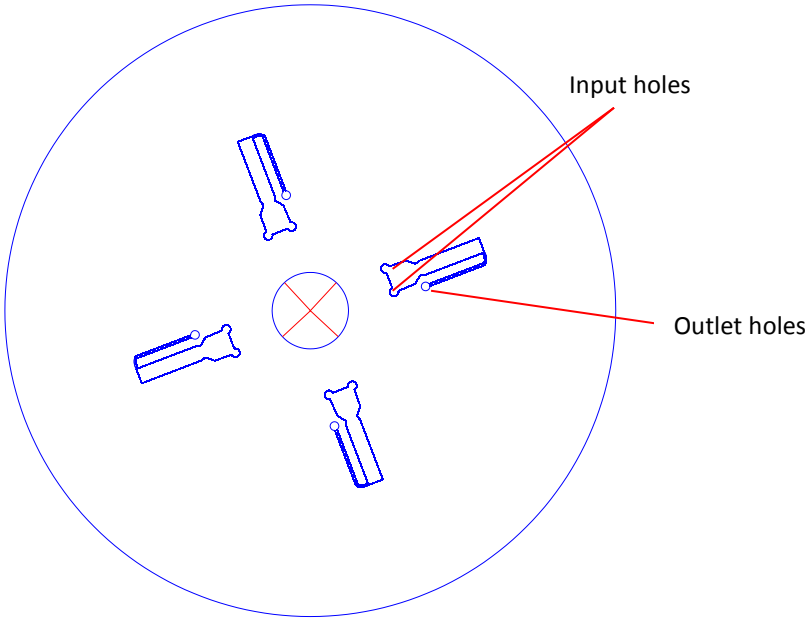

Figure 3.1: Schematic of autocad design used to create PMMA/PSA chips to test the sedimentation of 10um and 20um beads at 10Hz. The "x" symbol indicates the centre of rotation. The narrow channel, parallel to the active assay area, is included to facilitate the release of pressure and overflow of liquid when the chip is spun at high speeds. Outlets of this nature are standard in all centrifugal microfluidic designs and are included in all designs that follow.

The same design was then cut into the top layer of 86um PSA and then the PSA was used to bond the cut PMMA layer to a backing of 1.5mm PMMA, resulting in a testable chip. These chips were then inserted into a PMMA chip holder, as seen in Figure 3.2.

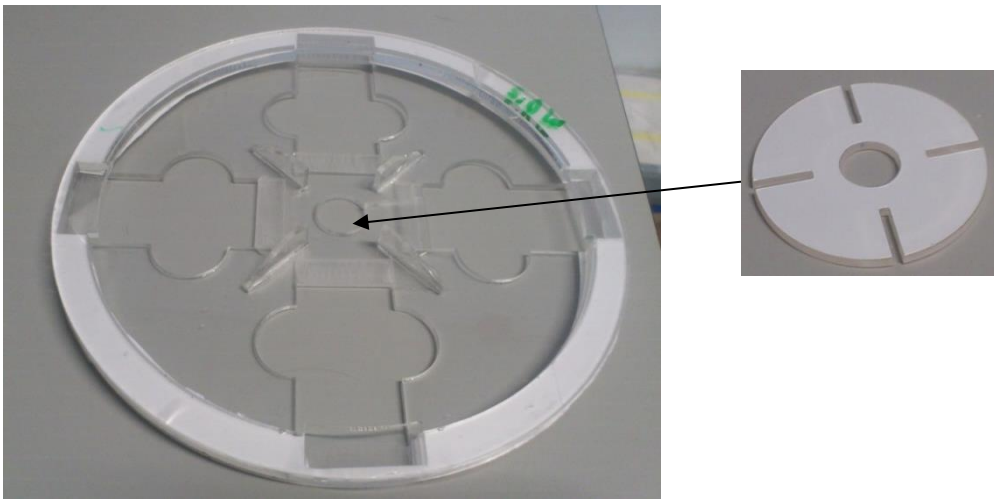

Figure 3.2: PMMA chip holder and lid (inset) for single PMMA chip testing. The chips were secured in this holder using a PMMA "lid". Spin speeds were limited to ~ 15Hz as movement of the chips within the holder was too significant at spin speeds above this level for taking high quality stroboscopic measurements.

Following loading with 4µL of 0.01% w/v BSA in PBS, a 4µL mixture of 10µm and 20µm beads was inserted into the chips, which were then spun at 10Hz. It was observed that no notable separation due to differing sedimentation speeds was observed in these chips. Therefore, it was decided to lengthen chips to quantify the appropriate length for a physical size filtration design. Following further tests to quantify the appropriate length of the channels, the first set of filters/cups was set at a distance of at least 2.6cm from the fluid inlet for all designs thereafter.

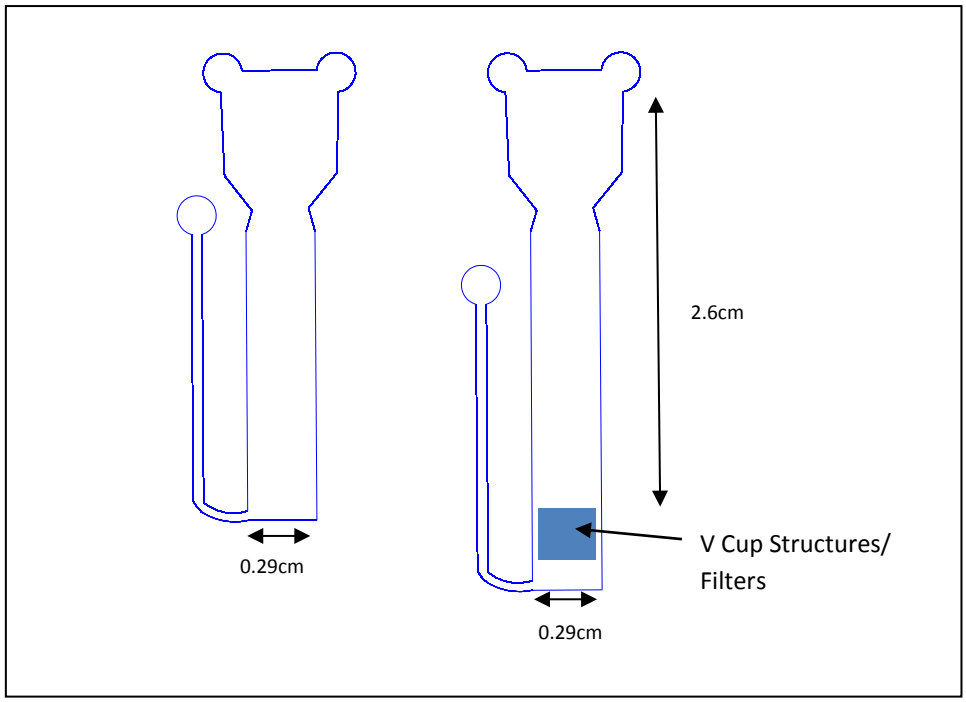

Figure 3.3: Schematic of **(a)** initial PMMA/PSA chip for bead sedimentation and **(b)** lengthened chip, including size filtration structures.

The next sections will outline the various centrifugally-driven size filtration designs tested over the course of this work and the results associated with them. In each case the chips were designed on AutoCAD software and fabricated as described in sections 2.1.1-2.1.3, chapter 2. Following disc fabrication, each PDMS chip was degassed in a vacuum jar for at least 1hr, to remove air from the chip. The chip was removed from the vacuum jar and immediately filled with a mixture of 4µL 0.01% BSA in PBS, to ensure stop flow conditions. The chip was then spun at 10Hz to drive the liquid buffer into the whole chip and to prevent air bubbles from forming, which would disrupt fluid flow into the chip.

3.1.2 Filter and V-Cup Design

Using the successful V-Cup chips assays developed by Burger *et al.* [129] as a basis for bead capture and separation, a new PDMS size filtration chip was designed, as seen in Figure 3.4. Polystyrene beads of 5µm, 10µm and 20µm in diameter were used as biomimetic particles to develop a usable size filtration design, which will eventually be tested with white blood cells. 6µm V shaped cups were placed at the bottom of the chip, with 10µm and 15µm filters above.

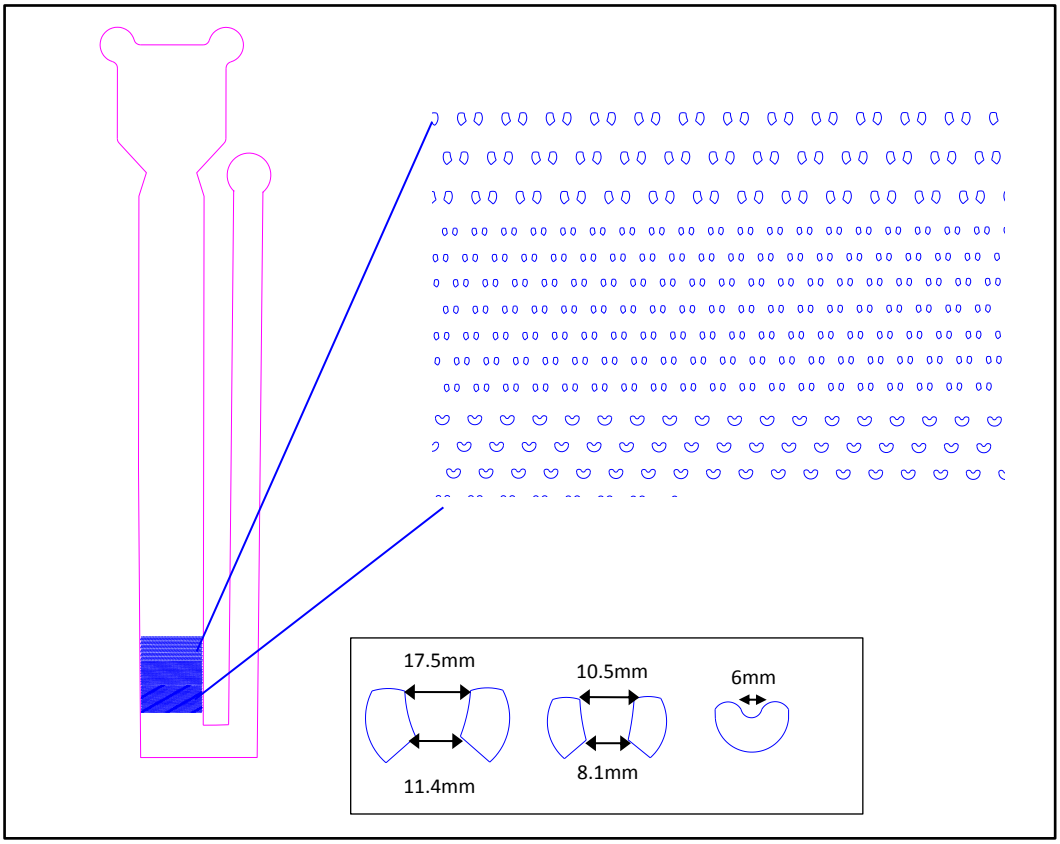

Figure 3.4: Schematic of size filtration chips, with zoomed in view of physical size filtration features. 6µm V shaped cups were placed at the bottom of the chip, with 10µm and 15µm filters above, creating a structure that should capture 15µm and 10µm beads singly, while allowing the 6µm beads to filter through and become trapped in the 6µm cups.

The maximum and minimum gap sizes in the filters can also be seen in Figure 3.4. These sizes were chosen to allow smaller particles to get through, while capturing the target beads singly. These chips were fabricated as outlined in chapter 2, section 2.1.3, with ~20µm and ~25µm cup/filter heights fabricated using photolitography and PDMS moulding techniques. The height of the cups and filter structures were verified by checking the ridge height of the SU-8 layer heights fabricated at different spin speeds using a Dektak profilometer. For this design and the one that follows in section 3.1.3,

three SU-8 moulds were fabricated, two of ~20µm feature height and one of ~25µm feature height. The values recorded from the profilometer are outlined below:

	Mould 1 feature height (µm) – 3025 SU-8 spun at 3000rpm	**SU-8 Mould 2 feature height (µm) – 3025 SU-8 spun at 3500rpm**	**SU-8 Mould 2 feature height (µm) – 3025 SU-8 spun at 3500rpm**
	25.2	21.2	21.8
	25.2	21.2	21.9
	24.5	21.3	21.6
		21.1	21.7
Average	25.0 ± 0.4	21.2 ± 0.1	21.8 ± 0.1

Table 3.1: SU-8 feature height as measured on a Dektak V150 profilometer.

Different feature heights were tested to evaluate which aspect ratio provided the most effective and consistent results. It was envisaged that when a mixture of 5µm and 10µm beads were inserted into the chips, that the 5µm beads would occupy the 6µm cups singly, while the 10µm filters would retain the 10µm beads singly.

Results and Discussion

A volume of 4uL of beads in PBS was loaded into each assay on the chip individually, so that a real-time video of the bead behaviour entering the chip could be recorded using the stroboscopic centrifugal set-up. As the 2012 article by Burger *et al.* [129] states "...that the spinning frequency does not have a decisive impact on the capture efficiency, but only on the time required for the sedimentation of the particles.". The assay in the work by Burger *et al.* was spun at speeds of 40Hz initially, to push the beads toward the obstacles and then a speed of 20Hz. In the same article by Burger et al, the speed was alternately increased to 40Hz for 10s, using an acceleration of 75 Hz s^{-1}, and then decreased down to 2Hz for 10s. The "shake-mode" step referenced in the aforementioned Lab on a Chip paper was utilised in this work to try to reduce the clogging at the ridge and at the 15µm features.

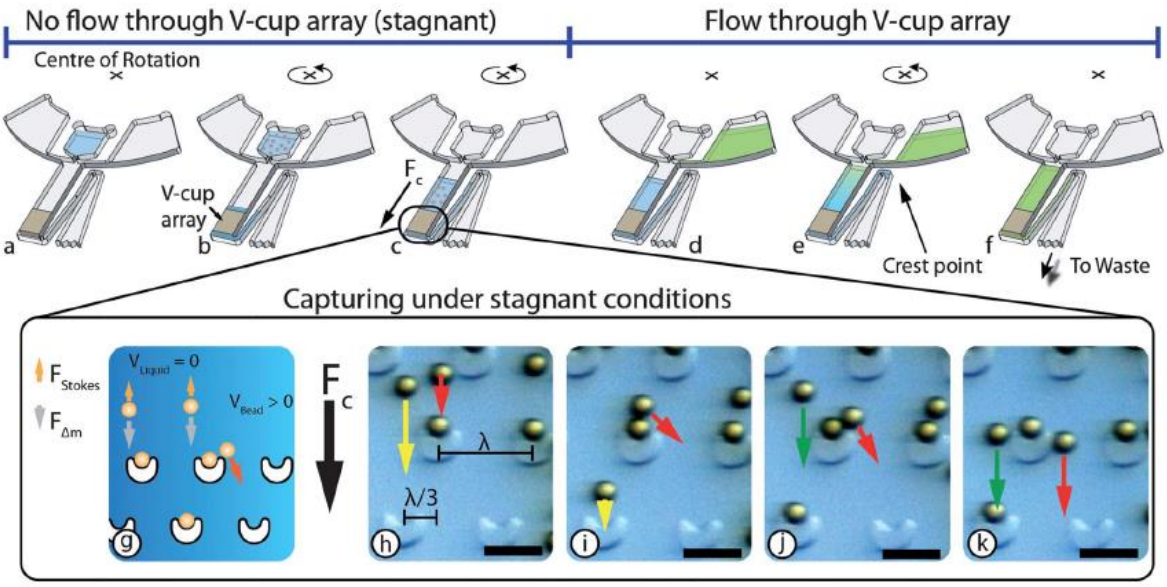

Figure 3.5 Schematic outlining the working principle of the centrifugally driven V-Cup bead capture platform by Burger *et al.* **(a)** Buffer is introduced into the V Cup array **(b)** The disc is then spun to initiate stagnant flow conditions in the chip. **(c)&(g)** The bead sample is introduced into the chip and sediments through the buffer solution, into the V Cup traps. Beads that reach an already occupied trap sediment downwards until an empty cup is found, due to the staggered nature of the rows on the v cup array, Figures **(h)-(k).** Sample and reagent fluids can also be exchanged in the V-Cup platform, Figures **(d)-(f).** The reagent is introduced into the inlet and the device is spun, leading to the exchange of media with little mixing of the sample and reagent liquid.

In this work the same rate of acceleration was used, with the speed switched from 2.5Hz to 25Hz, again for 10s at each speed. Unfortunately, while this step was useful for improving single occupancy of cups in the article by Burger et al, it was not effective in de-clogging at the 200µm step and at the filters in the design described in this thesis. Mixtures of 5µm, 10µm and 20µm beads were tested, as well as mixtures of just 5µm and 10µm beads. As 15µm beads were unavailable, 20µm polystyrene beads were used to test the filtering ability of the 15µm trapping structures. Figure 3.6 illustrates 20µm beads captured in 15µm filters:

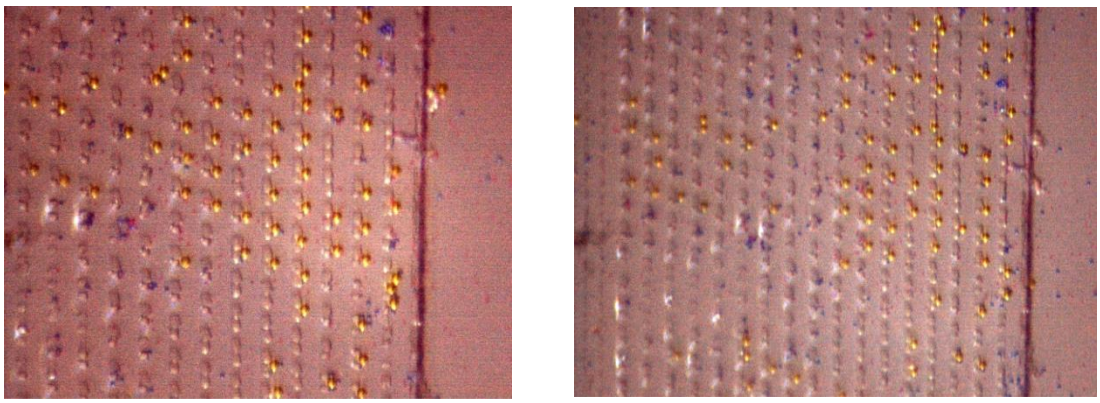

Figure 3.6: Images of 20µm particles (yellow) captured singly in 15µm filters. Physical size filtration features are 25µm in height, with the centre of rotation to the right of the images. The line to the right of the centre of each image is the 200µm PDMS step.

Unfortunately, the 20µm beads often became clogged at the ridge of the chip or at the 15µm filters, leading to the rest of the chip becoming unusable. This can be seen in Figure 3.7.

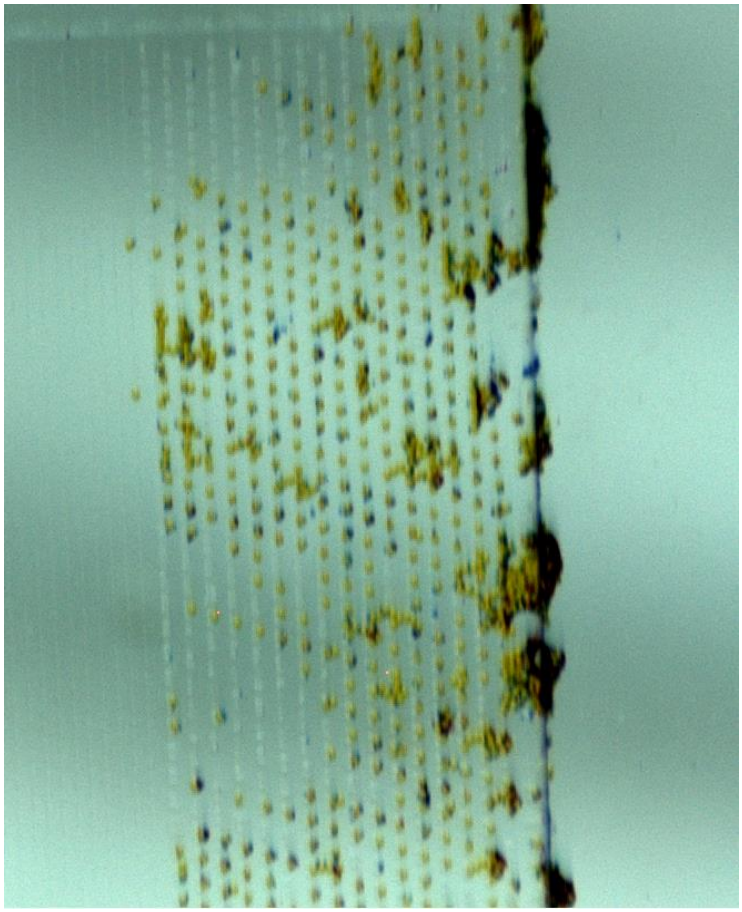

Figure 3.7: Image of clogging of 20µm particles at ridge, obstructing 5µm and 10µm beads from moving through the chips. While the "shake mode" actuation did alleviate some of the clogging temporarily, 20µm particles continued to clog in the above design at the ridge and at some of the 15µm filters.

As this clogging persisted throughout the testing of this design, the results from inputting a mixture of 5µm and 10µm beads will primarily be discussed in the following section. Over the course of a number of assay tests, single and double occupancy of 6µm cups with 5 µm beads was observed. Unfortunately, as can be seen in Figure 3.8, many 10µm beads get also stuck in the 6µm cups.

Figure 3.8: Image of 10µm beads (blue) and 5µm beads (red) occupying 6µm cups. A mixture of both beads occupied the cups, as well as each bead type singly. In some cases a mixture of both beads occupied the cups, while single occupancy of both 5µm and 10µm beads was also observed.

While these cups are tailored to be small enough prevent their occupancy by any beads larger than ~6µm, there is clearly some potential for some slightly larger beads to occupy them, provided that the size difference between the target bead and the cup size is not too great. This challenge was not encountered in the work of Burger *et al.* as a mixture of beads of different sizes was not tested. Each set of cups was tailored specifically for single bead occupancy with the ratio of bead diameter, b_d and cup diameter b_c, equal to one when single occupancy was desired. Furthermore, the challenge of fabricating suitably resolved cups for 5µm beads involved elongating the sides of the each cup, potentially leading to a larger capture surface. In addition, the 10µm filters appeared to have demoulded poorly; possibly due to the high aspect ratios of the 10µm filter structures or the poor resolution of the SU-8 mask. This lead to the 10µm beads to flow over and through the 10µm filters, as illustrated in Figures 3.9 (a) – (e) that follow, preventing single occupancy capture from occurring.

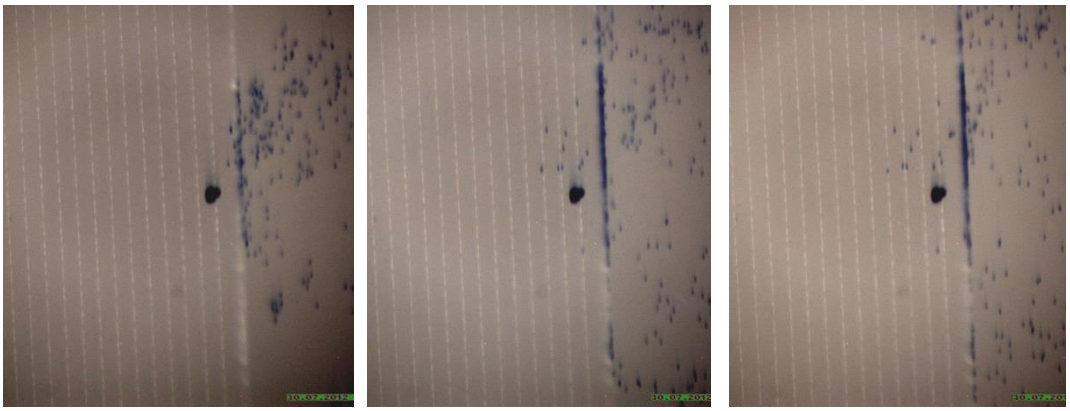

(a) **(b)** **(c)**

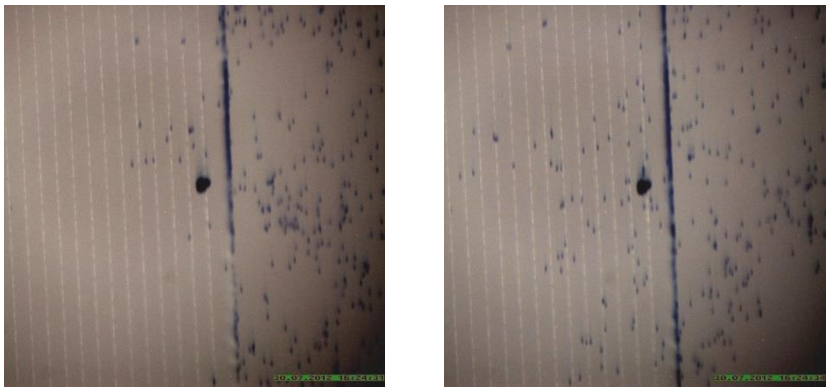

(d) **(e)**

Figure 3.9 (a)-(e) Illustration of a time lapsed sequence of 10µm beads flowing over/past 10µm filters rather than being captured. This issue is likely to be due to poor demoulding of the PDMS mould due to high aspect ratios of the features.

In order to alleviate the issues associated with poor demoulding, the exposure time of the SU-8 structures during the photolithographic process was modified from 52s to 16s for the Karl Suss mask aligner, in an effort to find a compromise between overexposing the smaller features and underexposing the larger features. The effects of various different photolithographic exposure times was evaluated by sputter-coating the SU-8 moulds and using an optical profilometer (as outlined in section 2.1.4-2.1.5) to image the filter and cup structures. Figure 3.10 illustrates some examples of the effects of photolithographic overexposure on SU-8 10µm filters, with Figure 3.11 illustrating the result of near optimal UV exposure on SU-8 structures.

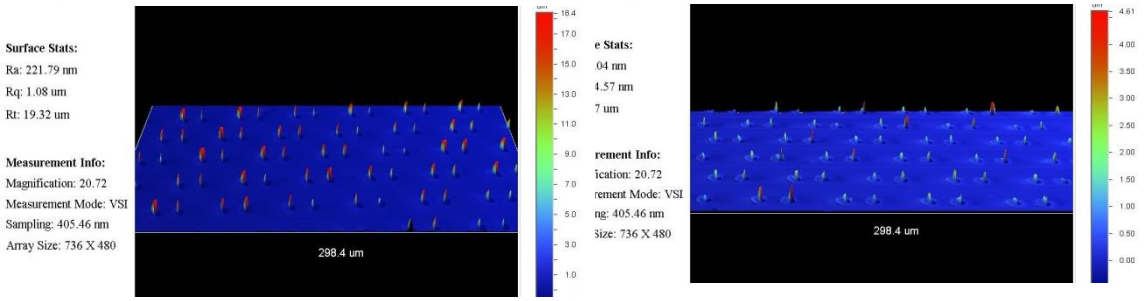

(a) **(b)**

Figure 3.10: Reversed optical profilometer images of photolithographic overexposure on SU-8 features. **(a)** A spin speed of 3500rpm was used with 3025 SU-8 to produce 10µm filters with an exposure time of 52s, with a slower spin speed of 2500rpm used in the case of (b) above. The 10µm filter structures are clearly distorted and much smaller than expected.

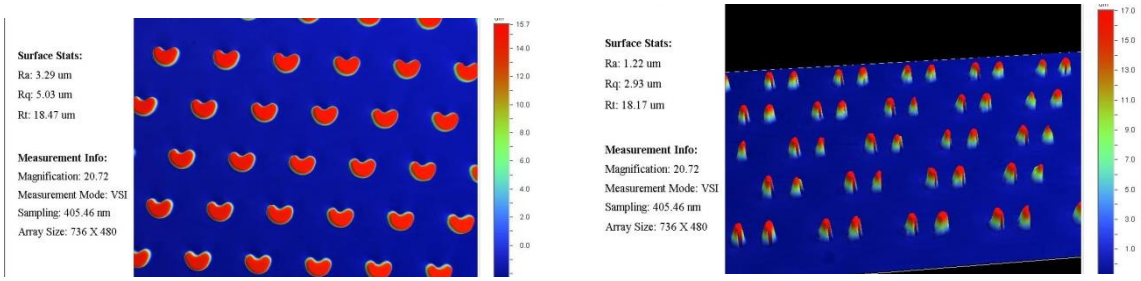

(a) **(b)**

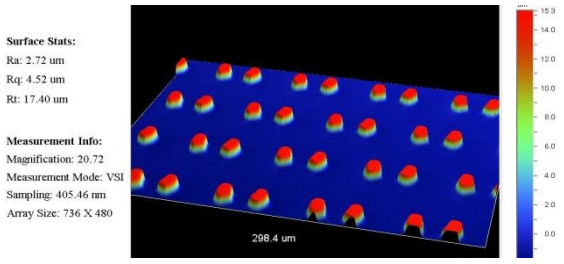

(c)

Figure 3.11: Reversed optical profilometer images of 6µm cups and 10µm and 15µm filter features in SU-8, with a spin speed of 4000rpm of 3025 SU-8 and an exposure time of 20s. The profilometer images above are reversed to illustrate the likely shape of the demoulded PDMS features, provided the demoulding process is successful. All features are clearly defined, although the 10µm filters are slightly overexposed, Figure 3.11 **(b)**.

Clearly, the exposure time of the SU-8 material has a huge impact on the quality of the SU-8 mould and, consequently, on the PDMS feature resolution. Issues still persisted with 10µm beads passing through the 10µm filters, despite the optimised exposure time of 20s, due to the small size of the filter features. With these limitations and the aforementioned fabrication challenges in mind, a new design based on a series of differently sized v cups was pursued, as outlined in the following section.

3.1.3 Assorted size V-Cup Design

In this second size filtration design, arrays of 6µm, 10µm, 15µm and 20µm cups were arranged in order of size from small to large, as illustrated in Figure 3.12.

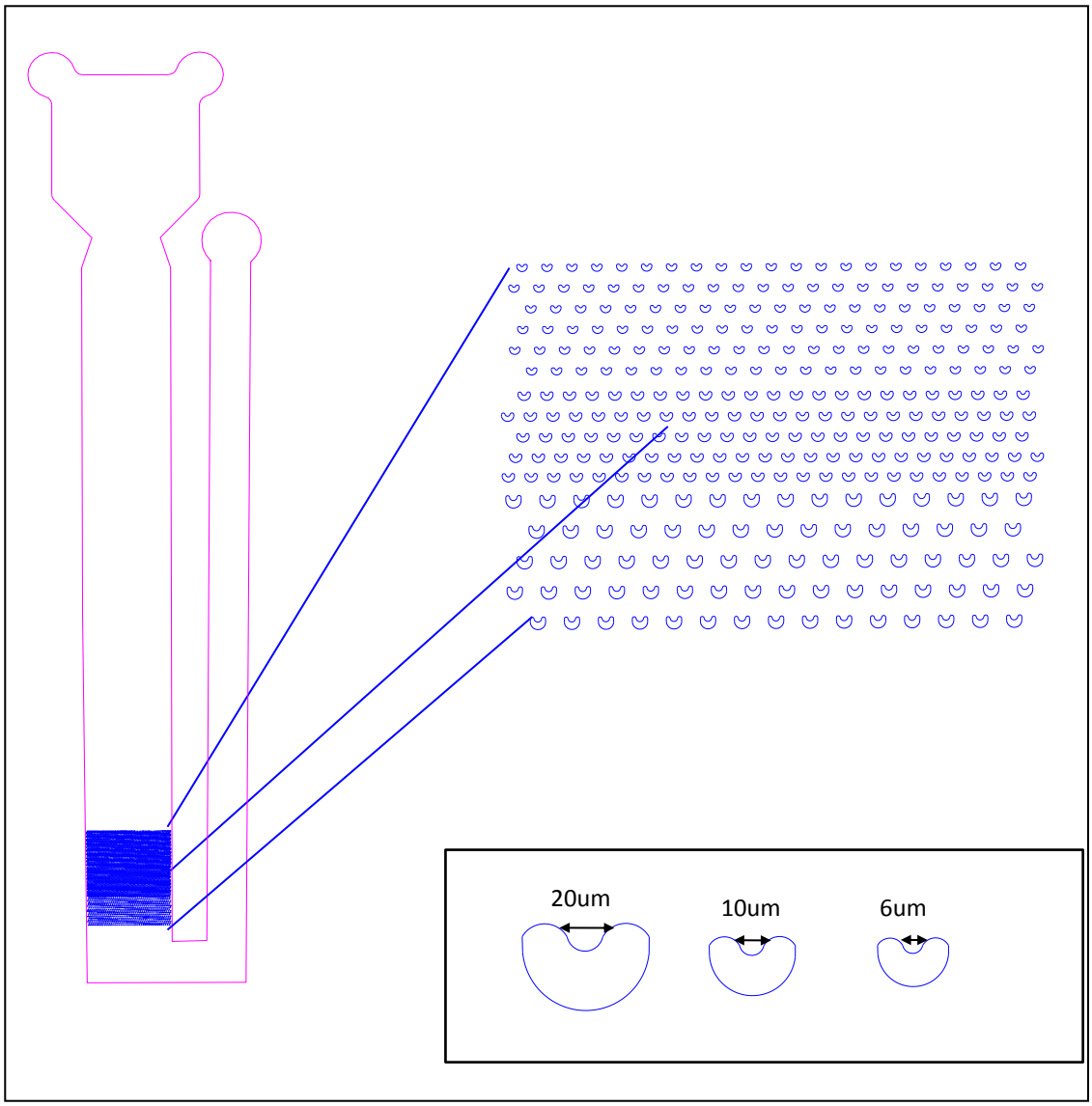

Figure 3.12: Schematic of assorted v-cup features, with zoomed in view of the 6µm, 10µm and 15µm V shaped cups. Chips with combinations of just two cup sizes were also fabricated; of 10µm and 15µm, and 15µm and 20µm cup arrays respectively.

In contrast to the first design, this arrangement was selected based on the nature of 10µm and 20µm V cup occupancy illustrated in the 2012 article by Burger *et al.* [129]. It was observed that when a cup became occupied by a bead that all other beads moved around this obstacle until they also occupied a cup singly. An almost 100% occupancy rate was observed for a low bead to cup ratio i.e. a bead to cup ratio of <<1. In the

design described in this thesis, there were ~ 4107 cups in the 6µm, 10µm and 15µm arrangement, ~ 3774 cups in the 10µm and 15µm arrangement and 1736 cups in the 15µm and 20µm arrangement. As the concentration of beads in solution was on the order of 10^3 beads per µL of solution, the ratio of beads to cups was ~0.5 in the case of the 6µm, 10µm and 15µm cup arrangement, when a 2µL sample of bead solution was tested.

Results and Discussion

This design, based on an assortment of various v-cup arrays arranged on the basis of size, from small to large was tested with the same spin speeds and acceleration as outlined for the previous chip design in section 3.1.2. The lengthening of the channels that was carried out in section 3.1.1 was a crucial element to the success of this chip design as, by the stop flow, and therefore sedimentation based driving force of the chip, the larger particles would reach the chip first. This allows the larger beads to move around the smaller cups and to reside in their specifically tailored cups at the bottom of the chip, reducing the likelihood of the smaller particles occupying larger cups. While some single occupation of cups was observed, unfortunately multiple 5µm and 10µm particles resided in all cups, as well as mixtures of both, as illustrated in Figures 3.13 and 3.14 that follow.

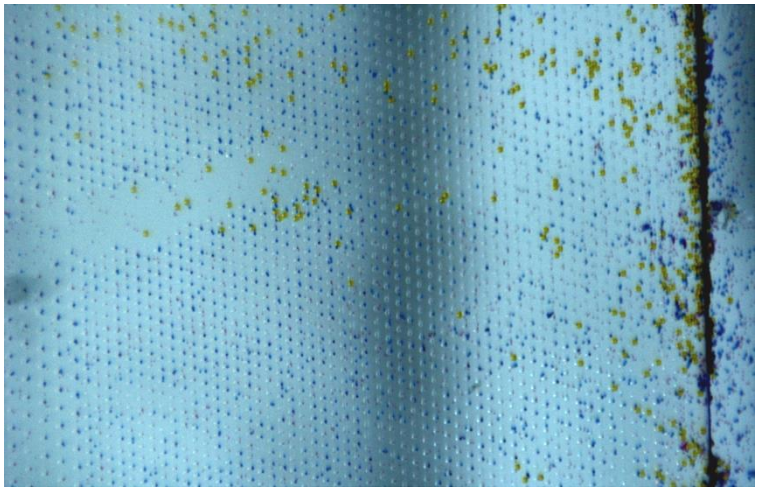

Figure 3.13: Image of 6µm, 10µm and 15µm cups (right to left) and occupancy of 5µm (red), 10µm (blue) and 20µm (yellow) beads. 20µm beads get trapped at various points on the assay but only a very limited number reach the 20µm cups. The 20µm, 10µm and 5µm cups are occupied with a mixture of 10µm and 5µm beads, with most cups filled with a number of beads.

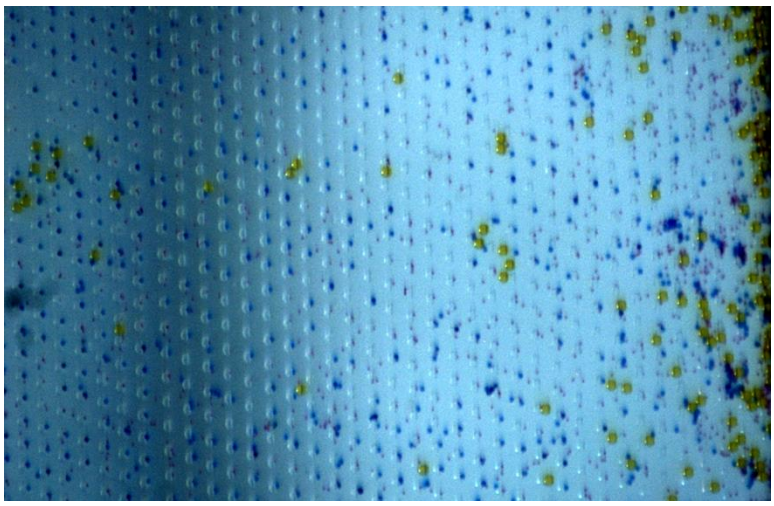

(a)

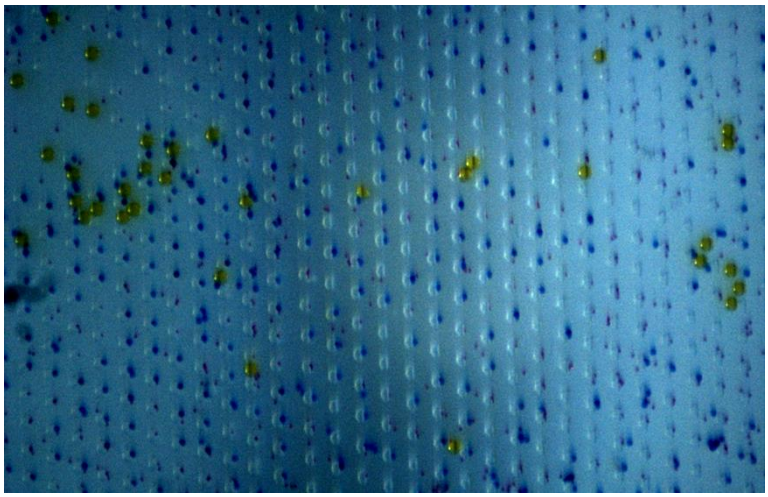

(b)

Figure 3.14: (a) Zoomed in image of 6µm (right and centre) and 10µm (left) cups. While a sizable number of 6µm cups are filled singly with 5µm beads, they are also filled singly with 10µm beads, as well as with mixtures of both. Similarly, the 10µm cups contain some single 10µm beads but also combinations of 5µm and 10µm beads. **(b)** Occupancy of 10µm and 6µm cups again, but with greater zoom. The double occupancy of 10µm cups with 10µm beads is particularly visible to the left of the image.

While single occupancy was not achieved using the 6µm, 10µm and 15µm cup array design, results were significantly better for the 15µm and 20µm cup array in terms of single occupancy of 20µm beads, as illustrated in Figure 3.15 below.

(a)

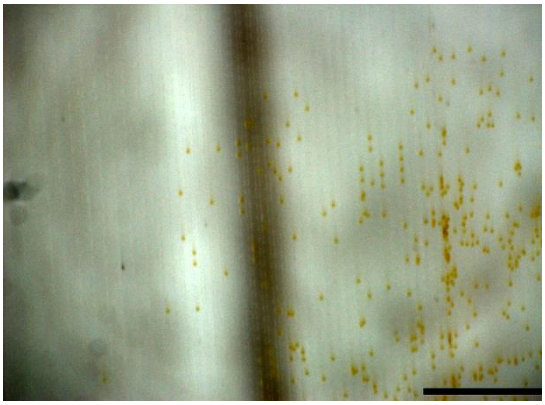

(b)

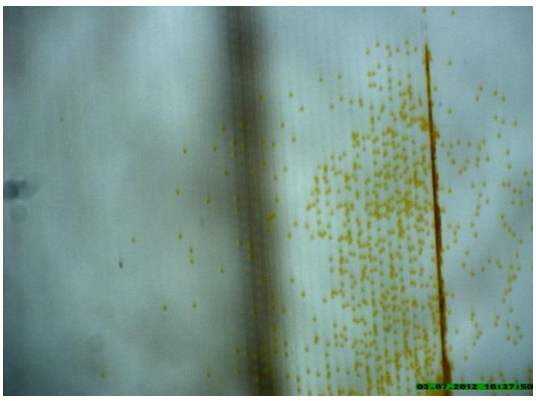

(c)

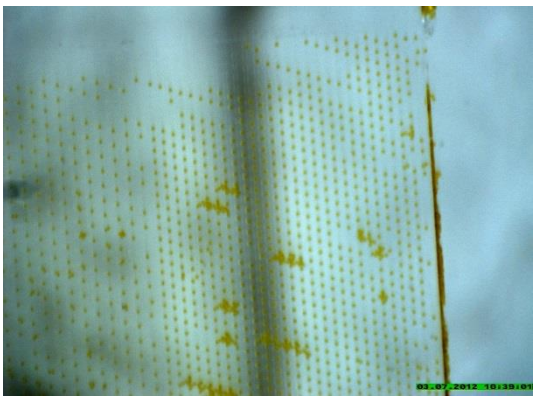

(d)

(e)

Figure 3.15: (a)-(e) Time lapsed sequence of 20µm beads filling 15µm and 20µm cups singly. Figures **(a) – (d)** show the beads filling the cups singly, but with some clogging of beads in a few areas. Following a "shake mode" step, this clogging was reduced somewhat, as seen in Figure **(e).**

The successful single occupancy of both 15µm and 20µm cups with 20µm beads, as well as the mixed occupancy of the 6µm, 10µm and 20µm arrays illustrates the power of the v cup design but also some of its limitations in relation to differentiating between mixtures of particles that are similar in size. As discussed previously, the occupancy of a

20µm or 10µm cup can be tightly regulated by modifying the bead diameter to cup diameter ratio, R_c, outlined by Burger *et al.* [129] for 20µm and 10µm beads respectively. However, when a number of different bead sizes are mixed, it has been demonstrated that controlling the occupancy of the cups becomes significantly more challenging. Unfortunately, neither arrangement outlined in sections 3.1.2 or 3.1.3 proved to be selective enough to provide single occupancy and differentiation of all beads. This problem would be greatly magnified when working with particles and cells of small differences in size, such as WBCs and RBCs. Therefore, new designs based on the work of McFaul *et al.* [212] and Kim *et al.* [213] (sections 3.1.4-3.1.6) were developed, that were more suitable for the small size differences between cells and their deformability.

3.1.4 Parabolic Funnel Ratchet Design

This physical size differential design was adapted from the pump-driven assay developed by McFaul *et al.* [212] McFaul's design consisted of filter structures similar to those used in the assay design 3.1.2 described previously.

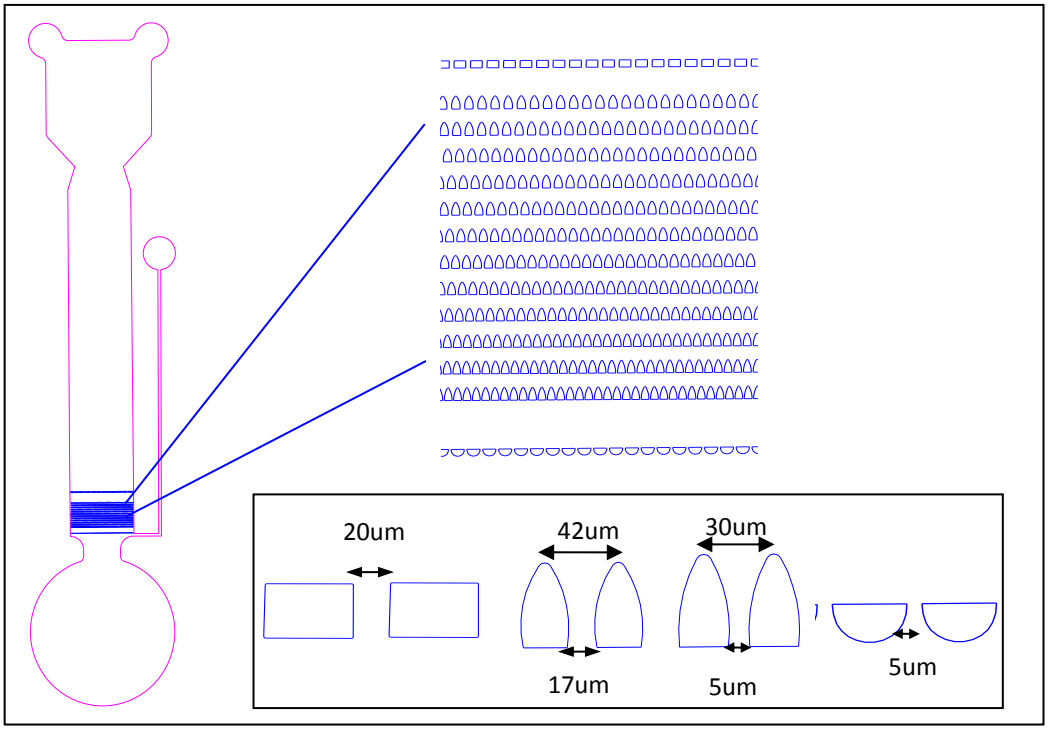

Figure 3.16: Schematic of the parabola filter chip, with zoomed in view of the top filter structure, parabolas and stop features. The top of the chip features a row of rectangular filters, used to prevent impurities and clumps of beads or cells, which may have stuck together, from entering the parabolic filter structure. The smallest gap in the parabolic filters ranges in size, from 17µm down to 5µm in steps of ~1µm. This is to facilitate the separation of particles with small differences in their diameter. Finally, a row of semi-circular stops were added at the end of the assay, to prevent beads/particles from going into the lower section of the chips.

The operating principle of this elongated, parabolic shape is illustrated in Figure 3.17.

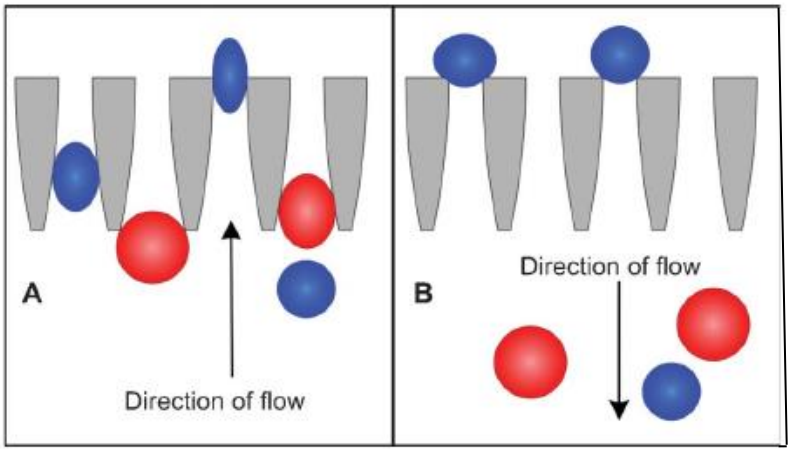

Figure 3.17: Schematic of the parabolic funnel ratchet separation structure developed by McFaul *et al.* [212]. Smaller particles (blue) squeeze through the funnel ratchets in Figure A, while the larger red particles remain behind. Once the direction of flow is switched, the smaller particles cannot get back to their original position due to the width of the top of the parabolic structures, while the larger particles remain on the opposite side. Repeating this process leads to a continuous "sifting" of particles, leading to their complete separation into different rows of the device.

In the microfluidic assay by McFaul et al, syringe pumps were used to create an oscillatory flow to circulate the microparticle and cell samples back and forth through the parabolic funnel ratchets. This lead to the separation of mouse lymphoma cells (LMOs) from microparticles of similar size, based on their deformability and size. Similarly, LMOs were separated from peripheral blood mononuclear cells (PBMCs), whose size ranged from 8µm to 14.5µm and from 6µm to 8.5µm respectively. Therefore, this design was a suitable basis for the development of a platform for the 3-fold differentiation of white blood cells i.e. lymphoctyes, eosinophils and neutrophils, due to their variation in size and the small differences in size between them i.e. on the order of microns. The design tested in this thesis was initially driven by the centrifugal flow alone, to establish the performance of the parabolic filters and their suitability for capturing and trapping 5µm and 10µm beads. The "shake mode" described earlier in this thesis was used as a way of providing a "counter-flow" moving in the opposing direction to the centrifugal force, to facilitate bead separation. However, the degree of bioparticle separation and flow control achievable using this method is clearly far inferior to the design outlined in the work by McFaul *et al.* Therefore, to create an assay that behaves analogously to the work in the literature, a counter flow is introduced to the chip in the form of a magnet, embedded at the bottom of the chip. This design will be discussed in detail in section 3.1.5.

Results and Discussion

To gauge the performance of the assay, a mixture of 5µm and 10µm beads in PBS was tested initially. Although the beads would not be able to deform in the parabolic structures, these initial tests were used gauge the likelihood of clogging in the assay and other limitations before a cell sample was introduced.

5µm beads were introduced into the assay initially, to test the accuracy of the parabola dimensions. As can be seen in the series of images that follow in Figure 3.18, 5µm particles get through all obstacles, including the 5µm parabolic filters at the bottom of the assay.

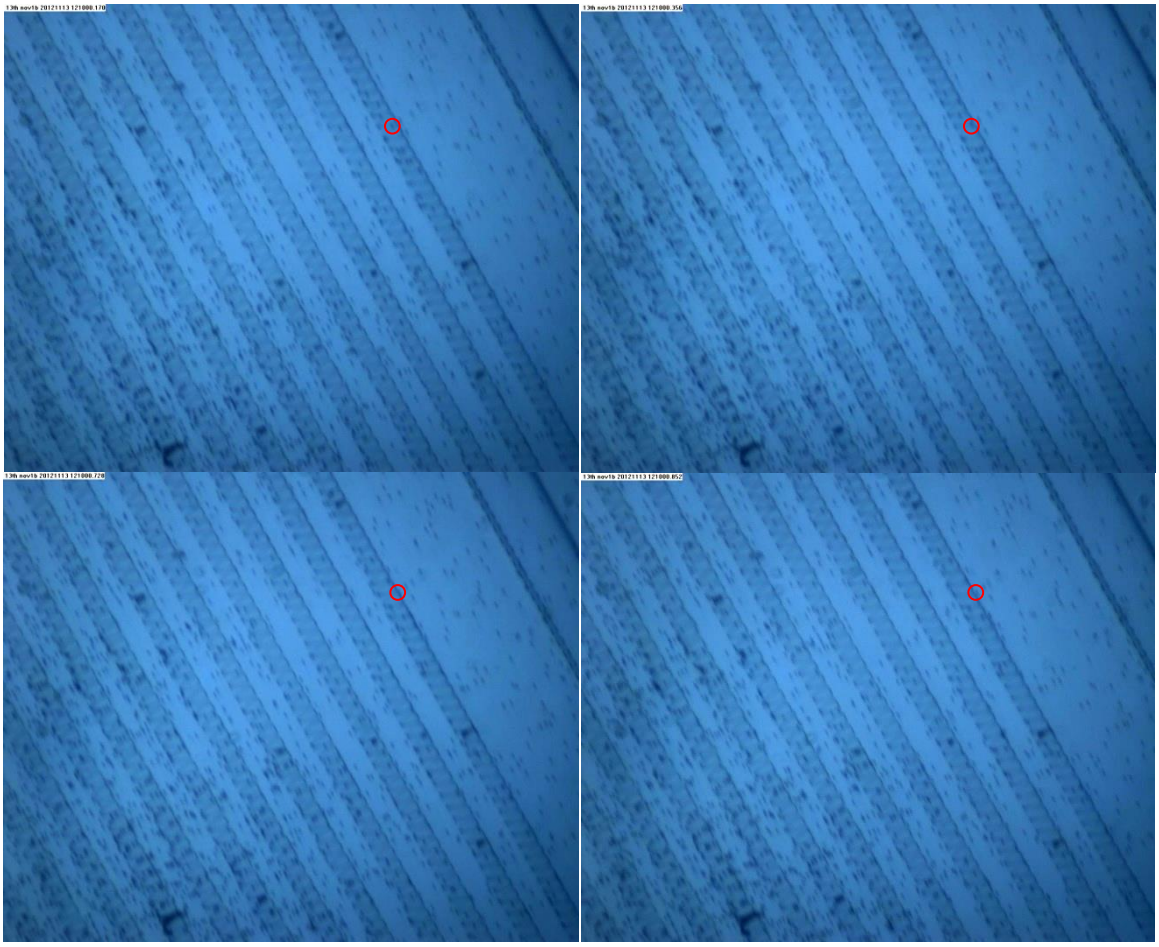

Figure 3.18: Sequence of images illustrating flow of 5µm particles through all parabolic filters. The red circle follows a 5µm particle from entry through the other side of a set 5µm parabolic gaps.

This was an issue that persisted through a number of PDMS/PMMA chips developed, as the challenges of fabricating SU-8 and subsequently PDMS structures at this scale photolithographically was significant, as referred to in previous sections. Underexposure of the 5µm parabolic structures or poor contact between the glass

photomask and the SU-8 chip leads to slanted SU-8 moulds, producing PDMS structures that were wider at the top than at the bottom, which could be the cause of the 5µm particles passing through filtration features, as illustrated in Figure 3.18. On the other hand, overexposure of the SU-8 structures would lead to SU-8 structure that was sloped inwards, causing poor demoulding of PDMS and potential clogging of beads throughout the chip. As the 5µm particles above persistently fell through the filters, 10µm particles were used a benchmark instead for the performance of the assay.

The typical behaviour of 10µm particles tested in this parabolic assay, which was spun at 20Hz following the insertion of the beads can be seen in Figure 3.19.

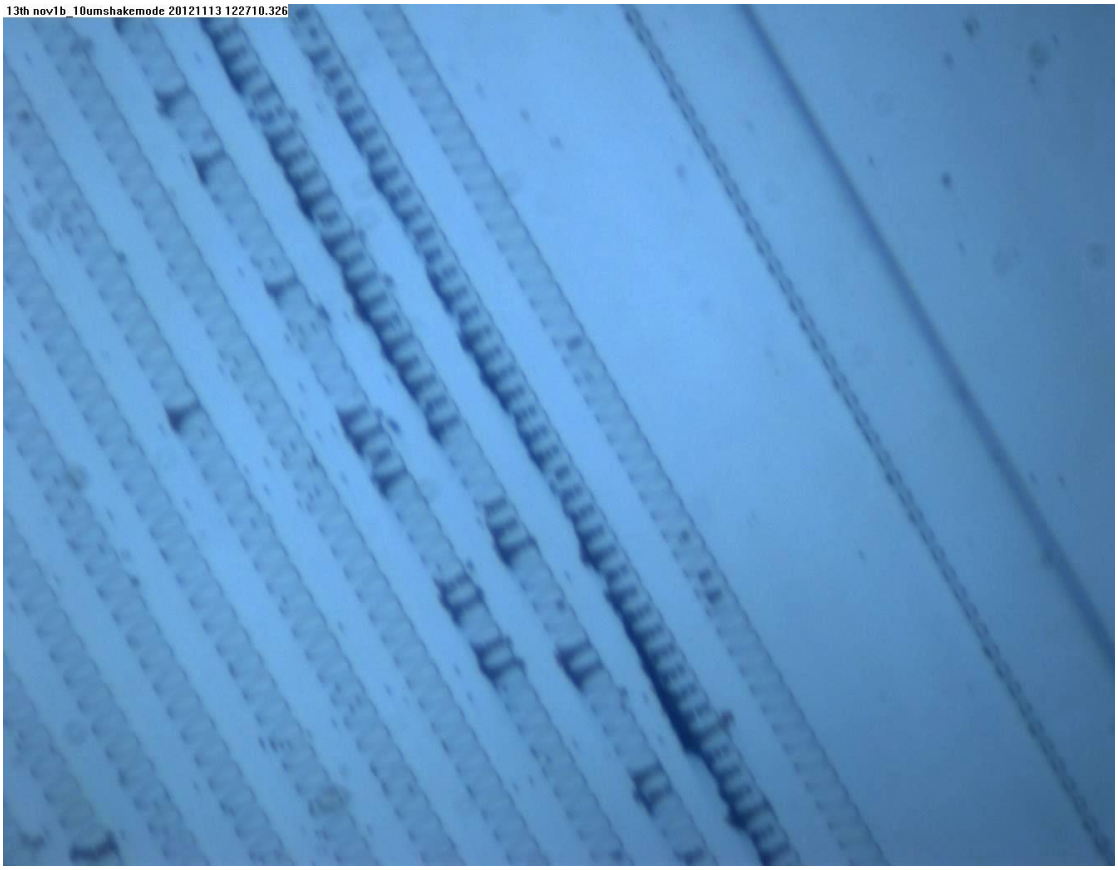

Figure 3.19: Image of 10µm beads caught in rows of parabolic filters with 8µm, 7µm and 6µm filter gaps. 10µm beads are captured in these features and begin to clog as more beads enter the assay.

The capture of the 10µm beads in the filters tailored to 6µm, 7µm and 8µm particles confirms that there were also fabrication issues at this scale, with the gaps between features appearing to be ~1-2µm larger than expected, as observed during the 5µm bead tests. As Figure 3.19 illustrates the 5µm and 10µm bead mixture are separated, although single capture and occupancy of 10µm beads is not achieved under centrifugation, as expected.

However, following a "shake mode" step, which simulates the sifting counter flow idea employed by McFaul *et al.*, a good degree of filtration and de-clogging of the features is observed.

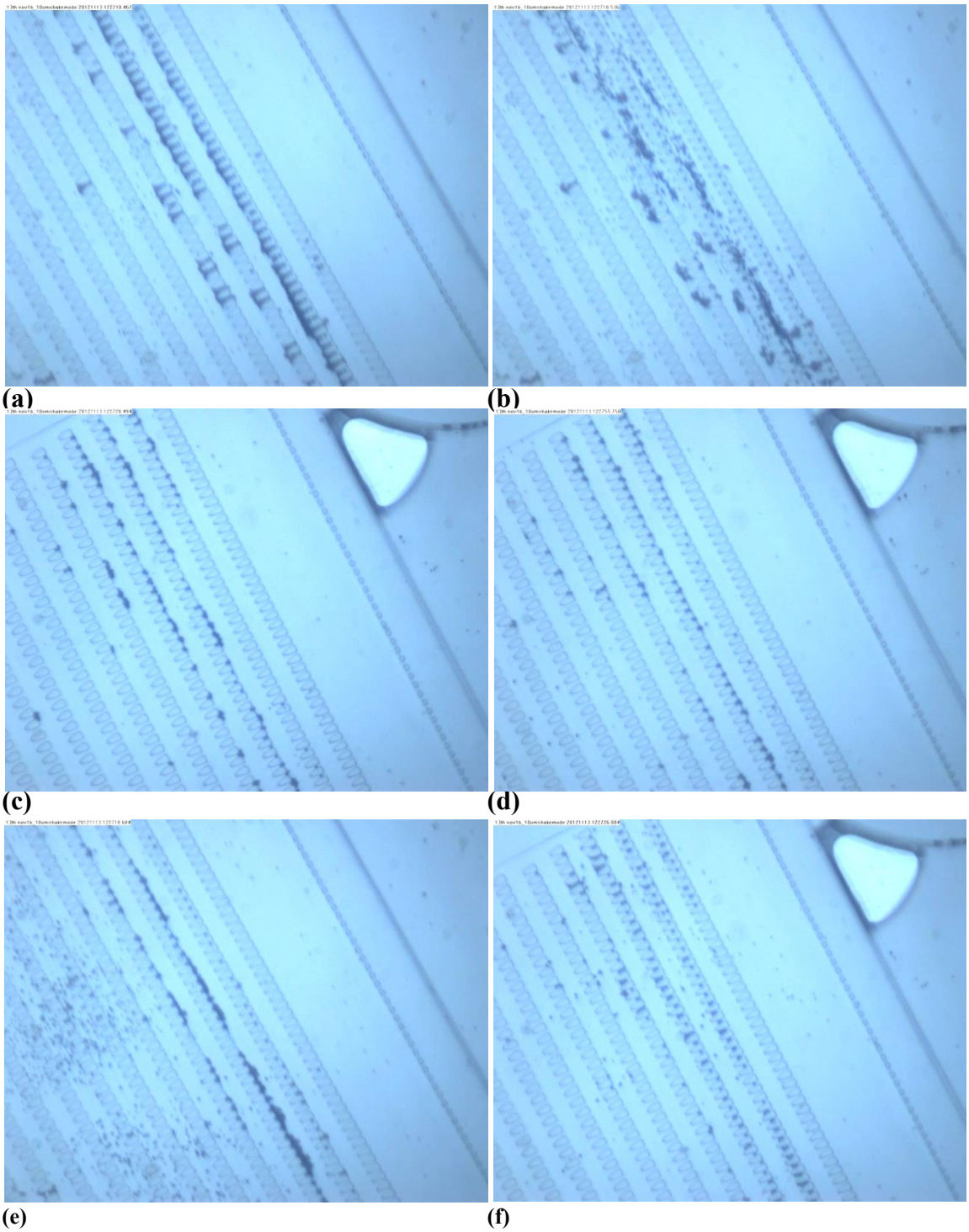

Figure 3.20: Capture of 10μm beads (blue) and sifting of particles using "shake mode".

This result is promising, as the shake mode method of providing a counter flow is by no means optimal and was used as a proof of concept before the much more refined version

of this design was attempted. This design is outlined in the section that follows and uses a combination of magnetic actuation and centrifugal flow. In addition, the deformability of the cells, which is not applicable for the bead experiments above will add another level of control to the separation capabilities of this design, as cells with different deformability but similar size will be separated from each other by the curved ratchets. It should also be noted that the design of the rows of parabolic structures above was not tailored to trap beads/bioparticles singly but rather to sift particles of the same type (size and deformability) into row(s) separate from other particles. In the article by McFaul *et al.*, additional flows are provided perpendicular to the input and counter flows, to remove the separated particles from the separation structure. It was thought that once the above design was optimised for cell separation using centrifugal forces that the cells could be removed from the structure as demonstrated by McFaul et al; perhaps by expanding upon the magnetic actuation scheme outlined in the next section.

3.1.5 Parabolic Funnel Ratchet Design – Magnetic Actuation

One of the key elements to the parabolic funnel ratchet design by McFaul *et al.* outlined previously is the oscillatory flow induced by the birfurcation of the inlet fluid into 128 identical streams, [212] as seen in Figure 3.21.

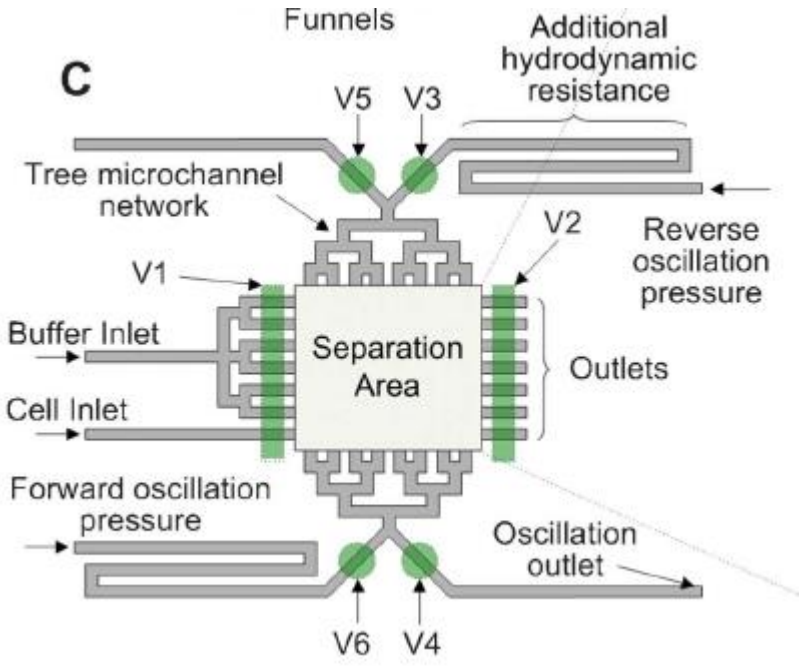

Figure 3.21: Outline of flow inlets and outlets for microfluidic funnel ratchet device by McFaul *et al.* A single planar flow is bifurcated into 128 separate flow streams to ensure that each cell experiences the same hydrodynamic pressure.

Buffer and cell inlets, V1, and outlets, V2, enable the injection and removal of the sample from the assay, while V3-V6 indicate the separating flow streams. This design differs somewhat from designs in sections 3.1.2-3.1.4, as these schemes utilise centrifugally driven sedimentation in stagnant flow conditions, in addition to staggered capture structures to capture the sample of interest. However, a similar strength actuation mechanism, facilitating a greater degree of flow control, would increase the likelihood of bead/cell separation. Therefore, a magnetically actuated scheme adapted from the work of Burger *et al.* [214] was applied to design 3.1.4 to improve flow control in the parabolic funnel ratchet platform. Figure 3.22 illustrates the basic operating principles of the original magnetic actuation scheme developed by Burger *et al.*, used to enhance bead redistribution and retrieval from a microfluidic V Cup array.

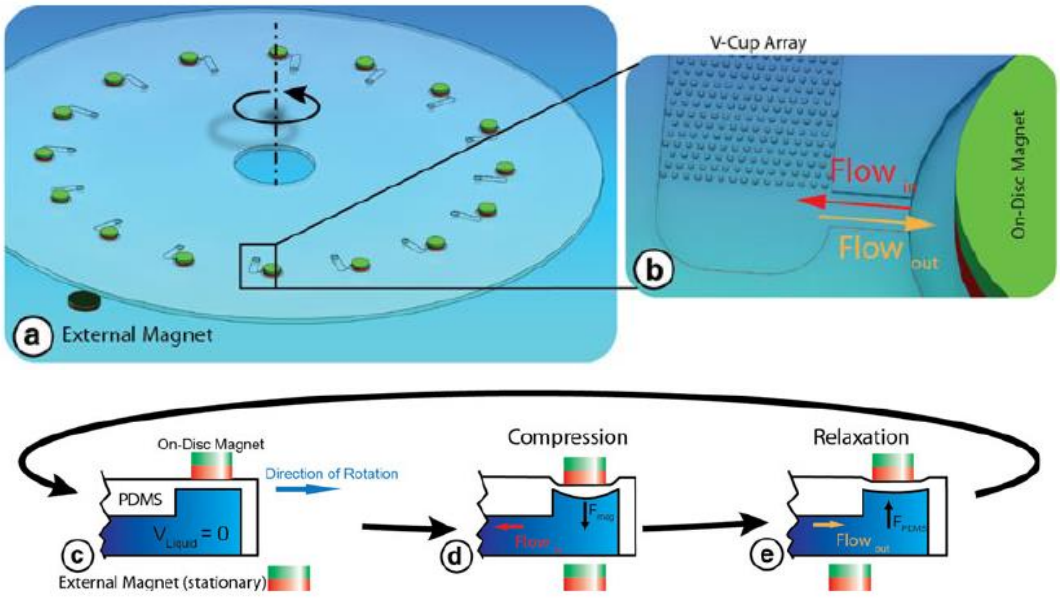

Figure 3.22: (a) Illustration of the PDMS/PMMA V-Cup chip, with magnetic actuation for bead redistribution [214]. **(b)** Zoomed in image of V Cup array and embedded stationary magnet, with flow direction indicated. **(c) - (e)** Step-by- step schematic of the magnetic actuation process. In Figure **(c)** the external magnet is too far away from the embedded on-chip magnet and therefore no actuation occurs. However, once the external stationary magnet is in proximity to the embedded magnet, **(d)**, the attractive force of the magnets causes the PDMS below the embedded magnet to compress, leading to an inward flow ($Flow_{in}$) into the V-Cup array. As the disc rotates, and the embedded magnet moves away from the stationary magnet, the PDMS relaxes, causing a flow outward from the V-Cup array, $Flow_{out}$. This process repeats, provided that the spin speed does not go above a certain threshold level, where the time that the two magnets are in proximity with each other is too small to generate a compression of the PDMS.

In this work a similar scheme was employed, with the stationary magnet located in a 3D-printed magnet holder (Figure 3.23), suspended above the on-disc 0.24cm^3 cylindrical magnet, rather than under it.

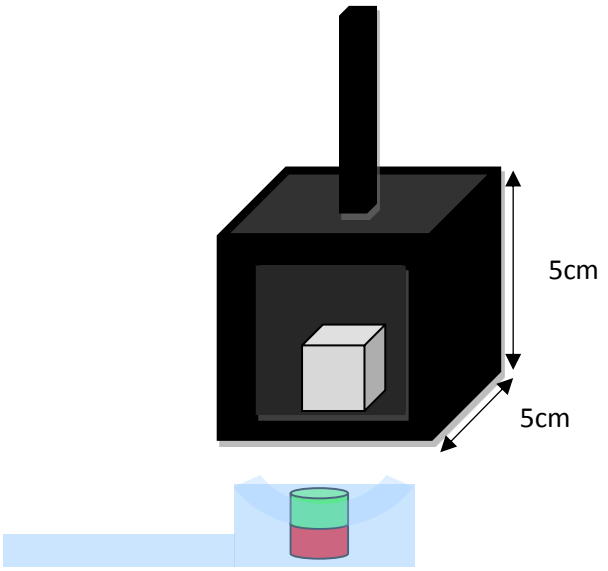

Figure 3.23: Conceptual image of 3D magnet holder with 1cm^3 magnet inside. This holder had a square window on its base to expose the magnet and was clamped above the disc in Figure 3.24 that follows.

While the scheme by Burger *et al.* uses the attractive force between two magnets to create an actuating flow, in this work the orientation of the stationary magnet was flipped, to induce a sufficient repulsive force to actuate the microfluidic channel. In addition, the embedded magnets on the disc are positioned at the bottom of the separation structure, rather than at the side, as seen in Figure 3.24.

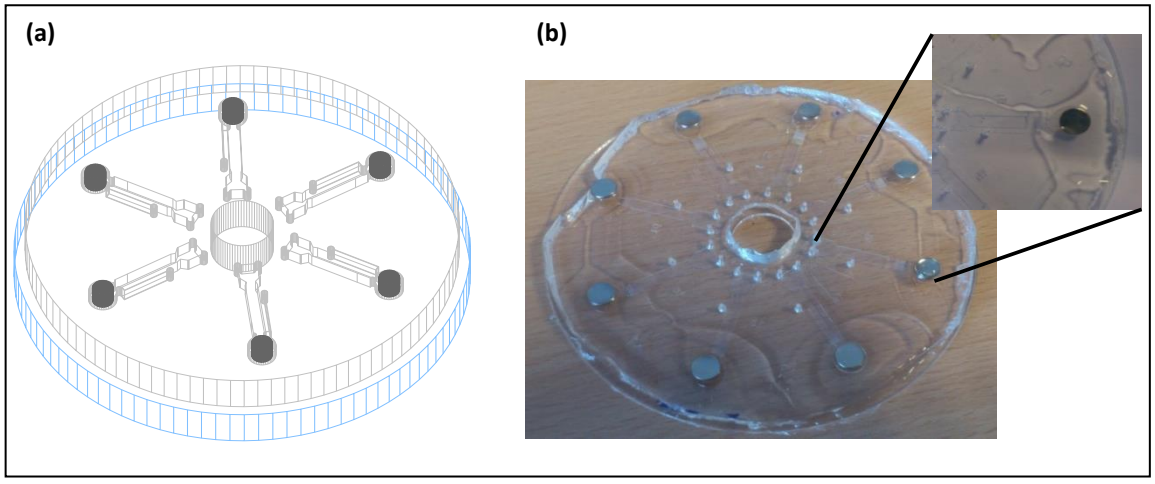

Figure 3.24: (a) 3D visualisation of magnetically actuated parabolic funnel ratchet filtration disc and **(b)** photographic image of same disc, with zoomed in photograph of a single microfluidic structure, with an embedded magnet.

As stated in the work of Burger et al, the magnetic actuation is at its greatest at slower spin speeds, as the stationary and non-stationary magnets are in proximity for longer. The spin speeds were varied initially in this work to find the slowest rate of rotation that

still produced fluid flow due to magnetic actuation, which was found to be approximately 2Hz.

Magnetic actuation was used in this thesis to prevent clogging and promote single bead capture. This was demonstrated in the case of the capture of 10µm beads, where a number of rows of single bead occupancy were observed, Figure 3.25:

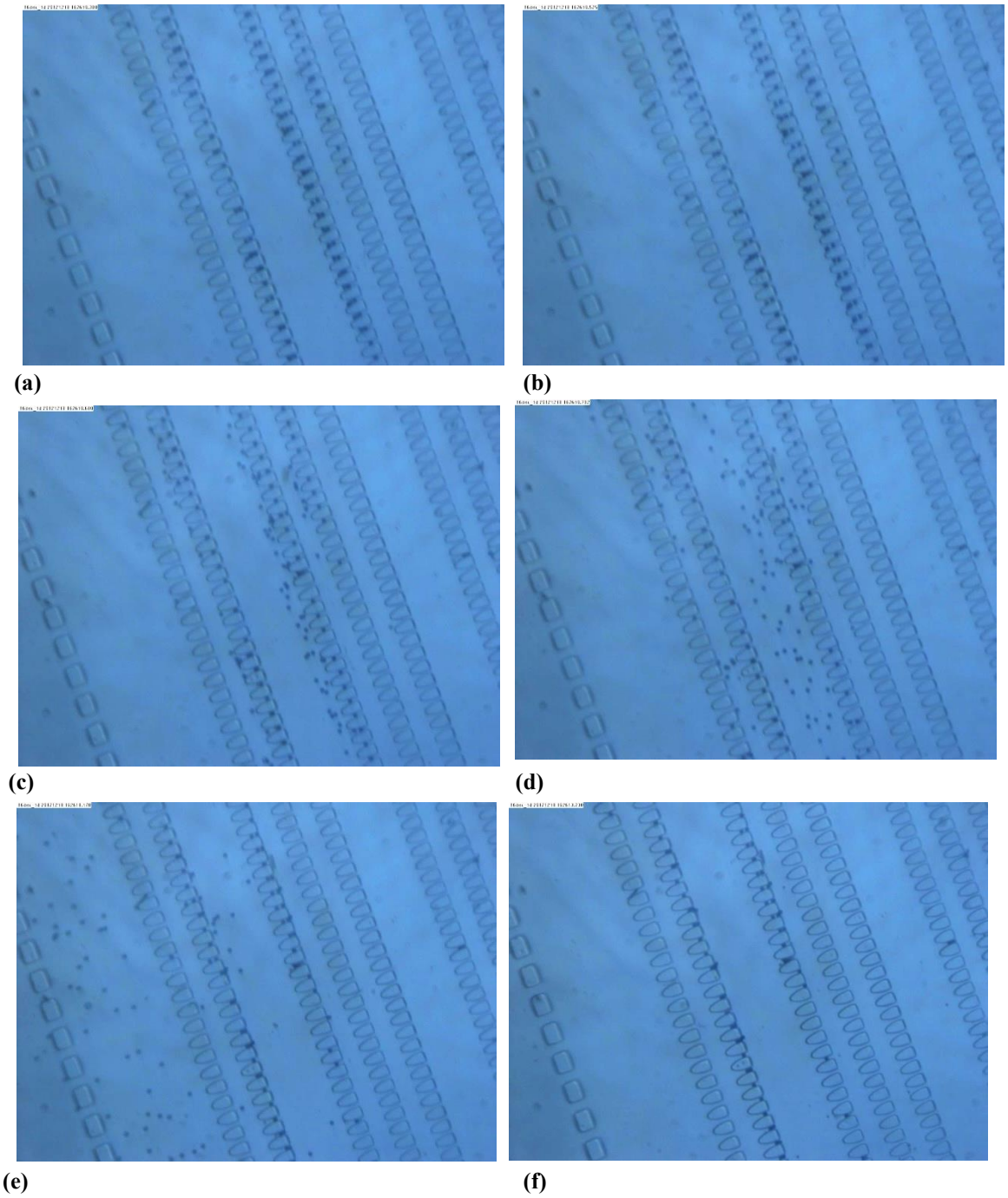

Figure 3.25: Time lapse sequence of 10µm particles being actuated by the embedded magnet on chip and external magnet off chip. As the 10µm particles are declogged and move in the opposite direction to that of the centrifugal force, most of the particles become trapped singly in 2 rows of the chip.

While the separation and trapping observed in Figure 3.25 is by no means optimal, as some 10µm particles passed through the filters and others clogged, it does illustrate the power of the magnetic actuation module for de-clogging and separation applications. This actuation mechanism is inexpensive, compact and easy to fabricate, requiring no bulky external pumping mechanisms to provide an opposing force to the centrifugal force.

As with the shake-mode actuated design in section 3.1.4, 5µm particles pass through all obstacles on this chip, including those tailored specifically for the capture of 5µm particles/cells, Figure 3.26 (a)-(d):

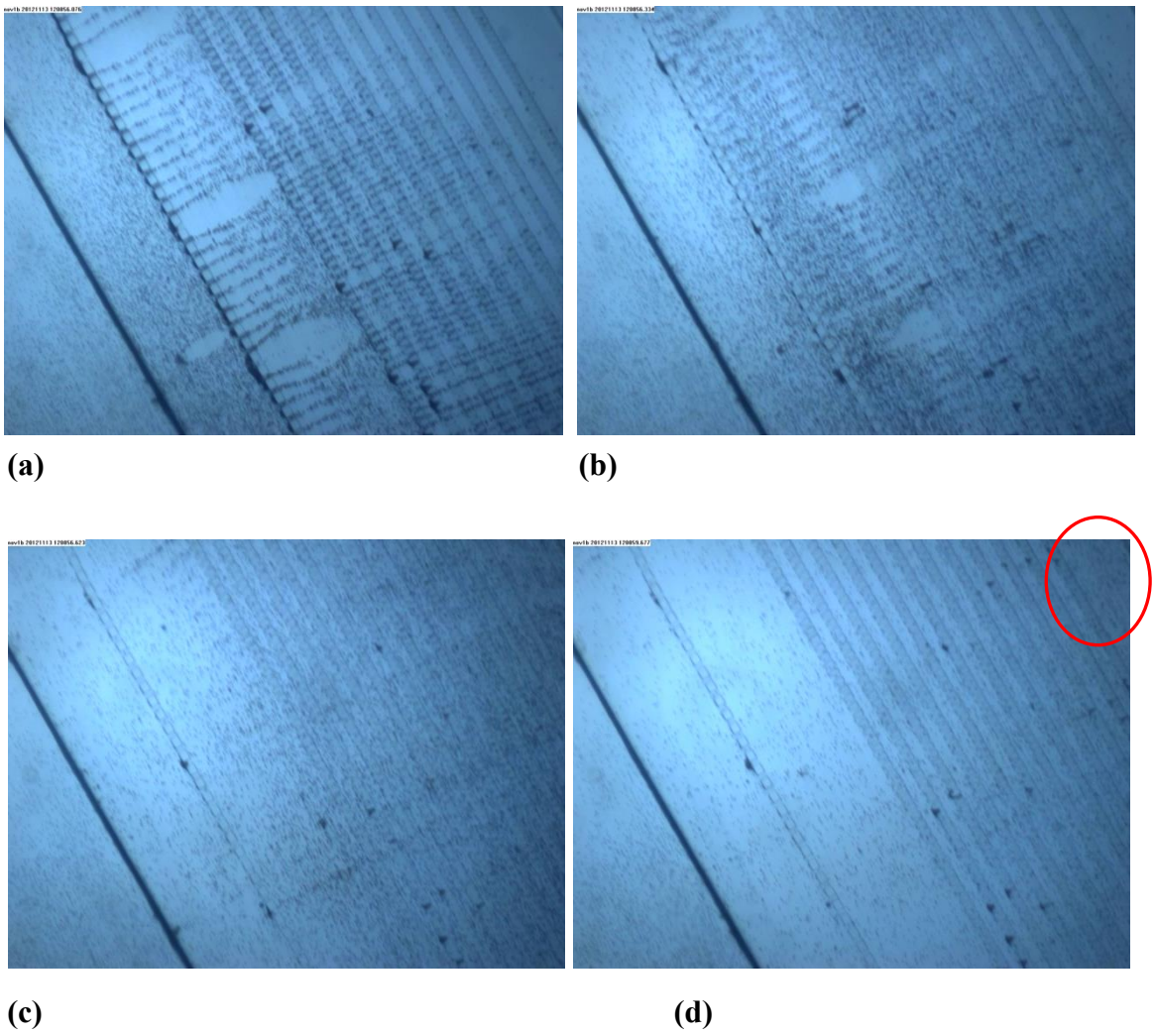

(a) **(b)**

(c) **(d)**

Figure 3.26: Time lapse images of 5µm particles (red) passing through the parabolic filter chip under 15Hz centrifugation. It can be clearly seen that the 5µm particles pass through all of the filters – they can also be seen at the other side of the filter structures as indicated by the circle in (d).

Unfortunately, the fabrication issues associated with this design illustrate that, at the very least, a significant amount of time would need to be invested to ascertain the correct processing steps to fabricate a device capable of separating different sized beads

and cells in a predictable manner. From the results above and the Table of parabola gap sizes in section 5.2 of the appendix, it can be concluded that this fabrication method is unlikely to produce a device capable of separating different sized beads and cells in a predictable manner. There is a notable variation in the gaps between parabolas within rows, as well as deviations from what is expected from each row of parabola gaps. Therefore, it is far more likely that a more precise (and most likely more expensive) fabrication approach e.g. silicon on glass etching as in the work by McFaul *et al.* [212] would be needed to obtain the resolution necessary to produce a suitably accurate sorting device in this configuration, particularly for cell-based applications, as illustrated in section 3.1.7.

The design in section 3.1.6 that follows was tested in parallel with the above design as an alternative cell separation and trapping structure, again with the integrated magnetic actuation component.

3.1.6 Multiple Obstacle Structures

This design was adapted from the selective size amplification, multiple obstacle architecture (SSA-MOA) platform developed by Kim *et al.*, Figure 3.27 [213].

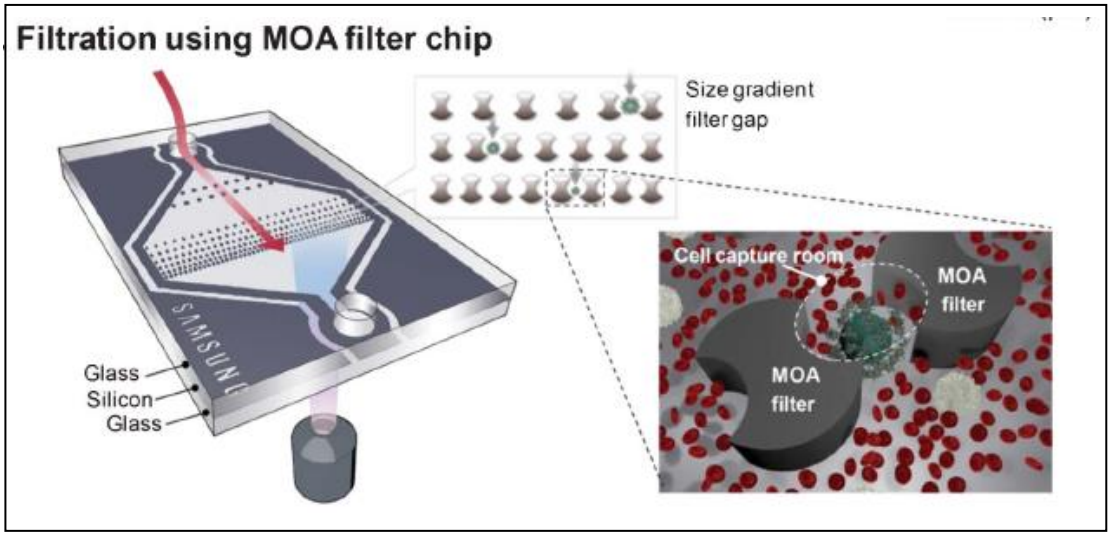

Figure 3.27: SSA-MOA filter chip, with zoomed in schematic of size amplified CTC cell captured in a multiple obstacle architecture trap [213]. CTCs are size amplified using anti-EpCAM conjugated beads and are captured according to their size in the MOA traps. This size amplification allows the CTCs to be distinguished and caught from a sample containing similarly sized white blood cells. The direction of pumped fluid flow is indicated by the red arrow, with the MOA shielding the cells from any excessive hydrodynamic shear forces and preventing clogging in the device.

In the work by Kim et al, differentiation of cells of similar sizes was carried out using the SSA-MOA approach, resulting in the differentiation of MCF-7 cells from WBCs and RBCs in whole blood. The size overlap between WBCs and MCF-7 cells (illustrated in Figure 3.28) in particular is problematic as the average size of MCF-7 cells was found to be 16.6µm ± 2.3µm, with WBCs varying in size up to 17µm, despite having an average size of 8.5µm [213].

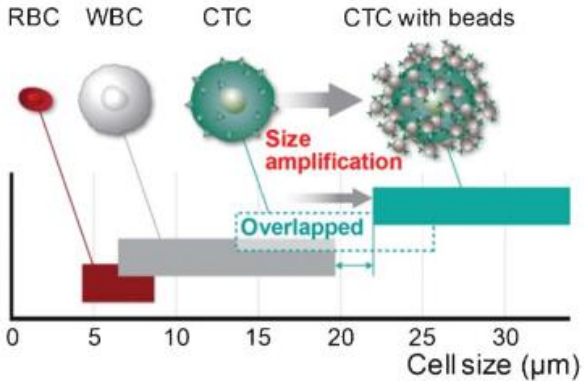

Figure 3.28 Schematic of the effect of size amplification of CTCs with 3µm beads, towards the differentiation of CTCs from whole blood [213].

To overcome this obstacle, the MCF-7 cells were coated in beads of various sizes to ensure a clear differentiation between WBCs in whole blood, enabling single MCF-7 cell capture in the multi-obstacle architecture. 3µm, anti-epcam coated beads were found to be the most suitable for SSA, with a 92% recovery rate achieved for MCF-7 samples in whole blood. The gap between the top of the obstacles is ~2µm larger than the bottom of the obstacles, creating a trap with has an integrated shielding effect on the captured cells. This feature is important to avoid excessive shear stresses on the captured cells, which may damage the cell or change the intrinsic characteristics of the cell, which could be used as key indicators in disease diagnosis [213,215-217]. Therefore this design is an improvement on previous assay in that respect, as there should be minimal shear stresses exerted on the cells. However, before the selective size amplification aspect of the chip could be investigated using cell samples, a less complex version of the design by Kim *et al.* was tested initially, to establish the working parameters of the multiple obstacle architecture approach. As in previous designs, 5µm, 10µm and 20µm beads were tested in this chip design illustrated in Figure 3.29.

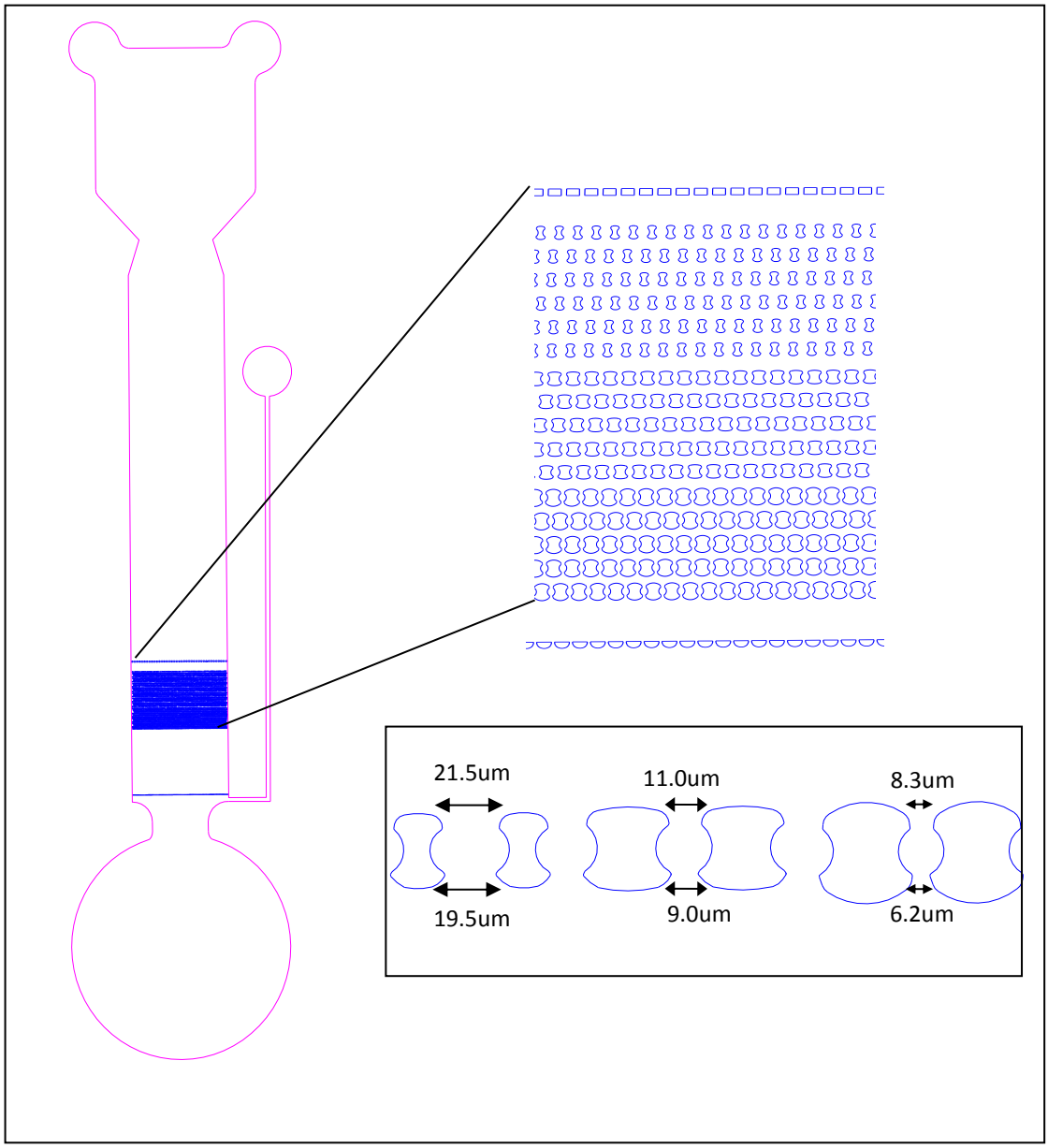

Figure 3.29: Schematic of the centrifugally driven multiple obstacle architecture (MOA) filter chip, with zoomed in view of the top filter structure, trapping structures and stop features. The trapping structures are fabricated with gaps tailored to suit 5µm, 10µm and 20µm beads, with a smaller gap at the bottom of the obstacle to trap the beads. A row of semi-circular stops are included at the end of the assay, to prevent beads/particles from going into the lower section of the chips.

Using the same centrifugation speeds used in previous sections (20Hz) to drive the sample towards the chips features, the largest beads, of 20µm in diameter, get clogged at the beginning of the chip once more - this time at the pre-filter structures. Furthermore, there were continuing issues with 5µm particles passing through the device, as illustrated by the following examples, with no red 5µm beads visible in the smallest capture structures. This is further illustrated by the varying obstacle gap values recorded on the Wyko profilometer for MOA structures in the appendix. Despite these

difficulties, a number of notable and positive separation and filtration processes were observed, using shake mode actuation and magnetic actuation, as in the previous approach. While 10µm beads are observed to clog at the second set of MOA features, Figure 3.30 illustrates the declogging of 10µm beads using the "shake mode" outlined previously.

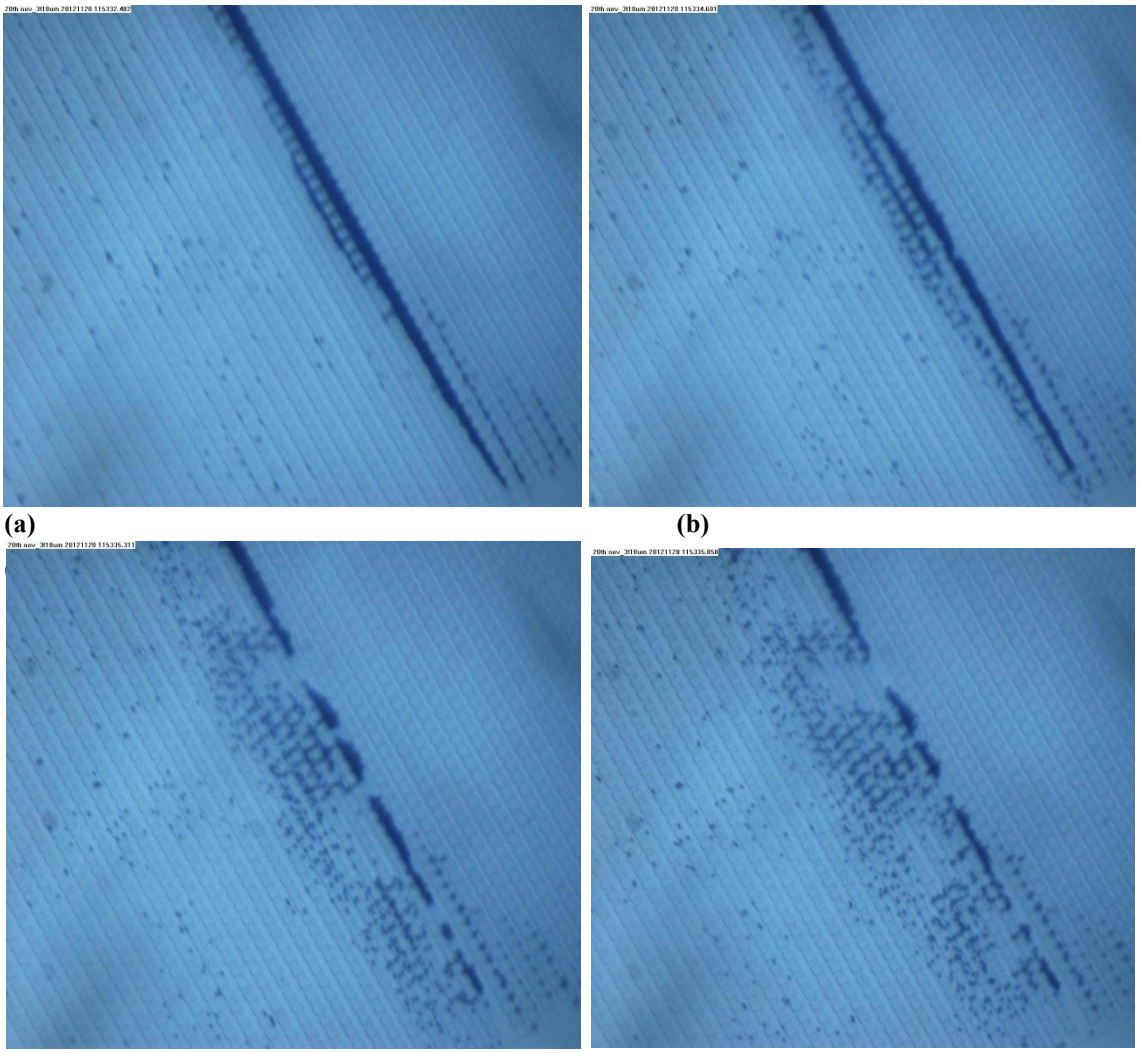

Figure 3.30: (a) – (d) Time lapse sequence of declogging of 10µm particles (blue) using centrifugally driven shake mode". **(a)** Beads are initially pushed towards the second set of MOA filters by centrifugation, with Figures **(b) - (d)** illustrating the effect of increasing and decreasing the centrifugal spin speed using the "shake mode" process.

While this process is useful for declogging of 10µm beads, the ultimate goal of this work is to separate and capture biomimetic particles singly. Examples of this single bead capture were observed over the course of this work, with increased separation and differentiation of 10µm beads with each shake mode step (Figure 3.31)

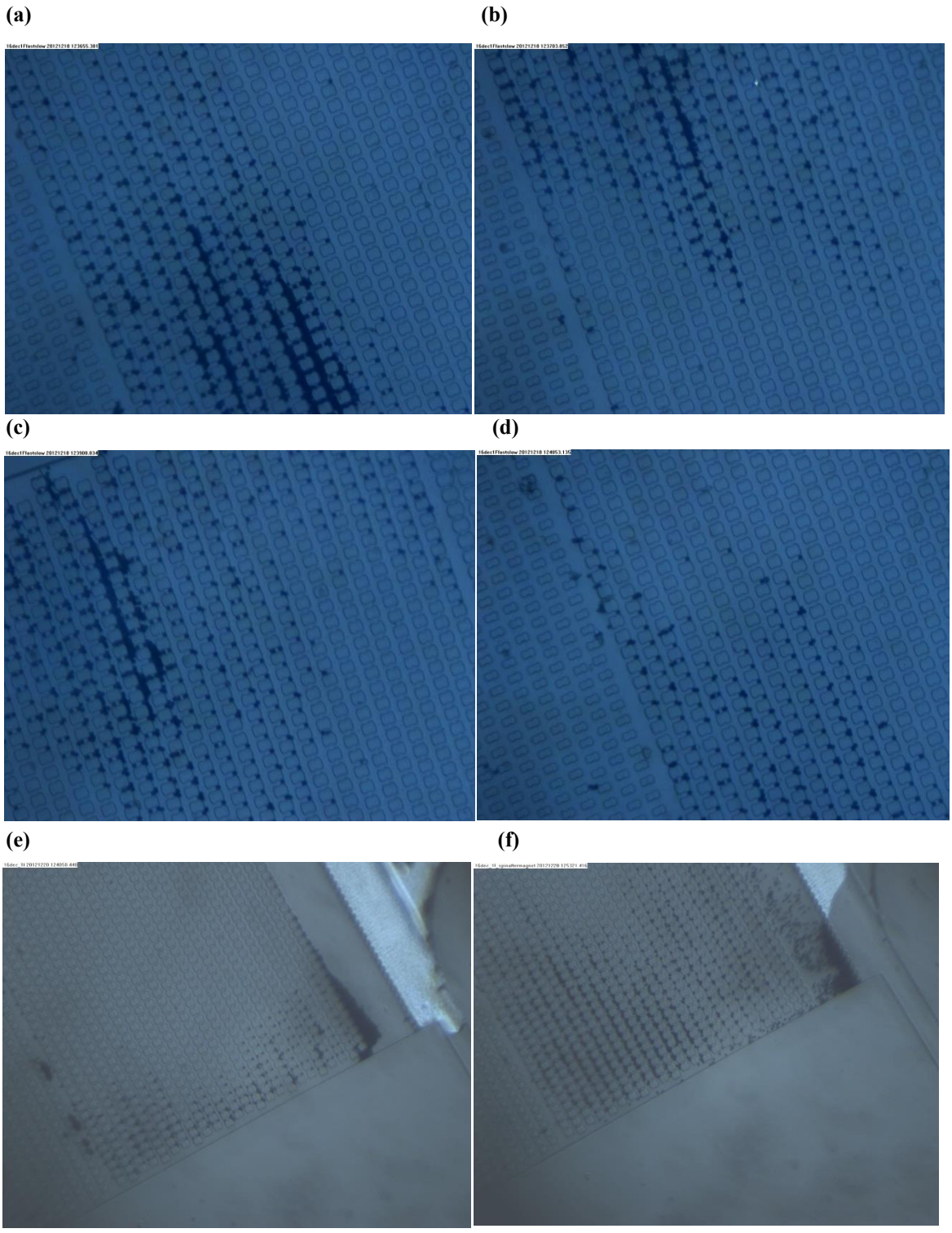

Figure 3.31 (a) – (f) Examples of de-clogging and single bead capture brought about by shake mode actuation. **(a) - (d)** Time lapse of movement of 10µm beads to single occupancy positions with increased shake mode steps. **(e) – (f)** Another example of redistribution of particles through shake mode actuation.

In addition, the magnetic actuation process outlined previously produced similar improved de-clogging and increased single bead capture. As the number of magnetic actuation steps increases, the tendency of the 10µm beads to become trapped singly increases significantly, as illustrated in Figure 3.32.

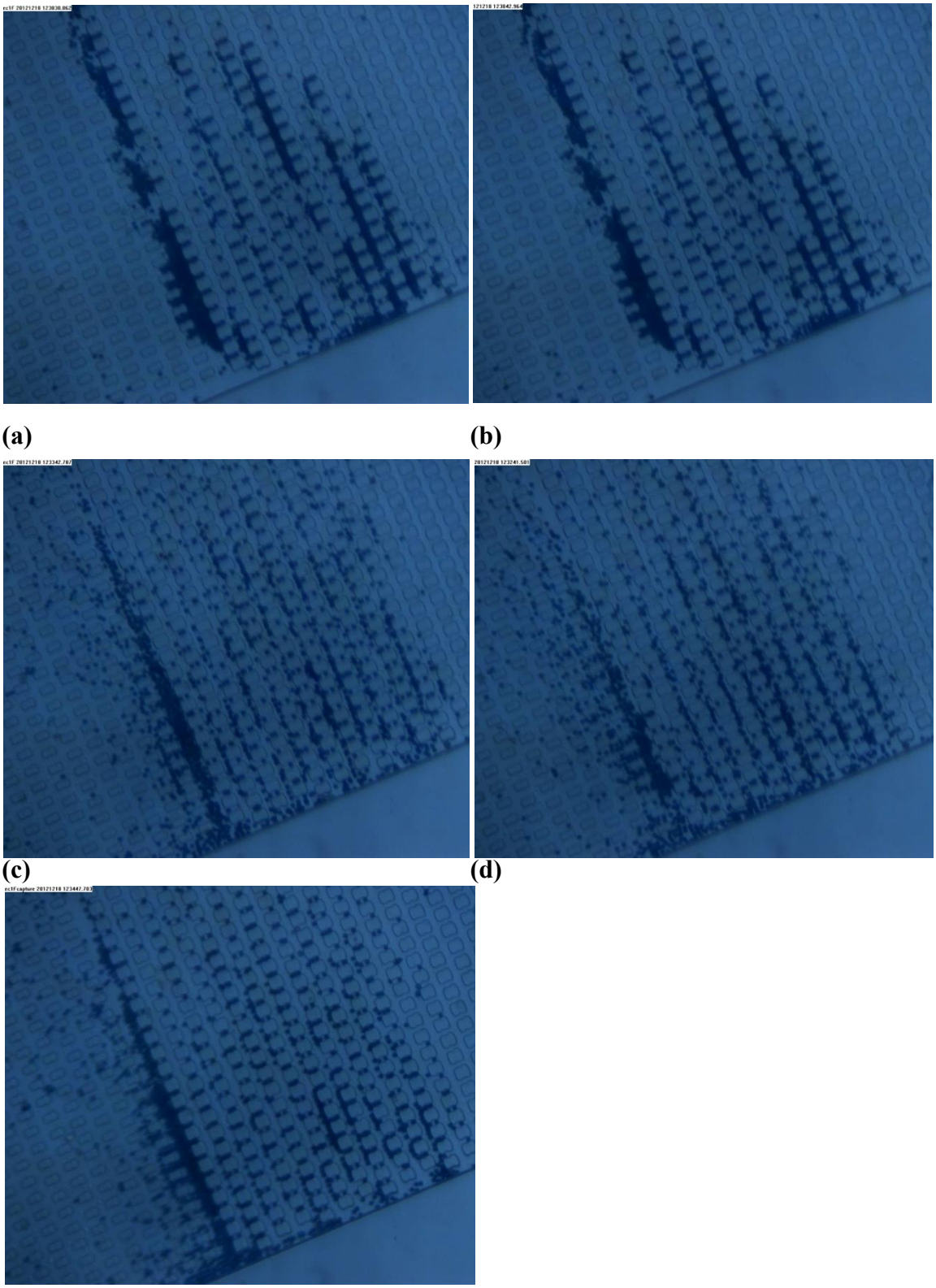

(a) **(b)**

(c) **(d)**

(e)

Figure 3.32 Magnetic actuation of 10µm beads in MOA features, leading to increased de-clogging of 10µm MOA features and single bead capture.

While both of the approaches toward bead separation taken in sections 3.1.5 and 3.1.6 illustrate uses in terms of de-clogging and the promotion of single bead capture for 10µm beads, this approach clearly needs to be developed further to produce controlled

single bead capture and to overcome the manufacturing challenges alluded to previously. In addition, the adoption of the single size amplification approach put forward by McFaul *et al.* [212] should be investigated toward establishing a 3-fold WBC differential platform. The SSA approach would be particularly useful to differentiate between the similarly sized granulocytes, leukocytes and RBCs. It should be noted, however, that this approach requires a somewhat complex and time-consuming "off-chip" incubation step with anti-epcam conjugated beads, and would generally introduce more complexity into a potential lab-on-a-chip device, with clogging of any unbound beads likely to occur in the MOA features, as indicated from the results in this section.

The following and final short section of results on physical size filtration experiments will focus on some preliminary tests of Hl60 and MCF-7 cells in the parabolic funnel ratchet and MOA separation and trapping designs.

3.1.7 Cell Trapping and Separation Experiments on a Centrifugal Microfluidic Platform

Biomimetic particles, such as the polystyrene beads used in this work, are often utilised in biomedical research to test prototype platforms and provide a method for visualising the likely performance of a device for biological samples. However, as has been stated previously, to develop a working platform for cell handling and separation, cells must be tested due to their inherent physical characteristics i.e. their deformability and their tendency to aggregate and adhere to surfaces. While the results in section 3.1.1 – 3.1.6 did not produce an idealised bead separation and trapping platform, many of these techniques were tailored toward differentiating cells rather than beads. In addition, while the behaviour of cells under the force of stagnant flow centrifugation has been illustrated on a number of other platforms such as the aforementioned V-Cup assay by Burger *et al.*[129], the effect of counter actuation mechanisms including "shake mode" and magnetic actuation on cells is a more recent development. Therefore, the results in the section that follows will provide a useful starting point for future work on cell separation and trapping platforms incorporating these techniques as well as future approaches to improving the designs outlined in sections 3.1.1 – 3.1.6.

Hl60 and MCF-7 cells from culture were chosen for cell differentiation experiments due to their availability and differing sizes of ~12.4μm and 15μm-17μm respectively [218,219]. Cell solutions were prepared as outlined in section 2.2.4, with

cell concentrations of 590,000 cells/ml for Hl60 cells and 390,000 cells/ml for MCF-7 cells used. PDMS/PMMA chips were prepared as before, with 2µL of each cell solution was inserted into the assays, which were then spun at 21Hz initially, to drive the cells towards the platform features. Few cells were observed moving through either the parabolic funnel ratchet features or the MOA features, with a further 2uL of each cell solution added to each assay to address this. Movement of Hl60 cells through the parabolic filters was observed, as illustrated in Figure 3.33 below.

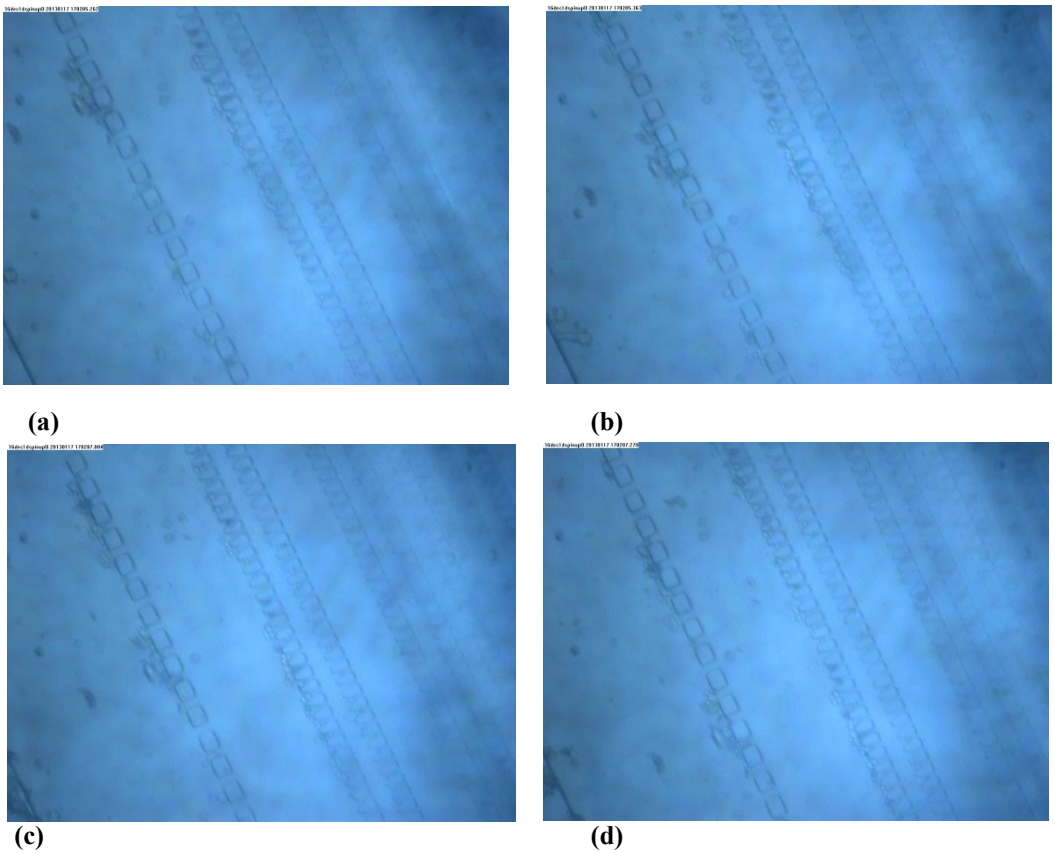

Figure 3.33 (a) – (d) Time lapsed images of Hl60 cells clogging in the first set of parabolic filters and being redistributed singly following a shake mode step.

Hl60 cells were seen to clog initially at the first set of funnel ratchets, with shake mode steps employed to alleviate this issue. Following shake mode steps alternating the spin speed from 15Hz to 2.5Hz, Hl60 cells were then seen to move through the first number of rows of parabolic funnel ratchets, which were tailored towards cells of ~18µm – 14µm in diameter. Additional shake mode steps lead to the Hl60 cells becoming trapped singly, as seen in image (d) of Figure 3.34.

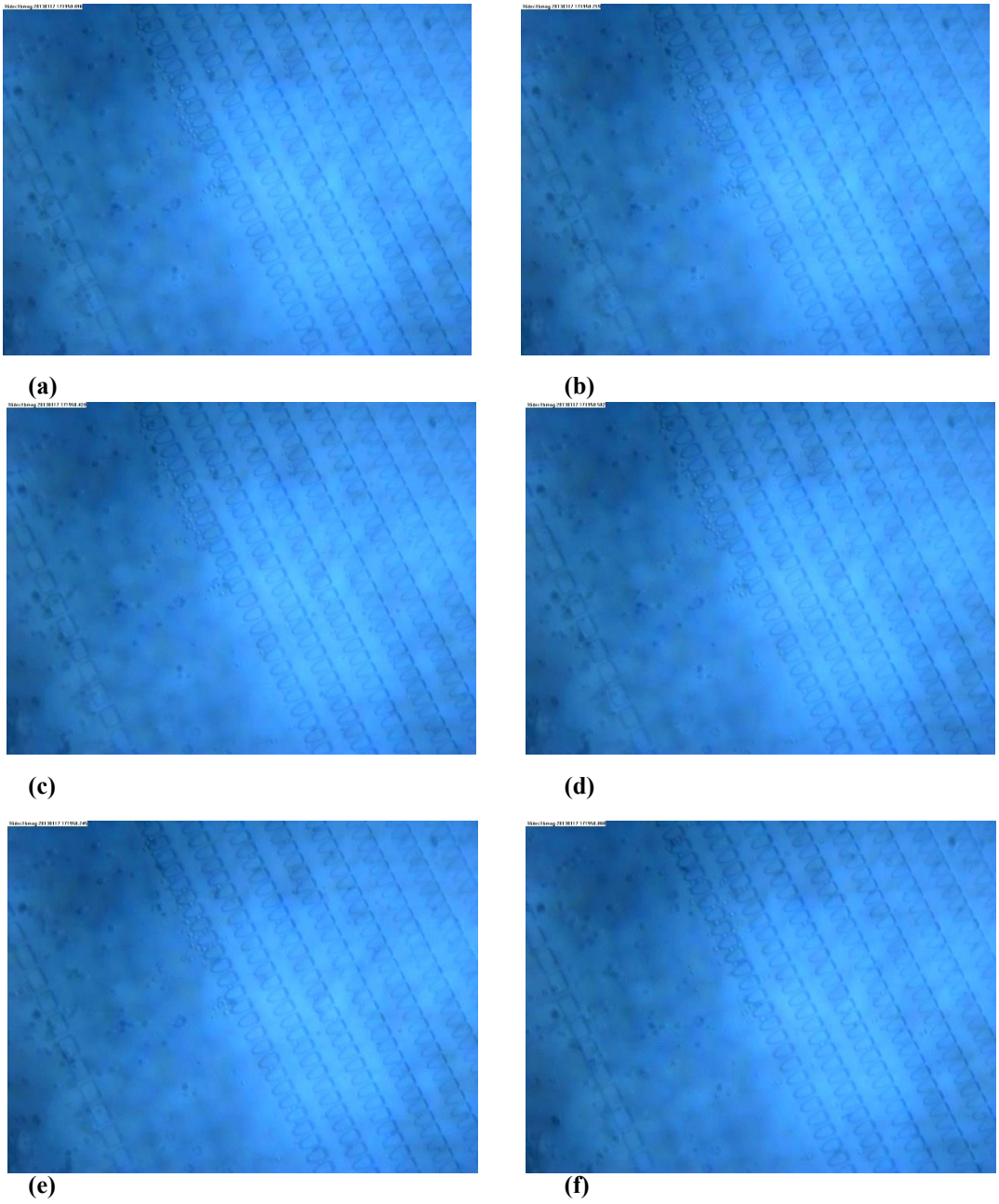

Figure 3.34 (a) – (f) Time lapsed series of images of Hl60 cells flowing through parabolic filter structures and being captured singly using the "shake mode" procedure. The cells inherent deformability makes these structures particularly well-tailored towards the sifting and separation of similarly sized cells.

Magnetic actuation was also employed during cell experiments, with Hl60 cells exhibiting similar behaviour to that observed during shake mode actuation. In this approach cells were seen to pass through the parabolic filters, with some deforming to squeeze through filters with gap sizes smaller than the cell's diameter. Ideally the cells of varying sizes should squeeze through a number of funnel ratchets until the ratchet becomes too small to pass through, even with cell deformation. At this point shake

mode or magnetic actuation would be employed, causing the cells to be separated according to their size and deformability. Unfortunately MCF-7 cells were not observed entering the parabolic features, with aggregation and clogging preventing them from entering the separation region of the platform. This hampered any meaningful discussion of the cell separation capabilities of the parabolic funnel ratchet assay. The cell aggregation effect was also observed in the MOA platform, illustrated in Figure 3.35.

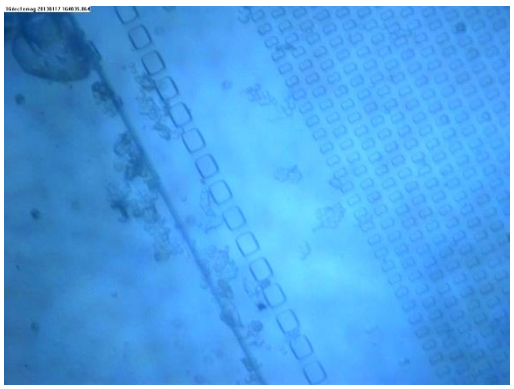

Figure 3.35 Image of clogging of MCF-7 and Hl60 cells at ridge and filter structures of MOA platform.

This issue persisted with the remainder of the assays tested, indicating the additional challenges associated with separating and trapping biological samples rather than idealised biomimetic particles.

While some notable steps toward a fully integrated cell separation and single cell trapping platform have been undertaken in the previous sections, it is clear that a great deal of future work is needed to establish a reliable and high capture rate cell separation platform. The approaches in sections 3.1.1 to 3.1.6 all exhibit particular strengths for a variety of bead and cell separation and isolation applications. In particular, the integration of centrifugally and magnetically driven counter flows on cell separation platforms is likely to prove particularly useful in any future work undertaken in this field. As illustrated by the results of v-cup capture approach outlined in section 3.1.3, the separation and capture of particles of various sizes from a mixed solution is an extremely tricky one. This is particularly true for cells due to the additional obstacles of cell aggregation and the random order at which cells of differing diameters but similar densities arrive at the separation features. Selective size amplification by beads as illustrated by the work of McFaul *et al.* could be used in future work to alter the densities of cells and to enable easier separation of cells of similar sizes. Furthermore, the addition of higher concentrations of anti-aggregation solutions could be employed in future experiments in an effort to alleviate some of the aggregation and clogging issues.

3.2 Microcontact Printing for Single Cell Capture

3.2.1 Introduction

Following the limitations exposed in section 3.1 on the physical size filtration approach to a 3-fold differentiation of WBCs in our microfluidic systems, an alternative approach, utilising the inherent affinity of cells and their antibodies was explored using microcontact printing. Antibodies were used in the work of Burger *et al.* to facilitate multiplexed bead-based immunoassays in the V-cup capture structure, enabling the capture and counting of individual cells of interest, Figure 3.36.

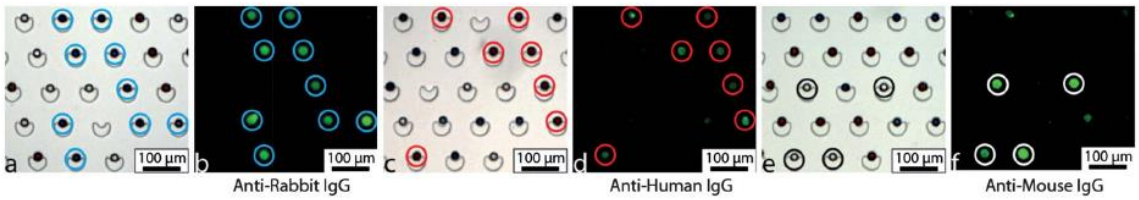

Figure 3.36: Image sequence of a multiplexed immunoassay using coloured beads. In Figures **(a)** and **(b)** the blue beads have been coated with rabbit IgG and will only display an affinity for anti-rabbit IgG in the analyte; in Figures **(c) & (d)** red beads previously coated in human IgG only have an affinity for human IgG; and in Figures **(e) & (f)** white beads previously coated in mouse IgG only exhibit an affinity for anti-human IgG.

This approach relies on the v-cup capture structure to capture similar sized beads of interest, with the fluorescent antibody facilitating particle identification and counting. The work in this thesis attempts to simplify this approach by using microcontact printing techniques to capture single cells of varying sizes, with specific antibody affinities, to antibody spots. This eliminates the need for additional steps within the microfluidic immunoassay, such as employing a secondary antibody for fluorescence measurements and carrying out further time-consuming washing steps. It was also envisaged that this antibody spot capture approach could potentially be implemented as a further cell selection step to refine the cell differentiation brought about by physical size filtration designs, such as those outlined in sections 3.1.2-3.1.6. A schematic of a possible design is illustrated in Figure 3.37.

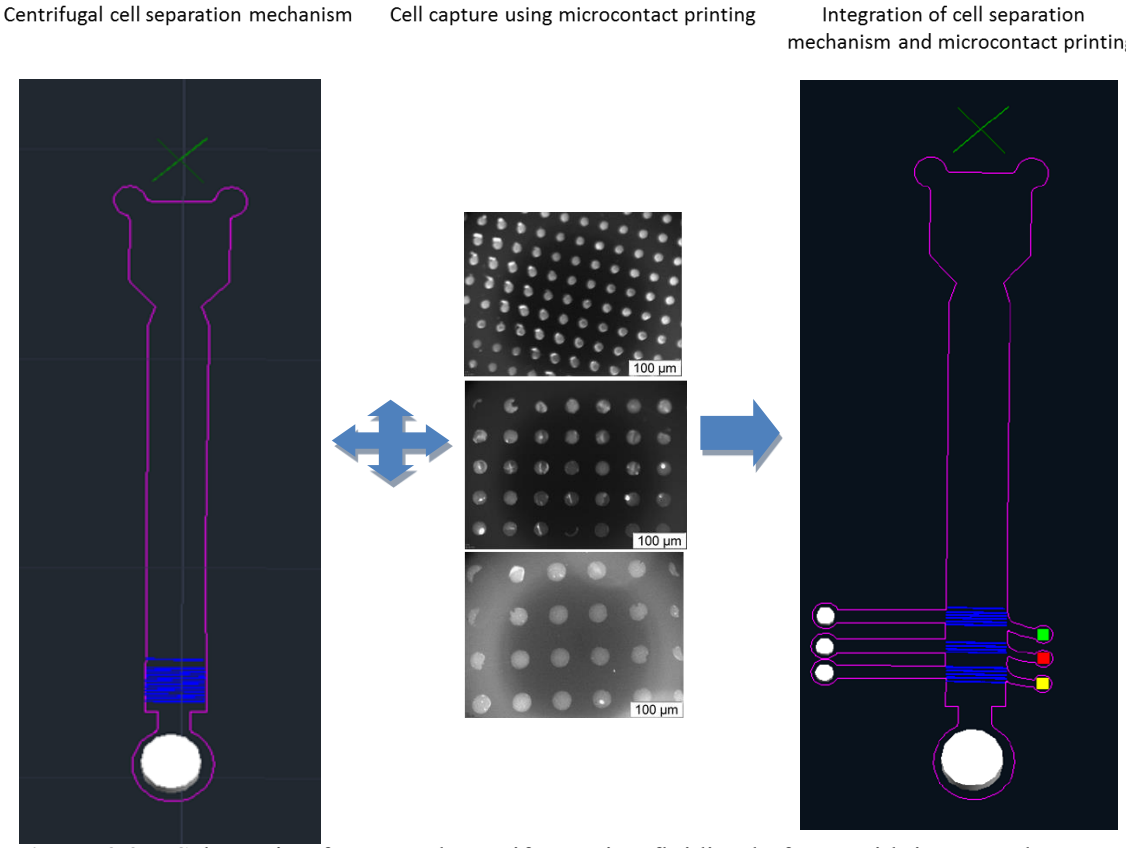

Figure 3.37: Schematic of proposed centrifuge-microfluidic platform, with integrated magnetic actuation for cell and microcontact printed capture spots. By enhancing the already magnetically actuated separation regimes outlined in section 3.1 by including more embedded magnets to the left of the separation structure, the separated cells could be directed into separate chambers on the right of the microfluidic disc. If microcontact printed antibody spots were created in these chambers, cells could be captured singly and counted easily using fluorescence detection.

With the aforementioned cell capture design in mind, the author set out to develop a suitable methodology for cell capture and differentiation using microcontact printing. The materials and methods used for microcontact printing in this thesis are outlined in section 2.2. The section that follows outlines the results of this antibody-based single-cell capture approach and discusses some of the main challenges associated with such a design.

3.2.2 Microcontact Printing on Functionalised Glass Slides for Single Cell Capture

In order to optimise the microcontact printing technique for WBCs, anti-Epcam was first used along with the Epcam-positive MCF-7 cell line, due to the strong known affinity between the two [220]. In all cases for the rest of this section, the number of cells in solution was on the order of $0.1 - 1 \times 10^6$ cells per ml of media, i.e. much greater than the number of antibody spots on each assay (~10^3 antibody spots per glass

slide). The photolithographic and soft lithography methods outlined in section 2.2 were used to create 10µm, 20µm, 30µm and 40µm PDMS stamps for microcontact printing, as illustrated in section 2.2.1. Initial experiments focussed on using (3-Aminopropyl)triethoxysilane (APTES) functionalised PMMA and PDMS substrates to facilitate microcontact printing with O_2 plasma treated PDMS stamps. The functionalisation of the substrates with APTES results in amine groups on the substrate, which allow the antibodies of interest to covalently bond to the surface [221]. The optimised process used to obtain the results below is outlined in section 2.2.2. 10µm, 20µm, 30µm and 40µm anti-Epcam spots were successfully stamped onto APTES coated glass slides, as illustrated in Figure 3.38.

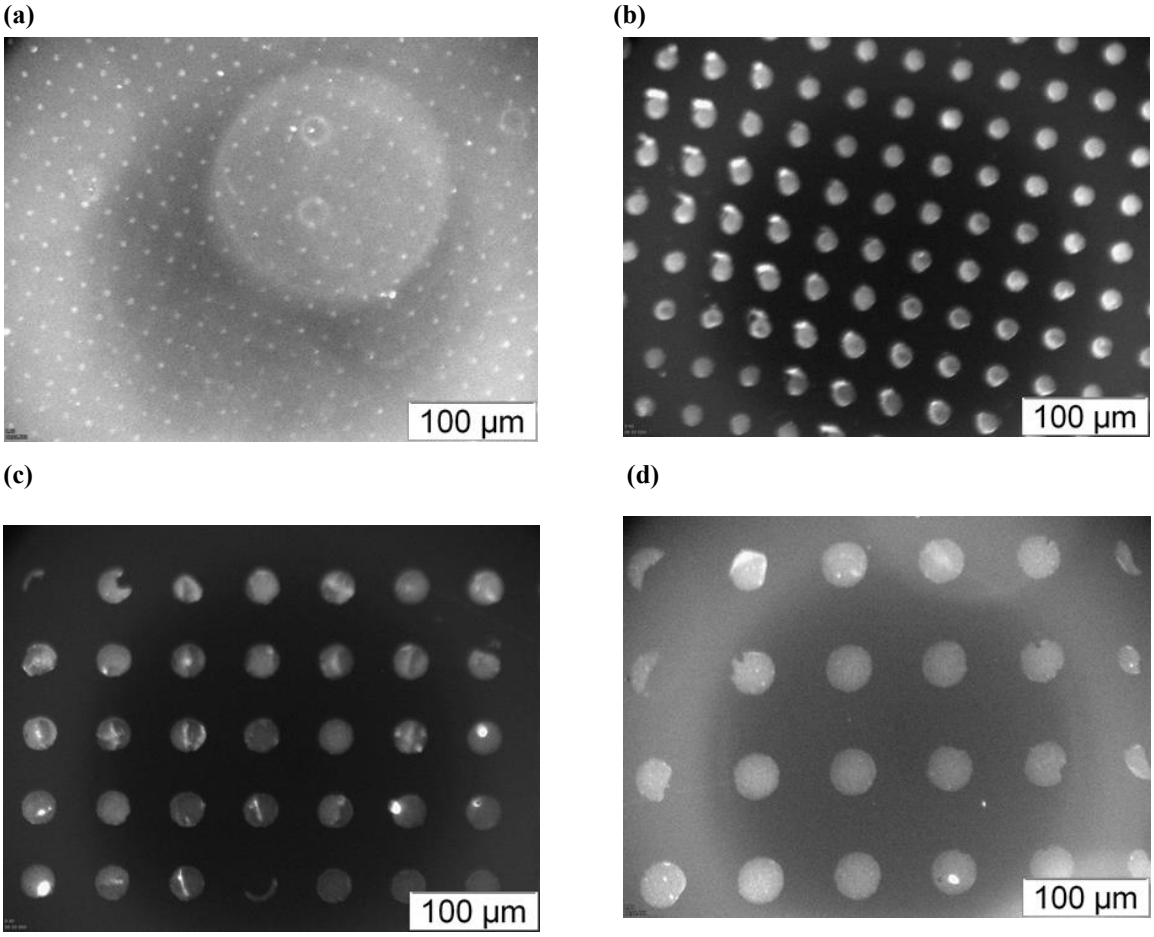

Figures 3.38 (a-d): 10µm, 20µm, 30µm and 40µm Anti-epcam printed spots on APTES functionalised glass. The glass substrates were exposed to O_2 plasma for 5 minutes at 1000mTorr, and then placed into a solution of 90% APTES in ethanol for 45 minutes. The substrates were then baked at 120^{o}C for 1 hour.

As expected the larger antibody spots demonstrate a stronger fluorescent signal compared to the 10µm spots, illustrating the challenge associated with single-cell capture at such scales. Unfortunately, following wash steps with PBS and a blocking step of 3% BSA in PBS the antibody spots had weakened significantly as illustrated in

Figure 3.39. This effect was evident over the course of repeated experiments and indicated either a poorly functionalised glass surface or poor adhesion of the antibody to the substrate.

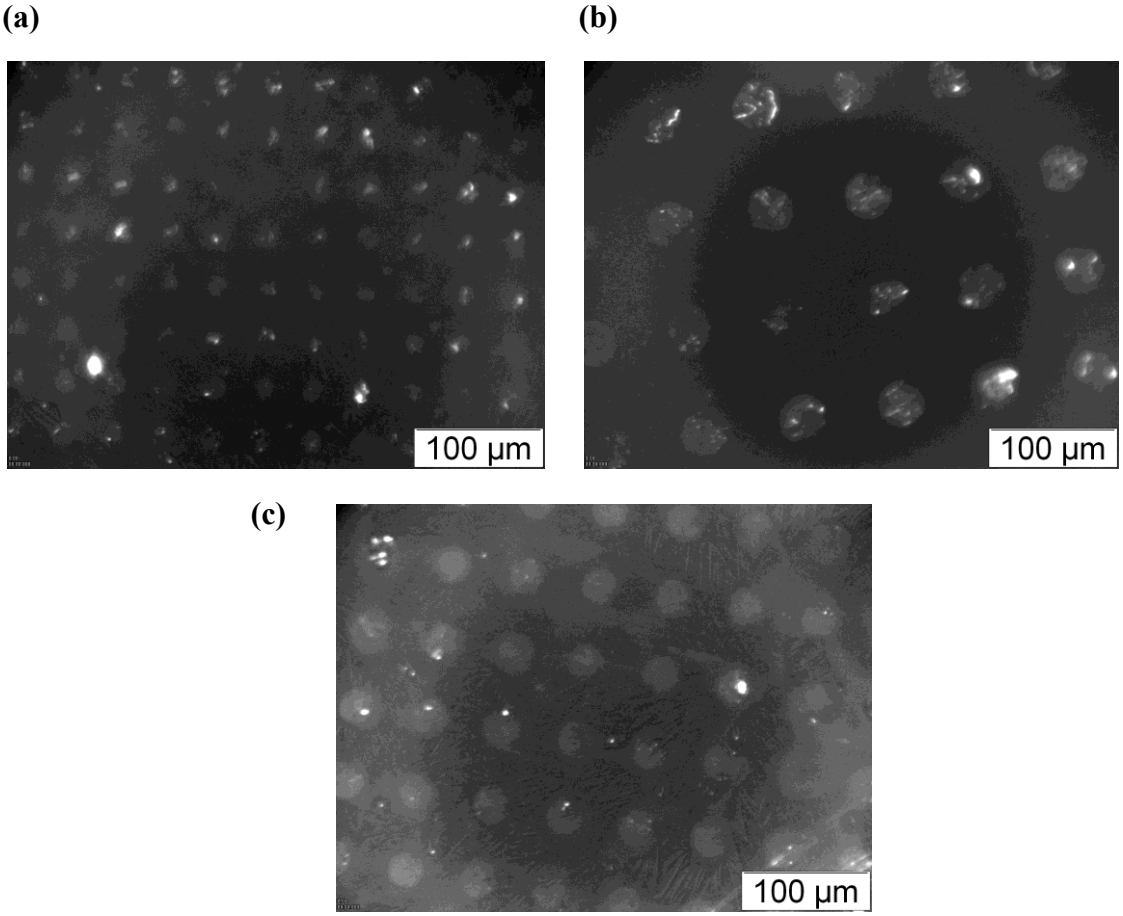

Figure 3.39: Fluorescent images of 20µm, 30µm and 40µm printed anti-Epcam spots following a wash step of 3% BSA in PBS. It is clear from the diminished fluorescent signal that the quantity of antibody remaining on the APTES coated glass slide has significantly decreased following the wash step. This resulted in an unreadable signal from the 10µm antibody spot sample and greatly reduced signals from the other samples.

While Figure 3.38 illustrates some clear antibody spots on the APTES coated slide, difficulties were found with delivering reproducible results, with some printing producing fluorescent spot signals of equivalent quality, while many others failed to do so. In addition, the issue of the antibody washing away from the functionalised glass slide persisted for repeated experiments (Figure 3.39). Following the addition of MCF-7 cells onto the glass slides as outlined in section 2.2, and post a wash step with 3% BSA in PBS, little cell adherence was observed. In addition, cell adhesion that was observed was sporadic as illustrated in Figure 3.40, indicating either non-specific binding and/or poor adhesion of the antibody spots.

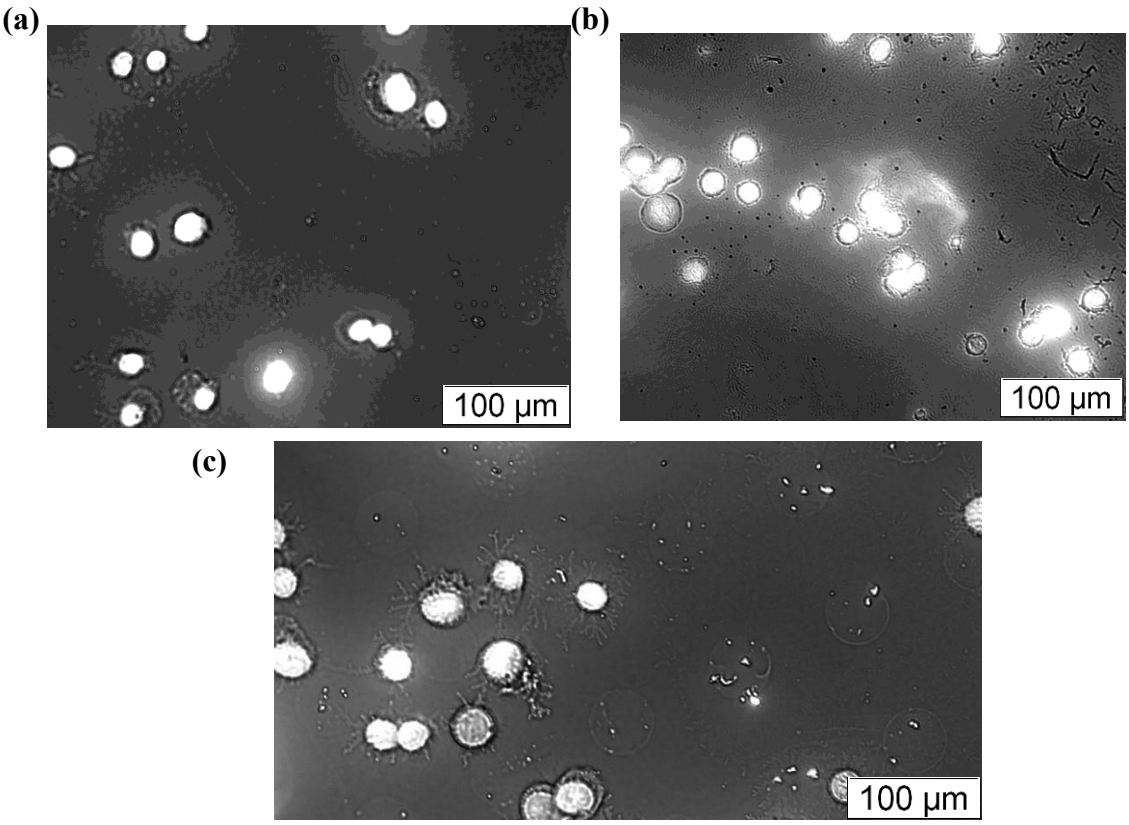

Figure 3.40: DAPI fluorescence microscope image of MCF-7 cells on APTES functionalised and anti-epcam microcontact printed glass substrates. Images **(a) – (c)** above were recorded following a blocking step with 3% BSA in PBS.

It was thought that the removal of the antibody spots following the wash step and the poor adhesion of the cells of interest could be due to issues with the APTES functionalization process. Although new APTES liquid was tested using the optimised functionalization protocol outlined in section 2.2, a white residue still developed on the treated glass slide, indicating inhomogenous functionalization. To investigate further, contact angle measurements were taken for an untreated glass slide, a slide functionalised with the original batch of APTES liquid and with the new APTES liquid. As can be seen from the results in Table 3.2, it is not clear whether the APTES liquid itself or the functionalization process was at the centre of the poor reproducibility of printing and the difficulties following the wash steps.

CA for untreated glass slide	**CA for original APTMS glass**	**CA for new APTMS glass**
58.3	42.6	55.0
62.8	42.6	54.1
69.2	47.3	55.8
64.7	44.1	55.0
61.5	45.0	54.5
65.5	37.2	51.1
65.9	57.5	54.3
63.8	54.0	61.1
68.0	55.0	68.1
	60.1	54.1
	58.0	62.1
	57.3	60.2
Average CA: 64.4	**50.1**	**57.1**
Standard Deviation: 3.3	**7.7**	**4.8**

Table 3.2 Table of contact angle (CA) values recorded for a clean, untreated glass slide, a glass slide functionalised with APTMS used in initial experiments and a glass slide functionalised with a newer batch of APTMS solution. Average contact angle values are recorded in the second last row, with standard deviation values in the final row of the Table.

While the average contact angles for both APTES coated slides lies within the expected range of APTES functionalised materials, a wide range of values were recorded for each surface – proving consistent with the hypothesis noted above that the slides were undergoing inhomogeneous functionalization. Due to these ongoing challenges poly-l-lysine functionalised slides were purchased (Sigma Aldrich) for microcontact printing experiments. As outlined by Seurynck-Servoss *et al.* in their research article on surface chemistries for antibody arrays[222], antibodies bind to poly-l-lysine through physical adsorption. While this method of attachment is not as strong as covalent bonding and has some potential to allow interaction of the capture antibody with reagents and blocking agents in solution[222], Seurynck-Servoss *et al.* concluded that such non-

covalent methods performed comparably to their covalent counterparts, with similar levels of assay performance and comparable limits of detection. Antibody printing was successfully carried out successfully on a number of substrates, including poly-l-lysine, using a GeSiM NanoPlotter 2.1 noncontact printer, with antigen binding observed for a number of ELISA sandwich assays [222].

As before, 20µm, 30µm and 40µm antibody spots were successfully printed onto poly-l-lysine coated slides, as illustrated in Figure 3.41. Unfortunately, printing of the 10µm spots was not as consistent as the other spot sizes. However, this was also the case for the APTES functionalised slides, as noted previously (Figure 3.38) by their fluorescence being narrowly greater than the background fluorescence measured.

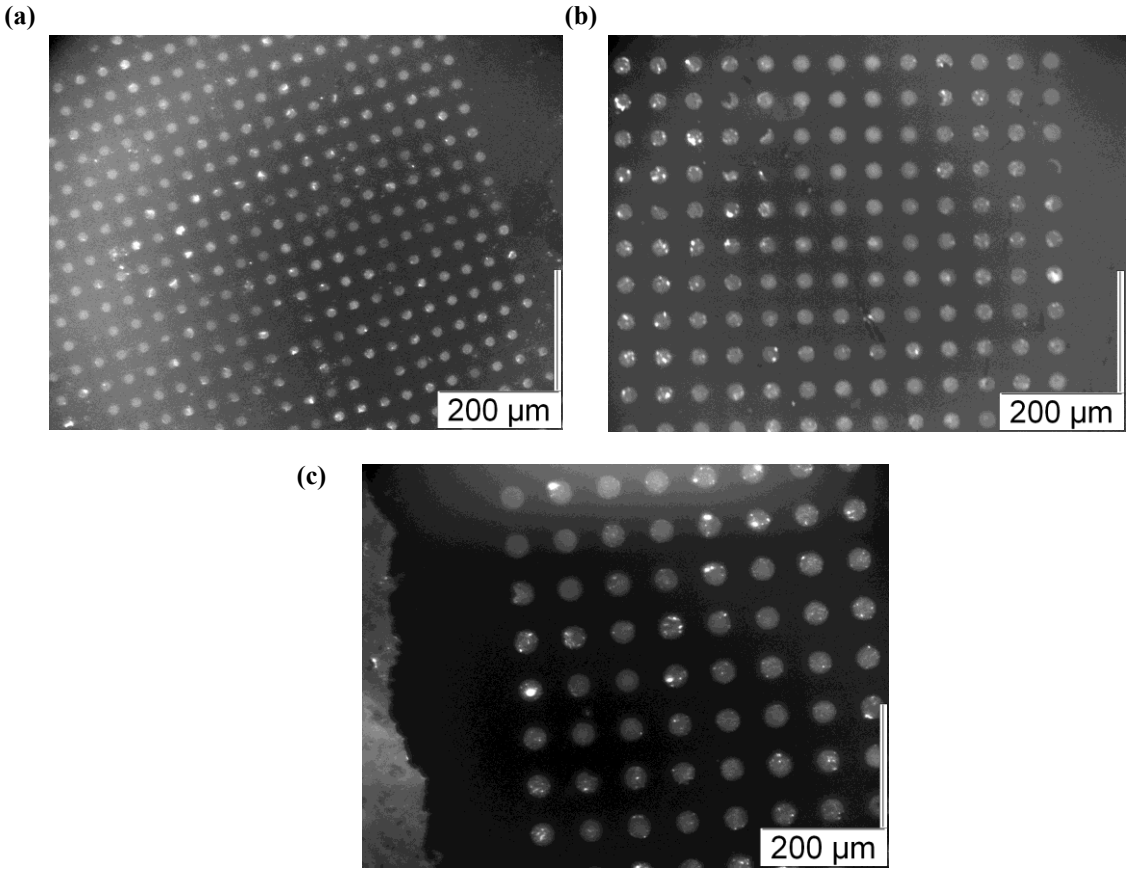

Figure 3.41 (a) – (c) FITC fluorescent microscopy images of 20µm, 30µm and 40µm antibody spots printed onto a poly-l-lysine functionalised glass substrate.

In order to assess the quantity of the antibody actually present on the poly-l-lysine surface, MCF-7 cells were added to the poly-l-lysine slides using a dropper, incubated for 10 minutes (while covered with foil to prevent photobleaching), and rinsed with PBS. This was done without carrying out any blocking step to see if cell adhesion and non-specific binding would take place. Cell adhesion was observed as expected, with

MCF-7 cells binding to 20µm antibody spots as illustrated in Figure 3.42.

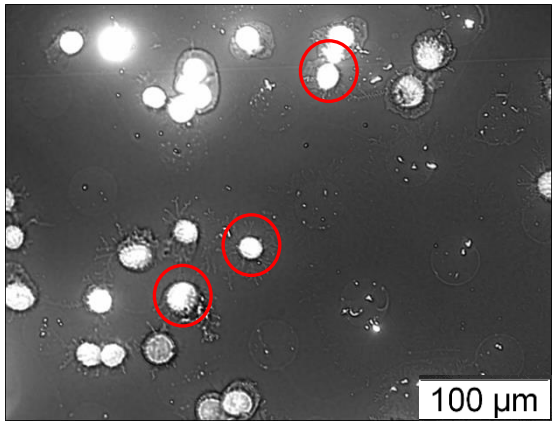

Figure 3.42 Image of MCF-7 cells adherent to antibody spots on poly-l-lysine coated slide. While targeted adhesion of cells to the antibody spots is clearly observed, there is also a good deal of non-specific binding as expected, due to the lack of a blocking buffer.

As the goal of this work was to develop a platform for single-cell adhesion onto antibody spots, and as cells adsorb easily onto poly-l-lysine surfaces, a blocking step must be carried out to ensure that cells of interest became trapped on the antibody spots and not sporadically throughout the glass slide. To this end, two blank slides were coated with 3% BSA in PBS and 5% Casein in PBS respectively. Following a wash step with PBS, the cells were added to the slide and a great deal of non-specific binding occurred, as illustrated in Figure 3.43.

(a) **(b)**

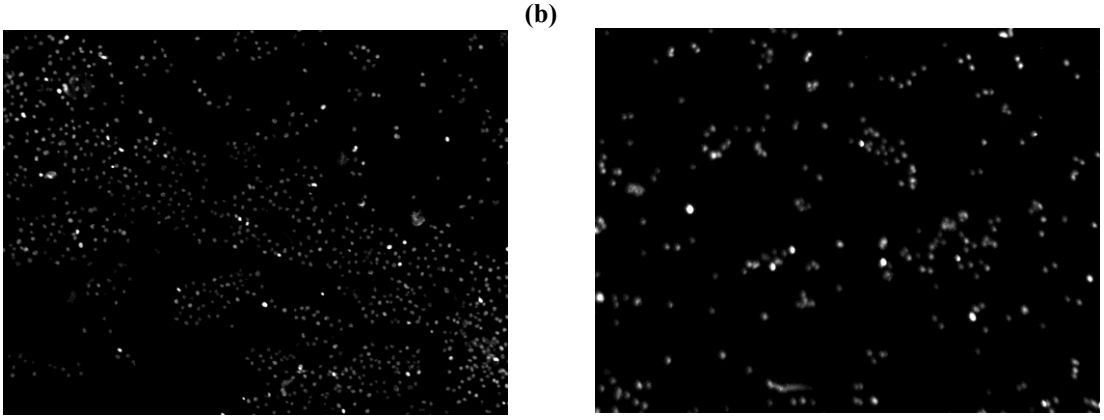

Figure 3.43: **(a) – (b)** DAPI fluorescent microscopy images MCF-7 cells on poly-l-lysine functionalised glass slides. **(a)** The first slide has been blocked with a solution of 5% casein in PBS while **(b)** was coated with 3% BSA in PBS. Slides were washed with the blocking solution, rinsed with PBS and then deionised water.

This non-specific binding was thought to be due to the length of the blocking time as the slides were initially just coated with the blocking solution using a dropper and then rinsed with PBS and deionised water. For all further blocking steps throughout this work, a blocking time of 15 minutes was used. This was done to ensure that the parts of

the slide that were not coated in antibody would not facilitate cell adhesion. In addition, due to the difficulties of creating a uniform solution of BSA in PBS using BSA salts, a concentration of 5% casein in PBS was favoured over BSA for all further blocking steps carried out for the duration of the project.

While repeated printing experiments continued to produce initially bright fluorescent antibody spots, indicating good adhesion of the anti-epcam to the poly-l-lysine surface, an unfortunate side effect of the newly established blocking and washing protocol was the washing away of significant quantities of the antibody spots. This effect mirrored that observed previously on the APTES coated slides. Therefore, in order to enhance cell to antibody adhesion and alleviate this effect, glutaraldehyde was added to the anti-Epcam solution, producing a 2% glutaraldehyde antibody solution. Glutaraldehyde was added to the antibody solution to promote adhesion of MCF-7 cells to the glutaraldehyde in the antibody spots, and to circumvent the issues caused by some of the antibody was being washed away during blocking and washing steps. Figure 3.44 that follows illustrates the results of microcontact printing and cell adhesion experiments on the 20μm and 30μm antibody/glutaraldehyde spots. Following a 15 minute blocking step with casein and wash step with PBS buffer, 1ml of MCF-7 cells in clean media was incubated on the microcontact printed surface as before, and rinsed gently using PBS.

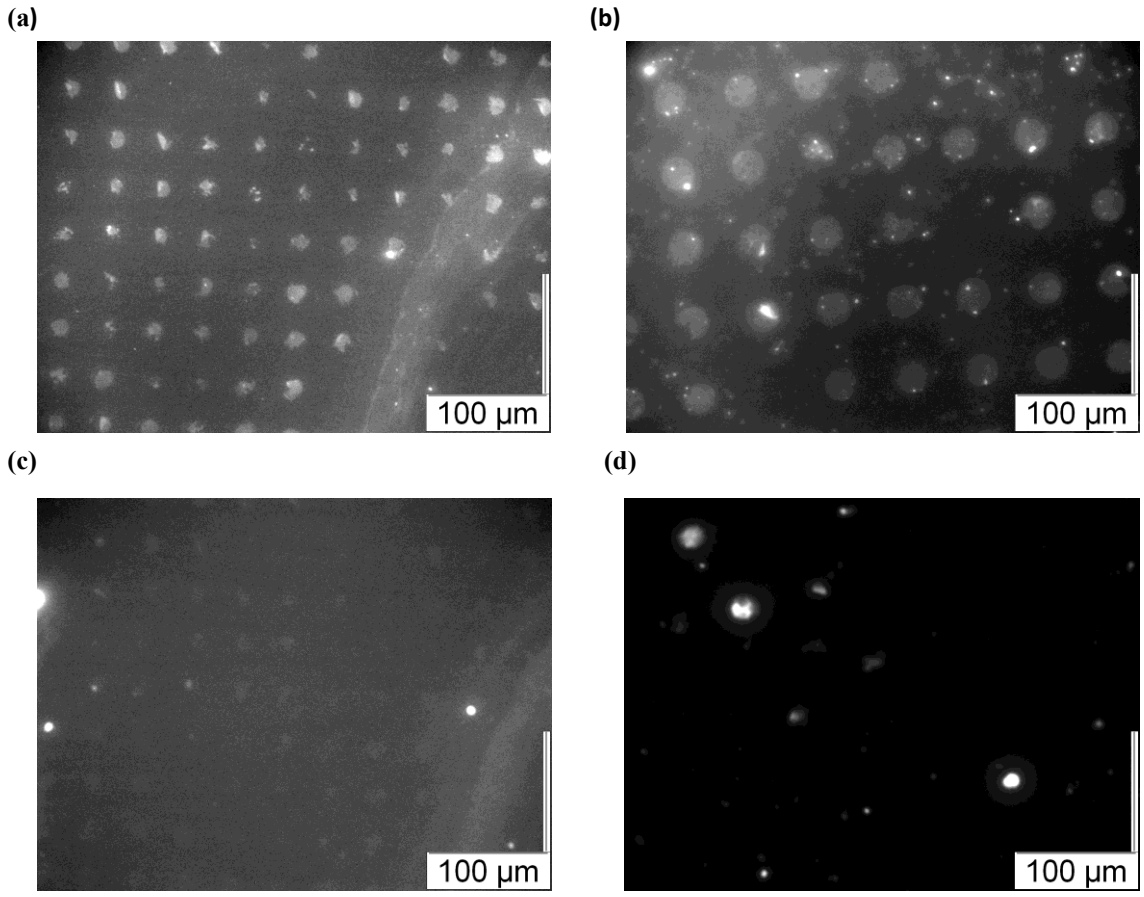

Figure 3.44: (a) & (b) Images of 20µm and 30µm spots using a FITC filter on a fluorescence microscope, with antibody spots clearly visible after blocking and washing steps. **(c) & (d)** DAPI filter images of the same spots following 10 minutes incubation with MCF-7 cells.

As illustrated in Figure 3.44 (a)-(b), while some antibody loss has occurred, antibody spots are still visible following blocking and washing steps. However, cell adhesion remains very low, as illustrated in (c)-(d), with just a few MCF-7 cells visible on the substrate. In an effort to improve upon the cell capture performance of this chip, a variety incubation protocols for the cells were tested including changes to the incubation time and temperature as illustrated in Figure 3.45.

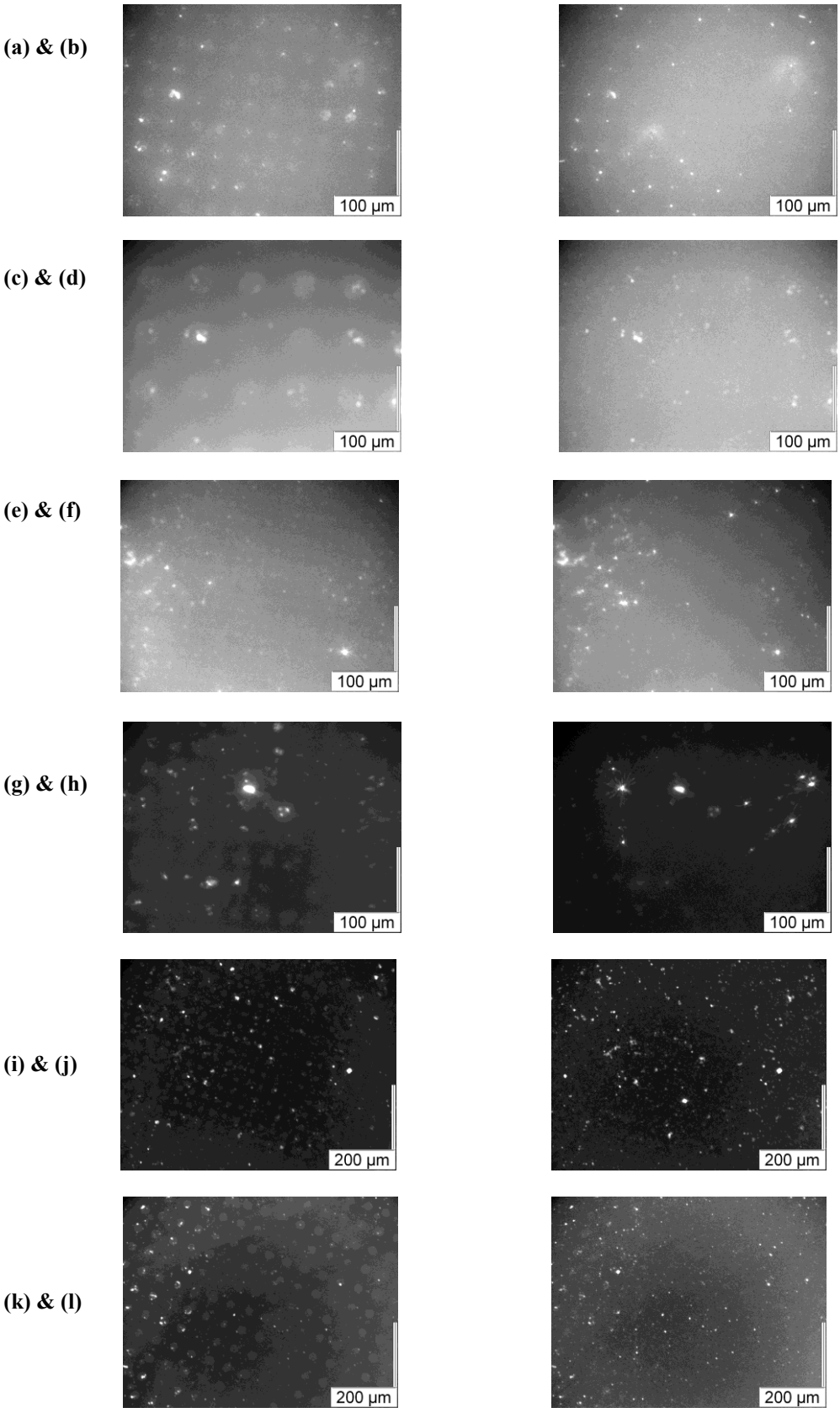

Figure 3.45 (a)-(l) FITC and DAPI filter fluorescence images of microcontact printed slides following cell incubation using a variety of protocols. **(a) - (d)** The cell incubation time was increased to 1 hour, with 10ml of fresh media added to the cell solution. The sample was covered with a lid and tin foil and placed on a rocker at a low rate to ensure that the cells are continuously flowing over the microcontact printed slide. **(e)-(h)** Images taken following the same protocol used in **(a) - (d)** but with the rocker temperature set to 37^{o}C to ensure that the cells are kept viable, before testing on the fluorescent microscope. **(i) - (l)** Images taken following the same protocol used in **(e) - (h)** but with an extended incubation time of 20 hours.

While some cell adhesion was observed above, it is clearly not specific to the antibody spots, nor is it sufficient cell adhesion to conclude that there is widespread non-specific binding of the cells. It appeared that there was a barrier to the cells either reaching or remaining on the antibody surface. A possible contributing factor was that the cells initially adhered to the antibody spots/poly-l-lysine glass surface but were being removed during the washing steps. Another alternative was that some of the cells were adhering to the petri dish containing the glass substrate rather than flowing across it, preventing cell adhesion to the antibody spots. The latter point was investigated by increasing the rocking rate to 70 during cell incubation to deduce if the cells were adhering to the petri dish and failing to flow across the glass surface. Figure 3.46 illustrates clumps of MCF-7 cells at the edge of the microcontact printed slide – indicating that the cells were getting stuck at the edge of the glass slide, contributing to the difficulties in promoting single cell adhesion.

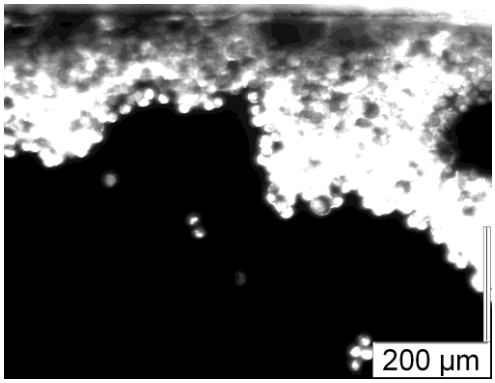

Figure 3.46 DAPI image of MCF-7 cells aggregating at the edge of the glass substrate.

Efforts to alleviate this issue were undertaken by creating a PDMS boundary around the microcontact printed area of the glass slide. A 25mm x 75mm slab of PDMS was cured and a "cell-containing" area was cut into its centre using a blade. This PDMS boundary was placed directly on top of the poly-l-lysine glass slide, isolating the cells on top of the active area of the functionalised slide as shown in Figure 3.47.

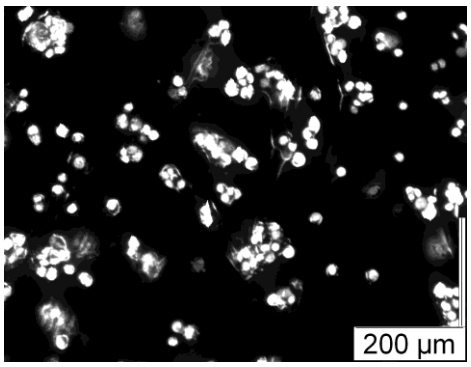

Figure 3.47 DAPI fluorescent microscopy image of MCF-7 cells on 20µm antibody spot microcontact printed slide. The cell incubation for this assay was carried out using a piece of PDMS to isolate the cells on the microcontact printed surface, and acts as a boundary to prevent cells from flowing onto the petri dish containing the substrate.

However, this cell isolation method was prone to leaking and should be replaced in future work with a more robust substitute, such as custom-built 3D-printed holder. In addition, despite the improvement in cell incubation on the substrate, issues with antibody loss following washing steps and poor selectivity in the cell adhesion remained, as can be seen in Figure 3.48, with fluorescence images taken from the same aforementioned substrate.

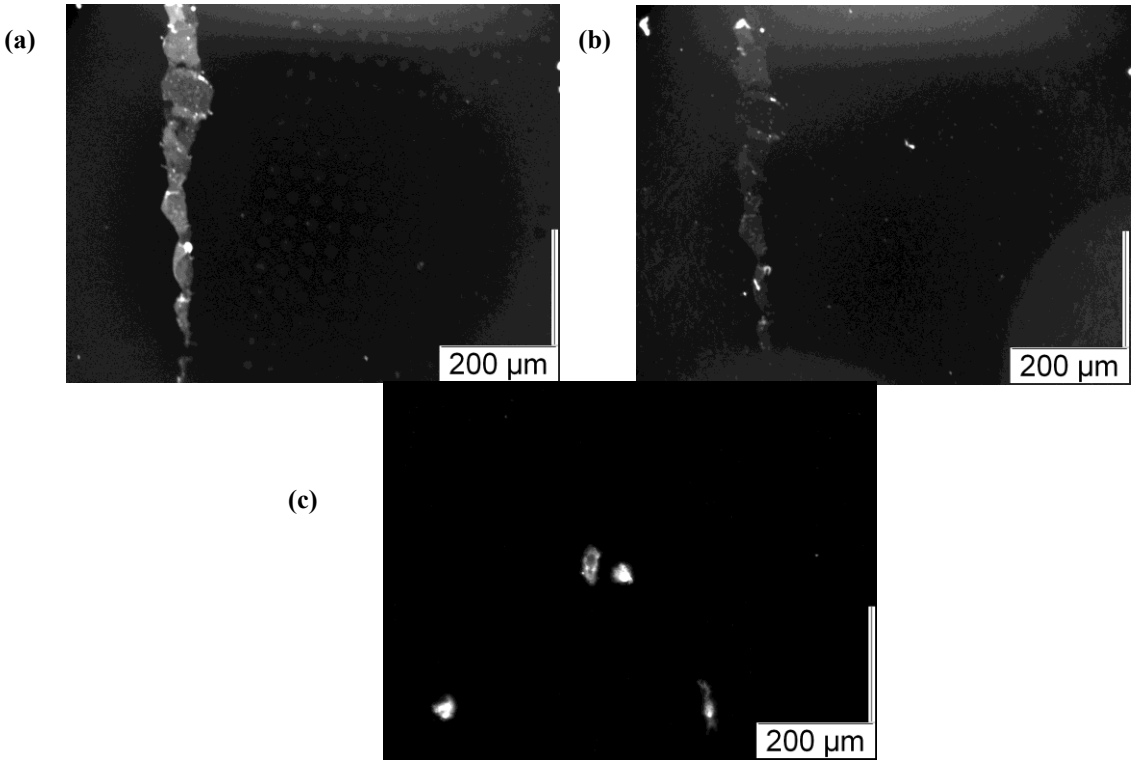

Figure 3.48 Images of 20µm spots recorded using a FITC filter on a fluorescence microscope **(a)** before **(b)** and after blocking and washing steps. The reduction in the quantity of antibody remaining on the spots is clearly visible in **(b)**, with **(c)** illustrating the absence of cell adhesion in the DAPI microscopy image.

Therefore, while the development of an appropriate incubation chamber/holder for the MCF-7 cells or other cells of interest would be an improvement on the scheme outlined above, issues still remain with poor antibody adhesion following any washing or blocking steps, which significantly slowed down the progress of this work towards a functional single-cell capture platform. While the direct contact printing method outlined above vastly simplifies the preparation of the substrates and the general microcontact printing protocol compared to the more commonly used schemes utilising the strong affinity between biotin and streptavidin etc., to anchor the antibody and cell to the surface [134], the functionalization of the substrate of interest is a key aspect of microcontact printing, particularly when blocking and washing steps are necessary to prevent non-specific binding of cells to the assay. In this work 10μm, 20μm, 30μm and 40μm anti-epcam spots were successfully stamped onto APTES functionalised and poly-l-lysine coated glass. Single cell adhesion onto 20μm microcontact printed spots was observed. However, with the results from this section in mind, future work should focus on determining whether the non-covalent bond between anti-epcam and poly-l-lysine, or APTES for that matter, is sufficient to ensure that enough antibody remains on the substrate following blocking and washing steps. This investigation should be carried out with a view towards testing some of the alternative surface functionalisation approaches outlined in section 1.2.2. In addition, challenges remain with printing 10μm antibody spots due to the manufacturing challenges associated with fabricating PDMS pillars at such resolutions. Deformation of the PDMS features and the aspect ratios involved indicate that printing spots on the order of ~20μm would be more feasible and may still be suitable for single cell capture, as illustrated in Figure 3.42. Finally, as the aforementioned samples were tested on glass substrates, the integration of microcontact printed substrates onto centrifugo-microfluidic platforms remains a key challenge for future work in this area. While glass can be integrated onto PDMS-based centrifugo-microfluidic chips, the weight and integration challenges associated with this could introduce disc wobble into a spinning platform. As PDMS is a challenging substrate for microcontact printing due to its deformability, hydrophobicity and porosity, microcontact printing has been successfully carried out on other polymers such as PMMA [137]. Microcontact printing onto PMMA could be used as one alternative approach to facilitate single-cell capture, integrating this technology onto low cost, disposable centrifugo-optofluidic platforms.

3.3 Optofluidic Detection

3.3.1 Raised and Embedded Waveguides on PMMA Substrates

The fabrication of embedded waveguides was tested for ease of integration of the sol-gel waveguides onto a PMMA/PDMS substrate. However, it was too difficult to locate the waveguide edge for coupling light into the waveguide, as both materials are transparent to the naked eye. Therefore, the "raised waveguide" approach was adopted, as the waveguides can be clearly seen, as in Figure 3.49.

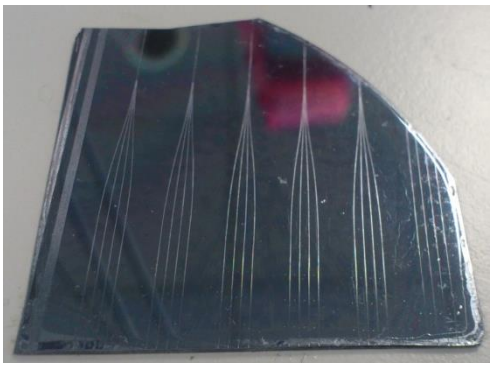

Figure 3.49: Series of diverging 10:2.5:0.25 hybrid sol-gel waveguides on a buffer layer of 10:2.1:0.25 sol-gel materials.

Coupling of 635nm light from an OELDD-200 30mW laser diode was achieved using an optical fiber and the 6μm x 6μm waveguides were fabricated using the approach outlined in section 2.3.2. A faint but visible near-field image of the light coupled into the waveguide was observed, similar to that obtained in the work of Oubaha *et al.*, as illustrated in Figure 3.50 [197]. While this provided a basis for the waveguiding properties of the sol-gel material, the main focus of this work was to integrate the waveguiding capabilities of the sol-gel with the excellent microfluidic properties of PDMS/PMMA to achieve a fully integrated device.

Figure 3.50: Near field image of 1.55μm light output from a 7μm x 7μm rectangular zirconium sol-gel waveguide [197]. This image is similar to that obtained in this work using a coupling wavelength of 625nm light into 6μm x 6μm waveguides.

The process for creating embedded waveguides was carried out on 1.5mm thick pieces of PMMA. As with the silicon substrates, the embedded waveguides were very difficult to locate to enable coupling to light into the waveguides and observing and output signal. Therefore the main focus of this work was shifted onto the "raised" waveguide approach outlined in section 2.3.2 for subsequent experiments. In addition, as the glass transition temperature of PMMA is ~105^{o}C[223] the 30 minute stabilisation step outlined in the sol-gel deposition process in section 2.3.2 lead to bowing of the PMMA initially, and was therefore reduced to 15 minutes for the rest of the project. Images of these raised waveguides can be seen in Figure 3.51.

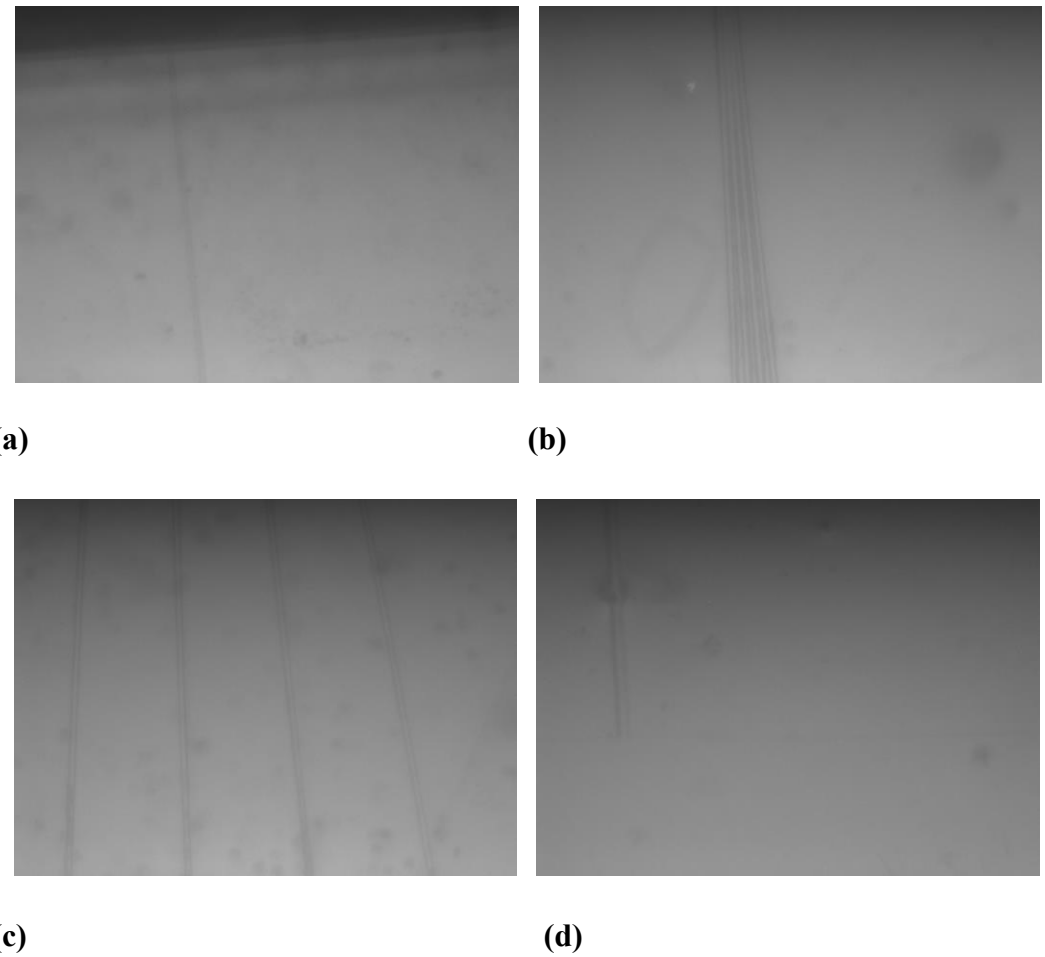

(a) **(b)**

(c) **(d)**

Figure 3.51 (a) – (d) Images of a diverging rectangular waveguide on a PMMA substrate. Images **(a) - (d)** illustrate the waveguide diverging into four separate waveguides, from the input at (a) to waveguide output at **(d)**.

While sol-gel waveguides were successfully integrated onto the planar PMMA substrate, one of the key challenges associated with this process was obtaining a suitable edge on the PMMA material for light coupling into the waveguide. A number of approaches were tested to obtain a suitably smooth edge. Firstly the Zing Epilog laser cutter was used on a variety of speed and power settings; between 12% power, 8%

speed and 15% power, 10% speed, to cut through the PMMA and obtain a smooth edge for optical coupling. Both settings resulted in edges that enabled weak coupling of light into and out of the sol-gel waveguides. However, as illustrated in Figure 3.52, the edges achieved in this approach were too rough for efficient coupling of light for analytical applications.

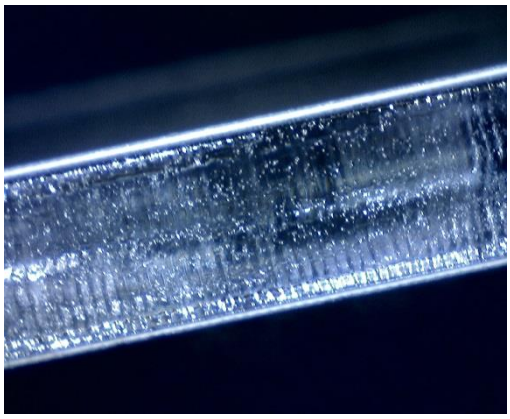

Figure 3.52: Side-on image of PMMA edge following machining on Epilog Zing laser at a power setting of 15% and a speed setting of 10%. Despite trying a number of different speed:power ratios, the edge quality of the PMMA was not improved.

A 100W MicroMaster Optec laser system was used as an alternative but this also proved unsuccessful in obtaining a suitably smooth edge when tested on the optical fiber light coupling set up. In addition, this technique also removed some of the waveguides from the edge of the PMMA, due to the high powers used.

As the machining facilities available to cut the PMMA provided too rough an edge for the optofluidic applications above, some further mechanical smoothing techniques were employed, Diamond polishes with 3µm, 6µm and 9µm diamond particles and silicon carbide papers were used to polish the edges of the PMMA, resulting in improved smoothness as illustrated in Figure 3.53 that follows.

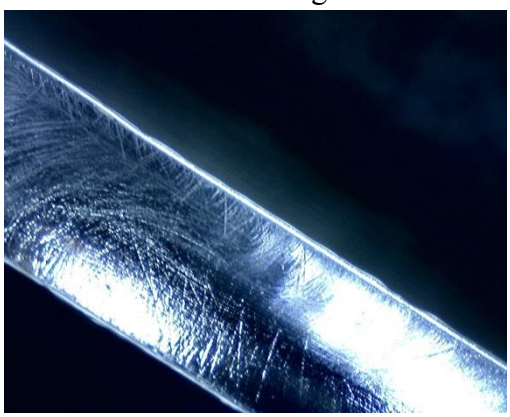

Figure 3.53: Image of PMMA edge following hand smoothing with a selection of diamond polishes. This surface is a vast improvement on that of Figure 3.52 above but still retains a number of notable smaller scratches, making wave guiding applications challenging.

Unfortunately the edge of the PMMA retains quite a “cloudy” appearance, indicating smaller but widespread scratches across the PMMA edge. As mechanical methods failed to produce the desired surface, a chemical treatment was tested to improve the optical quality of the PMMA edge. Chloroform was applied to PMMA in both its vapour and liquid form to soften and reflow the plastic, with the aim of producing a smooth plastic edge. Chloroform liquid (Sigma Aldrich) was applied directly to the PMMA edge using a dropper; however, this method was not easily controllable or sufficiently effective to produce a uniform and smooth edge. Similarly submerging the PMMA edge in chloroform liquid resulted in an uneven softening and flowing of the PMMA, with limited control over the morphology of the PMMA edge for waveguiding applications. Furthermore the vapour exposure method outlined by Ogilvie *et al.* [224] was not strong enough to eliminate the scratches produced by the Epilog Laser machining referred to previously.

As can be seen from the results and discussion outlined previously, some notable first steps have been taken towards the integration of the high resolution, highly tunable optical waveguiding sol-gel technology, and inexpensive and easily fabricated PMMA material. High quality waveguides have been successfully transferred from the easily cleaved and robust silicon substrate to a PMMA substrate, without any notable damage to the PMMA. However, the significant challenge of producing of a suitable edge on PMMA and alternative polymeric materials remains. Further work will be needed to tackle or circumvent this issue, particularly if sol-gel materials are to become a driving force behind the widespread development of centrifugo-optofluidic platforms. A more detailed discussion of future work in this area will be outlined in chapter 4.

The preceding chapter outlines the results, analysis and associated errors of the author’s work on developing a sample-to-answer 3-fold differential white blood cell analysis assay on a centrifugally driven platform. Biomimetic particles of 5µm, 10µm and 20µm in size were used to model the performance of lymphocyte, eosinophil and neutrophil cells within the novel physical size filtration devices, while under the influence of centrifugal forces. Some single bead capture was observed, although additional work is needed to address the issues with the optimisation of fabrication methods, particle clogging and the differentiation of beads/cells which have size differences of only a few microns. In addition to the progress made through testing a variety of physical size filtration designs, the possible applications associated with utilising magnetic actuation to declog and actuate such polymeric centrifugal platforms was clearly demonstrated. As an alternative approach, microcontact printing was utilised

on functionalised glass substrates to test the viability of using this technique within a centrifugal platform for single cell capture and analysis. The results indicated that while improved surface functionalisation may increase the chances of single cell capture on spots of 10µm or 20µm, it is in fact far more likely that larger spot of 30µm or 40µm will be necessary to promote the capture of target bioparticles. Future work will also determine whether antibody-cell adhesion is enough to withstand the forces brought about by centrifugation when removing waste liquids and carrying out wash steps. Finally, sol-gel materials were successfully transferred from standard silicon wafers onto PMMA substrates. However, as referred to previously, issues remain with developing a suitable high quality input and output surface for the successful coupling of light into and out of the optical waveguides for cell interrogation and detection. A more detailed summary of the work undertaken in this thesis, as well as future avenues for development, will be outlined in the chapter that follows.

Chapter 4: Summary and Future Work

4.1 Summary of Work Presented

This work has laid the foundations towards differentiation and detection components for an inexpensive, compact and easy to use integrated centrifugal device, for the 3-fold differentiation of WBCs from whole blood. A number of novel approaches utilising centrifugal actuation and arrays of physical filters and traps were tested, with some successful differentiation and single-bead trapping observed on a number of designs. While the degree of differentiation or single-bead trapping was not sufficient to lead to comprehensive testing with cells, a number of useful research outcomes resulted from the above work. In sections 3.1.2 and 3.1.3 10μm and 5μm beads were caught singly and with double occupancy in 6μm V-shaped cups. In addition, 20μm beads were captured singly in 15μm cups. Unfortunately, as beads of differing sizes were captured in the various sized V-Cup traps, it appears that this approach is not suitable for cell differentiation. In addition, while the filter design outlined in section 3.1.2 did show some improvement on the clogging issues experienced with the V-Cup traps, the fabrication of these small features proved very challenging for the SU-8 mould/PDMS replica approach. In sections 3.1.4-3.1.6, 10μm particles were captured in both the parabolic and multiple-obstacle architecture structures. While some of these beads were caught singly, particularly after shake mode or magnetic actuation, some form of actuation mechanism was necessary to de-clog the structures. Fabrication issues faced in earlier experiments were also relevant for these novel structures, with 5μm particles passing through all MOA obstacle gaps, including the stopping filters at the end of the device. In fact, the unpredictability of the gaps between geometric filters and traps in the devices tested in section 3.1 remains one of the main stumbling blocks in this work. Nevertheless, a great deal of promising work went into the ongoing issues with clogging in all designs in this thesis. “Shake mode” and magnetic actuation steps were tested extensively, with the magnetic actuation approach, in particular, showing great promise for applications to other platforms. Magnetic actuation offers another method of flow control on centrifugal platforms, is cost effective, easy to integrate on-disc and can be used at multiple points on a platform to actuate flow in a number of directions.

As illustrated in section 3.1, microcontact printed spots of 10μm, 20μm, 30μm and 40μm in diameter were successfully printed onto functionalised glass substrates,

with some single cell adhesion of MCF-7 cells observed. Issues persisted with substrate functionalisation, and suitable blocking steps will need to be addressed before this approach becomes a reliable one for single-cell capture on the proposed platform.

In terms of optical detection approaches, sol-gel waveguides hold a great degree of promise for future centrifgo-optofluidic applications. This work successfully accomplished the transition of photocurable hybrid sol-gel materials from the typically used silicon substrate to an inexpensive and highly versatile PMMA alternative. While light was successfully coupled into and out of the sol-gel waveguides deposited on the PMMA platform, ongoing issues with the optical surface quality of the edge of the PMMA remained.

4.2 Future Work

Future work on the methods and results outlined in this thesis would focus on developing a more consistent and effective bead, and therefore cell, separation method. While Burger *et al.* [129-132] demonstrated effective bead and cell differentiation on their V-Cup platform, this was not performed with mixtures of different sized beads. Cell differentiation was carried out on beads and cells of similar size, with fluorescently tagged antibodies enabling optical detection and differentiation. The systems outlined in section 3.1 of this thesis relied solely on physical size filtration to differentiate between beads and, eventually cells, in an effort to reduce the complexity and number of assay steps on the platform. However, as highlighted by the work of Kim *et al.* [213], there is a great deal of overlap in size between a number of cells including WBCs and RBCs. Therefore, the addition of microcontact printing steps or other immuno-targeting steps to differentiate between cells could help strengthen the approaches taken above to produce a 3-fold differential platform. As noted previously, the magnetic actuation scheme employed in sections 3.1.5-3.1.7 could again be used on a newer platform to aid de-clogging and to actuate differentiated cells into outlet chambers, perhaps containing V-Cup or similar geometric traps.

For future work on the optical detection components, clearly there is much room for the further integration of sol-gel wave guiding platforms on PMMA substrates. While challenges were encountered in producing a surface with sufficient optical quality to couple light into and out of the sol-gel waveguides on the PMMA surface, this fabrication challenge may be overcome using other solvents to reflow the plastic or with better machining capabilities. Additionally, different plastic substrates that can be used,

which are more easily tailored to have a high-quality optical edge. The possibilities of integrating a material like photocurable sol-gels, which can produce optical and microfluidic features of high resolution using standard photolithographic methods, on centrifugally driven microfluidic platforms are vast. The development of such a platform would be a major step towards the fully integrated lab-on-a-chip platform outlined in section 4.3 that follows.

4.3 Future Work for Cell Analysis on Centrifugal Microfluidic Platforms

The field of microfluidics is ever-changing, with centrifugal microfluidics providing a huge step forward towards the full integration of sample preparation, assaying and detection components on a single, inexpensive polymeric chip. Chin *et al.* have recently outlined the current level of commercialisation of point-of-care microfluidic devices, [36] including a discussion of the challenges associated with making this commercialisation a reality, including full device integration, market sentiment, lack of financing, mass production and device accuracy. Clearly the development of centrifugally driven devices in the near future will focus primarily on the full integration of all sample-to-answer unit operations, complete with miniaturised and inexpensive detection and imaging capabilities. As can be seen from the discussion of the literature in chapter 1 of this thesis, a great deal of unit operations can now be carried out on centrifugal microfluidic platforms such as blood metering, purification and cell separation, capture and analysis. However, the final jump to fully integrate all of the above operations, along with facilitating reagent storage and delivery on a single platform remains elusive. In particular the development of optofluidics provides new hope towards the integration of optical detection components on chip, as well as providing a solution to detection and imaging in low resource settings, as a result of interfacing with cell phones and standard optical disc drives. Finally, the diagnostic performance levels of future microfluidic assays must compete favourably and even surpass those of current laboratory standards to become commonplace in the biomedical diagnostics sphere.

Chapter 5: Bibliography and Appendix

5.1 Bibliography

1. Yarnell, J. W., Baker, I. A., Sweetnam, P. M., Bainton, D., O'brien, J. R., Whitehead, P., & Elwood, P. C. (1991). Fibrinogen, viscosity, and white blood cell count are major risk factors for ischemic heart disease. The Caerphilly and Speedwell collaborative heart disease studies. *Circulation*, *83*(3), 836-844.
2. Kannel, W. B., Anderson, K., & Wilson, P. W. (1992). White blood cell count and cardiovascular disease. *JAMA: the journal of the American Medical Association*, *267*(9), 1253-1256.
3. Grimm Jr, R. H., Neaton, J. D., & Ludwig, W. (1985). Prognostic importance of the white blood cell count for coronary, cancer, and all-cause mortality. *JAMA: the journal of the American Medical Association*, *254*(14), 1932-1937.
4. Vozarova, B., Weyer, C., Lindsay, R. S., Pratley, R. E., Bogardus, C., & Tataranni, P. A. (2002). High white blood cell count is associated with a worsening of insulin sensitivity and predicts the development of type 2 diabetes. *Diabetes*, *51*(2), 455-461.
5. Tong, P. C., Lee, K. F., So, W. Y., Ng, M. H., Chan, W. B., Lo, M. K., Chan, N. N., & Chan, J. C. (2004). White blood cell count is associated with macro-and microvascular complications in Chinese patients with type 2 diabetes. *Diabetes care*, *27*(1), 216-222.
6. Elkind, M. S., Cheng, J., Boden-Albala, B., Paik, M. C., & Sacco, R. L. (2001). Elevated white blood cell count and carotid plaque thickness the Northern Manhattan stroke study. *Stroke*, *32*(4), 842-849.
7. Brown, D. W., Giles, W. H., & Croft, J. B. (2001). White blood cell count: an independent predictor of coronary heart disease mortality among a national cohort. *Journal of clinical epidemiology*, *54*(3), 316-322.
8. Cheng, X., Irimia, D., Dixon, M., Sekine, K., Demirci, U., Zamir, L., Tompkins, R. G., Rodriguez, W., & Toner, M. (2007). A microfluidic device for practical label-free CD4+ T cell counting of HIV-infected subjects. *Lab on a Chip*, *7*(2), 170-178.
9. Masur, H., Ognibene, F. P., Yarchoan, R., Shelhamer, J. H., Baird, B. F., Travis, W., Suffrendini, A. F., Deyton, L., Kovacs, J. A. Falloon, J., Davey, R., Polis, M., Metcalf, J., Baseler, M., Wesley, R., Gill, V. J., Fauci, A. S., & Lane, C. (1989). CD4 counts as predictors of opportunistic pneumonias in human immunodeficiency virus (HIV) infection. *Annals of internal medicine*, *111*(3), 223-231.
10. Hogg, R. S., Yip, B., Chan, K. J., Wood, E., Craib, K. J., O'Shaughnessy, M. V., & Montaner, J. S. (2001). Rates of disease progression by baseline CD4 cell count and viral load after initiating triple-drug therapy. *JAMA: the journal of the American Medical Association*, *286*(20), 2568-2577.
11. Bunn, H. F. (1997). Pathogenesis and treatment of sickle cell disease. *New England Journal of Medicine*, *337*(11), 762-769.
12. Harris, T. G., Burk, R. D., Palefsky, J. M., Massad, L. S., Bang, J. Y., Anastos, K., Minkoff, H., Hall, C. B., Bacon, M. C., Levine, A. M., Watts, D. H., Silverberg, M. J., Xue, X., Melnick, S.L., & Strickler, H. D. (2005). Incidence of cervical squamous intraepithelial lesions associated with HIV serostatus, CD4 cell counts, and human papillomavirus test results. *JAMA: the journal of the American Medical Association*, *293*(12), 1471-1476.
13. Nyfeler, B., & Pichler, W. J. (1997). The lymphocyte transformation test for the

diagnosis of drug allergy: sensitivity and specificity. *Clinical & Experimental Allergy*, *27*(2), 175-181.
14. Christopoulos, A. (2002). Allosteric binding sites on cell-surface receptors: novel targets for drug discovery. *Nature Reviews Drug Discovery*, *1*(3), 198-210.
15. Verpoorte, E., & De Rooij, N. F. (2003). Microfluidics meets MEMS. *Proceedings of the IEEE*, *91*(6), 930-953.
16. Reyes, D. R., Iossifidis, D., Auroux, P. A., & Manz, A. (2002). Micro total analysis systems. 1. Introduction, theory, and technology. *Analytical chemistry*, *74*(12), 2623-2636.
17. Manz, A., Graber, N., & Widmer, H. M. (1990). Miniaturized total chemical analysis systems: a novel concept for chemical sensing. *Sensors and actuators B: Chemical*, *1*(1), 244-248.
18. Whitesides, G. M. (2006). The origins and the future of microfluidics. *Nature*, *442*(7101), 368-373.
19. Ohno, K. I., Tachikawa, K., & Manz, A. (2008). Microfluidics: applications for analytical purposes in chemistry and biochemistry. *Electrophoresis*, *29*(22), 4443-4453.
20. Becker, H., & Locascio, L. E. (2002). Polymer microfluidic devices. *Talanta*, *56*(2), 267-287.
21. Stroock, A. D., & Whitesides, G. M. (2002). Components for integrated poly (dimethylsiloxane) microfluidic systems. *Electrophoresis*, *23*, 3461-3473.
22. Duffy, D. C., McDonald, J. C., Schueller, O. J., & Whitesides, G. M. (1998). Rapid prototyping of microfluidic systems in poly (dimethylsiloxane). *Analytical chemistry*, *70*(23), 4974-4984.
23. Myers, F. B., & Lee, L. P. (2008). Innovations in optical microfluidic technologies for point-of-care diagnostics. *Lab on a Chip*, *8*(12), 2015-2031.
24. Sia, S. K., & Kricka, L. J. (2008). Microfluidics and point-of-care testing. *Lab on a Chip*, *8*(12), 1982-1983.
25. Tüdős, A. J., Besselink, G. A., & Schasfoort, R. B. (2001). Trends in miniaturized total analysis systems for point-of-care testing in clinical chemistry. *Lab on a Chip*, *1*(2), 83-95.
26. Chin, C. D., Linder, V., & Sia, S. K. (2012). Commercialization of microfluidic point-of-care diagnostic devices. *Lab on a Chip*, *12*(12), 2118-2134.
27. Ducrée, J., Haeberle, S., Lutz, S., Pausch, S., Von Stetten, F., & Zengerle, R. (2007). The centrifugal microfluidic bio-disk platform. *Journal of Micromechanics and Microengineering*, *17*(7), S103.
28. Madou, M., Zoval, J., Jia, G., Kido, H., Kim, J., & Kim, N. (2006). Lab on a CD. *Annu. Rev. Biomed. Eng.*, *8*, 601-628.
29. Nolte, D. D. (2009). Invited Review Article: Review of centrifugal microfluidic and bio-optical disks. *Review of Scientific Instruments*, *80*, 101101.
30. Haeberle, S., Brenner, T., Zengerle, R., & Ducrée, J. (2006). Centrifugal extraction of plasma from whole blood on a rotating disk. *Lab on a Chip*, *6*(6), 776-781.
31. Holdich, R. G. (2002). *Fundamentals of particle technology*. Midland Information Technology and Publishing.
32. Burger, R., Kirby, D., Glynn, M., Nwankire, C., O'Sullivan, M., Siegrist, J., Kinahan, D., Aguirre, G., Kijanka, G., Gorkin, R., & Ducrée, J. (2012). Centrifugal microfluidics for cell analysis. *Current Opinion in Chemical Biology*.
33. Burger, R., & Ducrée, J. (2012). Handling and analysis of cells and bioparticles on centrifugal microfluidic platforms. *Expert Review of Molecular Diagnostics*, *12*(4), 407-421.

34. Gorkin, R., Park, J., Siegrist, J., Amasia, M., Lee, B. S., Park, J. M., Kim, J., Kim, H., Madou, M., & Cho, Y. K. (2010). Centrifugal microfluidics for biomedical applications. *Lab on a Chip*, *10*(14), 1758-1773.
35. Steigert, J., Brenner, T., Grumann, M., Riegger, L., Lutz, S., Zengerle, R., & Ducrée, J. (2007). Integrated siphon-based metering and sedimentation of whole blood on a hydrophilic lab-on-a-disk. *Biomedical microdevices*, *9*(5), 675-679
36. Li T., Fan Y., Chenga Y. & Yang J. (2013) An electrochemical Lab-on-a-CD system for parallel whole blood analysis *Lab on a Chip***,**13**, 2634**-2640
37. Zhang, X. B., Wu, Z. Q., Wang, K., Zhu, J., Xu, J. J., Xia, X. H., & Chen, H. Y. (2012). Gravitational sedimentation induced blood delamination for continuous plasma separation on a microfluidics chip. *Analytical chemistry*, *84*(8), 3780-3786.
38. Godino, N., Gorkin III, R., Linares, A. V., Burger, R., & Ducrée, J. (2013). Comprehensive integration of homogeneous bioassays via centrifugo-pneumatic cascading. *Lab on a Chip*, *13*(4), 685-694.
39. Amasia, M., & Madou, M. (2010). Large-volume centrifugal microfluidic device for blood plasma separation. *Bioanalysis*, *2*(10), 1701-1710.
40. Lee, S. K., Yi, G. R., & Yang, S. M. (2006). High-speed fabrication of patterned colloidal photonic structures in centrifugal microfluidic chips. *Lab on a Chip*, *6*(9), 1171-1177.
41. Garcia-Cordero, J. L., Barrett, L. M., O'Kennedy, R., & Ricco, A. J. (2010). Microfluidic sedimentation cytometer for milk quality and bovine mastitis monitoring. *Biomedical microdevices*, *12*(6), 1051-1059.
42. Gong, M., Bohn, P. W., & Sweedler, J. V. (2009). Centrifugal sedimentation for selectively packing channels with silica microbeads in three-dimensional micro/nanofluidic devices. *Analytical chemistry*, *81*(5), 2022-2026.
43. Cho, Y. K., Lee, J. G., Park, J. M., Lee, B. S., Lee, Y., & Ko, C. (2007). One-step pathogen specific DNA extraction from whole blood on a centrifugal microfluidic device. *Lab on a Chip*, *7*(5), 565-573.
44. Park, J. M., Cho, Y. K., Lee, B. S., Lee, J. G., & Ko, C. (2007). Multifunctional microvalves control by optical illumination on nanoheaters and its application in centrifugal microfluidic devices. *Lab on a Chip*, *7*(5), 557-564.
45. Steigert, J., Grumann, M., Brenner, T., Riegger, L., Harter, J., Zengerle, R., & Ducree, J. (2006). Fully integrated whole blood testing by real-time absorption measurement on a centrifugal platform. *Lab on a Chip*, *6*(8), 1040-1044.
46. Mark, D., Metz, T., Haeberle, S., Lutz, S., Ducrée, J., Zengerle, R., & von Stetten, F. (2009). Centrifugo-pneumatic valve for metering of highly wetting liquids on centrifugal microfluidic platforms. *Lab on a Chip*, *9*(24), 3599-3603.
47. Gorkin III, R., Nwankire, C. E., Gaughran, J., Zhang, X., Donohoe, G. G., Rook, M., O'Kennedy, R., & Ducrée, J. (2012). Centrifugo-pneumatic valving utilizing dissolvable films. *Lab on a Chip*, *12*(16), 2894-2902.
48. Mark, D., Haeberle, S., Metz, T., Lutz, S., Ducree, J., Zengerle, R., & von Stetten, F. (2008, January). Aliquoting structure for centrifugal microfluidics based on a new pneumatic valve. In *Micro Electro Mechanical Systems, 2008. MEMS 2008. IEEE 21st International Conference on* (pp. 611-614). IEEE.
49. Siegrist, J., Gorkin, R., Clime, L., Roy, E., Peytavi, R., Kido, H., Bergeron, M., Veres, T., & Madou, M. (2010). Serial siphon valving for centrifugal microfluidic platforms. *Microfluidics and nanofluidics*, *9*(1), 55-63.
50. Ouyang Y., Wang S., Li J., Riehl P.S., Begley M., Landers J.P. (2013) Rapid patterning of 'tunable' hydrophobic valves on disposable microchips by laser printer lithography. *Lab on a Chip,* 13(9),1762-71
51. Kim, J., Kido, H., Rangel, R. H., & Madou, M. J. (2008). Passive flow switching

valves on a centrifugal microfluidic platform. *Sensors and Actuators B: Chemical*, *128*(2), 613-621.
52. Li, T., Zhang, L., Leung, K. M., & Yang, J. (2010). Out-of-plane microvalves for whole blood separation on lab-on-a-CD. *Journal of Micromechanics and Microengineering*, *20*(10), 105024.
53. Abi-Samra, K., Hanson, R., Madou, M., & Gorkin III, R. A. (2011). Infrared controlled waxes for liquid handling and storage on a CD-microfluidic platform. *Lab on a Chip*, *11*(4), 723-726.
54. Nan, L., Jiang, Z., & Wei, X. (2013). Emerging microfluidic devices for cell lysis: A review. *Lab on a Chip*.
55. Lutz, S., Lang, P., Faltin, B., Haeberle, S., von Stetten, F., Zengerle, R., & Ducrée, J. (2007, October). Towards a comprehensive centrifugal process integration by rotationally induced lyophilisate dissolution and cell lysis. In *11th International Conference on Miniaturized Systems for Chemistry and Life Sciences. Paris, France* (pp. 7-11).
56. G. J. Kellogg, T. E. Arnold, B. L. Carvalho, D. C. Duffy, and N. F. Sheppard. (2000) Centrifugal microfluidics: Applications. In 4th International Conference on Miniaturized Systems for Chemistry and Life Sciences, pages 239–242, 14 – 18
57. Wang, H. Y., Bhunia, A. K., & Lu, C. (2006). A microfluidic flow-through device for high throughput electrical lysis of bacterial cells based on continuous dc voltage. *Biosensors and Bioelectronics*, *22*(5), 582-588.
58. Kido, H., Micic, M., Smith, D., Zoval, J., Norton, J., & Madou, M. (2007). A novel, compact disk-like centrifugal microfluidics system for cell lysis and sample homogenization. *Colloids and Surfaces B: Biointerfaces*, *58*(1), 44-51.
59. Kim, J., Johnson, M., Hill, P., & Gale, B. K. (2009). Microfluidic sample preparation: cell lysis and nucleic acid purification. *Integrative Biology*, *1*(10), 574-586.
60. Sun, Y., & Kwok, Y. C. (2006). Polymeric microfluidic system for DNA analysis. *Analytica chimica acta*, *556*(1), 80-96.
61. Dimov, N., Gaughran, J., Clancy, E., Barry, T., Smith, T. J., & Ducree, J. (2013, June). Automated on-disc total RNA extraction from whole blood towards point-of-care for early stage diagnostics. In *Solid-State Sensors, Actuators and Microsystems (TRANSDUCERS & EUROSENSORS XXVII), 2013 Transducers & Eurosensors XXVII: The 17th International Conference on* (pp. 2548-2551). IEEE.
62. Amasia, M., Cozzens, M., & Madou, M. J. (2012). Centrifugal microfluidic platform for rapid PCR amplification using integrated thermoelectric heating and ice-valving. *Sensors and Actuators B: Chemical*, *161*(1), 1191-1197.
63. Siegrist, J., Gorkin, R., Bastien, M., Stewart, G., Peytavi, R., Kido, H., Bergeron, M., & Madou, M. (2010). Validation of a centrifugal microfluidic sample lysis and homogenization platform for nucleic acid extraction with clinical samples. *Lab on a Chip*, *10*(3), 363-371.
64. Grumann, M., Geipel, A., Riegger, L., Zengerle, R., & Ducree, J. (2005). Batch-mode mixing on centrifugal microfluidic platforms. *Lab on a Chip*, *5*(5), 560-565.
65. Riegger, L., Grumann, M., Steigert, J., Lutz, S., Steinert, C. P., Mueller, C., Viertel, J., Prucker, O., Rühe, J., Zengerle, R., & Ducrée, J. (2007). Single-step centrifugal hematocrit determination on a 10-$ processing device. *Biomedical microdevices*, *9*(6), 795-799.
66. Schaff, U. Y., Tentori, A. M., & Sommer, G. J. (2010, October). Differential white cell count by centrifugal microfluidics. In *14th International Conference*

on Miniaturized Systems for Chemistry and Life Sciences. Groningen, The Netherlands (pp. 3-7).
67. H. Shiono and Y. Ito. Novel method for continuous cell separation by density gradient centrifugation: Evaluation of a miniature separation column. Preparative biochemistry & biotechnology, 33:87–100, 2003.
68. H. Shiono, H. M. Chen, T. Okada, and Y. Ito. Colony-forming cell assay for human hematopoietic progenitor cells harvested by a novel continuous-flow cell separation method. Journal of Chromatography a, 1151:153–157, 2007.
69. H. Shiono, T. Okada, and Y. Ito. Application of a novel continuous-flow cell separation method for separation of cultured human mast cells. Journal of Liquid Chromatography & Related Technologies, 28:2071–2083, 2005.
70. Park, J. M., Lee, J. Y., Lee, J. G., Jeong, H., Oh, J. M., Kim, Y. J., Park, D., Kim, M. S., Lee, H. J., Oh, J. H., Lee, S. S., Lee, W. Y., & Huh, N. (2012). Highly efficient assay of circulating tumor cells by selective sedimentation with a density gradient medium and microfiltration from whole blood. *Analytical chemistry*, *84*(17), 7400-7407.
71. Nilsson, J., Evander, M., Hammarström, B., & Laurell, T. (2009). Review of cell and particle trapping in microfluidic systems. *Analytica chimica acta*, *649*(2), 141-157.
72. Yi, C., Li, C. W., Ji, S., & Yang, M. (2006). Microfluidics technology for manipulation and analysis of biological cells. *Analytica Chimica Acta*, *560*(1), 1-23.
73. Huh, D., Gu, W., Kamotani, Y., Grotberg, J. B., & Takayama, S. (2005). Microfluidics for flow cytometric analysis of cells and particles. *Physiological measurement*, *26*(3), R73.
74. Chung, T. D., & Kim, H. C. (2007). Recent advances in miniaturized microfluidic flow cytometry for clinical use. *Electrophoresis*, *28*(24), 4511-4520.
75. Godin, J., Chen, C. H., Cho, S. H., Qiao, W., Tsai, F., & Lo, Y. H. (2008). Microfluidics and photonics for Bio System on a Chip: A review of advancements in technology towards a microfluidic flow cytometry chip. Journal of biophotonics, 1(5), 355-376.
76. Sun, T., & Morgan, H. (2010). Single-cell microfluidic impedance cytometry: a review. *Microfluidics and Nanofluidics*, *8*(4), 423-443.
77. Helou, M., Reisbeck, M., Tedde, S. F., Richter, L., Bär, L., Bosch, J. J., Stauber, R. H., Quandt, E., & Hayden, O. (2013). Time-of-flight magnetic flow cytometry in whole blood with integrated sample preparation. *Lab on a Chip*, *13*(6), 1035-1038.
78. Krüger, J., Singh, K., O'Neill, A., Jackson, C., Morrison, A., & O'Brien, P. (2002). Development of a microfluidic device for fluorescence activated cell sorting. *Journal of Micromechanics and Microengineering*, *12*(4), 486.
79. Dittrich, P. S., & Schwille, P. (2003). An integrated microfluidic system for reaction, high-sensitivity detection, and sorting of fluorescent cells and particles. *Analytical chemistry*, *75*(21), 5767-5774.
80. McClain, M. A., Culbertson, C. T., Jacobson, S. C., & Ramsey, J. M. (2001). Flow cytometry of Escherichia coli on microfluidic devices. *Analytical Chemistry*, *73*(21), 5334-5338.
81. Tung, Y. C., Zhang, M., Lin, C. T., Kurabayashi, K., & Skerlos, S. J. (2004). PDMS-based opto-fluidic micro flow cytometer with two-color, multi-angle fluorescence detection capability using PIN photodiodes. *Sensors and actuators B: Chemical*, *98*(2), 356-367.

82. Wang, L., Flanagan, L. A., Jeon, N. L., Monuki, E., & Lee, A. P. (2007). Dielectrophoresis switching with vertical sidewall electrodes for microfluidic flow cytometry. *Lab on a Chip*, *7*(9), 1114-1120.
83. Lin, C. H., Lee, G. B., Fu, L. M., & Hwey, B. H. (2004). Vertical focusing device utilizing dielectrophoretic force and its application on microflow cytometer. *Microelectromechanical Systems, Journal of*, *13*(6), 923-932.
84. Bhagat, A. A. S., Kuntaegowdanahalli, S. S., Kaval, N., Seliskar, C. J., & Papautsky, I. (2010). Inertial microfluidics for sheath-less high-throughput flow cytometry. *Biomedical microdevices*, *12*(2), 187-195.
85. Hur, S. C., Tse, H. T. K., & Di Carlo, D. (2010). Sheathless inertial cell ordering for extreme throughput flow cytometry. Lab on a Chip, 10(3), 274-280.
86. Christiansen, T. L., Trosborg, J., Tanzi, S., Larsen, S. T., & Taboryski, R. J. (2012). A Pressure Controlled Pinched Flow Fractionation Device for Continuous Particle Separation.
87. Yamada, M., Nakashima, M., & Seki, M. (2004). Pinched flow fractionation: continuous size separation of particles utilizing a laminar flow profile in a pinched microchannel. *Analytical chemistry*, *76*(18), 5465-5471.
88. Srivastav, A., Podgorski, T., & Coupier, G. (2012). Efficiency of size-dependent particle separation by pinched flow fractionation. *Microfluidics and nanofluidics*, *13*(5), 697-701.
89. Cupelli, C., Borchardt, T., Steiner, T., Paust, N., Zengerle, R., & Santer, M. (2013). Leukocyte enrichment based on a modified pinched flow fractionation approach. *Microfluidics and Nanofluidics*, 1-13.
90. Morijiri, T., Sunahiro, S., Senaha, M., Yamada, M., & Seki, M. (2011). Sedimentation pinched-flow fractionation for size-and density-based particle sorting in microchannels. *Microfluidics and nanofluidics*, *11*(1), 105-110.
91. Wahl, L. M., Katona, I. M., Wilder, R. L., Winter, C. C., Haraoui, B., Scher, I., & Wahl, S. M. (1984). Isolation of human mononuclear cell subsets by counterflow centrifugal elutriation (CCE): I. Characterization of B-lymphocyte-, T-lymphocyte-, and monocyte-enriched fractions by flow cytometric analysis. *Cellular immunology*, *85*(2), 373-383.
92. Banfalvi, G. (2008). Cell cycle synchronization of animal cells and nuclei by centrifugal elutriation. *Nature protocols*, *3*(4), 663-673.
93. Morijiri, T., Yamada, M., Hikida, T., & Seki, M. (2012). Microfluidic counterflow centrifugal elutriation system for sedimentation-based cell separation. *Microfluidics and Nanofluidics*, 1-9.
94. Pamme, N. (2007). Continuous flow separations in microfluidic devices. *Lab on a Chip*, *7*(12), 1644-1659.
95. Çetin, B., & Li, D. (2011). Dielectrophoresis in microfluidics technology. *Electrophoresis*, *32*(18), 2410-2427.
96. Yih, T. C., & Talpasanu, I. (2008). *Micro and nano manipulations for biomedical applications*. Norwood: Artech House.
97. Martinez-Duarte, R., Gorkin III, R. A., Abi-Samra, K., & Madou, M. J. (2010). The integration of 3D carbon-electrode dielectrophoresis on a CD-like centrifugal microfluidic platform. *Lab on a Chip*, *10*(8), 1030-1043.
98. Martinez Duarte, R., Renaud, P., & Madou, M. J. (2011). A novel approach to dielectrophoresis using carbon electrodes. Electrophoresis, 32(17), 2385-2392.
99. M. Boettcher, M. S. Jaeger, L. Riegger, J. Ducrée, R. Zengerle, and C. Duschl.(2006) Lab-on-chip-based cell separation by combining dielectrophoresis and centrifugation. Biophys. Rev. Lett., 1:443–451
100. Pamme, N., & Manz, A. (2004). On-chip free-flow magnetophoresis: continuous flow separation of magnetic particles and agglomerates. Analytical Chemistry,

76(24), 7250-7256.
101. Zhu, T., Cheng, R., Lee, S. A., RajaRaman, E., Eiteman, M. A., Querec, T. D., Unger E. R., & Mao, L. (2012). Continuous-flow ferrohydrodynamic sorting of particles and cells in microfluidic devices. Microfluidics and Nanofluidics, 13(4), 645-654.
102. Zeng, J., Deng, Y., Vedantam, P., Tzeng, T. R., & Xuan, X. (2013). Magnetic separation of particles and cells in ferrofluid flow through a straight microchannel using two offset magnets. Journal of Magnetism and Magnetic Materials, 346, 118-123.
103. Plouffe, B. D., Mahalanabis, M., Lewis, L. H., Klapperich, C. M., & Murthy, S. K. (2012). Clinically relevant microfluidic magnetophoretic isolation of rare-cell populations for diagnostic and therapeutic monitoring applications. Analytical chemistry, 84(3), 1336-1344.
104. Shen, F., Hwang, H., Hahn, Y. K., & Park, J. K. (2012). Label-free cell separation using a tunable magnetophoretic repulsion force. *Analytical chemistry*, *84*(7), 3075-3081.
105. Mizuno, M., Yamada, M., Mitamura, R., Ike, K., Toyama, K., & Seki, M. (2013). Magnetophoresis-Integrated Hydrodynamic Filtration System for Size- and Surface Marker-Based Two-Dimensional Cell Sorting. Analytical chemistry, 85(16), 7666-7673.
106. Kirby, D., Siegrist, J., Kijanka, G., Zavattoni, L., Sheils, O., O'Leary, J., Burger, R., & Ducrée, J. (2012). Centrifugo-magnetophoretic particle separation. Microfluidics and nanofluidics, 13(6), 899-908.
107. Siegrist, J., Burger, R., Kirby, D., Zavattoni, L., Kijanka, G., & Ducrée, J. (2011, October). Stress-free centrifugo-magnetic 2D-separation of cancer cells in a stopped-flow mode. In 15th International Conference on Miniaturized Systems for Chemistry and Life Sciences (uTAS). Seattle, USA (pp. 2-6).
108. Glynn, M., Kirby, D., Chung, D., Kinahan, D. J., Kijanka, G., & Ducrée, J. (2013). Centrifugo-magnetophoretic Purification of CD4+ Cells from Whole Blood toward Future HIV/AIDS Point-of-Care Applications. Journal of laboratory automation, 2211068213504759.
109. Furlani, E. P. (2007). Magnetophoretic separation of blood cells at the microscale. Journal of Physics D: Applied Physics, 40(5), 1313.
110. Gijs, M. A. (2004). Magnetic bead handling on-chip: new opportunities for analytical applications. Microfluidics and Nanofluidics, 1(1), 22-40.
111. Petersson, F., Åberg, L., Swärd-Nilsson, A. M., & Laurell, T. (2007). Free flow acoustophoresis: microfluidic-based mode of particle and cell separation. Analytical chemistry, 79(14), 5117-5123.
112. Shi, J., Huang, H., Stratton, Z., Huang, Y., & Huang, T. J. (2009). Continuous particle separation in a microfluidic channel via standing surface acoustic waves (SSAW). Lab Chip, 9(23), 3354-3359.
113. Lenshof, A., Magnusson, C., & Laurell, T. (2012). Acoustofluidics 8: Applications of acoustophoresis in continuous flow microsystems. Lab on a Chip, 12(7), 1210-1223.
114. Thévoz, P., Adams, J. D., Shea, H., Bruus, H., & Soh, H. T. (2010). Acoustophoretic synchronization of mammalian cells in microchannels. Analytical chemistry, 82(7), 3094-3098.
115. Haeberle, S., Naegele, L., Burger, R., Stetten, F. V., Zengerle, R., & Ducrée, J. (2008). Alginate bead fabrication and encapsulation of living cells under centrifugally induced artificial gravity conditions. Journal of microencapsulation, 25(4), 267-274.
116. Um, E., Lee, D. S., Pyo, H. B., & Park, J. K. (2008). Continuous generation of

hydrogel beads and encapsulation of biological materials using a microfluidic droplet-merging channel. Microfluidics and Nanofluidics, 5(4), 541-549.
117. Ozkan, M., Wang, M., Ozkan, C., Flynn, R., & Esener, S. (2003). Optical manipulation of objects and biological cells in microfluidic devices. Biomedical Microdevices, 5(1), 61-67.
118. Wang, M. M., Tu, E., Raymond, D. E., Yang, J. M., Zhang, H., Hagen, N., Dees, B., Mercer, E. M., Forster, A. H., Kariv, I., Marchand P. J., & Butler, W. F. (2004). Microfluidic sorting of mammalian cells by optical force switching. Nature biotechnology, 23(1), 83-87.
119. Yang, A. H., Moore, S. D., Schmidt, B. S., Klug, M., Lipson, M., & Erickson, D. (2009). Optical manipulation of nanoparticles and biomolecules in sub-wavelength slot waveguides. Nature, 457(7225), 71-75.
120. Perroud, T. D., Kaiser, J. N., Sy, J. C., Lane, T. W., Branda, C. S., Singh, A. K., & Patel, K. D. (2008). Microfluidic-based cell sorting of Francisella tularensis infected macrophages using optical forces. Analytical chemistry, 80(16), 6365-6372.
121. Tsutsui, H., & Ho, C. M. (2009). Cell separation by non-inertial force fields in microfluidic systems. Mechanics research communications, 36(1), 92-103.
122. Clausell-Tormos, J., Lieber, D., Baret, J. C., El-Harrak, A., Miller, O. J., Frenz, L., Blouwolff, J., Humphry, K. J., Korster, S., Duan, H., Holtze, C., Weitz, D. A., Griffiths, A. D., & Merten, C. A. (2008). Droplet-based microfluidic platforms for the encapsulation and screening of mammalian cells and multicellular organisms. Chemistry & biology, 15(5), 427-437.
123. Kim, N., Dempsey, C. M., Zoval, J. V., Sze, J. Y., & Madou, M. J. (2007). Automated microfluidic compact disc (CD) cultivation system of Caenorhabditis elegans. Sensors and Actuators B: Chemical, 122(2), 511-518.
124. Chen, C. C., Zappe, S., Sahin, O., Zhang, X. J., Fish, M., Scott, M., & Solgaard, O. (2004). Design and operation of a microfluidic sorter for Drosophilae mbryos. Sensors and Actuators B: Chemical, 102(1), 59-66.
125. Devendra, R., & Drazer, G. (2012). Gravity Driven Deterministic Lateral Displacement for Particle Separation in Microfluidic Devices. *Analytical chemistry*, *84*(24), 10621-10627.
126. Lee S.W., Kanga J.Y., Lee I.H., Ryua S.S., Kwak S.M., Shin K.S., Kima C., Jung H.I. and Kima T.S., "Single-cell assay on CD-like lab chip using centrifugal massive single-cell trap", *Sensors and Actuators A* **143**, (2008) 64–69.
127. Kubo, I., Furutani, S., & Matoba, K. (2011). Use of a novel microfluidic disk in the analysis of single-cell viability and the application to Jurkat cells. *Journal of bioscience and bioengineering*, *112*(1), 98-101.
128. Furutani, S., Nagai, H., & Kubo, I. (2008). Single cell isolation on a centrifugal flow disk with integrated tandem microchambers. *Sensor Letters*, *6*(6), 961-965.
129. Burger R., Reith P., Kijanka G., Akujobi V., Abgrall P. and Ducrée J., "Array-based capture, distribution, counting and multiplexed assaying of beads on a centrifugal microfluidic platform", *Lab On A Chip* 12, (2012) 1289 – 1295.
130. Burger, R., Reith, P., Abgrall, P., Kijanka, G., & Ducrée, J. (2011, January). Multiplexing of highly reproducible, bead-based immunoassays on a centrifugal microfluidic platform. In *Micro Electro Mechanical Systems (MEMS), 2011 IEEE 24th International Conference on* (pp. 1170-1172). IEEE.
131. Burger, R., Kijanka, G., Sheils, O., O'Leary, J., & Ducrée, J. (2011, October). Arrayed capture, assaying and binary counting of cells in a stopped-flow sedimentation mode. In *15th International Conference on Miniaturized Systems for Chemistry and Life Sciences (uTAS). Seattle, Washington, USA* (pp. 2-6).

132. Burger R., Kurzbuch D., Gorkin R, Glynn M., Kijanka G. and Ducrée J., "Laser-based manipulation and fluorescent detection of individual, centrifugally arrayed bioparticles", (Society for Chemistry and Micro-Nano Systems) Proc. *The 16th International Conference on Miniaturized Systems for Chemistry and Life Sciences (μTAS2012), Okinawa, Japan*. (2012) 2245.
133. Di Carlo, D., Aghdam, N., & Lee, L. P. (2006). Single-cell enzyme concentrations, kinetics, and inhibition analysis using high-density hydrodynamic cell isolation arrays. *Analytical chemistry*, *78*(14), 4925-4930.
134. Bernard, A., Renault, J. P., Michel, B., Bosshard, H. R., & Delamarche, E. (2000). Microcontact printing of proteins. *Advanced Materials*, *12*(14), 1067-1070.
135. Renault, J. P., Bernard, A., Bietsch, A., Michel, B., Bosshard, H. R., Delamarche, E., Kreiter, M., Hecht, B., & Wild, U. P. (2003). Fabricating arrays of single protein molecules on glass using microcontact printing. The Journal of Physical Chemistry B, 107(3), 703-711.
136. Kane, R. S., Takayama, S., Ostuni, E., Ingber, D. E., & Whitesides, G. M. (1999). Patterning proteins and cells using soft lithography. Biomaterials, 20(23), 2363-2376.
137. Schmalenberg, K. E., Buettner, H. M., & Uhrich, K. E. (2004). Microcontact printing of proteins on oxygen plasma-activated poly (methyl methacrylate). Biomaterials, 25(10), 1851-1857.
138. Hunt, H. C., & Wilkinson, J. S. (2008). Optofluidic integration for microanalysis. *Microfluidics and Nanofluidics*, *4*(1-2), 53-79.
139. Fan, X., & White, I. M. (2011). Optofluidic microsystems for chemical and biological analysis. *Nature photonics*, *5*(10), 591-597.
140. Myers, F. B., & Lee, L. P. (2008). Innovations in optical microfluidic technologies for point-of-care diagnostics. *Lab on a Chip*, *8*(12), 2015-2031.
141. Steigert, J., Grumann, M., Brenner, T., Riegger, L., Harter, J., Zengerle, R., & Ducree, J. (2006). Fully integrated whole blood testing by real-time absorption measurement on a centrifugal platform. Lab on a Chip, 6(8), 1040-1044.
142. Zhu, H., Mavandadi, S., Coskun, A. F., Yaglidere, O., & Ozcan, A. (2011). Optofluidic fluorescent imaging cytometry on a cell phone. Analytical chemistry, 83(17), 6641-6647.
143. Chinowsky, T. M., Quinn, J. G., Bartholomew, D. U., Kaiser, R., & Elkind, J. L. (2003). Performance of the Spreeta 2000 integrated surface plasmon resonance affinity sensor. Sensors and Actuators B: Chemical, 91(1), 266-274.
144. Liu, G. L., & Lee, L. P. (2005). Nanowell surface enhanced Raman scattering arrays fabricated by soft-lithography for label-free biomolecular detections in integrated microfluidics. Applied Physics Letters, 87(7), 074101-074101.
145. Zhu, H., Isikman, S. O., Mudanyali, O., Greenbaum, A., & Ozcan, A. (2013). Optical imaging techniques for point-of-care diagnostics. Lab on a Chip, 13(1), 51-67.
146. Kim, S. B., Bae, H., Koo, K. I., Dokmeci, M. R., Ozcan, A., & Khademhosseini, A. (2012). Lens-free imaging for biological applications. Journal of laboratory automation, 17(1), 43-49.
147. Stybayeva, G., Mudanyali, O., Seo, S., Silangcruz, J., Macal, M., Ramanculov, E., Dandekar, S., Erlinger, A., Ozcan, A., & Revzin, A. (2010). Lensfree holographic imaging of antibody microarrays for high-throughput detection of leukocyte numbers and function. Analytical chemistry, 82(9), 3736-3744.
148. Moon, S., Keles, H. O., Ozcan, A., Khademhosseini, A., Hæggstrom, E., Kuritzkes, D., & Demirci, U. (2009). Integrating microfluidics and lensless imaging for point-of-care testing. Biosensors and Bioelectronics, 24(11), 3208-

3214.
149. King, D., O'Sullivan M., & Ducrée, J., (2013). Optical Detection Strategies for Centrifugal Microfluidic Platforms. *Journal of Modern Optics* (In print)
150. Grumann M, Steigert J, Riegger L, Moser I., Enderle B, Urban G, Zengerle R, and J. Ducrée J, "Sensitivity enhancement for colorimetric glucose assays on whole blood by on-chip beam-guidance", *Biomedical Microdevices*, **8(3)** (2006) 209-214.
151. Steigert J., Grumann M., Dube M, Streule W., Riegger L., Brenner T., Koltay P., Mittmann K., Zengerle R., Ducrée J, "Direct hemoglobin measurement on a centrifugal microfluidic platform for point-of-care diagnostics" *Sensors & Actuators A*, **130-131**, (2006) 228 - 233.
152. Hoffmann J., Riegger L., Bundgaard F., Mark D., Zengerle R. and Ducrée J., "Optical non – contact localization of liquid – gas interfaces on disk during rotation for measuring flow rates and viscosities", *Lab On A Chip*, **12**, (2012) 5231 – 5236.
153. Van De Hurst, H. C. (2010). Light Scattering by Small Particles (Structure of Matter Series.).
154. Biosurfit (Lisbon, Portugal) http://www.biosurfit.com/
155. Kim J., Liu G.L. and Lee L.P., "Lens-scanning Raman micro - spectroscopy system using compact disc optical pickup technology", *Optics Express*, **13(12)**, (2005) 4780 – 4785.
156. Choi D., Kang T., Cho H., Choi Y. and Lee L.P., "Additional amplifications of SERS via an optofluidic CD-based platform", *Lab On A Chip*, **9**, (2009) 239 – 243.
157. Cho H. and Lee L.P., "A novel integrated microfluidic SERS-CD with high-throughput centrifugal cell trapping array for quantitive biomedicine", (Society for Chemistry and Micro-Nano Systems) Proc. *The 10th International Conference on Miniaturized Systems for Chemistry and Life Sciences (μTAS2006), Tokyo, Japan*. (2006) 642 - 644.
158. Han, X. X., Zhao, B., & Ozaki, Y. (2009). Surface-enhanced Raman scattering for protein detection. *Analytical and bioanalytical chemistry*, *394*(7), 1719-1727.
159. Nwankire C.E., Donohoe G.G., Zhang X., Siegrist J., Somers M., Kurzbuch D., Monaghan R., Kitsara M., Burger R., Hearty S., Murrell J., Martin C., Rook M., Barrett L., Daniels C., McDonagh C., O' Kennedy R. and Ducrée J., "At-Line Bioprocess Monitoring by Immunoassay with Rotationally Controlled Serial Siphoning and Integrated Supercritical Angle Fluorescence Optics", Analytica Chimica Acta, 781, (2013) 54– 62.
160. Grumann, M., Brenner, T., Beer, C., Zengerle, R., & Ducrée, J. (2005). Visualization of flow patterning in high-speed centrifugal microfluidics. Review of scientific instruments, 76(2), 025101-025101.
161. Yu, H. Z., Li, Y., & Ou, L. M. L. (2012). Reading Disc-Based Bioassays with Standard Computer Drives. Accounts of Chemical Research, 46(2), 258-268.
162. Yu, H. Z. (2004). New chemistry on old CDs. Chemical communications, (23), 2633-2636.
163. Varma, M. M., Inerowicz, H. D., Regnier, F. E., & Nolte, D. D. (2004). High-speed label-free detection by spinning-disk micro-interferometry. *Biosensors and Bioelectronics*, *19*(11), 1371-1376.
164. Peng, L., Varma, M. M., Regnier, F. E., & Nolte, D. D. (2005, April). The adaptive BioCD: interferometric immunoassay on a spinning disk. In Proc. of SPIE Vol (Vol. 5692, p. 225).

165. Peng, L., Varma, M. M., Cho, W., Regnier, F. E., & Nolte, D. D. (2007). Adaptive interferometry of protein on a BioCD. *Applied optics*, *46*(22), 5384-5395.
166. Ramachandraiah, H., Amasia, M., Cole, J., Sheard, P., Pickhaver, S., Walker, C., Wirta, V., Lexow, P., Lione, R., & Russom, A. (2013). Lab-on-DVD: standard DVD drives as a novel laser scanning microscope for image based point of care diagnostics. *Lab Chip*,*13*(8), 1578-1585.
167. Imaad, S. M., Lord, N., Kulsharova, G., & Liu, G. L. (2011). Microparticle and cell counting with digital microfluidic compact disc using standard CD drive. *Lab on a Chip*, *11*(8), 1448-1456.
168. Li, Y., Ou, L. M., & Yu, H. Z. (2008). Digitized molecular diagnostics: reading disk-based bioassays with standard computer drives. Analytical chemistry, 80(21), 8216-8223.
169. Morais, S., Tortajada-Genaro, L. A., Arnandis-Chover, T., Puchades, R., & Maquieira, A. (2009). Multiplexed microimmunoassays on a digital versatile disk. Analytical chemistry, 81(14), 5646-5654.
170. Tortajada-Genaro, L. A., Santiago-Felipe, S., Morais, S., Gabaldón, J. A., Puchades, R., & Maquieira, A. (2011). Multiplex DNA detection of food allergens on a digital versatile disk. *Journal of agricultural and food chemistry*,*60*(1), 36-43.
171. Bernini, R., Campopiano, S., Zeni, L., & Sarro, P. M. (2004). ARROW optical waveguides based sensors. Sensors and Actuators B: Chemical, 100(1), 143-146.
172. Yin, D., Seamer, D. W., Schmidt, H., Barber, J. P., & Hawkins, A. R. (2004). Integrated optical wave guides with liquid cores. Applied Physics Letters, 85(16), 3477-3479.
173. Neumann, K. C., & Block, S. M. (2004). Optical trapping. Review of scientific instruments, 75(9), 2787-2809.
174. Tsarevich, A., Rubin, B., Bedford, M., & Korean, K. G. (2010, December). Magnetic Nano rods for Optoelectronic Applications. In AIP Conference Proceedings (Vol. 1311, p. 204).
175. Han, B., Choi, N., Kim, K. H., Lim, D. W., & Choo, J. (2011). Application of silver-coated magnetic microspheres to a SERS-based optofluidic sensor. *The Journal of Physical Chemistry C*, *115*(14), 6290-6296.
176. Lee, S. K., Kim, S. H., Kang, J. H., Park, S. G., Jung, W. J., Kim, S. H., Yi, G. R., & Yang, S. M. (2008). Optofluidics technology based on colloids and their assemblies. *Microfluidics and Nanofluidics*, *4*(1-2), 129-144.
177. Brody J, Quake S (1999) A self-assembled microlensing rotational probe. Appl Phys Lett 74:144–146
178. Wolfe, D. B., Conroy, R. S., Garstecki, P., Mayers, B. T., Fischbach, M. A., Paul, K. E., Prentiss, M., & Whitesides, G. M. (2004). Dynamic control of liquid-core/liquid-cladding optical waveguides. *Proceedings of the National Academy of Sciences of the United States of America*, *101*(34), 12434-12438.
179. Vezenov, D. V., Mayers, B. T., Wolfe, D. B., & Whitesides, G. M. (2005). Integrated fluorescent light source for optofluidic applications. *Applied Physics Letters*, *86*(4), 1104.
180. Testa, G., & Bernini, R. (2012). Integrated tunable liquid optical fiber. Lab Chip, 12(19), 3670-3672.
181. Sowa, S., Watanabe, W., Tamaki, T., Nishii, J., & Itoh, K. (2006). Symmetric waveguides in poly (methyl methacrylate) fabricated by femtosecond laser pulses. *Optics Express*, *14*(1), 291-297.
182. Zoubir, A., Lopez, C., Richardson, M., & Richardson, K. (2004). Femtosecond

laser fabrication of tubular waveguides in poly (methyl methacrylate). *Optics letters*, *29*(16), 1840-1842.
183. Suriano, R., Kuznetsov, A., Eaton, S. M., Kiyan, R., Cerullo, G., Osellame, R., Chichkov, B. N., Levi, M., & Turri, S. (2011). Femtosecond laser ablation of polymeric substrates for the fabrication of microfluidic channels. *Applied Surface Science*, *257*(14), 6243-6250.
184. Scully, P. J., Jones, D., & Jaroszynski, D. A. (2003). Femtosecond laser irradiation of polymethylmethacrylate for refractive index gratings. *Journal of Optics A: Pure and Applied Optics*, *5*(4), S92.
185. Wochnowski, C., Cheng, Y., Meteva, K., Sugioka, K., Midorikawa, K., & Metev, S. (2005). Femtosecond-laser induced formation of grating structures in planar polymer substrates. *Journal of Optics A: Pure and Applied Optics*, *7*(9), 493.
186. Gomez, D., Goenaga, I., Lizuain, I., & Ozaita, M. (2005). Femtosecond laser ablation for microfluidics. *Optical engineering*, *44*(5), 051105-051105.
187. Day, D., & Gu, M. (2005). Microchannel fabrication in PMMA based on localized heating by nanojoule high repetition rate femtosecond pulses. *Opt. Express*, *13*(16), 5939-5946
188. Osellame, R., Maselli, V., Vazquez, R. M., Ramponi, R., & Cerullo, G. (2007). Integration of optical waveguides and microfluidic channels both fabricated by femtosecond laser irradiation. *Applied physics letters*, *90*(23), 231118-231118.

189. Copperwhite, R., O'Sullivan, M., Boothman, C., Gorin, A., McDonagh, C., & Oubaha, M. (2011). Development and characterisation of integrated microfluidics on waveguide-based photonic platforms fabricated from hybrid materials. *Microfluidics and nanofluidics*, *11*(3), 283-296.
190. Balslev, S., Jorgensen, A. M., Bilenberg, B., Mogensen, K. B., Snakenborg, D., Geschke, O., Kutter, J. P., & Kristensen, A. (2006). Lab-on-a-chip with integrated optical transducers. *Lab on a chip*, *6*(2), 213.
191. Micro Chem Corp (2014) http://www.microchem.com/Prod-SU83000.htm SU-8 3000. Retrieved from http://www.microchem.com/pdf/SU-8%203000%20Data%20Sheet.pdf
192. Laurell Corporation (2010-2014) www.laurell.com 150mm Spin Coater WS-400-6NPP. Retrieved from http://www.laurell.com/spin-coater/?model=WS-400-6NPP-LITE
193. Beebe, D. J., Moore, J. S., Bauer, J. M., Yu, Q., Liu, R. H., Devadoss, C., & Jo, B. H. (2000). Functional hydrogel structures for autonomous flow control inside microfluidic channels. *Nature*, *404*(6778), 588-590.
194. Rolland, J. P., Van Dam, R. M., Schorzman, D. A., Quake, S. R., & DeSimone, J. M. (2004). Solvent-resistant photocurable "liquid teflon" for microfluidic device fabrication. *Journal of the American Chemical Society*, *126*(8), 2322-2323.
195. Fiorini, G. S., Jeffries, G. D., Lim, D. S., Kuyper, C. L., & Chiu, D. T. (2003). Fabrication of thermoset polyester microfluidic devices and embossing masters using rapid prototyped polydimethylsiloxane molds. *Lab on a Chip*, *3*(3), 158-163.
196. Sudarsan, A. P., Wang, J., & Ugaz, V. M. (2005). Thermoplastic elastomer gels: an advanced substrate for microfluidic chemical analysis systems. *Analytical chemistry*, *77*(16), 5167-5173.
197. Oubaha, M., Kribich, R. K., Copperwhite, R., Etienne, P., O'dwyer, K., MacCraith, B. D., & Moreau, Y. (2005). New organic inorganic sol–gel material with high transparency at 1.55 μm. *Optics communications*, *253*(4), 346-351.
198. Oubaha, M., Copperwhite, R., Gorin, A., Purlys, V., Boothman, C., O'Sullivan, M., Godanas, R., McDonagh, C., & MacCraith, B. D. (2011). Novel tantalum

based photocurable hybrid sol–gel material employed in the fabrication of channel optical waveguides and three-dimensional structures. Applied Surface Science, 257(7), 2995-2999.
199. http://www.himt.de/en/products/dwl66fs.php
200. Li, Z., Zhang, Z., Emery, T., Scherer, A., & Psaltis, D. (2006). Single mode optofluidic distributed feedback dye laser. *Optics Express*, *14*(2), 696-701.
201. Cho, S. H., Godin, J., & Lo, Y. H. (2009). Optofluidic waveguides in Teflon AF-coated PDMS microfluidic channels. *Photonics Technology Letters, IEEE*, *21*(15), 1057-1059.
202. Mao, X., Waldeisen, J. R., Juluri, B. K., & Huang, T. J. (2007). Hydrodynamically tunable optofluidic cylindrical microlens. *Lab on a Chip*, *7*(10), 1303-1308.
203. Lee, J. N., Park, C., & Whitesides, G. M. (2003). Solvent compatibility of poly (dimethylsiloxane)-based microfluidic devices. *Analytical chemistry*, *75*(23), 6544-6554.
204. Pattani, V. P., Li, C., Desai, T. A., & Vu, T. Q. (2008). Microcontact printing of quantum dot bioconjugate arrays for localized capture and detection of biomolecules. Biomedical microdevices, 10(3), 367-374.
205. Dusseiller, M. R., Schlaepfer, D., Koch, M., Kroschewski, R., & Textor, M. (2005). An inverted microcontact printing method on topographically structured polystyrene chips for arrayed micro-3-D culturing of single cells. Biomaterials, 26(29), 5917-5925.
206. Watson, M. W., Abdelgawad, M., Ye, G., Yonson, N., Trottier, J., & Wheeler, A. R. (2006). Microcontact printing-based fabrication of digital microfluidic devices. Analytical chemistry, 78(22), 7877-7885.
207. Dixit, C. K., Vashist, S. K., MacCraith, B. D., & O'Kennedy, R. (2011). Multisubstrate-compatible ELISA procedures for rapid and high-sensitivity immunoassays. *Nature Protocols*, *6*(4), 439-445.
208. Goyal, D. K., & SubRamanian, A. (2010). In-situ protein adsorption study on biofunctionalized surfaces using spectroscopic ellipsometry. Thin Solid Films, 518(8), 2186-2193.
209. Gorin, A., Copperwhite, R., Elmaghrum, S., McDonagh, C., & Oubaha, M. (2011, June). Hybrid zirconium sol-gel thin films with high refractive index. In*International Symposium on Photoelectronic Detection and Imaging 2011* (pp. 81911Q-81911Q). International Society for Optics and Photonics.
210. Oubaha, M., Smaıhi, M., Etienne, P., Coudray, P., & Moreau, Y. (2003). Spectroscopic characterization of intrinsic losses in an organic–inorganic hybrid waveguide synthesized by the sol–gel process. *Journal of non-crystalline solids*, *318*(3), 305-313.
211. Versace, D. L., Oubaha, M., Copperwhite, R., Croutxé-Barghorn, C., & MacCraith, B. D. (2008). Waveguide fabrication in UV-photocurable sol–gel materials: influence of the photoinitiating system. *Thin Solid Films*, *516*(18), 6448-6457.
212. McFaul, S. M., Lin, B. K., & Ma, H. (2012). Cell separation based on size and deformability using microfluidic funnel ratchets. *Lab on a chip*, *12*(13), 2369-2376.
213. Kim, M. S., Sim, T. S., Kim, Y. J., Kim, S. S., Jeong, H., Park, J. M., Moon, H-S., Kim, Sung. Il., Gurel, O., Lee, S. S., Lee, J.-G. & Park, J. C. (2012). SSA-MOA: a novel CTC isolation platform using selective size amplification (SSA) and a multi-obstacle architecture (MOA) filter. *Lab on a Chip*, *12*(16), 2874-2880.
214. Burger, R., Reith, P., Akujobi, V., & Ducrée, J. (2012). Rotationally controlled

magneto-hydrodynamic particle handling for bead-based microfluidic assays.*Microfluidics and Nanofluidics*, *13*(4), 675-681.

215. Gusterson, B. A., Warburton, M. J., Mitchell, D., Ellison, M., Neville, A. M., & Rudland, P. S. (1982). Distribution of myoepithelial cells and basement membrane proteins in the normal breast and in benign and malignant breast diseases. *Cancer research*, *42*(11), 4763-4770.
216. Trimmer, P. A., Swerdlow, R. H., Parks, J. K., Keeney, P., Bennett, J. P., Miller, S. W., Davis, R. E., & Parker, W. D. (2000). Abnormal mitochondrial morphology in sporadic Parkinson's and Alzheimer's disease cybrid cell lines. *Experimental neurology*, *162*(1), 37-50.
217. Bennett, J. M., Catovsky, D., Daniel, M. T., Flandrin, G., Galton, D. A., Gralnick, H. R., & Sultan, C. (1989). Proposals for the classification of chronic (mature) B and T lymphoid leukaemias. French-American-British (FAB) Cooperative Group. *Journal of Clinical Pathology*, *42*(6), 567-584.
218. Rosenbluth, M. J., Lam, W. A., & Fletcher, D. A. (2006). Force microscopy of nonadherent cells: a comparison of leukemia cell deformability. *Biophysical journal*, *90*(8), 2994-3003.
219. BNID: 108926, Milo *et al.* Nucl. Acids Res. (2010) 38 (suppl 1): D750-D753. http://bionumbers.hms.harvard.edu/bionumber.aspx?&id=108926&ver=1
220. Münz, M., Murr, A., Kvesic, M., Rau, D., Mangold, S., Pflanz, S., Lumsden, J., Volkland, J., Fagerberg, J., Riethmuller, G., Ruttinger, D., Kufer, P., Bauerle, P. A., & Raum, T. (2010). Side-by-side analysis of five clinically tested anti-EpCAM monoclonal antibodies. *Cancer Cell Int*, *10*, 44.
221. Jang, L. S., & Liu, H. J. (2009). Fabrication of protein chips based on 3-aminopropyltriethoxysilane as a monolayer. *Biomedical microdevices*, *11*(2), 331-338.
222. Seurynck-Servoss, S. L., White, A. M., Baird, C. L., Rodland, K. D., & Zangar, R. C. (2007). Evaluation of surface chemistries for antibody microarrays.*Analytical biochemistry*, *371*(1), 105-115.
223. Condo, P. D., Paul, D. R., & Johnston, K. P. (1994). Glass transitions of polymers with compressed fluid diluents: type II and III behavior.*Macromolecules*, *27*(2), 365-371.
224. Ogilvie, I. R. G., Sieben, V. J., Floquet, C. F. A., Zmijan, R., Mowlem, M. C., & Morgan, H. (2010). Reduction of surface roughness for optical quality microfluidic devices in PMMA and COC. *Journal of Micromechanics and Microengineering*, *20*(6), 065016.

5.2: Appendix

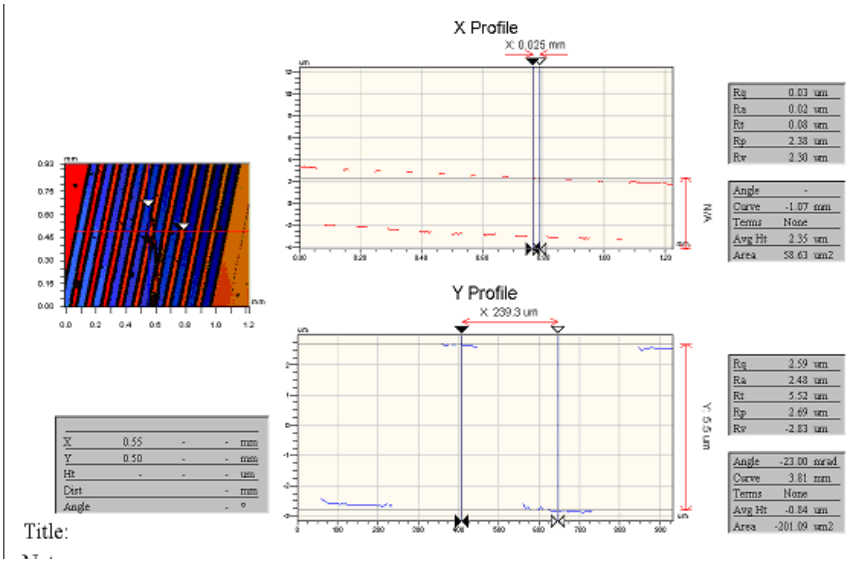

Figure 5.1: Optical profilometer height measurement of a 6µm x 6µm sol-gel waveguides fabricated on a silicon substrate.

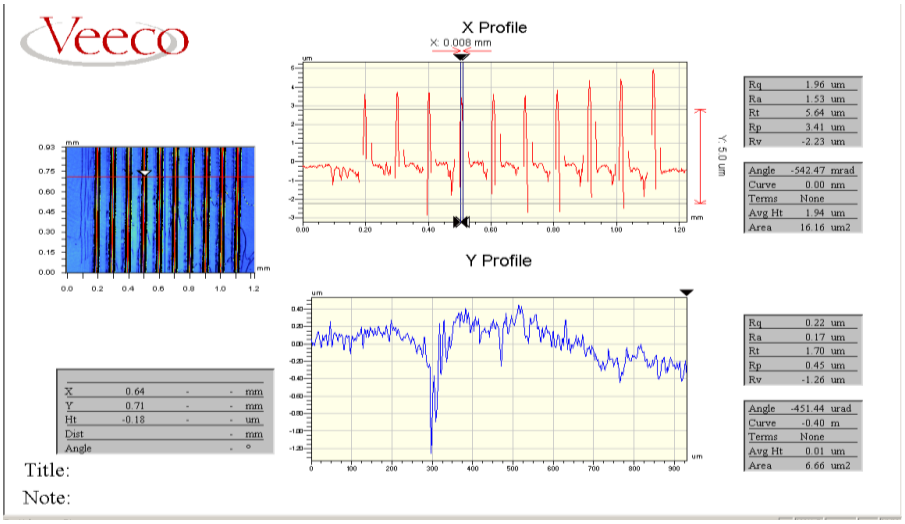

Figure 5.2: Optical profilometer width measurement of a 6µm x 6µm sol-gel waveguides fabricated on a silicon substrate.

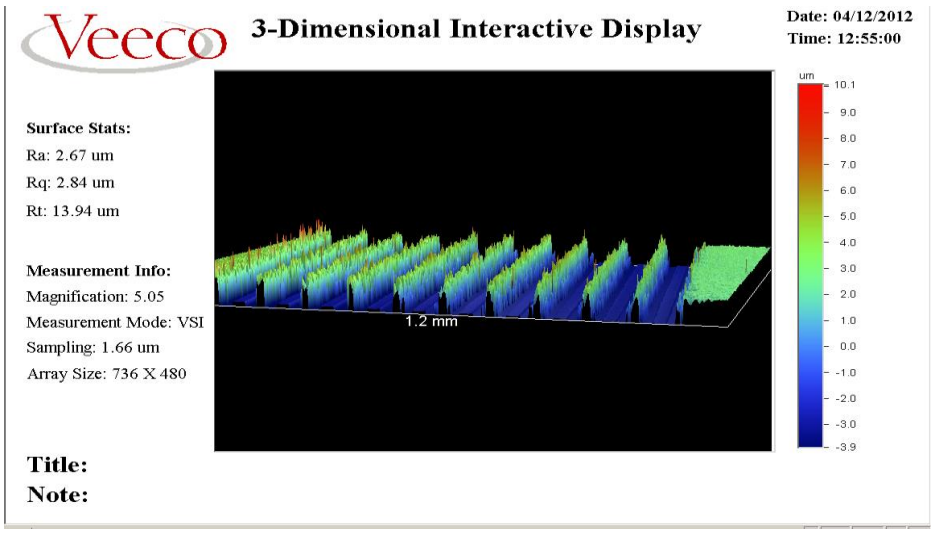

Figure 5.3 Optical profilometer imaging of 6µm x 6µm optical sol-gel waveguides on a silicon substrate.

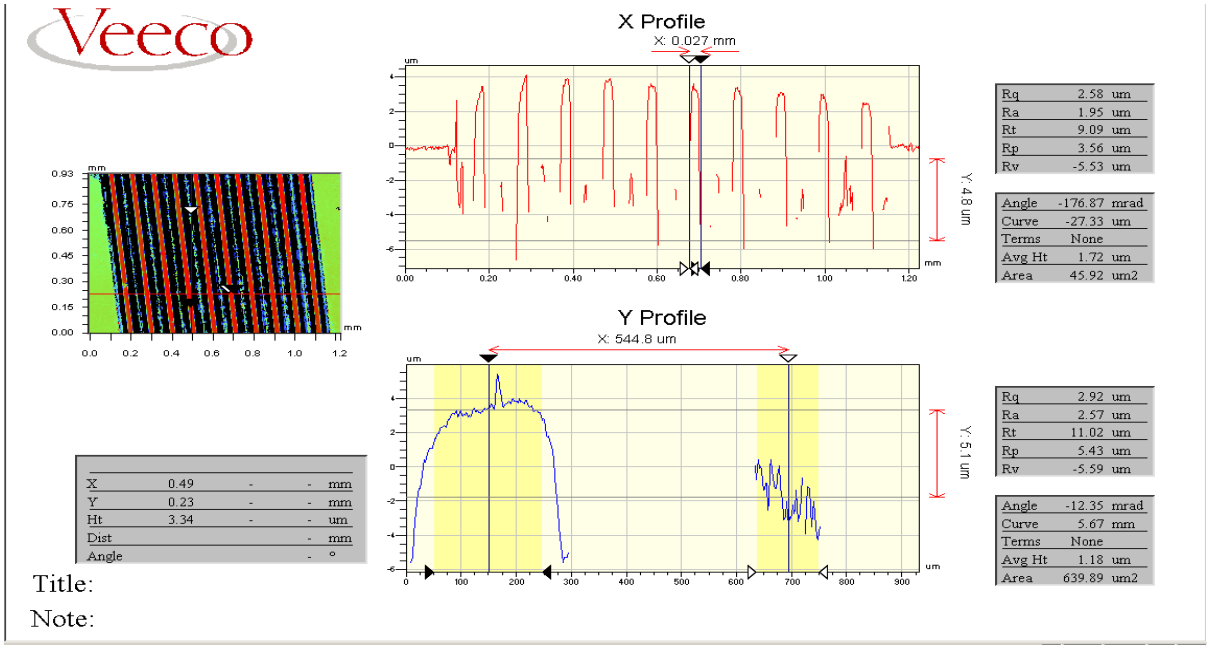

Figure 5.4: Optical profilometer height and width measurements of a 6 µm x 30µm sol-gel waveguides fabricated on a silicon substrate.

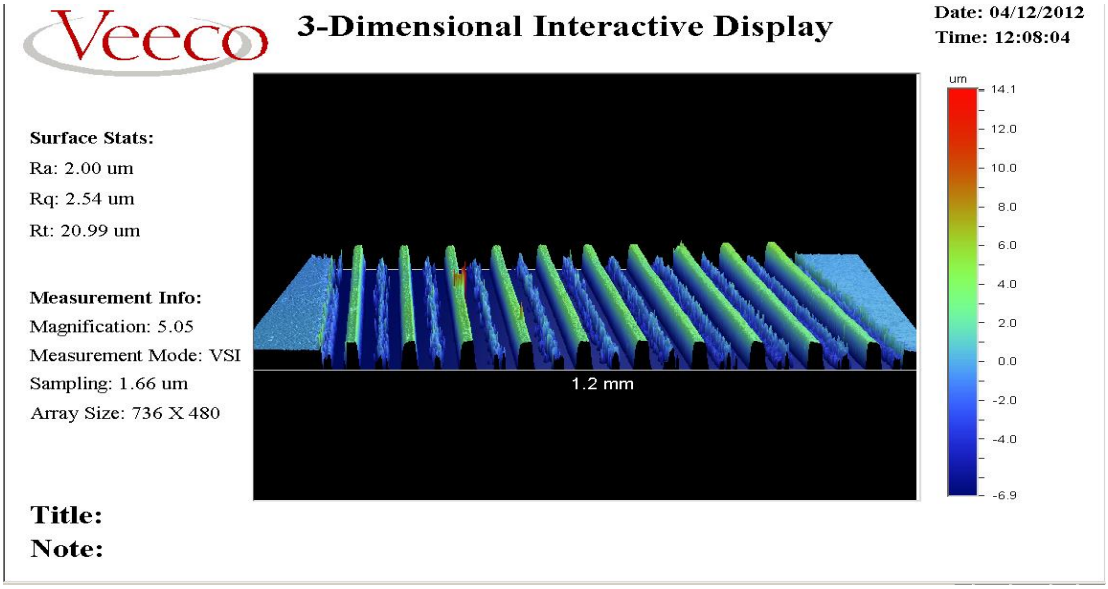

Figure 5.5 Optical profilometer image of 6µm high, 30µm wide optical sol-gel waveguides on a silicon substrate.

Parabolic filter gaps (µm) (Set 1)

	15.4	15.4	14.6	12.2	13.8	19.5	8.1	8.1	10.5	17.8	17.8	19.5
	13.8	14.6	13.0	13.8	13.8	17.8	6.5	9.7	8.9	15.4	18.7	18.7
	13.8	14.6	12.2	11.4	13.8	18.7	6.5	8.1	8.9	16.2	17.0	19.5
	15.4	13.8	13.0	13.8	15.4	18.7	8.1	8.5	11.4	17.8	20.3	17.8
		14.6	16.2	12.2	12.2	17.8	8.1	9.7	8.9	16.2	19.5	17.8
Experimental Average	**14.6**	**14.6**	**13.8**	**12.7**	**13.8**	**18.5**	**7.5**	**8.8**	**9.7**	**16.7**	**18.7**	**18.7**
Standard Deviation	0.9	0.6	1.6	1.1	1.1	0.7	0.9	0.8	1.2	1.1	1.3	0.9
Expected Value	**15.0**	**14.0**	**13.0**	**5.0**	**6.0**	**7.0**	**17.0**	**15.0**	**14.0**	**5.0**	**6.0**	**7.0**
Difference Between Expected and Experimental Value	0.4	0.6	0.8	7.7	7.8	11.5	9.5	6.2	4.3	11.7	12.7	11.7

Parabolic filter gaps (µm) (Set 2)

	21.1	19.5	16.2	18.7	19.5	25.1	16.2	17.0	17.8	10.5	11.4	12.2
	21.1	21.1	16.2	17.8	19.5	25.9	14.6	17.8	18.7	12.2	10.5	13.0
	19.5	21.9	17.0	19.5	20.3	24.3	14.6	16.2	18.7	11.4	13.0	12.2
	17.0	18.7	17.0	17.0	18.7	25.1	15.4	16.2	17.0	14.6	10.5	12.2
	17.8	19.5	15.4	17.8	18.7	23.5	13.8	17.0	17.8	10.5	11.4	11.4
Experimental Average	**19.3**	**20.1**	**16.4**	**18.2**	**19.3**	**24.8**	**14.9**	**16.8**	**18.0**	**11.8**	**11.4**	**12.2**
Standard Deviation	1.9	1.3	0.7	1.0	0.7	0.9	0.9	0.7	0.7	1.7	1.0	0.6
Expected Value	**17.0**	**15.0**	**14.0**	**5.0**	**6.0**	**7.0**	**17.0**	**15.0**	**14.0**	**5.0**	**6.0**	**7.0**
Difference Between Expected and Experimental Value	2.3	5.1	2.4	13.2	13.3	17.8	2.1	1.8	4.0	6.8	5.4	5.2

Table 5.1: Two sets of optical profilometry data, illustrating the fabrication challenges associated with producing reproducible parabolic filter structures in sections 3.1.4, 3.1.5 and 3.1.7. Wide variations within each size of parabolic gap, and between the recorded and expected values are shown.

Multi-Obstacle Architecture (MOA) filter gaps (µm) (Set 1)

16.2	16.2	29.4	15.4	18.7	28.4
17.8	16.2	27.6	15.4	18.7	28.4
23.5	17.0	28.4	13.8	19.5	29.2
26.8	17.8	29.2	16.2	18.7	28.4
17.8	18.7	30.0	17.8	20.3	28.4
21.9	17.0	27.6	14.6	18.7	28.4
30.8	18.7	29.2	14.6	20.3	28.4
16.2	17.0	28.4	15.4	20.3	30.0

Experimental Average	**21.4**	**17.3**	**28.7**	**15.4**	**19.4**	**28.7**
Standard Deviation	5.4	1.0	0.9	1.2	0.8	0.6
Expected Value	**6.2**	**9.1**	**18.9**	**6.2**	**9.1**	**18.9**
Difference Between Expected and Experimental Value	15.2	8.2	9.8	9.2	10.3	9.8

Multi-Obstacle Architecture (MOA) filter gaps (µm) (Set 2)

14.6	26.8	16.2	30.0
15.4	25.1	16.2	29.2
15.4	25.1	17.8	27.6
17.0	25.9	20.3	28.4
16.2	25.9	19.5	25.9
13.8	26.8	19.5	28.4
16.2	25.1	16.2	25.9
16.2	26.8	19.5	25.9

Experimental Average	**15.6**	**25.9**	**18.2**	**27.7**
Standard Deviation	1.0	0.8	1.8	1.6
Expected Value	**9.2**	**19.2**	**9.2**	**19.2**
Difference Between Expected and Experimental Value	6.4	6.7	9.0	8.5

Table 5.2: Two sets of optical profilometry data, illustrating the fabrication challenges associated with producing reproducible multiple obstacle architecture filter structures in sections 3.1.6 and 3.1.7. Wide variations within each size of multiple obstacle architecture gap, and between the recorded and expected values are shown.